Probing the protein homeostasis mechanisms in long-lived naked mole-rats

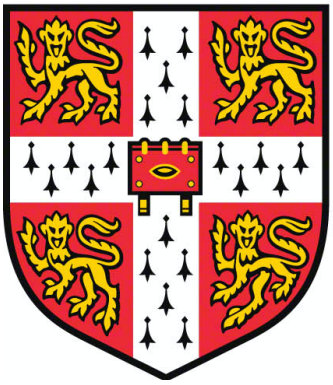

Zhen Du

Darwin College

University of Cambridge

Supervisors: Prof. Laura S Itzhaki & Dr. Janet R Kumita

This dissertation is submitted for the Degree of Doctor of Philosophy

January 2021

Declaration

This thesis is the result of my own work and includes nothing which is the outcome of work done in collaboration except as declared in the preface and specified in the text.

It is not substantially the same as any work that has already been submitted before for any degree or other qualification except as declared in the preface and specified in the text.

It does not exceed the prescribed word limit for the Biology Degree Committee.

Zhen Du
31 January 2021

Probing the protein homeostasis mechanisms in long-lived naked mole-rats

Zhen Du

The naked mole-rat (NMR) is a fascinating animal which has unique biological features including eusociality, strict subterranean inhabitation and poikilothermy. It is the longest-living rodent, showing negligible senescence over the majority of its lifespan and high resistance to diseases such as cancer and neurodegeneration. This animal is therefore a compelling system for understanding ageing and age-related diseases. Recent evidence suggests that protein homeostasis (proteostasis) mechanisms may play a vital role in mediating the resistance to multiple forms of stress and diseases and, subsequently, contribute to the exceptional longevity of the NMR. However, this view has been predominately based on protein-level and/or cell viability analyses, and our knowledge is still limited about the modulation of proteotoxic stress responses at the transcriptional level due to a lack of reliable and validated molecular tools.

This thesis sets out to develop, optimise and apply new methods to investigate two important and complex proteostatic mechanisms, namely the unfolded protein response (UPR) in the endoplasmic reticulum (ER) and macroautophagy (autophagy), in the NMR. Using these methodologies, the effects of pharmacologically induced *in vitro* stress and the effects of disease-related neurotoxic protein species on the UPR and autophagy in NMR fibroblasts were investigated. In Chapter 3, RNA-based methods, including an *Xbp1* splicing assay and quantitative PCR (RT-qPCR) assays were successfully established to probe the activation and outputs of the UPR in a NMR kidney fibroblast cell line in response to tunicamycin (TU) and thapsigargin (TG)-induced ER stress. In Chapter 4, differences between the UPR of NMR kidney fibroblasts and mouse homologues were identified, where a notably higher threshold of pharmacologically induced UPR activation was observed in the NMR under conditions of mild ER stress. In Chapter 5, LC3B turnover and transcriptional changes of autophagy markers under rapamycin (RA) and chloroquine (CQ)-treated conditions were monitored in an NMR skin fibroblast cell line, where the sensitivity of the NMR skin fibroblasts to CQ, when compared to NMR kidney fibroblasts and mouse NIH3T3 embryonic cells, seemed to be partly attributed to the downregulation of TFEB, a master transcription factor of autophagy. In Chapter 6, the effects of amyloid-beta (Aβ) and α-synuclein oligomers, which are believed to be the major pathogenic species of Alzheimer's and Parkinson's diseases, respectively, on the UPR and/or autophagy were investigated in NMR and mouse cells using a combination of

molecular and cellular tools. Although no significant changes of UPR markers were observed under Aβ oligomer-treated conditions, the chronic toxicity of wild-type α-synuclein oligomers seemed to be associated with downregulation of genes encoding ER chaperones and autophagy proteins. In Chapter 7, we demonstrate the utility of rational design to create a protein-specific binding probe for the NMR LC3B protein by introducing a peptide derived from a LC3-interacting region (LIR) motif into the inter-repeat loop of a consensus-designed tetratricopeptide repeat protein (CTPR). The results provide proof-of-concept validation of using CTPR-based probes to detect proteins in emerging animal models.

Having established a set of reliable methods to investigate the molecular details of the UPR and autophagy in the NMR, we have demonstrated unique features of the NMR, at the transcriptional level, when different forms of *in vitro* stress are employed. Exploiting these assays to measure the UPR and autophagy, as well as other proteostastic mechanisms, in the NMR under more disease-relevant conditions, may ultimately shed light on therapeutic developments to combat age-related neurodegenerative diseases.

To my family

Acknowledgements

I would like to express my deepest gratitude to my supervisors, Professor Laura Itzhaki and Dr. Janet Kumita, without whom none of this work would have been possible. Thank you, Laura and Janet, for providing me with the opportunity to work with you, for your insightful ideas and incredible patience, and for always encouraging, supporting and pushing me towards being an independent scientist. I have been so lucky to carry out my PhD research in Cambridge and even luckier to have both of you as my mentors. I would also like to thank the late Professor Sir Christopher Dobson for his tremendous support for this project. Special thanks go to Dr. Ewan St. John Smith, for providing the cute mole-rats and insightful advice.

Thanks in particular to the following people within the Itzhaki Group and in the Department of Pharmacology and Centre for Misfolding Disease: Dr. Pamela Rowling for her additional input and advice and for expertise on repeat proteins and biophysics; Catherine Xu, the α-synuclein expert who knows everything about chemistry and the confidante since we first met; Dr. Sampurna Chakrabarti and Dr. Yavuz Kulaberoglu for their invaluable advice and support for the UPR manuscript; Andrew Countryman for his work on CTPR; Marta Castellana-Cruz for her assistance in oligomer and fibril preparation; Dr. Gerard Callejo, Dr. Zoé Husson, and Dr. Laura Schuhmacher for their expertise on the neuronal cultures of NMRs; Dr. Fazal Hadi for providing me with NMR cell lines and primary cells; everyone in the Itzhaki Group for their support and for always making delicious cakes!

Thank you to the following people outside the lab: Dr. Wei Meng and Dr. Cen Zhang for always trusting, supporting and understanding me; Shengjun Ren, the technical expert and trustful friend; Ning Ding for always being there when I need help and for emotional support; Chengyi Xu, Jiazhen Shen and Weining Ning for their companion and support particularly during the thesis writing and COVID-19 lockdown.

A special thank you to Professor Allen Phillips, the great mentor of mine at Penn State, for teaching me everything about molecular cloning and protein purification, and for always encouraging me to pursue a career in science and research.

I would like to thank Herchel Smith Fund for providing incredible opportunities to connect young scientists at Cambridge and Harvard and for supporting us, Darwin College for supporting me in the past five years, and the Rosetree Trust for supporting this project.

This thesis is dedicated to my family – my parents and grandparents – who have been supporting me for nearly thirty years and who will always be here supporting me for the rest of my life.

这篇博士论文献给我最亲爱的父母、爷爷奶奶、外公外婆。
感谢您们近三十年来的养育、包容和支持。

Table of Contents

List of Figures

List of Tables

1. Introduction

1.1. The exceptional longevity of naked mole-rats (NMRs)

Naked mole-rats (NMRs) (*Heterocephalus glaber*), native to East Africa and within the genus *Heterocephaslus* of the African mole-rats (family Bathyergidae), are the longest-living rodents known[1] (**Figure 1.1**). The NMR was first characterised as a species in 1842 by Edward Rüpell and was first studied in captivity in 1957[2]. The most striking feature of the NMR is their exceptional longevity, with a maximum lifespan of over 30 years, about five-fold greater than predicted allometrically for a rodent weighing 40 grams and eight times longer than the lifespan of the similar-sized mouse[3]. They demonstrate negligible senescence, as indicated by only slight age-related metabolic and vascular changes, sustained fertility and neurogenesis for over two decades, and remarkable resistance to cancer and neurodegeneration[4]. These findings have established the NMR as a prime model organism in ageing and longevity research.

Figure 1. 1. The naked mole-rat. Photo credit to Juliette Martineau.

Several mechanisms have been proposed to contribute to the longevity of NMRs, most of which align to the established hallmarks of ageing[5], including the behavioural and physiological traits adapted to their living environment, oxidative stress resistance, telomere maintenance, cancer resistance, and well-maintained protein homeostasis (i.e., the state of a balanced and healthy proteome).

The strictly subterranean habitation shields NMRs from external predators and hazards, and the eusocial, cooperative lifestyle further increases the chance of survival for NMRs. The NMR is one of only two eusocial mammals which live in large colonies of up to 300 individuals[6]. In each colony, only one breeding queen mates with one to three males, whereas the remaining mole-rats assist in the rearing and foraging of pups and colony maintenance and defense[6]. Notably, female mole-rats display no menopause and can maintain high fertility beyond the age of >30, with the older breeders producing larger pups, although with lower survival, than the less established breeders[7]. NMRs reside in an extensive maze of burrows 0.5-2.5 meters below ground with limited heat and gas exchange, resulting in hypoxic and hypercapnic conditions[8]. They have evolved a set of traits that are well adapted to their natural habitat. NMRs are considered the only poikilothermic mammal, with a lower body temperature at ~32°C, same as the ambient temperature of sealed burrows, and have a higher rate of thermal conductance[9]. They are highly resistance to hypoxia, even at 3% oxygen, which is associated with a substantially decreased metabolic rate[10]. The downregulation of basal metabolism in NMRs may also be associated with the low levels of growth hormones, thyroid hormones, insulin, insulin-like growth factor 1 (IGF-1), which has been linked to prolonged longevity[7,11]. In addition, NMRs have pronounced resistance to a wide range of stressors *in vivo* and *in vitro* such as heavy metals and glucose deprivation, which may well represent the harsh milieu in which NMRs live.

The oxidative stress theory of ageing postulates that the cellular dysfunction observed during ageing can be attributed to the deleterious effects of reactive oxygen species (ROS)[12]. The NMR is an exception to the rule. Comparative studies between young, physiologically age-matched NMRs and mice showed that the NMRs, whose hypoxic habitation facilitate H_2O_2 production, accumulate higher levels of ROS in arteries[13] and more oxidative damages to macromolecules including DNAs, lipids and proteins in urine and various tissues with significantly lower levels of antioxidants such as glutathione peroxidase[14–17]. However, these levels of oxidative damages remain stable throughout the NMR lifespan, and the arteries of

NMRs appear to be highly resistant to proapoptotic effects of ROS[15,16,18]. Several endogenous protective mechanisms have been identified that may prevent the exacerbation of accumulated oxidative damage in the NMR, including the enhanced ability of mitochondria to eliminate ROS[19] and increased activity of erythroid 2-related factor (Nrf2) signalling, which induces the expression of cytoprotective components in redox homeostasis such as peroxiredoxin 1 and thioredoxin reductase 1[20,21]. Taken together, these findings suggest that the strong tolerance of high-level oxidative stress, but not the absolute magnitude of the cellular oxidative stress, may contribute to the longevity of NMRs. It is noteworthy that the constitutive upregulation of Nrf2 pathways also enhances proteasome activity and the expression of molecular chaperones in NMR fibroblasts, which may play a critical role in counteracting the higher levels of oxidative stress[20,21].

Telomere length progressively decreases with advancing age and is considered a biomarker of ageing[22]. In NMRs, genes including *Terf1, Tep1* and *BRCA1* that regulate telomere length have undergone positive selection[23,24]. A higher copy number of *TINF2*, a protector of telomere integrity, and *CEBPG*, a regulator of DNA repair, was also found in the NMR, thus suggesting the increased stability of its telomere and genome[25]. Telomerase RNA genes in NMR stem cells have shown unique polymorphisms and promoter structures that may also contribute to an increased telomerase activity[26]. However, studies directly evaluating the telomere length and telomerase activity in NMRs have obtained equivocal and contradictory results[27]. Seluanov *et al.* found higher telomerase activity but shorter telomeres in NMR somatic cells than mice counterparts[28]. Gomes *et al.* reported that the telomeres of NMRs were only one-third to half of those of laboratory mice and rats, approximately as long as human telomeres, with decreased telomerase activity in NMR dermal fibroblasts, which was one-third of that in mouse cells[29]. A recent study showed no age-associated attrition but mild elongation in the telomeres from NMR leukocytes, whereas the telomeres in mice and rats declined with age[30]. These data suggest that telomere length and telomerase activity may be highly dependent on the types of tissues and cells, as well as the ages of animals examined. Given the complicated role played by telomeres in ageing and cancer[22], the relationship between telomere maintenance and the longevity of the NMR needs careful further investigation.

Cancer incidence in the NMR is very rare. Experiments on NMR skin fibroblasts transduced with SV40 large T antigen (SV40LT) and Ras^{G12V} showed that they entered crisis and were unable to generate tumours following the transplantation into immunodeficient mice, whereas

similarly transduced mouse and rat cells formed tumours[31]. Increased levels of tumour suppressor protein p16 have been suggested to contribute to the 'early contact inhibition' observed in NMR primary dermal fibroblasts and may mediate cancer resistance[32]. Further analysis revealed that the *INK4* locus in the NMR encoded a novel hybrid p15/p16 isoform of tumour suppressor protein[33]. NMR-induced pluripotent stem cells also do not display teratoma-forming tumorigenicity, which is likely due to the activation of a tumour-suppressor alternative reading frame and a disruption mutation of the oncogene ES cell-expressed Ras[34]. Tian *et al.* reported that the cancer resistance of NMRs was mediated by high-molecular-mass hyaluronan produced by NMR cells and showed that wild-type NMR cells, but not cells with disrupted hyaluronan expression, were resistant to the transformation by SV40LT and oncogenic $hRas^{G12V}$[35]. However, the Khaled and St John Smith labs successfully transformed NMR cells from multiple tissues and animals by SV40LT and $HRAS^{G12V}$, although using a different lentiviral system, and showed that the cancer resistance of NMRs might be related to a unique microenvironment and/or immune system[36]. Single-cell RNA-sequencing also showed that the NMR immune system was characterised by a high myeloid-to-lymphoid cell ratio, which might constitute its novel myeloid-based system of innate immunosurveillance for cancer[37]. More studies need to be carried out to identify and validate the decisive factors for the NMR's cancer resistance.

Recently, accumulating evidence has indicated that the maintenance of protein homeostasis (or proteostasis) may be a determinant for the healthy longevity of the NMRs, which has also been observed in long-lived bivalve molluscs including *Arctica islandica* (maximum lifespan >500 years)[38] and pigeons (maximum lifespan up to 35 years)[39], suggesting a universal role of proteostasis in longevity across the animal kingdom.

1.2. Protein homeostasis

Proteins are fundamental structural and functional building blocks in every cell and play a vital role in almost all biological processes. In order to carry out biological activities, proteins must fold into their correct three-dimensional structures that bring key functional groups into close proximity to develop selectivity to interact with their natural partners and long-term stability in biological environments[40]. During folding, each protein navigates a unique energy landscape encoded by its amino acid sequence and forms a thermodynamically stable, native structure that represents an energy minimum in the landscape under physiological conditions[40]. Since

the folding process is a stochastic search of the many conformations accessible to a polypeptide chain, a protein may also adopt a kinetically stable (trapped) non-native structure that is prone to intermolecular interactions, thus leading to the formation of aggregated species that can be more thermodynamically favourable than the native structure and potentially toxic (**Figure 1.2)**[40,41]. In cells, newly synthesised polypeptide chains can start folding co-translationally on the ribosome or in the cytosol after dissociation from the ribosome, whereas others fold in specific cellular compartments such as endoplasmic reticulum (ER) and mitochondria[40,42]. These nascent chains and partially folded intermediates inevitably expose to the solvent some regions that are normally buried in their native structures and are prone to aggregation in the highly crowded cellular environment[40,42]. The stability of folded proteins may also be compromised by environmental challenges such as increased temperature, harsh pH, ROS and heavy metals. Therefore, cells have evolved a sophisticated quality control network to assist in correct protein folding and prevent the accumulation of misfolded species, both during *de novo* protein folding and under stressed conditions, and maintain proteostasis[41]. The proteostasis network encompasses machineries and systems that are essential for protein biogenesis and degradation, including molecular chaperones and proteolytic degradation pathways including the ubiquitin-proteasome system (UPS), autophagy, and the ER-associated degradation (ERAD) (**Figure 1.3**). Under stressed conditions, the protein-folding and protein-degradation capacity can be monitored and enhanced by multiple pathways including the heat shock response (HSR) in the cytosol and the unfolded protein response (UPR) in the ER and mitochondria to counteract proteotoxicity[43].

The proteostasis network is, however, impaired with ageing, which leads to the accumulation of damaged or misfolded proteins and contributes to cellular dysfunction and pathologies[5,44–46]. The pathologic process of protein aggregation is associated with a number of age-associated diseases, and in particular, neurodegenerative disorders such as Alzheimer's disease (AD) and Parkinson's disease (PD) that are characterised by insoluble deposits and inclusions composed of highly ordered, cross-β-sheet-enriched amyloid fibrils[47]. AD is characterised by deposition of amyloid beta (Aβ) plaques and neurofibrillary tangles (hyperphosphorylated tau protein aggregates). In PD, aggregates of the 14 kDa protein α-synuclein are the major components of Lewy bodies and neutrites, which emerge as the pathological hallmark of the disease, together with loss of dopamine neurons in the substantia nigra pars compacta. It is now widely accepted that it is the soluble oligomeric species, rather than amyloid deposits or inclusions, that are the most toxic and pathogenic species[48–53].

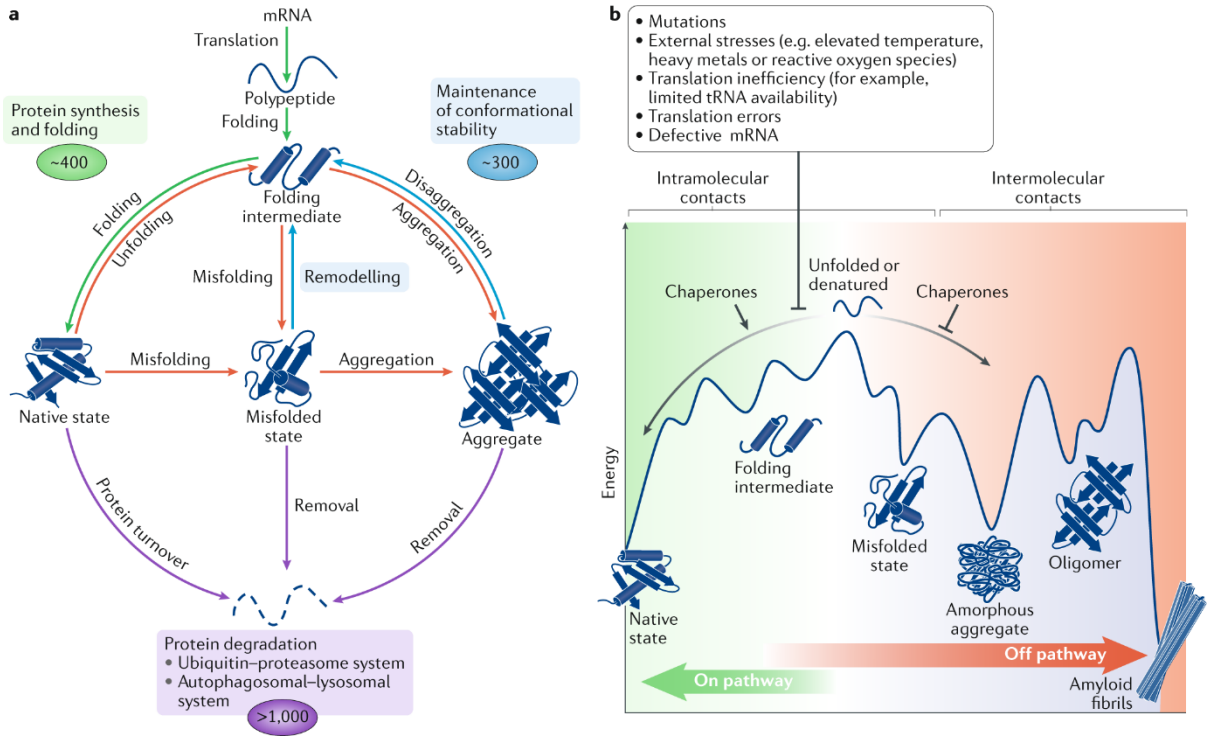

Figure 1. 2. Protein folding and misfolding. (a) The protein homeostasis network tightly regulates the functional levels of proteins in their native states and minimises the formation of aberrant, off-pathway products. The human proteostasis network comprises ~2000 proteins and is clustered into three major functional arms: protein synthesis and folding (green), conformational maintenance (blue) and degradation (purple). **(b)** Each protein navigates a complicated energy landscape during folding, gradually forming native intramolecular interactions towards the thermodynamically stable, native state. Intermolecular contacts between non-native states may result in the formation of aggregated species such as oligomers, amorphous aggregates and amyloid fibrils which may present a global minimum in the energy landscape. Various external stresses and cellular defects may lead to protein misfolding and aggregation, which can be prevented or rescued by molecular chaperones. Oligomeric species are the most neurotoxic species and have been increasingly implicated in the pathogenesis of a number of neurodegenerative diseases. Figure reprinted from the reference with permission[41].

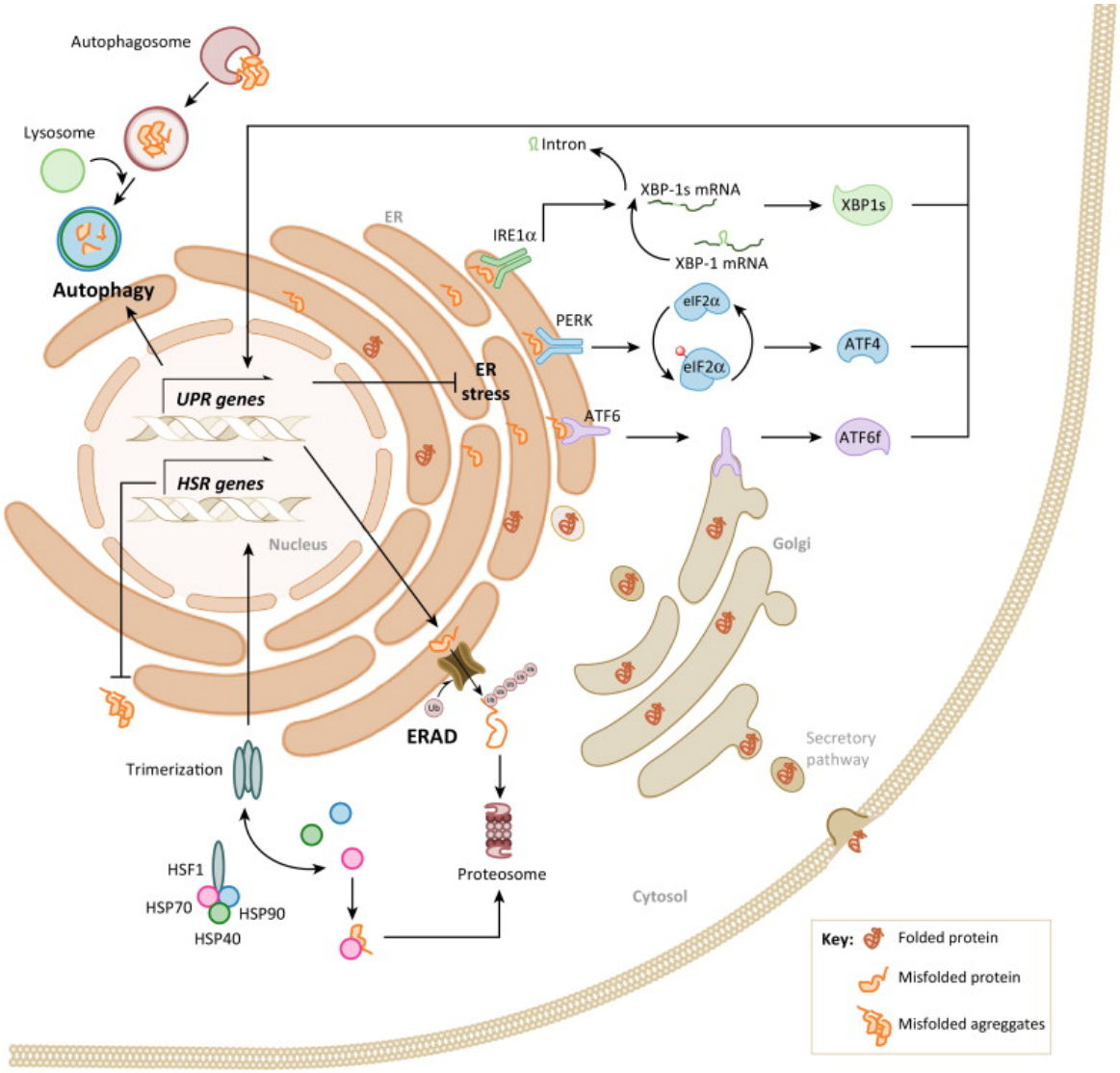

Figure 1. 3. The proteostasis network. The proteostasis network comprises molecular chaperones and proteolytic degradation mechanisms including UPS, autophagy and ERAD. Stress-induced responses including HSR, UPR in the ER and mitochondria, also play an important role in modulating protein homeostasis within the cell. Figure reprinted from the reference with permission[43].

Cells and tissues from aged short-lived organisms display decreased levels of basal and stress-induced expression of heat shock protein 70 (Hsp70)[54–56], reduced expression and activity of ER chaperones and protein disulphide isomerases (PDIs)[57–59], altered proteosome structure, expression and activity of proteasome[60,61] and reduced macroautophagic proteolysis[62], although some of these changes are not universal and can be tissue-specific. Studies have also shown that when challenged with a toxic insult such as heat shock or the ER stress inducer tunicamycin, the induction levels of HSR- and UPR-related genes in *C. elegans* were markedly reduced throughout the soma at an early stage of adulthood[63,64]. This age-dependent collapse of proteostasis, however, could be restored by genetically enhancing the expression of stress responsive factors HSF1 or DAF-16 (in the case of heat shock), and XBP1s (in the case of ER stress)[63,64]. In addition, overexpression of proteostasis components, including chaperones[65,66], UPR-[67] and autophagy-related[68,69] proteins, have contributed to a decrease in disease-relevant protein aggregation and toxicity in various disease models.

In contrast to short-lived species, long-lived NMRs seem to have robust abilities to maintain proteostasis, which does not change over time. NMR liver tissue homogenates showed marked resistance to *in vitro* unfolding stress (urea) when compared to mice tissues[16]. Triosephosphate isomerase and cytosolic peroxiredoxin, although heavily carbonylated in NMR kidneys, remained functional[70]. These findings suggest that NMRs may have evolved inherent protective mechanisms against protein damage. NMRs may regulate damaged protein via increased translational fidelity, which is linked to its unique fragmented 28S ribosomal RNA structure and thus decreases chances of aberrant protein folding during translation[71]. Enhanced UPS and autophagy mechanisms have also been revealed in the NMR, which ensure efficient degradation of damaged proteins from the cell. NMR liver lysates showed an increased proteasome activity when compared with mouse liver lysates, which was accompanied by a lower level of ubiquitination, an unaltered level of cysteine oxidation during ageing[16] and higher levels of molecular chaperones including HSP70, HSP40, HSP25 and heat-shock factor 1 (HSF-1)[72]. The NMR proteasome is protected from inhibition by a transferable chaperone-containing cytosolic factor that interacts with the proteasome and enhances its activity[73]. NMR skin fibroblasts also showed higher levels of HSP70 and HSP40 and 20S proteasome activity compared to mouse homologous both under normal and stressed induced conditions[74]. Nrf2, which regulates the proteasome system and expression of molecular chaperones, is also highly expressed in NMR fibroblasts[20,21]. In multiple tissues from NMRs, higher basal-level autophagy was observed compared with those from young mice, as suggested by a higher level

of LC3 (light chain 3) proteins, despite a lower level of Beclin-1[75]. NMR skin fibroblasts also displayed increased autophagic degradation under normal and stress-induced conditions[74]. Taken together, these findings suggest that the robust ability of NMRs to maintain protein homeostasis is closely associated with and may be the most critical determinant for, the NMR's exceptional longevity. Intriguingly, although resistant to a number of different stressors, NMR skin fibroblasts are sensitive to two endoplasmic reticulum (ER) stressors, tunicamycin (TU) and thapsigargin (TG), which can activate the unfolded protein response (UPR), a critical proteostasis mechanism that has not been investigated previously in the NMR[76]. Outstanding questions are: *Why do NMR fibroblasts seem to be particularly resistant to ER stressors? Does the UPR in the NMR possess any unique features that differ from the UPR in other short-lived counterparts?* Appropriate and highly reliable methods to probe the UPR in the NMR need to be established to answer these questions, which will be presented in Chapter 3. Molecular insights into the UPR activation in response to ER stressors in the NMR fibroblasts will be further explored in Chapter 4.

NMRs exhibit vitamin D deficiency[77] and high levels of oxidative stress[17], which are the two risk factors of neurodegeneration. Furthermore, compared with a transgenic mouse model of AD, NMRs express comparable levels of Aβ and phosphorylated tau proteins[78,79]. However, neither plaque formation nor an age-related increase in Aβ has been observed in NMRs at various ages from 2 to >20 years old[36]. Levels of neurotoxicity in mouse hippocampal neurons after the exogenous addition of human or NMR $A\beta_{1-42}$ peptide were almost identical despite little variations in the $A\beta_{1-42}$ peptide sequences and their propensity to aggregate[36]. In contrast to the somatodendritic accumulation of mislocalised, hyperphosphorylated tau proteins in the AD mouse hippocampal neurons, NMRs do not develop the neurofibrillary tangle pathology in brains and maintain tau expression within the axonal compartments[79]. Therefore, it appears that novel mechanisms must be involved in NMRs that enable them to tolerate sustained high levels of Aβ and phosphorylated tau proteins and protect the brain from harmful effects. It has been shown that NMR brains can maintain high levels of autophagy throughout the majority of their lifespan[80], suggesting that autophagy, and potentially other proteostasis mechanisms in the NMR, may enhance its capability to process and degrade those disease-relevant, aggregation-prone protein species. A recent study has demonstrated that NMR skin fibroblasts are resistant to the toxicity of polyglutamine (polyQ), a well-established model of protein aggregation, through the formation of aggresomes, and that autophagy seems to have the greatest effect on lowering the proteotoxic effects compared to the proteasome and molecular

chaperones[81]. *How do the proteostasis mechanisms in NMR cells, including autophagy and the UPR, respond to the stresses induced by other disease-relevant proteins, such as Aβ (in AD) and α-synuclein (in PD), and specifically, in the most toxic oligomeric forms?* This question will be explored in Chapter 6, following the establishment of assays to probe the autophagy, particularly the transcriptional regulation that has not been explored yet, in the NMR cells in Chapter 5.

1.3. Unfolded protein response (UPR)

The ER is an organelle essential for protein synthesis and transport in the secretory pathway. Nearly one-third of the human proteome is trafficked from the ER to other compartments in the endomembrane system, for secretion or display on the cell surface[40]. In eukaryotic cells, secretory proteins are synthesised by ER-bound ribosomes and folded and assembled in the ER lumen, which constitutes an oxidative environment rich in calcium, foldases (peptidyl prolyl isomerases and protein disulphide isomerases) and molecular chaperones. The protein-folding process in the ER can be challenged by various physiological disturbances and pathological conditions, a cellular state called ER stress that results in the accumulation of unfolded and misfolded proteins in the lumen. Sensing an insufficiency in the ER's capacity to handle the load of unfolded proteins, a collection of intracellular pathways is activated, termed the unfolded protein response (UPR), which either re-establishes homeostasis by adaptive responses or triggers cell death by apoptotic mechanisms[82] (**Figure 1.4**).

Under mild-level ER stress, UPR activation mediates the expansion of the ER membrane and operates through transcriptional regulation as a feedback loop that attenuates protein influx into the ER and enhances the protein folding, quality control and degradation machineries. Incorrectly folded proteins are retro-translocated back into the cytosol and degraded by the UPS, a pathway referred to as ER-associated degradation (ERAD)[83]. Severely misfolded proteins and protein aggregates can be degraded, along with the damaged ER, by autophagy[84]. Many of the components in ERAD and autophagy have been identified as UPR targets and are important for cell survival. Prolonged activity of the UPR, however, induces apoptosis under unmitigated ER stress, to eliminate rogue cells detrimental to the organism.

The mammalian UPR is mediated by three principal arms working in parallel, each defined by a class of stress sensors located at the ER membrane, including inositol-requiring enzyme 1

(IRE1), activating transcription factor 6 (ATF6) and protein kinase RNA-like ER kinase (PERK)[82]. In each branch, the respective membrane protein senses the status of protein folding in the ER lumen and transmits the signal across the membrane to cytoplasmic transcription factors that reprogramme gene expression and therefore remodel cellular physiology in response to ER stress (**Figure 1.4**).

The most conserved and the only UPR branch present in lower eukaryotes is initiated by IRE1. IRE1 is an ER-resident type I transmembrane protein which is composed of cytoplasmic protein kinase and endoribonuclease (RNase) domains, with a stress-sensing domain situated in the ER lumen[82]. In response to ER stress, inactive, monomeric IRE1 dimerises and stacks into higher-order oligomers[85,86], which juxtaposes the kinase domains for autophosphorylation, leading to a conformation change that activates the RNase domain[87]. Activated IRE1 cleaves the mRNA encoding the basic leucine zipper-type (bZIP) transcription factor, X-box binding protein 1 (XBP1), precisely at two positions, which excises a 26-nucleotide intron and shifts the coding frame of the mRNA[88]. The spliced 5' and 3' exons are ligated by the tRNA ligase complex[89,90], leading to the expression of a more active and stable form of the transcription factor, known as XBP1s (spliced XBP1). XBP1s is translocated to the nucleus and activates a subset of the UPR target genes involved in protein folding, ERAD and lipid biosynthesis[91,92]. The efficient splicing of XBP1 mRNA is mediated by XBP1u protein (unspliced XBP1), which pauses translation and drags the mRNA-ribosome-nascent-peptide complex to the ER membrane[93]. XBP1u is constantly expressed, and as recovery from ER stress occurs, it accumulates and dimerises with XBP1s to induce the degradation of the XBP1u/s complex by the UPS in the cytosol[94]. This negative feedback loop can attenuate the IRE1-XBP1 response in a timely manner[94].

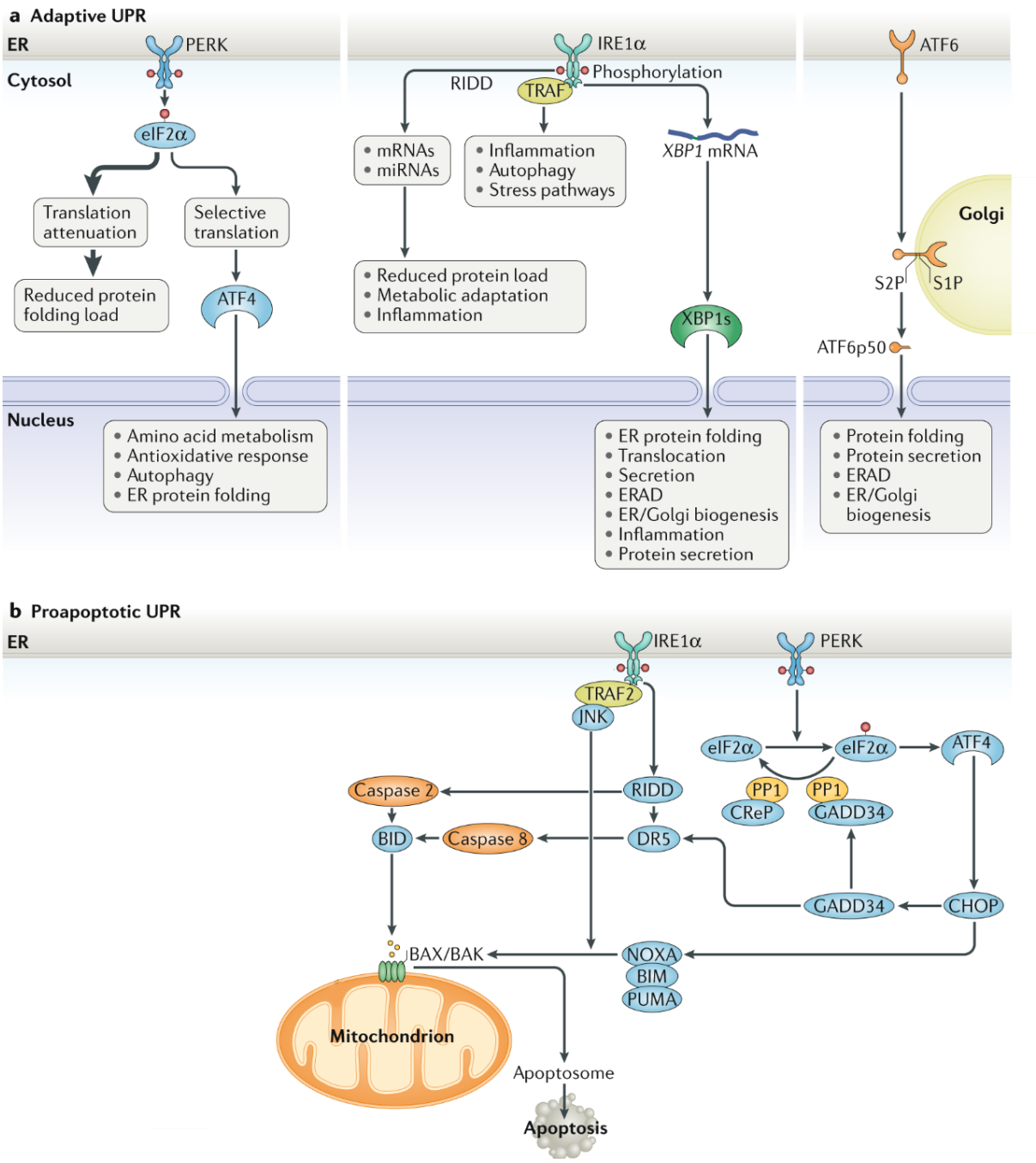

Figure 1. 4. Unfolded protein response in the ER. The UPR in the ER consists of three branches defined by three transmembrane proteins, IRE1, ATF6 and PERK. Accumulation of unfolded or misfolded proteins, or the ER stress, activates the UPR, which enhance protein-folding capacity and degradation to counteract the proteotoxic stresses **(a)**. However, prolonged activation of UPR may lead to detrimental effects and thus apoptosis **(b)**. Figure modified from the reference[95].

In mammalian cells, IRE1 can also function independently of XBP1 mRNA splicing. Activated IRE1 RNase can selectively degrade ER-localised mRNAs through the regulated IRE1-dependent decay (RIDD), which reduces the translational load early in the UPR[96–98]. However, IRE1 RNase can also cleave microRNAs that repress the translation of pro-apoptotic caspase-2[98], and the continued decay of mRNAs encoding ER-resident secretory cargo and chaperones under unmitigated ER stress may lead to cell death[96]. In addition, activated IRE1 can interact with TRAF2 (tumour necrosis factor receptor-associated factor-2)[99] to upregulate ASK1 (apoptosis single-regulating kinase-1) and its downstream target JNK (c-JUN N-terminal kinases)[100], as well as the caspase-12 that mediate the ER-stress-induced apoptosis[99] (**Figure 1.4 b**).

ATF6 is a novel signal transducer in the mammalian UPR. It is constitutively expressed in cells as an inactive precursor, which is an ER-resident type II transmembrane glycoprotein bearing a bZIP motif facing the cytoplasm and a stress-sensing ER-luminal domain[82]. Under ER stress, ATF6 is delivered from the ER to the Golgi apparatus, where it is processed by S1P (site-1 protease) and S2P (site-2 protease), which cleaves the luminal domain and the transmembrane anchor sequentially, releasing the cytoplasmic DNA-binding fragment (ATF6f)[101]. ATF6f moves to the nucleus and induces the transcription of major ER chaperones including GRP78/BiP (binding immunoglobulin protein) and GRP94 (glucose-regulated protein 94) as well as PDIs. ATF6f is also required for IRE1 signalling; the two pathways may merge through the regulation of XBP1 and the formation of an ATF6/XBP1 heterodimer to further upregulate the transcription of ERAD components[102].

The third ER stress transducer, PERK, like IRE1, is an ER-resident transmembrane protein which has a luminal stress-sensing domain and a cytoplasmic Ser/Thr protein kinase domain[82]. Activation of PERK involves oligomerisation and autophosphorylation; activated PERK in ER-stressed cells further phosphorylates eIF2α (the α subunit of eukaryotic translation initiation factor-2) at Ser-51[82]. This phosphorylation inhibits the guanine nucleotide exchange factor, eIF2B, from recycling eIF2 into its active GTP-bound form, thereby preventing the formation of the eIF2•GTP•Met-tRNA^{Met} ternary complex and inhibiting translation initiation, which subsequently reduces the load of protein destined to enter the stressed ER[82]. Whereas the PERK-mediated phosphorylation of eIF2α decreases global protein synthesis, it can induce the translation of certain mRNAs, including ATF4[103], an important transcription factor that regulates the levels of genes involved in redox balance, amino acid metabolism and transport,

protein folding, apoptosis and autophagy[104]. In stressed cells, reduced levels of the active eIF2-GTP allow ribosomes to scan through an upstream open reading frame (uORF), which blocks ATF4 expression under non-stressed conditions, so that the translation of ATF4 ORF can be reinitiated[103].

PERK/eIF2α signalling is cytoprotective at modest levels of signalling, but sustained eIF2α phosphorylation can induce cell death through the upregulation of CHOP (transcription factor C/EBP homologous protein)[105] and GADD34 (growth arrest and DNA damage-inducible 34)[106]. CHOP is a non-ER localised bZIP transcription factor that belongs to the C/EBP family and is highly induced during ER stress. It is a transcription factor regulating many physiological processes including cell differentiation, proliferation and apoptosis[107]. In ER-stressed cells, the expression of CHOP is induced predominantly through ATF4 binding to the promoter of *Ddit3* (which encodes CHOP) but may also be mediated by XBP1 and ATF6[108,109]. Deregulated *Ddit3* expression compromises cell survival, whereas *Ddit3* deletion protects cells from the lethal consequences of ER stress, indicating that CHOP mediates cell death under irreversible ER stress. It has been shown that CHOP suppresses the pro-survival protein Bcl-2 (B cell lymphoma-2) under ER stress conditions while upregulating proteins in the pro-apoptotic BH3-only family that induce BAX (BCL-2-associated X protein) and/or BAK (BCL-2 antagonist or killer)-dependent mitochondrial apoptosis[107]. A recent study noted that CHOP may also activate the expression of DR5 (death receptor 5) to trigger caspase-8-mediated apoptosis. GADD34 mediates another mechanism of CHOP-dependent cell death[110]. Under ER stress, GADD34 can be upregulated by CHOP and participate in a negative-feedback loop that limits the impact of PERK signalling[106]. GADD34 associates with the catalytic subunit of protein phosphatase 1 to promote the dephosphorylation of eIF2α *in vitro*, which restores protein synthesis[106]. The increased load of proteins into the stressed ER results in ATP depletion, oxidative stress and cell death. On the other hand, a GADD34-mediated regulatory loop can induce the expression of stress-induced UPR proteins for long-term adaption and may promote cell survival by limiting the activity of pro-apoptotic effectors such as CHOP[111]. Interestingly, it has also been shown that CHOP and ATF4 can cooperate to enhance protein synthesis in a manner that is independent of GADD34, presumably through transcriptional activation, indicating that other genes may also contribute to the translational recovery leading to the cell death[112] (**Figure 1.4 b**).

Altered ER function is common in neurodegenerative diseases, although most of the protein aggregates accumulate in the cytosol or are deposited extracellularly rather in the ER lumen (**Figure 1.5**). A number of studies of human autopsy brain samples and neuronal cells derived from patient-specific induced pluripotent stem cells (iPSCs) have demonstrated activation of the UPR, thus suggesting a critical role played by the ER stress in the pathogenic neuronal response. Increased levels of BiP expression and PERK signalling were reported in AD hippocampus[113] and temporal cortex[114]. Phosphorylated PERK and eIF2α were also seen in the substantia nigra pars compacta of PD cases but not in healthy controls[115]. Analysis of cortical neurons generated from iPSCs from PD patients harbouring α-synuclein mutations revealed strong and early ER stress which was accompanied by nitrosative stress and impaired ERAD[116]. Over the last decade, genetic and pharmacological manipulation of the UPR have also been used to understand the causal link between ER stress and neurodegeneration, wherein distinct UPR branches have specific, and sometimes opposite, effects on the disease pathophysiology depending on the disease type, the neurons affected and the stage of the disease. The role of IRE1 signalling has been extensively investigated in the context of the downstream XBP1s function, and most studies indicate a neuroprotective function of XBP1s in AD and PD. Overexpression of XBP1s suppresses Aβ toxicity in flies expressing two copies of human $A\beta_{1-42}$ and rat PC12 cells treated with $A\beta_{1-42}$ oligomers[117]. Downregulation of XBP1 in glial cells of an $A\beta_{1-42}$ transgenic *Drosophila* model enhances neurotoxicity and accumulation of $A\beta_{1-42}$ and polyubiquitinated proteins, suggesting a neuroprotective role of XBP1s, while overexpression of XBP1s reduces $A\beta_{1-42}$ levels and improved geotaxis in aged flies[118]. However, recent studies have proposed a pathological role of IRE1-XBP1 in AD. Chronic overexpression of XBP1s in a transgenic *Drosophila* model of AD expressing $A\beta_{1-42}$ specifically in the ER of neurons reduces the $A\beta_{1-42}$ levels but also causes age-dependent behavioural defects[67]. Conditional knockout of the RNase domain of IRE1 in the nervous system of the 5xFAD mouse model of AD reduces Aβ deposition and levels of $A\beta_{1-42}$ oligomers, improves cognitive and synaptic function, and attenuates astrogliosis[119]. In addition, levels of IRE1 phosphorylation directly correlate with the severity of AD neuropathology[119]. PERK signalling is the most studied therapeutic target within the UPR, and the successful use of several PERK and eIF2α phosphatase inhibitors has suggested its pathological role. Furthermore, local overexpression of ATF4 in the axons of AD mouse models mediated transmission of neurodegenerative signals through cell-nonautonomous mechanisms[120], and *Ddit3* deficiency proved to be protective in experimental PD[121]. The involvement of ATF6 has been poorly studied, although some studies have shown that in mouse models of PD, with

overexpressed ATF6α became hypersensitive to neurotoxins[122] and ATF6α knockout mice had decreased basal expression of BiP and accelerated degeneration of dopaminergic neurons[123], suggesting a neuroprotective role of ATF6. Further studies need to be conducted in order to establish the relationship between the UPR and the pathogenesis of neurodegenerative diseases.

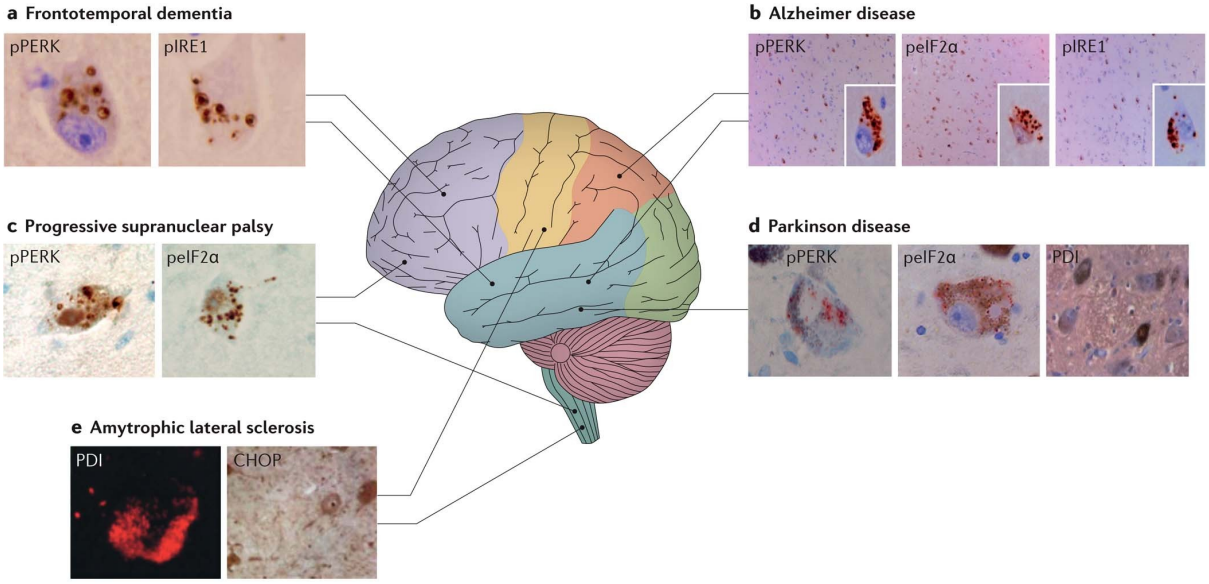

Figure 1. 5. UPR in neurodegenerative diseases. Increased levels of UPR markers have been detected in a number of neurodegenerative diseases, which share accumulation of protein aggregations and inclusions that contain specific proteins in distinct brain regions. Figure reprinted from the reference with permission[124].

1.4. Autophagy

Autophagy, derived from the Greek for 'self-eating', was coined by Christian de Duve over 50 years ago based on the observation of cytoplasmic materials including mitochondria and ER being engulfed within double-membrane vesicles and degraded by lysosome[125]. Substantial progress in the molecular understanding of autophagy has revealed its essential role in survival, development and homeostasis. Autophagy is an adaptive process induced by various conditions of stress, including starvation, infection, hypoxia, oxidative stress, protein aggregation, and ER stress[126]. Autophagy can be either nonselective (bulk degradation) or selective in the removal of unwanted and potentially toxic cytosolic materials such as superfluous or damaged organelles, intracellular protein aggregates, and invading microorganisms. Three types of autophagy have been identified so far, including macroautophagy, microautophagy, and chaperone-mediated autophagy, all of which result in degradation of cytosolic components by the lysosome[127]. In this thesis, we focus solely on macroautophagy (hereafter referred to as autophagy) (**Figure 1.6**).

Genetic studies have identified at least 30 autophagy-related genes encoding autophagy-related protein (ATGs) in yeast, of which almost half are conserved in mammals. These ATG proteins are essential for autophagosome formation and are grouped by their functional and physical interactions into five core machinery components[126]:

1) Unc-51-like kinase 1 (ULK1) complex: ULK1, FIP200 (focal adhesion kinase family interacting protein of 200 kD), ATG3, ATG101
2) Class III phosphatidylinositol 3-kinase complex (PI3KC3): Beclin 1 (ATG6 in yeast), VSP34 (vesicular protein sorting 34), p115 (general vesicular transport factor), ATG14 in PI3KC3 complex I, UVRAG in PI3KC3 complex II (UV radiation resistance-associated gene protein)
3) ATG9 trafficking system: ATG9
4) WIPI (WD repeat domain phosphoinositide-interacting): WIPI, ATG2
5) Two ubiquitin-like conjugation systems: the ATG12-ATG5·ATG16L1 complex; the ATG8 family-phosphatidylethanolamine (PE), ATG8 including light chain 3 (LC3) and γ-aminobutyric acid receptor-associated protein (GABARAP) subfamilies

The most well-characterised trigger of autophagy is amino acid deprivation, which results in the inhibition of the serine/threonine kinase mTOR (mammalian target of rapamycin), a master cell growth regulator that nucleates two distinct multi-protein complexes known as mTORC1 and mTORC2. mTORC1 consists of mTOR, Raptor (regulatory associated protein of mTOR), and mLST8 (mammalian lethal with Sec13 protein 8) and plays a central role in negatively regulating autophagy[128]. In high-nutrient conditions, mTOR phosphorylates ULK1 and ATG13 in the ULK1 complex and inhibits autophagy, while upon starvation, dissociation of mTORC1 from the ULK1 complex activates ULK1[129,130]. The activated ULK1 directly phosphorylates Beclin-1 in the PI3KC3 complex and activates VPS34, the only PI3K found in mammals, to phosphorylate phosphatidylinositol and produce phosphatidylinositol-3-phosphate (PI3P) for the assembly and nucleation of the phagophore[131,132]. The phagophore assembly site in mammalian cell remains to be fully determined, but it has been suggested that phagophores are nucleated at PI3P-enriched membrane compartments that are dynamically connected to the ER (termed 'omegasome'), which are marked by PI(3)P binding protein DFCP1 (double FYVE domain-containing protein 1)[133], as well as at the ER-mitochondria and ER-plasma membrane contact sites[134,135].

Expansion of the phagophore requires the involvement of two ubiquitin-like conjugation systems, ATG12-ATG5·ATG16L1 and ATG8-PE. Nascent proATG8 proteins are processed by ATG4 at C-termini, exposing a glycine residue that is essential for their conjugation to PE[136,137]. The processed ATG8s are then activated by the E1-like enzyme ATG7 and covalently attached to membrane-associated PE by E2-like ATG3, converting it from the cytosolic form (LC3-I) to the membrane-anchored, lipidated form (LC3-II), which is the signature of autophagosome formation[136,138]. This ATG3-mediated ATG8-PE conjugation needs to be enhanced *in vivo* by the E3-like activity carried out by the ATG12-ATG5·ATG16L1 complex. ATG12 is activated by E1-like ATG7 and conjugated to ATG15 by E2-like ATG10, which together bind ATG16L1 and are localised to the phagophore assembly site through the interaction of ATG16L1 with WIPI2[139–143]. While the autophagosome is forming, substrates can be incorporated into the phagophore in either a nonselective or selective manner. Selective autophagy in mammalian cells occurs through the action of autophagy receptors which are able to interact both with LC3-II via the LC3-interacting region (LIR)[144] and with the specifically labelled cargo destined for degradation, thus allowing for targeted delivery of cargo to the autophagosome. The best characterised mammalian autophagy receptor is p62, a multi-

functional adaptor molecule that promotes the degradation of poly-ubiquitinated protein aggregates through autophagy[144].

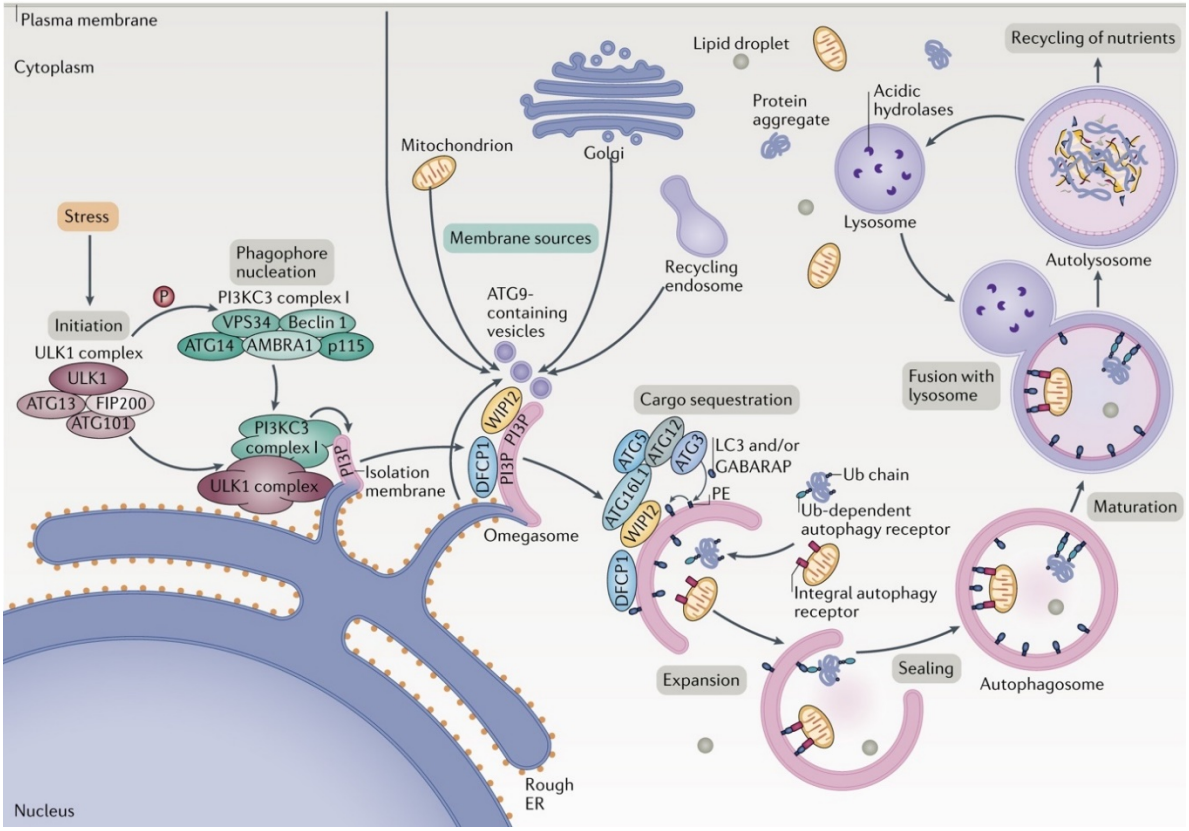

Figure 1. 6. Autophagy in a mammalian cell. Induction of autophagy leads to the recruitment of ATG proteins to the omegasome connected to the ER to initiate the phagophore nucleation. The isolation membrane eventually seals into a double-layered autophagosome, trapping the engulfed cytosolic materials. After the clearance of ATGs and delivery along microtubules to the lysosome, the outer membrane of the autophagosome fuses with the lysosomal membrane to form an autolysosome, which degrades the autophagic body together with its cargo by the autolysosomal hydrolytic milieu. Figure reprinted from the reference with permission[126].

Sealing of the phagophore membrane eventually gives rise to a double-layered autophagosome. The outer membrane of the autophagosome fuses with the lysosome to form an autolysosome after maturation, which involves the clearance of ATG proteins from the outer membrane of the nascent autophagosome and the recruitment of the machineries required for lysosomal delivery and fusion[126]. LC3s drive the maturation process through interactions with adaptor proteins such as FYCO1 (FYVE and coiled-coil domain-containing protein 1)[145] to promote trafficking. The membrane fusion is mediated by the SNARE (soluble *N*-ethylmaleimide-sensitive factor attachment protein receptor) proteins, including STX17 (Syntaxin 17) and SNAP29 (synaptosomal-associated protein 29) on the autophagosome and VAMP8 (vesicle-associated membrane protein 8) on the lysosome/endosome, which assemble into SNARE complexes to promote fusion of the two compartments[146]. This process is enhanced by homotypic fusion and protein sorting (HOPS)-tethering complex[147] and ATG14[148] through direct interactions with STX17. The fusion results in the release of a single-layered autophagic body into the lysosomal lumen, which is followed by the degradation of engulfed materials together with its cargo by acidic hydrolases in the autolysosome.

Dysregulation of autophagy has been implicated in several neurodegenerative diseases. Here we take the example of PD. Both pathological and genetic analyses have revealed that autophagy malfunction might contribute to the pathogenesis of PD, as shown by altered levels of LC3s and GABARAPs in PD brains[149] and PD risk genes involved in autophagy[150]. Ultrastructural examination of autophagosomes in the PD brain has suggested abnormal mitophagy[151], which is known to be associated with the function of several autosomal recessive PD-related genes. For example, mutations in *PRKN* (encoding Parkin, a cytosolic E3-like ligase) in *PINK1* (encoding PTEN-induced kinase 1), which are the most common cause the early-onset PD, abolish or hamper mitophagy in the substantia nigra of post-mortem PD brains. Different approaches have been applied to enhance basal-level autophagy in PD models with promising outcomes. Overexpression of Beclin1 in the brain of a PD mouse model ameliorated the synaptic and dendritic pathology and reduced the accumulation of α-synuclein in the limbic system without any significant deleterious effects[68]. Overexpression of ATG5 in a PD zebrafish model induced by neurotoxins alleviated or reversed pathological features[69]. Overexpression of TFEB (transcription factor EB), a master transcription factor of autophagy and lysosomal biogenesis, rescued dopamine neurons via autophagic clearance of α-synuclein oligomers[152]. These findings suggest an important role of autophagy in the pathogenesis of PD and provide novel targets involved in autophagy that can be modulated in PD therapeutics.

1.5. Project aims

This study sets out to understand proteostatic mechanisms related to ageing and age-associated diseases in long-lived NMRs. The *first* aim is to develop reliable tools for studying proteostasis within NMRs, including transcription-based assays of key proteins involved in stress-response pathways such as the UPR and autophagy. The *second* aim is to use these assays to investigate how NMRs respond differently from short-lived mice when challenged with the same stressed conditions, which may reveal unique molecular features of the UPR and autophagy in NMRs. The *third* aim is to identify important proteostatic mechanisms which may protect NMRs from disease-relevant misfolded protein species such as the Aβ and α-synuclein oligomers which are believed to be the primary pathogenic conformers in Alzheimer's and Parkinson's diseases, respectively[153,154]. *Lastly*, the study involves designing novel binding proteins for the detection of NMR autophagy-related protein markers based on repeat protein scaffolds, followed by their purification and characterisation using a variety of biochemical and biophysical techniques. This idea was driven by our previous findings that CTPR (consensus-designed tetratricopeptide repeat protein) scaffolds are extremely stable and amenable of protein engineering[155] and by the fact that no commercial antibodies are available for the NMR. Once validated, our home-designed probes can be used in combination with transcription-based assays to study autophagy and other mechanisms within the NMR. The results from this study may ultimately be applied towards therapeutic developments to combat neurodegenerative diseases.

2. Materials and Methods

All chemical and biological consumables and equipment were purchased from Thermo Fisher Scientific (Loughborough, UK) unless otherwise stated.

2.1. Preparation and characterisation of $A\beta_{1-42}$ and α-synuclein

Recombinant α-synuclein was prepared by Ewa Klimont and Swapan Preet (University of Cambridge). α-synuclein oligomers were prepared with the help of Catherine Xu (University of Cambridge); α-synuclein fibrils were prepared by Catherine Xu and Marta Castellana-Cruz (University of Cambridge). TEM analysis was performed with the help of Dr. Janet Kumita.

2.1.1. Preparation of $A\beta_{1-42}$ oligomers and fibrils

Unlabelled $A\beta_{1-42}$ (Millipore, Billerica, MA, USA) was dissolved in trifluoroacetic acid (TFA) (1 mL per mg of peptide) and sonicated (30 sec, 4 ˚C) on a Soniprep 150 MSE sonicator and lyophilised overnight on a Heto Lyolab 3000 lyophiliser (Heto-Holten A/S, Denmark) fitted with a Savant VLP120 vacuum pump. Hexafluoro-iso-propanol (HFIP) was added (1 mL per mg of peptide) and the solution was divided into working volumes of 5, 10, 20 and 50 µL. Amino acid analysis was used to determine the concentration of this solution and the aliquots were dried on a Savant SPD131DDA SpeedVac concentrator. Peptide films were stored at -20 ˚C. Lyophilised $A\beta_{1-42}$ peptide was dissolved in DMSO to a concentration of 5 mM. For small oligomer formation, the 5 mM peptide in DMSO was diluted with the low-salt phosphate buffer (10 mM $Na_2HPO_4 \cdot 2H_2O$, 10 mM NaCl, pH 7.4) (final concentration 100 µM) and incubated at 4 ˚C for 24 hr. For mature fibril formation, the 5 mM peptide in DMSO was diluted in phosphate buffered saline (PBS) (final concentration 100 µM) and incubated with agitation at 37 ˚C (48 h, 200 rpm).

HiLyte Fluor 488-labelled fluorescent $A\beta_{1-42}$ was purchased from Anaspec (Freemont, CA, USA) and was dissolved in 1% NH_4OH (final concentration of 2 mg/mL) and then diluted to 0.5 mg/mL in low-salt phosphate buffer. The peptide solutions were aliquoted into working volumes of 5 and 10 µL, flash frozen in liquid nitrogen and stored at -20 ˚C until further use. Lyophilised peptides were diluted in low-salt phosphate buffer (final concentration 100 µM)

and formation of oligomers and fibrils were performed using the same protocol as the unlabelled peptide.

2.1.2. Transmission electron microscopy (TEM)

TEM grids were prepared for analysis by applying $A\beta_{1-42}$ samples (5 µL of 10 µM solutions) onto formvar/carbon-coated 400- mesh stainless steel grids (Agar Scientific, Stansted, UK). Excess liquid was blotted using Whatman (Sigma-Aldrich, Gillingham, UK) gel blot filter paper and the grids were washed twice with ddH_2O. The samples were negatively stained with a 2% uranyl acetate solution (w/v in ddH_2O) (3 min). The sample was left to air dry. TEM analysis was conducted using a Philips Technai 20 transmission electron microscope (FEITM, Hillsboro, Oregon, USA).

2.1.3. 8-anilinonaphthalene-1-sulphonic acid (ANS) binding assay

8-Anilino-1-sulfonic acid (ANS) was added to $A\beta_{1-42}$ samples to a final concentration of 360 µM. Fluorescence emission spectra were recorded between 400-600 nm with an excitation wavelength of 350 nm, using a Cary Eclipse Fluorescence spectrophotometer (Agilent, Santa Clara, CA).

2.1.4. Purification of recombinant α-synuclein

α-synuclein was overexpressed in *Escherichia coli* (*E. coli*) using the pT7-7 plasmid encoding the protein. 1 µL plasmid and 25 µL BL21 Gold (DE3) cells were added to a 1.5 mL Eppendorf tube and incubated on ice for 30 min. The sample was heat shocked at 42°C for 20 sec and put back on ice for 2 min. 200 µL LB medium was added directly to the sample, followed by 1 hr shaking at 37°C. 100 µL of the sample was transferred onto a LB-ampicillin agar plate and incubated overnight at 37°C. Following transformation, BL21 cells were grown at 37°C in LB or 2xYT media in the presence of ampicillin (100 µg/ml) and induced with 1 mM isopropyl β-D-1-thiogalactopyranoside (IPTG) when the optical density at 600 nm reached 0.6. After overnight incubation at 28°C, 220 rpm, cells were harvested by centrifugation with a JLA-8.1000 rotor at 6238 x g at 4°C (45 min) (Beckman Coulter, High Wycombe, UK). The cell pellet was resuspended in PBS, centrifuged at 4000 rpm at 4°C for 1 hr, and resuspended in 10 mM Tris-HCl (pH 7.7), 1 mM EDTA supplemented with complete protease inhibitor cocktail

(1 tablet per 40 mL; Roche, West Sussex, UK), and lysed by sonication. The cell suspension was centrifuged at 13,000 rpm with a JA-25.5 rotor (Beckman Coulter) for 30 min at 4°C. The supernatant was collected and boiled at 80-90°C for 20-25 min. This was to precipitate heat-sensitive proteins, while intrinsically disordered α-synuclein remained soluble. The supernatant was collected after centrifugation at 13,500 rpm with a JA-25.5 rotor for 30 min at 4°C. Streptomycin sulphate was added to the supernatant (to 10 mg/mL) to precipitate DNA at 4°C for 15 min with stirring. The supernatant was collected by centrifugation at 13,500 rpm for 30 min at 4°C. Ammonium sulphate was added to the supernatant to 361 mg/mL to precipitate α-synuclein at 4°C for 30 min with stirring. The protein sample was pelleted by 30 min centrifugation at 135,000 rpm at 4°C, resuspended in 25 mM Tris-HCl, pH 7.7, and loaded onto HiLoad 26/10 Q Sepharose High Performance column (Cytiva, Little Chalfont, UK) connected to an ÄKTA Prime System (Cytiva) and eluted at room temperature with ~350 mM NaCl with a salt gradient from 0 M to 1.5 M NaCl in 25 mM Tris-HCl (pH 7.7). The combined eluants were concentrated and loaded onto a HiLoad Superdex 75 26/600 column (Cytiva) and eluted in PBS at room temperature. Protein concentration was determined by absorbance at 275 nm, using an extinction coefficient of 5600 M^{-1} cm^{-1}.

2.1.5. Preparation of α-synuclein oligomers and fibrils

α-synuclein oligomers and fibrils were prepared using the established protocols[154]. Purified α-synuclein was dialysed against dH_2O (4 L) (overnight, 4°C). 6 mg aliquots were lyophilised for 48 hr at room temperature using a Heto Lyolab 3000 freeze dryer unit attached to an Edwards nXDS-10i vacuum pump (Edwards Limited, UK). The lyophilised samples were resuspended in PBS (pH 7.4) to a final concentration of 840 μM (12 mg/mL) and passed through a 0.22 μM filter prior to incubation at 37°C for 20-24 hr. The samples were ultracentrifuged at 90,000 rpm (1 hr, 20°C) in a TLA-120.2 rotor using an Optima TLX Ultracentrifuge (Beckman Coulter, High Wycombe, UK) to remove fibrillar species. The remaining α-synuclein monomers and small oligomers were removed by filtration (9300 rcf, 2 min each, 4X) using the 100 kDa cut-off membrane (Millipore). The flow-through containing predominantly monomer from the first three passes was kept and reused up to five times. The oligomer concentration was estimated from the absorbance at 275 nm measured in a Cary UV spectrometer (Agilent Technologies UK, Stockport, UK) using a molar extinction coefficient of 7000 $M^{-1} \cdot cm^{-1}$.

F0 and F1 fibrils (0^{th} and 1^{st} generation of fibrils) were used in this study. F0 fibrils were prepared by incubating α-synuclein monomers at 70 μM (1 mg/ml) in PBS, 0.02% NaN_3 (pH 7.4) at 37 °C under constant agitation (200 rpm) for 3-4 days. The F0 fibrils were collected by centrifuging at 25°C (15 min at 13200 rpm) and washed twice with PBS before being resuspended into PBS. F1 fibrils (1^{st} generation of fibrils) were prepared by incubating 10 μM F0 fibrils with 100 μM α-synuclein monomers in PBS, 0.02% NaN_3 (pH 7.4) at 37 °C overnight without shaking. The final concentration of fibrils, that was typically ~100 μM in each sample, was estimated by measuring the absorbance at 275 nm using a molar extinction coefficient of 5600 $M^{-1}cm^{-1}$ after disaggregating an aliquot by the addition of guanidinium chloride to a final concentration of 4 M; this concentration therefore represents the total monomeric concentration present in the fibrillar sample.

2.2. Cell culture

Mouse primary sensory neurons were isolated by Dr. Gerard Callejo and Dr. Sampurna Chakrabarti (University of Cambridge). Calcium uptake assay was performed by Dr. Sampurna Chakrabarti (University of Cambridge).

2.2.1. Cell line culture

Two lines of NMR kidney immortalised fibroblasts (NMR-KF-1[156] used in Chapter 3 and NMR-KF2[236] used in Chapter 5 and 6), one line of NMR skin immortalised fibroblast (NMR-SF[36] used in Chapter 5) and NIH 3T3 mouse fibroblasts (3T3) were kind gifts from Dr. Ewan St. John Smith and Dr. Fazal Hadi (University of Cambridge). NMR-KF-1 was cultured in DMEM/F-12 (without L-glutamine) supplemented with 15% fetal bovine serum (FBS, Sigma-Aldrich), 800 μg/ml G418 (Santa Cruz Biotechnology, Dallas, USA), 2 mM L-glutamine and 100 U/ml penicillin and 100 μg/ml streptomycin (Sigma-Aldrich). NMR-KF-2 and NMR-SF cells were cultured in DMEM high glucose supplemented with 15% FBS, 1X MEM non-essential amino acids, 1 mM sodium pyruvate, 100 U/ml penicillin and 100 μg/ml streptomycin. 3T3 cells were cultured in DMEM high glucose supplemented with 10% FBS, 100 U/ml penicillin and 100 μg/ml streptomycin. Cell lines were grown in a humidified 37°C incubator with 5% CO_2 and used within 9-20 passages.

2.2.2. Animals

All experiments were conducted in accordance with the United Kingdom Animal (Scientific Procedures) Act 1986 Amendment Regulations 2012 under Project Licenses (70/7705 and P7EBFC1B1) granted to E. St. J. S. by the Home Office; the University of Cambridge Animal Welfare Ethical Review Body also approved procedures. Young adult NMRs (two females and eight males, 0.5–2 years old) and C57BL/6J mice (males, 10–14 weeks old) were sacrificed in this study. Mice were conventionally housed with nesting material and a red plastic shelter in temperature-controlled rooms (21 °C) with a 12-hr light/dark cycle and access to food and water ad libitum. NMRs were bred in-house and maintained in an inter-connected network of cages in a humidified (~55 %) temperature-controlled room (28 °C) with red lighting (08:00-16:00) and had access to food ad libitum. In addition, a heat cable provided extra warmth under 2-3 cages/colony. Mice were humanely killed by cervical dislocation of the neck and cessation of circulation, whereas naked mole-rats were killed by CO_2 exposure followed by decapitation.

2.2.3. NMR and mouse primary fibroblast isolation

Both kidneys were harvested and incubated in 5 mL isolation medium containing 500 µL of enzymatic solution (10 mg/mL collagenase (Roche, West Sussex, UK) and 1000 U/mL hyaluronidase (Sigma-Aldrich), in DMEM high glucose at 37°C for 30-60 min with gentle vortexing every 30 min. Dissociated tissues were collected by centrifugation at 500 g for 5 min. Cell pellets were resuspended in DMEM high glucose supplemented with 15% FBS, 1X MEM non-essential amino acids, 1 mM sodium pyruvate, 100 U/ml penicillin, 100 µg/ml streptomycin, and 100 µg/mL primocin (InvivoGen). Cell suspensions were passed through a 70 µM cell strainer (Corning) and were seeded in a T25 culture flask. NMR fibroblasts were cultured in a humidified 32°C incubator with 5% CO_2 and 3% O_2; mouse fibroblasts were cultured in a humidified 37°C incubator with 5% CO_2. Fibroblasts started to form colonies after one week and were subcultured to a T75 flask once 80% confluency was reached. Primary fibroblasts were analysed within 2-5 passages and kept in liquid nitrogen for long-term storage.

2.2.4. Mouse primary sensory neuron isolation

Sensory neurons from dorsal root ganglia and trigeminal ganglia were isolated following the protocol described in the reference[157]. Neurons from a single pup were plated at ~10,000 per

well in a 12-well culture plate pre-coated with poly-D-lysine (Sigma-Aldrich, UK) and laminin. Neurons were cultured at 37°C in a 5% CO_2 incubator in air in Leibovitz's L-15 medium with GlutaMAX supplemented with 10% FBS, 24 mM $NaHCO_3$, 38 mM glucose and 2% penicillin and streptomycin.

2.3. Cellular and biochemical assays probing UPR and autophagy

2.3.1. Drug formulation and cell treatment

Tunicamycin (TU), thapsigargin (TG) and rapamycin (RA) were purchased from Cell Signalling Technology (Danvers, USA) and reconstituted in DMSO to make master stocks (TU: 5 mg/mL, TG: 1.25 mM, RA: 100 μM) following the manufacturer's instructions. Chloroquine was purchased from Sigma-Aldrich (Gillingham, UK), reconstituted in dH_2O to make a 100 mM stock and filter sterilised. All stocks were aliquoted (10 μL) and stored in -20°C.

For the UPR study, TU and TG were first prepared with a series of dilutions in DMSO. Then an equal volume of each diluted sample (TU: 5 μL, TG: 1 μL) was added to 5 mL fresh medium and mixed thoroughly before applying to cells (2 mL per well in a 6-well plate, 1 mL per well in a 12-well plate, or 100 μL per well in a 96-well plate). For the autophagy study, 5 μL of RA and/or CQ stocks was added to 5 mL fresh medium and mixed thoroughly before applying to cells.

2.3.2. RT-qPCR assay

Cell treatment and RNA isolation

Fibroblasts were plated in a 6-well plate, 150,000 cells per well, for treatment with drugs or HBSS and in a 12-well plate, 100,000 cells per well, for treatment with $A\beta_{1\text{-}42}$ and α-synuclein species. Cells were washed once by ice-cold PBS after the treatment and lysed directly by the Buffer RLT supplied in the RNeasy Plus Mini and Micro Kit (Qiagen, Hilden, Germany). Total RNA was extracted following the manufacturer's instructions. An additional wash step with 500 μL Buffer RPE was performed to remove chaotropic salts. Carrier RNA was included in the extraction of neuronal RNA. RNA concentration and purity were evaluated by UV absorbance measurements on a NanoDrop 2000 spectrophotometer. Samples was immediately analysed or otherwise stored at -80°C.

RNA integrity

RNA sample was mixed with RNA gel loading dye (2X) and heated at 75°C for 5 min. ~500 ng of RNA was analysed on a 1% agarose gel running at 110 V for 30-40 min then stained with GelRed™ (Biotium, Fremont, USA) or SYBR™ Safe and visualised under UV light. RNA samples showing smearing bands were degraded and excluded from downstream analyses.

Reverse transcription (RT)

Reverse transcription (RT) was performed in an ABI 2720 thermal cycler (Applied Biosystems, Waltham, USA) or a Techne TC-512 thermal cycler (Cole-Parmer, Saint Neots, UK). First-strand cDNA was synthesised in a 20 µL reaction using the ImProm-II Reverse Transcription System (Promega, Southampton, UK) or LunaScrip RT SuperMix Kit (New England BioLabs, Hitchin, UK). For fibroblasts, RNA input was 1 µg for each sample per reaction. For neurons, RNA input was 500 ng or less for each sample per reaction due to the limited yield.

In the ImProm-II Reverse Transcription System, RNA template was mixed with random hexamers (Qiagen, Hilden, Germany) and dNTPs incubating at 65°C for 5 min. The mixture was chilled to 4°C for 5 min, mixed with 1X ImProm-II 5X reaction buffer, 0.01 M dithiothreitol (DTT), 3 mM $MgCl_2$ and 1 µL ImProm-II Reverse Transcriptase, and incubated at 25°C for 5 min for primer annealing, followed by extension (42°C, 45 min) and transcriptase inactivation (72°C, 15 min). In LunaScript RT SuperMix, RNA was mixed with 4 µL 5X LunaScript RT SuperMix and nuclease-free water to a total volume of 20 µL. The mixture was incubated at 25°C for 2 min for primer annealing, 55°C for 10 min for cDNA synthesis and 95°C for 1 min for heat inactivation. Negative controls (no-RNA-template and no-reverse-transcriptase) were set up along with each batch of RT. All cDNA products were analysed immediately by qPCR or otherwise frozen at -20°C.

Real-time quantitative PCR (qPCR)

SYBR-Green-based quantitative PCR (qPCR) was performed using the StepOnePlus Real-Time PCR System (Thermo Fisher Scientific). Experiments were set up on MicroAmp fast optical 96-well reaction plates following the sample maximisation method[158]. Each 20 µL reaction contained 5 ng cDNA, 0.2 µM primers, 1X Fast or PowerUP SYBR Green Master Mix. Two replicates of each reaction were performed.

Fast SYBR reactions were performed under a standard-cycling mode: 95°C for 10 min for the initial denaturation and activation of AmpliTaq Fast DNA polymerase UP, followed by 42 cycles of denaturation (95°C, 15 sec), annealing and extension (60°C, 1 min). PowerUP SYBR reactions started with the activation of uracil-DNA glycosylate (UDG) at 50°C for 2 min and the activation of Dual-Lock DNA polymerase at 95°C for 2 min, followed by 42 cycles of denaturation (95°C, 15 sec) and annealing and extension (60°C, 1 min). The threshold cycle (Ct or Cq) of each qPCR reaction was calculated from the amplification plot by StepOnePlus Software v2.3. Relative expression levels of target genes were determined by comparative Ct (or ddCt) method[159]. A dissociation step was performed after the qPCR run to generate a melting curve (60 to 95°C) of each qPCR reaction. The product of each run was validated by running the post-reaction mixture on a 2% agarose gel.

Primer design and validation

Mouse qSTAR qPCR primer pairs were designed and purchased from OriGene (Rockville, MD, USA). For NMR genes, primers were either self-designed using Primer-BLAST and the mRNA templates from the NCBI Reference Sequence (RefSeq) collection[160,161] or taken from published literature[75,162].

The efficiency of qPCR assays was determined by a standard curve method[159]. Briefly, a qPCR reaction was performed using the selected primers and a series of 2- or 5-fold dilutions of the cDNA template. A linear-fit standard curve was constructed by plotting Cq values versus log-transformed cDNA concentration using Prism GraphPad 8 (GraphPad Software Inc, La Jolla, USA). qPCR efficiency (E) was calculated from the slope of the standard curve using equation (2.1):

$$\mathrm{E} = \left(1 + 10^{-\frac{1}{\mathrm{slope}}}\right) \times 100\% \qquad (2.1)$$

For primers with efficiencies of <90% or >110%, different annealing temperatures (55-60°C) were tested, and if this still failed to reach ideal efficiency, new primers were designed until the criterion was met.

A complete list of the qPCR primers used to probe genes in NMRs was shown in **Table 2.1** (reference and UPR genes) and **Table 2.2** (autophagy genes).

Table 2. 1. qPCR primers used to probe reference and UPR genes in NMRs.

Gene	Protein	NCBI Access Num.	Primer	Tm (°C)	GC%	Product (bp)	Efficiency
Hprt1	Hypoxanthine-guanine phosphoribosyltransferase (HPRT)	NM_001310288.1	Forward 5'-tgatcagtcaacaggggaca-3'	51.4	50	73	103.63%
			Reverse 5'-caagacattctttccagttaaagttg-3'	53.7	34.62		
Rpl13a	60S ribosomal protein L13a (RPL13A)	XM_004866919.3 XM_004866921.3	Forward 5'-tgaggttggctggaagtatcag-3'	54.84	50	74	91.60%
			Reverse 5'-agtggatcttggccttctcctt-3'	55.64	50		
Gapdh	Glyceraldehyde-3-phosphate dehydrogenase (GAPDH)	XM_004869398.2	Forward 5'-cctgccgcctggagaaa-3'	53.11	64.71	59	96.14%
			Reverse 5'-cgcctgcttcaccaccttt-3'	53.84	61.11		
B2m	Beta-2-microglobulin (B2M)	XM_021241676.1 XM_021241675.1 XM_021241677.1	Forward 5'-gcataccaacttcaccccca-3'	52.04	55	72	98.91%
			Reverse 5'-ggttcctccagagtgacgtg-3'	53.62	60		
Hspa5	Binding immunoglobulin protein (BiP)	XM_004849378.2	Forward 5'-tcttgcgtcggagtgttcaa-3'	54.31	50	156	93.46%
			Reverse 5'-cgtgttctcggggttagagg-3'	54.38	60		

Herpud1	Homocysteine-responsive endoplasmic reticulum protein (HERP)	NM_001308515.1	Forward 5'-ccaaagcaggaaaaacgaca-3'	51.5	45	197	98.85%
			Reverse 5'-catccagagggagaaaggttc-3'	52.42	52.38		
Syvn1	Synoviolin 1 (Syvn1)	XM_013074921.1 XM_004852420.3 XM_004852419.3	Forward 5'-aggtgatgggcaaggtgttc-3'	52.65	55	114	105.61%
			Reverse 5'-cccgaaaaacggtgaaggc-3'	52.97	57.89		
Ddit3	C/EBP homologous protein (CHOP)	XM_013078272.2 XM_013078273.2 XM_004861228.3 XM_004861229.3	Forward 5'-gagctggaagcctggtatga-3'	53.89	55	93	105.67%
			Reverse 5'-attctcttcgtttccaggggg-3'	53.86	52.38		
Bloc1s1	Biogenesis of lysosome-related organelles complex 1 subunit 1 (BLOC1S1)	XM_021241548.1 XM_004861377.3 XM_004861376.3	Forward 5'-ctcgcctgctcaaagaacac-3'	54.39	55	108	103.94%
			Reverse 5'-ggtcgcagcagtgatagctt-3'	53.15	55		
Pdia4	Protein disulphide isomerase family A member 4 (PDIA4)	XM_004860468.3	Forward 5'-cgtgctgagtgttgagggtt-3'	54.31	55	103	101.32%
			Reverse 5'-atcgttggaggtcttgcggt-3'	55.23	55		
Dnajb11	DnaJ heat shock protein family (Hsp40) member B11 (DNAJB11)	XM_021255933.1 XM_004834832.3	Forward 5'-gctcctggcaaacggaaatg-3'	54.4	55	103	105.5%
			Reverse 5'-gacactcatcgcagaccact-3'	53.9	55		

Pdia4	Protein disulphide isomerase family a member 4 (PDIA4)	XM_004860468.3	Forward 5'-cgtgctgagtgttgagggtt-3'	54.3	55	100	99.98%
			Reverse 5'-atcgttggaggtcttgcggt-3'	55.2	55		
Hsp90b1	Glucose-regulated protein 94 (GRP94)	XM_004844837.3	Forward 5'-cgccttccttgtggcagata-3'	55.1	55	138	98.01%
			Reverse 5'-attgttgttccccgtcccag-3'	52.7	55		

Table 2. 2. qPCR primers used to probe autophagy genes in NMRs.

Gene	Protein	NCBI Access Num.	Primer	Tm (°C)	GC%	Product (bp)	Efficiency
Map1lc3b	Microtubule associated protein 1 light chain 3 beta (LC3B)	XM_004842761.3	Forward 5'-gcagtcctgagtgacgtgta-3'	53.4	55	75	106.4%
			Reverse 5'-ccaagcagacgaaatgccac-3'	54.44	50		
Atg5	Autophagy related 5 (ATG5)	XM_004866919.3 XM_004866921.3	Forward 5'-agcagctttggatgggactac-3'	54.47	52.38	167	101.84%
			Reverse 5'-cagccacaggacgaaatagc-3'	54.06	55		
Becn1	Beclin 1	XM_013077692.2 XM_004859306.2 XM_021240236.1 XM_021240237.1	Forward 5'-gttcaaagaggaggtggagaag-3'	53.4	50	201	98.60%
			Reverse 5'-gaggaaacccaggcaagac-3'	51	57.89		
Lamp1	Lysosomal associated membrane protein 1 (LAMP1)	XM_004858503.3	Forward 5'-gaatgcgacctttcacctgc-3'	53.86	55	126	103.49%
			Reverse 5'-gtgaattccagggtcagcga-3'	53.75	55		
Tfeb	Transcription factor EB (TFEB)	XM_004846600.2	Forward 5'-ccaaccccgagaaggagttt-3'	53.03	55	100	93.46%
			Reverse 5'-agcgtgttgggcatctgtag-3'	53.01	55		
Sqstm1	Sequestosome 1 or ubiquitin-binding protein p62	NM_001308515.1	Forward 5'-gtggtgggaactcggtacaa-3'	51.77	55	90	96.63%
			Reverse 5'-gttgtgctccctgtgaatgc-3'	53	55		

Reference gene selection

Reference genes were experimentally determined by geNORM[163]. qPCR was performed to obtain Cq values of each housekeeping gene under experimental conditions. The average expression stability value (M) of each candidate gene was determined from Cq values using the geNORM algorithm in the Microsoft Excel software[158,163]. The candidate genes were ranked by M values where the two genes with the lowest M values were chosen to be the reference genes for data normalisation under tested conditions[163]. The mean coefficient of variance (CV) was determined to validate the choice of reference genes in different types of samples: < 25% in homogenous samples and < 50% in heterogenous samples[158].

Relative mRNA expression level determination

qPCR results were analysed using the comparative Ct (or ddCt) method[159]. The expression of target genes in both experimental samples and untreated controls were first normalised against the expression of reference genes in the same sample[163]. The normalised expression of a target gene in an experimental sample (dCt, experimental) was then compared with the normalised expression of that target gene in the control sample (i.e. dCt, control), and the fold change of mRNA of a target gene was determined by 2^{-ddCt} [159].

Equations involved in each step of the calculation are provided below:

$$\mu C_{t,reference} = \sqrt[2]{\mu C_{t,reference\ gene\ 1} \times \mu C_{t,reference\ gene\ 2}} \quad (2.2)$$

where the reference genes were determined by geNORM and the arithmetic mean (μ) of the reference genes Ct from replicates were calculated by StepOnePlus Software v2.3.

$$dC_{t,experimental} = \left(\mu C_{t,target} - \mu C_{t,reference}\right)_{experimental} \quad (2.3)$$

$$dC_{t,control} = \left(\mu C_{t,target} - \mu C_{t,reference}\right)_{control} \quad (2.4)$$

where the arithmetic mean (μ) of the target and reference genes Ct from replicates were calculated by StepOnePlus Software v2.3.

$$ddC_t = \mu(dC_{t,experimental}) - \mu(dC_{t,control}) \quad (2.5)$$

$$\text{Fold change of mRNA} = 2^{-ddCT} \quad (2.6)$$

2.3.3. *Xbp1* splicing assay

A PCR reaction was performed to amplify *Xbp1s* and *Xbp1u* using cDNA and mouse *Xbp1* primers: 5'-acacgcttgggaatggacac-3' (forward) and 5'-ccatgggaagatgttctggg-3'(reverse)[164] or NMR *Xbp1* primers: 5'-gaaccaggaattaaggatgcg-3' (forward) and 5'-atccatggggagatgttctg-3'(reverse). 25 µL PCR reaction mixture contained 0.5 µM primers, 1X DreamTaq buffer, 0.25 mM dNTPs, 3% DMSO, 50 ng cDNA and 2.5 U DreamTaq DNA polymerase. The reaction included initial denaturation at 95°C for 10 min, 30 cycles of denaturation (95°C, 30 s), annealing (55°C, 30 s), extension (72°C, 30 s), followed by a final cycle of extension (72°C, 10 min). The PCR products were analysed by DNA electrophoresis on a 6% Novex TBE gel at 200 V for 35-40min and visualised under UV light. The intensity of *Xbp1u* and *Xbp1* bands were quantified by ImageJ[165].

2.3.4. Western blot

Fibroblasts were plated at 15,000 cells per well in a 6-well culture plate and two wells of cells were collected per treatment. Cells were washed twice by PBS and lysed by 100 µL of NP40 cell lysis buffer (Invitrogen, UK) supplemented with SIGMAFAST Protease Inhibitor Cocktail Tablets (Sigma-Aldrich). Cell suspension was incubated for 30 min on ice with vortexing at 10 min intervals and spun (14,000 rpm, 10 min, 4°C) to collect clear supernatant for total protein quantification and downstream analysis.

Total protein concentration was determined by the Pierce BCA Protein Assay Kit using the microplate procedure following the manufacturer's instructions. Protein standards (20-2000 µg/mL) were prepared by diluting the Pierce bovine serum albumin (BSA) standard in the cell lysis buffer. Samples were diluted and analysed in triplicate. Absorbance was measured at 562 nm on a CLARIOstar plate reader (BMG Labtech, Ortenberg, Germany). A linear-fit standard curve was generated by plotting the absorbance of each standard versus its concentration using the Microsoft Excel software. The protein concentration of each sample was determined from the standard curve.

15% 1mm polyacrylamide gels were casted using the Mini-PROTEAN Tetra handcast system (Bio-Rad Laboratories, Hercules, USA). The resolving gel was made by mixing 5 mL ProtoGel, 2.5 mL 4X resolving buffer, 100 µL ammonium persulfate (APS), 10 µL TEMED and 2.4 mL

dH_2O. The stacking gel was made by mixing 0.33 mL ProtoGel, 0.63 mL 4X stacking buffer, 25 µL APS, 2.5 µL TEMED and 1.5 mL dH_2O. 10-20 µg of each protein sample was mixed with NuPAGE LDS Sample Buffer (4X) and heated at 70°C for 10 min. Samples were loaded to the gel, along with the Spectra Multicolour Broad Range protein ladder, which was run in the fresh running buffer (0.25 M Tris, 1.92 M glycine, 1% w/v SDS) at 150 V. The proteins were transferred onto a Immobilon-P polyvinylidene difluoride (PVDF, Millipore) using a Pierce Power Blot Cassette (25V, 1.3 A, 7 min). The membrane was then blocked for 1 hr in 3% w/v BSA in Tris-buffered saline, 0.1% v/v Tween 20 (TBS-T). The membrane was incubated (overnight at 4°C) with an anti-LC3B antibody (Cell Signalling Technology, #2775; 1:100) or an anti-KDEL antibody (Abcam, ab12223; 1:100) or an anti-GAPDH antibody (Proteintech, 10494-1-AP; 1:100) in blocking buffer. The membrane was washed three times with TBS-T, 5 min each, and then incubated with a goat anti-mouse IgG/ HRP secondary antibody (P0447; Dako Denmark, Glostrup, Denmark; 1:3000) or a swine anti-rabbit IgG/HRP secondary antibody (P0399; Dako Denmark; 1:3000) in blocking buffer (room temperature, 1 hr). The membrane was washed three times with TBS-T, 5 min each and was detected using Clarity Western ECL Blotting Substrate (Bio-Rad Laboratories). The image was acquired by Odyssey Fc imaging system (LI-COR Biosciences, Lincoln, USA) with an exposure time of 30 sec and analysed by ImageJ[165].

2.3.5. Immunostaining and confocal microscopy

The No.1 square coverslips were rinsed with 70% ethanol, coated with 10 µg/mL fibronectin (room temperature, 30 min) and washed three times with PBS. Each pre-treated coverslip was placed in the well of 6-well culture plates, and mouse 3T3 and NMR kidney fibroblasts were plated at 1×10^5 cells per well (about 200 cells per mm^2 on the coverslip). Mouse neurons were plated onto the Corning BioCoat 12mm No.1 German Glass Coverslips in a 24-well plate at ~10,000 per well.

HiLyte Fluor 488-labelled $A\beta_{1\text{-}42}$ oligomers (200 µM) were added with the serum-free medium. After incubation at 37°C for 5 hr, the cells were washed three times with DPBS and fixed in 4% (w/v) paraformaldehyde for 20 min. The cells were rinsed three times with HBSS after the fixation. The cells were incubated with the Alexa Fluor 647-labelled WGA (5 µg/mL) in HBSS for 10 min and washed two times with PBS-T (PBS with 0.05% v/v Tween 20), 5 min each. The cells were stained with DAPI (Sigma-Aldrich) (room temperature, 5 min) and washed

three times with PBS-T, 5 min each. The cells were mounted with ProLong Gold Antifade Mountant and dried (room temperature, overnight). The coverslips were sealed with nail polish and stored in the fridge before imaging using a Leica SP5 Confocal Microscope (Leica, Wetzlar, Germany).

2.3.6. Cell viability assay

Fibroblasts were plated at a density of 5,000 cells per well in a 96-well opaque-white-walled, clear-bottomed plate. After the treatment, the amount of ATP in culture was determined by CellTiter-Glo luminescent cell viability assay (Promega) following the manufacturer's instructions. Luminescent signals were measured and recorded by a CLARIOstar plate reader (gain at 3600, no filter). Triplicates of each treated sample or control were analysed and the mean luminescence readings were taken to calculate the cell viability using the equation 2.7:

$$\text{Viable Cell \%} = \frac{Luminescence_{(Treatment)} - Luminescence_{(Blank,Nocell)}}{Luminescence_{(Negativecontrol,Medium)} - Luminescence_{(Blank,Nocell)}} \times 100\% \quad (2.7)$$

2.3.7. Caspase assay

NMR primary kidney fibroblasts were plated at a density of 5,000 cells per well in a 96-well opaque-white-walled, clear-bottomed plate. After the treatment, the caspase-3/7 activity was determined by Caspase-Glo 3/7 assay (Promega) following the manufacturer's instructions. Luminescent signals were measured by a CLARIOstar plate reader (gain at 3600, no filter). Triplicates of each treated sample or control were analysed and the mean luminescence readings were taken to calculate the percentage of apoptosis in culture following the equation 2.8:

$$\text{Apoptosis \%} = \frac{Luminescence_{(Treatment)} - Luminescence_{(Blank,No\ cell)}}{Luminescence_{(Positive\ control,Staurosporine)} - Luminescence_{(Blank,No\ cell)}} \times 100 \quad (2.8)$$

2.3.8. Calcium (Ca^{2+}) uptake assay

Cells plated in 20 mm dishes were incubated in 10 μM Fluo-4 AM (Invitrogen) for 30 min at room temperature (~21 °C). These dishes were then washed with extracellular solution (ECS), pH 7.4, containing 140 mM NaCl, 4 mM KCl, 1 mM $MgCl_2$, 2 mM $CaCl_2$, 4 mM glucose and

10 mM HEPES and imaged under an inverted Nikon Eclipse Ti microscope. Fluo-4 fluorescence was measured using an excitation wavelength of 470 nm LED (Cairn Research) and captured with a Zyla cSMOS camera (Andor) at 1 Hz with a 250 ms exposure time using Micro-Manager software (v1.4; NIH). A gravity-driven 12-barrel perfusion system was used to perfuse solutions in this system. During imaging, ECS was perfused for 10 s to establish the baseline, then thapsigargin (5, 50, 250 nM serially diluted in ECS) was perfused for 30 s. Each thapsigargin concentration was tested in separate culture dishes; 4 min after which ionomycin (10 µM, Cayman Chemicals) was applied for 10 s as a positive control in each dish. For quantifying increases in intracellular Ca^{2+}, mean gray values of cells were extracted from manually drawn regions of interest (ROIs) in the ImageJ software. These values were then fed into a custom-made R-toolbox (https://github.com/amapruns/Calcium-Imaging-Analysis-with-R.git) to compute the proportion of cells responding to each concentration of thapsigargin and their corresponding magnitude. Specifically, after subtraction of background intensities from the ROIs, the toolbox calculated the difference between 5 s of pre-compound application baseline and 2 s of peak drug response. Cells that had a peak drug response greater than baseline mean ± 5 standard deviation (threshold) were counted as "responders" which were then normalised to their peak ionomycin response. Cells not crossing threshold for positive controls were excluded from the analysis. Finally, cells that had a normalised peak less than 0.001, did not reach peak 30 s after termination of drug application and had a fluorescent decay of more than 10 % from baseline were excluded after manual evaluation.

2.4. Preparation and characterisation of CTPR-LIR constructs

Some CTPR4-LIR proteins used in this study were purified by Andrew Countryman (University of Cambridge). Chemical denaturation assay was performed with Andrew Countryman (University of Cambridge). Pull-down assay was performed by Dr. Janet Kumita.

2.4.1. Plasmids and DNA constructs

The pRSET B expression vector containing a multiple cloning site, a T7 promoter and ampicillin resistance was used in this study. The vector was previously altered in house to present a thrombin-cleavage site between sequences of the N-terminal 6*His tag and the protein of interest (pRSET-Thr). The pRSET-Thr vector was further modified by Dr. Pamela

J.E. Rowling with an addition of a 3'-end HiBiT sequence (pRSET_HiBIT) for subcloning and making HiBiT-containing constructs.

DNA constructs encoding NMR LC3B and CTPR4-LIR were designed to have a BamHI sequence at the 5' end and a HindIII sequence at the 3' end. CTPR4-RS (randomly scrambled) was designed to have a BamHI at the 5' end and an ECoRI sequence at the 3' end. All sequences were optimised for protein expression in *E. coli* using the GeneArt GeneOptimizer (Thermo Fisher Scientific) and purchased from Integrated DNA Technologies (Leuven, Belgium) as gBlock DNA fragments listed in **Table 2.3**.

Table 2. 3. gBlock DNA inserts used in this study.

Name of inserts	Sequence
CTPR4-LIR	GGGGGGGGATCCGCAGAAGCATGGTATAATCTGGGTAATGCATATTACAAACAGGGCGATTA TCAGAAAGCCATCGAGTATTATCAAAAGGCACTGGAACTGGACCCGAATAATGCCGAGGCCT GGTATAACTTAGGTAACGCCTACTATAAACAGGGTGATTACCAAAAGGCGATCGAATATTAC CAGAAAGCGCTGGAATTAGATCCGAACAACGATTATGAATCCGATGATGATAGCTATGAAGT TCTGGATCTGACCGAATATGATCCGAATAACGCGGAAGCGTGGTACAACCTGGGCAACGCGT ATTATAAGCAAGGTGATTATCAGAAGGCAATTGAATACTATCAGAAAGCGTTAGAGCTGGAC CCGAACAACGCTGAGGCATGGTACAATTTAGGCAATGCGTACTACAAACAAGGGGACTACCA AAAAGCGATTGAGTACTACCAAAAGGCCTTAGAACTTGACCCCAACAACTAATAAAAGCTTG GGGGGG
CTPR4-RS	GGGGGGGGATCCGCAGAAGCATGGTATAATCTGGGTAATGCATATTACAAACAGGGCGATTAT CAGAAAGCCATCGAGTATTATCAAAAGGCACTGGAACTGGACCCGAATAATGCCGAGGCCTG GTATAACTTAGGTAACGCCTACTATAAACAGGGTGATTACCAAAAGGCGATCGAATATTACC AGAAAGCGCTGGAATTAGATCCGAATAACGATGTGGAATATGAGTATACCTATGATAGCTCC GATGAACTGGATCTGGATGATCCGAACAATGCGGAAGCGTGGTACAACCTGGGCAACGCGTA TTATAAGCAAGGTGATTATCAGAAGGCAATTGAATACTATCAGAAAGCGTTAGAGCTGGACC CGAACAACGCTGAGGCATGGTACAATTTAGGCAATGCGTACTACAAACAAGGGGACTACCA AAAAGCGATTGAGTACTACCAAAAGGCCTTAGAACTTGACCCTAACAACGAATTCGGGGGG
NMR LC3B	GGGGGGGATCCATGCCGAGCGAAAAAACCTTTAAACAGCGTCGTACATTTGAACAGCGTGTT GAAGATGTTCGTCTGATTCGTGAACAGCATCCGACCAAAATTCCGGTTATTATCGAACGCTAT AAAGGCGAAAAACAGCTGCCGGTTCTGGATAAAACCAAATTTCTGGTTCCGGATCATGTGAA TATGAGCGAACTGATTAAAATCATTCGTCGTCGTCTGCAGCTGAATGCAAATCAGGCATTTTT TCTGCTGGTTAATGGTCATAGCATGGTTAGCGTTAGCACCCCGATTAGCGAAGTTTATGAAAG CGAAAAAGATGGTGATGGCTTCCTGTATATGGTTTATGCAAGCCAAGAAACCTTTGGTCGTGG TCTGAGCGTTTGTGATTAATAAAAGCTTGGGGGG

[+]Note: Restriction sites are highlighted including BamHI: yellow, HindIII: cyan, ECoRI: green.

2.4.2. Cloning of NMR LC3B and CTPR4-LIR

The gBlock constructs of the NMR LC3B and CTPR4-LIR were cloned into the pRSET_Thr vector for protein expression in *E. coli*. Lyophilised 500 ng DNA constructs were resuspended

in 10 µL nuclease-free water to a final concentration of 50 ng/µL. Each resuspended construct or insert (3 µL) was incubated at 37°C for 30 min in a 50 µL digestion mixture containing 1 µL BamHI-HF (New England BioLabs), 1 µL HindIII-HF (New England BioLabs), 5 µL 10X CutSmart Buffer (New England BioLabs) and nuclease-free water. The digested constructs were purified by Monarch PCR & DNA Cleanup Kit (New England BioLabs) following the manufacturer's protocol.

The pRSET_Thr vector (1 µg) was incubated at 37°C for 1 hr in a 30 µL digestion mixture containing 1 µL FastAP Thermosensitive Alkaline Phosphatase, 1 µL FastDigest BamHI, 1 µL FastDigest HindIII, 3 µL 10X FastDigest Green Buffer and nuclease-free water, followed by 5-min heat inactivation at 75°C. The digestion products were analysed on a 1% agarose gel stained with SYBR Safe from which the correct DNA band (~3 kb) was cut and purified using the Monarch DNA Gel Extraction Kit (New England BioLabs) following the manufacturer's instructions. The purified cut pRSET_Thr vector and inserts were quantified by NanoDrop 2000. Ligation was carried out at room temperature for 15 min in a 4 µL mixture containing vector (~100 ng) and the insert at a 1:6 molar ratio and 1 µL Anza T4 DNA Ligase Master Mix. A negative control was performed by replacing the insert with water in the above mixture.

Transformation was performed by adding 1-2 µL of the ligation products to 50 µL α-select bronze efficiency competent *E. coli* cells (BioLine). The component cells were incubated on ice for 30 min, heat shocked at 42°C for 45 sec, and placed back on ice for 2 min. 200 µL SOC Outgrowth Medium (New England BioLabs) was added to the mixture, followed by 1-hr incubation at 37°C with shaking (600 rpm). 100 µL of the mixture was plated onto a LB-Ampicillin agar plate and incubated overnight at 37°C. Individual colonies were picked and inoculated to 5 mL sterile 2xYT media supplemented with ampicillin (50 µg/mL). 5-mL liquid cultures were incubated at 37°C with shaking (220 rpm) for 18 hr, and the DNA plasmids were extracted by GeneJET Miniprep Kit or Monarch Plasmid Miniprep Kit (New England BioLabs). DNA concentrations were determined by NanoDrop 2000, and the sequencing was conducted by Eurofins Genomics using the T7 promoter sequencing primers.

2.4.3. Cloning of CTPR4-LIR-HiBiT and CTPR4-RS-HiBiT

A PCR was performed to amplify the protein-coding region on the CTPR4-LIR plasmid using a T7 promoter forward primer (5'-taatacgactcactataggg-3') and a reverse primer (5'-

gggggaattcgttgttggggtcaagttcta-3') designed to insert a 3'-end EcoRI restriction site for subcloning into the pRSET_HiBiT vector. The reaction contained the template CTPR4-LIR plasmid (500 ng), 10 µL 5X Phusion HF polymerase buffer, 1.5 µL of each 100 µM primer, 2 µL 5 mM dNTP, 1 µL Phusion polymerase and nuclease-free water to make a final volume of 50 µL and was performed with initial denaturation (98°C, 60 s), 25 cycles of amplifications (96°C for 30 s, 55°C for 30 s, 72°C for 1 min) and final extension (72°C, 10 min). The PCR products (10 µL) were digested with FastDigest BamHI and ECoRI ezymes (1 µL each) in 1X FastDigest Green Buffer diluted in nuclease-free water to a total reaction volume of 20 µL. After incubation at 37°C for 1 hr, the digestion mixture was analysed on a 1% agarose gel. The appropriate DNA band was cut and extracted using the Monarch Gel Kit (New England BioLabs), and the DNA concentration was measured on a NanoDrop 2000. The pRSET_HiBiT vector was also double digested with BamHI and EcoRI enzymes and gel purified. Ligation was performed using the purified cut pRSET_HiBiT vector and the DNA insert, followed by transformation, plasmid extraction and sequencing, using the same protocol described in the section 2.4.2. The gBlock construct of the CTPR4-RS was cloned directly into the pRSET_HiBiT vector to make the CTPR4-RS-HiBiT plasmid using the same protocol described in the section 2.4.2.

2.4.4. Protein purification

Buffers used in protein purification included:
Lysis buffer: 50 mM sodium phosphate pH 7.5, 150 mM NaCl, and 1 tablet of SIGMAFAST Protease Inhibitor Cocktail Tablets per 100 mL buffer
Wash buffer: 50 mM sodium phosphate pH 7.5, 150 mM NaCl, 30 mM imidazole
Elution buffer A: 50 mM sodium phosphate pH 7.5, 150 mM NaCl, 300 mM imidazole
Elution buffer B: 25 mM sodium phosphate pH 7.0, 100 mM NaCl
In addition, 1 mM DTT was added to all buffers used for LC3B purification.

Plasmids were transformed into *E. coli* C41 competent cells (New England BioLabs) by heat shock and plated on LB-Ampicillin plates as described in the section 2.4.2. After overnight incubation at 37°C, colonies grown on the LB-Ampicillin plates were transferred to sterile LB media containing 50 µg/mL ampicillin (666 mL culture per protein construct). Cultures were incubated at 37°C, 220 rpm and induced at O.D. (600 nm) of 0.6 with 0.2 mM IPTG at 25°C for 16-20 hr with shaking. Cells were harvested by centrifugation at 5,000 x g for 12 min,

resuspended in ice-cold lysis buffer (5 mL buffer per 1 mL cell pellet) and lysed on an Emulsiflex C5 homogeniser (Avestin, Mannheim, Germany) at 10000 psi. Cell debris was pelleted by centrifugation at 15,000 x g at 4°C for 45 min. The supernatant was loaded onto a HisTrap HP column (Cytiva) which was connected to an ÄKTA Pure System (Cytiva) and pre-equilibrated with the wash buffer. Target proteins were eluted with elution buffer A, and the combined eluants were loaded onto a HiPrep 26/10 desalting column (Cytiva) to remove imidazole. The proteins were eluted with elution buffer B, incubated overnight at 4°C with thrombin (Sigma-Aldrich) at 50 Units per litre of culture to cleave the 6*His tag, and loaded onto the HisTrap HP column. The His-tag-cleaved proteins were collected in the flow through, concentrated to a volume of <15 mL, loaded onto the desalting column, and eluted in elution buffer B. Protein samples collected from various steps were analysed by SDS-PAGE on precast NuPAGE 4 to 12% gels in NuPAGE MES SDS Running Buffer. The combined eluants were concentrated, snap-frozen on dry ice and stored at -80°C. Protein concentrations were determined by measuring absorbance at 280 nm on a NanoDrop 2000. Protein moleular weight and purity were confirmed by mass spectrometry.

2.4.5. Circular dichroism (CD) spectroscopy

Secondary structure of the CTPR4 constructs was evaluated by circular dichroism (CD) spectroscopy using a Chirascan CD spectrometer (Applied Photophysics, Leatherhead, UK) in a 1-mm-pathlength Precision Cell (110-QS; Hellma Analytics, Müllheim, Germany) at 25°C, 80°C and 95°C. Protein samples (20 μM) were prepared in 50 mM sodium phosphate buffer (pH 6.8), 150 mM NaCl, and the far-UV CD spectra were measured between 200 and 250 nm using a 1-nm bandwidth. Measurements were taken at 1-nm intervals and were collected every 0.5 s; each reading was repeated five times and the mean values were used for data analysis.

2.4.6. Chemical denaturation monitored by fluorescence

Chemical denaturation experiments were performed as described previously[166]. Briefly, stocks of PBS buffer (pH 7.0), guanidinium chloride (GdmHCl) solution (6.5 M in PBS), and protein samples (10 μM) were prepared. 150 μl aliquots of protein at different concentrations of GdmHCl were dispensed into black, 96-well, flat-bottom, polystyrene plates with a Microlab ML510B dispenser (Hamilton, Reno, USA) in concentration steps of 0.1 M GdmHCl. Plates were covered with 96-well Microplate Aluminum Sealing Tape (Corning) to prevent

evaporation and incubated at 25°C for 1 hr. Intrinsic fluorescence of protein samples was measured on a CLARIOstar Plate Reader with a tryptophan-detection setting consisting of three filters, an excitation of 295 nm, a dichroic PL325 nm, and an emission at 360 nm at 25°C. Measurements were taken with three technical replicates on the same plate and repeated on three plates.

Denaturation data were analysed in GraphPad Prism 8 using the two-state model where a native [N] and a denatured [D] are the only populated states[167,168]:

$$F = \frac{(\alpha_N+\beta_N[D])+(\alpha_D+\beta_D[D])exp\left(\frac{m_{D-N}([D]-[D_{50\%}])}{RT}\right)}{1+exp\left(\frac{m_{D-N}([D]-[D_{50\%}])}{RT}\right)} \quad (2.9)$$

where F is the fluorescence intensity, m_{D-N} is the m-value, and $D_{50\%}$ is the concentration of denaturation at which 50% of the proteins are unfolded (the midpoint of unfolding). R is the gas constant, and T is the temperature (K). The native and denatured fluorescence show a linear dependence on denaturant concentration. α_N is the native signal at the lowest concentration of denaturant and β_N is the slope of the native baseline. α_D is the native signal at the highest concentration of denaturant and β_D is the slope of the denatured baseline. The free energy of unfolding in water is calculated using equation 2.10.

$$\Delta G_{D-N}^{H2O} = m_{D-N} \times [D_{50\%}] \quad (2.10)$$

where ΔG_{D-N}^{H2O} is the free energy of unfolding in water, m_{D-N} is the m-value, and $D_{50\%}$ is the midpoint of unfolding.

2.4.7. Isothermal titration calorimetry (ITC)

ITC experiments were performed on a MicroCal iTC200 (GE Healthcare) at 193K (10°C), 293K (20°C) or 298K (25°C). NMR LC3B, CTPR4-LIR and CTPR4-random proteins were diluted to appropriate concentrations and dialysed overnight at 4°C or at room temperature for 3 hr into the dialysis buffer (25 mM sodium phosphate, 100 mM NaCl, 1 mM TCEP, pH 7.0). The protein concentrations were measured on a NanoDrop 2000. All samples were degassed at 25°C for 10 min before loading to the instrument. The initial injection was performed at 5

μL followed by 29 injections of 10 μL with a spacing of 120 s. Control experiments were performed using the same setting as above, except that the iTC200 cell was filled with dialysis buffer. Data were fitted with non-linear regression using a one-site binding model from Origin 7.0 (MicroCal, Inc)[169].

2.4.8. Dot blot assay

NMR LC3B proteins were prepared with a series of dilutions (0 to 1 μg/μL) in PBS (pH 7.0), and 5 μL of each diluted sample (0 to 5 μg NMR LC3B) was spotted onto the nitrocellulose membrane. Once the membrane was completely dried, it was incubated in the blocking buffer (3% BSA in TBS) for 1 hr at room temperature with gentle rocking. The membrane was incubated overnight at 4°C with 25 μg/mL CTPR4-LIR-HiBiT probe in PBS or anti-LC3B antibody (Cell Signalling Technology, #2775; 1:100) in TBS-T, and washed three times with TBS-T, 5 min each.

For the membrane incubated with the CTPR4-LIR-HiBiT probe, signals were developed using the Nano-Glo HiBiT Blotting System (Promega) following the manufacturer's protocol. Briefly, the membrane was incubated with the LgBiT (Large BiT)/buffer solution for 1 hr at room temperature with gentle rocking. The LgBiT protein complements the HiBiT tag on the protein of interest to form the luminescent NanoBiT enzyme in the presence of furimazine substrate. The Nano-Glo Luciferase Assay Substrate was diluted 500-fold into the LgBiT/buffer solution, and after 5-min incubation at room temperature, the blot was imaged on an Odyssey Fc imaging system (LI-COR Biosciences, Lincoln, USA) with 10-min exposure. For the membrane incubated with the anti-LC3B antibody, anti-IgG/HRP secondary antibody staining, and signals development were performed as described in Section 2.3.3.

2.4.9. Pull-down assay

NMR skin immortalised fibroblasts were cultured as previously described. SIGMAFAST Protease Inhibitor (12 mg of a crushed tablet) and 10 μL of TCEP (0.5M) were added to NP40 buffer (1 mL). The NMR fibroblasts (~ 10 million cells) were resuspended in NP40 buffer (100 μL) and incubated on ice (30 min), vortexing briefly every 10 min. The suspension was centrifuged (14,000 rpm, 10 min, 4°C), and the supernatant was removed and saved.

40 µL PureProteome Nickel Magnetic beads (Merck Millipore UK Ltd.) were washed with 50 mM $NaPO_4$ (pH 8.0), 150 mM NaCl (3X, 100 µL). The magnetic beads were incubated with 100 µL of either 50 µM His-tagged CTPR4-LIR or His-tagged CTPR-RS (30 min, RT, tube roller). The conjugated beads were washed with 50 mM $NaPO_4$ (pH 8.0), 150 mM NaCl (3X, 100 µL). The conjugated beads were incubated with NMR cell lysate (50 µL, 10 min, RT). The beads were washed with 50 mM $NaPO_4$ (pH 8.0), 150 mM NaCl (3X, 100 µL). The proteins were eluted by incubating the beads with 0.5M Imidazole in 50 mM $NaPO_4$ (pH 8.0), 150 mM NaCl (20 µL).

The eluted samples, along with purified LC3B (5 µL, 0.2 µM) were run on a 15% SDS-PAGE acrylamide gel. WB Master Protein standard (GenScript, Oxford, UK) were used as molecular markers. Western blot transfer onto PVDF was performed using a Pierce Power Blot Cassette (25V, 1.3 A, 7 min) and the membrane was blocked in 5% skimmed milk (in TBS-T) for 1 hr. The membrane was incubated (overnight, 4°C) with an LC3B antibody (GeneTex. GTX127375; 1:1000 in 5% skimmed milk/TBS-T). The membrane was washed three times (5 min each) with TBS-T and then incubated with the anti-IgG/HRP secondary antibody (1:5000 in 5% skimmed milk/TBS-T; RT, 1 hr). The membrane was washed three times (5 min each) with TBS-T and samples were detected using Amersham ECL reagent extreme (Cytiva Life Sciences Ltd) following the manufacturer's instructions. The western blot was imaged by the Odyssey Fc imaging system with an exposure time of 30 sec.

2.5. Statistical analysis

All data were expressed as mean ± standard deviation (S.D.) from at least three biological repeats unless otherwise indicated. For a particular cell line, results from *Xbp1* splicing, RT-qPCR, cell viability and caspase assays under treated conditions were compared with those from untreated controls using unpaired t-tests. For inter-species comparison (NMR versus mouse fibroblasts) in response to the same treatments, differences in the *Xbp1s*-to-*Xbp1u* ratio, gene expression levels, cell viability and Ca^{2+} uptake were tested by two-way ANOVA tests and Sidak's multiple comparisons tests. All statistical analyses were carried out using Prism GraphPad 8 (GraphPad Software Inc, La Jolla, USA) unless otherwise indicated. $p<0.05$ was considered statistically significant. *$p<0.05$, **$p<0.01$, ***$p<0.001$, ****$p<0.0001$.

3. Building a robust toolkit for probing transcriptional changes of the UPR in the NMR

3.1. Introduction

Valid and reliable methods have been established to monitor the UPR outputs in mammalian systems such as mice and humans[170]. Two sets of analytical methods, including RNA-based analysis of UPR-induced transcripts and western blot-based analysis of UPR-induced proteins or protein modifications, have been widely used to allow assessment of the activation of different signalling pathways within the UPR. Probing UPR outputs of the NMR is of great interest but can be challenging as much of its genome has not been annotated extensively, and molecular tools including NMR-specific commercial antibodies are limited[23]. In this chapter, we develop and optimise RNA-based methods to probe the UPR outputs in NMR cells at the transcript level, which consist of the isolation and reverse transcription (RT) of RNA to cDNA, followed by subsequent analysis by either conventional PCR (*Xbp1* splicing assay) or quantitative PCR (qPCR). Using this robust toolkit, we examined the activation of all three branches of the UPR in an immortalised NMR kidney fibroblast line (NMR-KF1) in response to *in vitro* ER stress induced by two common agents, tunicamycin (TU) or thapsigargin (TG).

3.1.1. Activation of UPR by tunicamycin (TU) and thapsigargin (TG)

Tunicamycin (TU) and thapsigargin (TG) are two widely used ER stress-inducing compounds and can induce ER stress by different mechanisms of action. TU is a glucosamine-containing antibiotic produced by *Streptomycin lysosuperificus* which blocks N-linked glycosylation of glycoproteins in mammalian cells, thereby causing extensive protein misfolding in the ER that results in the activation of the UPR[171,172] (**Figure 3.1 A**). TG is a plant-derived tumour-promoting sesquiterpene lactone that specifically inhibits all known isoforms within the sarcoplasmic or endoplasmic reticulum Ca^{2+}-ATPase family (SERCA), this depletes Ca^{2+} storage in the ER which decreases the activity of Ca^{2+}-dependent chaperones, leading to an increase in unfolded proteins and the induction of UPR signalling[173–175] (**Figure 3.1 B**).

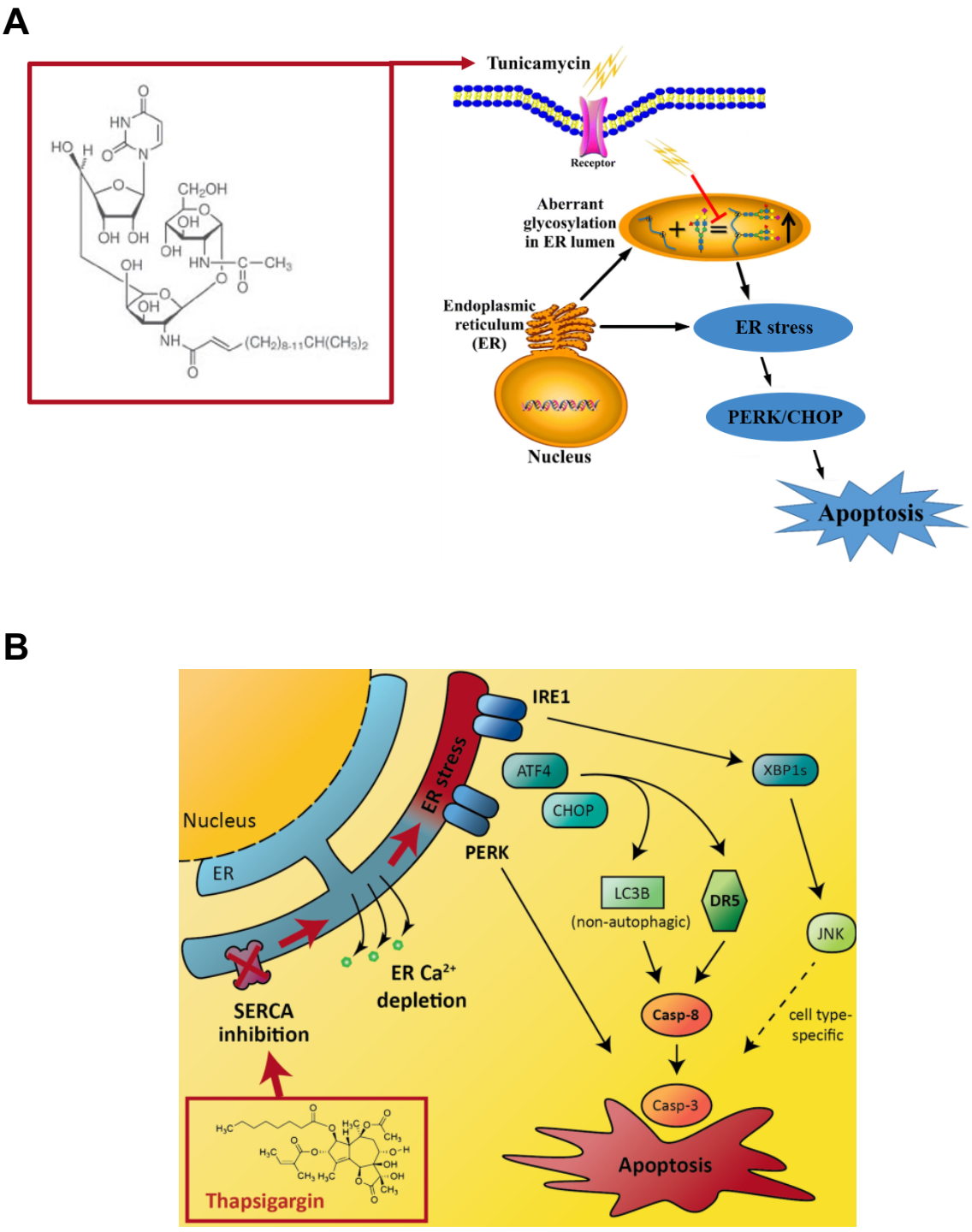

Figure 3. 1. Structures and actions of TU and TG. TU inhibits N-glycosylation in the ER lumen (**A**) while TG disrupts Ca2+ homeostasis in the ER through inhibition of SERCA (**B**) to induce ER stress and activate the UPR. TU structure was obtained from the manufacturer's website (Cell Signalling Technology). Figures modified from the references[176,177].

3.1.2. *Xbp1* splicing assay

The signalling output of the IRE1 branch of the UPR is XBP1, a basic-region leucine zipper (bZIP) transcription factor in metazoans[178,179]. During ER stress, *Xbp1* mRNA undergoes a two-step noncanonical splicing to generate a mature transcript (*Xbp1s*) which encodes an active transcription factor XBP1s. In the first step, dimerization-dependent autophosphorylation of the IRE1α cytosolic domain causes a conformational change, leading to the activation of the RNase domain, which cleaves a 26-nucleotide intron from the unspliced *Xbp1* (*Xbp1u*) mRNA[85,88,179–181]. Subsequently, the 5' and 3' fragments of IRE1-cleaved exons are ligated by the tRNA ligase RTCB in mammalian cells [89,90]. This unconventional splicing shifts the open reading frame of the *Xbp1* mRNA and promotes the translation of XBP1s which acts to elicit a robust transcriptional programme that restores ER homeostasis by enhancing protein folding capacity and inducing ER-associated degradation (ERAD) [91,182–184].

The abundance of *Xbp1u* and *Xbp1s* transcripts can be measured by conventional PCR on 2% agarose or 6% TBE gels using a pair of primers flanking the intron that is removed by IRE1α. *Xbp1s* amplicons migrate faster on a gel as compared with *Xbp1u* amplicons. The *Xbp1* splicing directly reflects IRE1 activity and therefore, the ratio of *Xbp1s*-to-*Xbp1u* mRNA serves as a proximal reporter of the level of ER stress[105,179].

3.1.3. qPCR analysis of UPR markers

Three transcription factors are known to respond to ER stress in mammals, including XBP1s, ATF6f (the liberated cytosolic fragment), and ATF4. For example, induction of *Syvn1*, which encodes HRD1, an E3 ubiquitin ligase involved in ERAD, is regulated by XBP1s, which binds to the unfolded protein response element (UPRE) II (CCGCGT) found in the mammalian *Syvn1* promoter[185,186]. Transcriptional induction of mammalian ER chaperones, including BiP and GRP94, are mediated by the *cis*-acting ER stress response element (ERSE, consensus sequence CCAAT-N_9-CCACG) present in their promoter regions[187]. The cytoplasmic ATF6 fragment binds directly to the CCACG part of the ERSE with assistance from the general transcription factor, NF-Y, which is bound to the CCAAT region[101,188]. Induction of *Ddit3* is highly PERK-dependent due to the presence of a C/EBP-ATF composite site to which ATF4, together with C/EBP-β, binds[108,109]. In addition, ATF6 and/or IRE-XBP1 pathways also regulate the optimal induction of *Ddit3* during ER stress through an ERSE site identified in its promoter[189]. These

transcriptional programmes of the UPR are tightly controlled and can be monitored by qPCR assays, which are developed following the Minimum Information for Publication of Quantitative Real-Time PCR Experiments (MIQE) guidelines to obtain accurate and reliable results in this study[190].

3.2. NMR's unique splicing of 28S ribosomal RNA (rRNA)

According to the MIQE guidelines, it is essential to document the quality assessment of RNA templates, including purity (A_{260}/A_{280} ratio) and integrity[190]. In this study, when NMR-KF1 cells were plated at a density of 150,000 cells per well in a 6-well plate, all extracted RNA samples showed good yields (2 - 3µg per sample) and good A_{260}/A_{280} (2.0) and A_{260}/A_{230} ratios (2.0-2.2). The RNA integrity was evaluated on an agarose gel stained with ethidium bromide, which produced sharp and clear rRNA bands, suggesting the absence of RNA degradation (**Figure 3.2**).

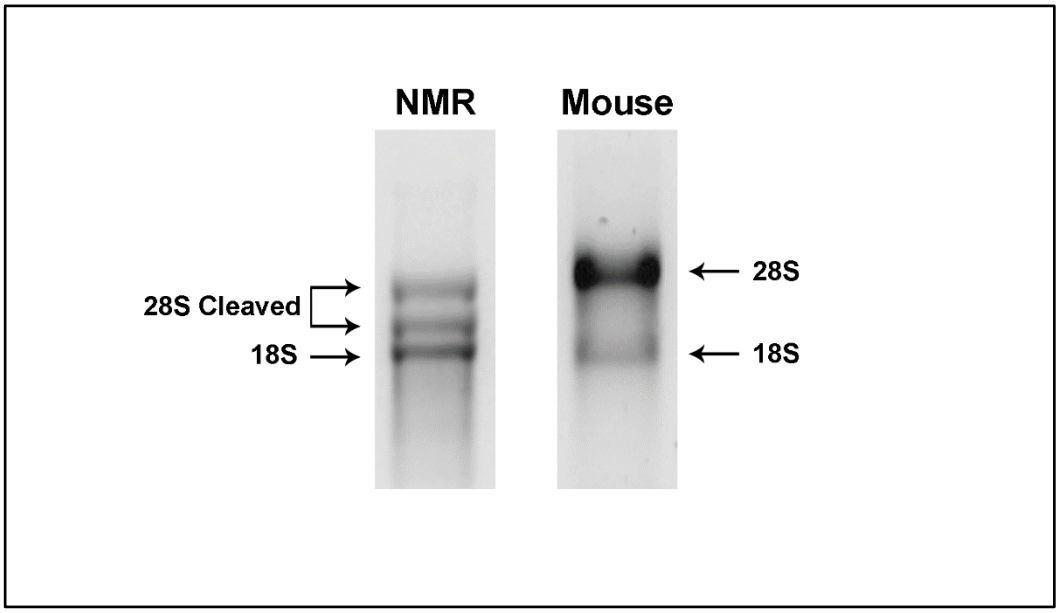

Figure 3. 2. RNA integrity of the NMR-KF1 (left) and mouse 3T3 cells (right) analysed on a 1% agarose gel. Intact NMR total RNA has three rRNA bands including two fragmented 28S rRNA species and one 18S rRNA band, while mouse total RNA has two bands (one 28S and one 18S).

Denaturation of intact total RNA of most mammalian cells, including the mouse 3T3, generates two rRNA bands, 28S (~5 kb) and 18S rRNA (~2 kb). Interestingly, the NMR-KF1 cells, as

reported previously, showed a unique rRNA migrating pattern on the agarose gel with three rRNA fragments, including a 18S rRNA and two processed 28S rRNA segments[71]. This 'hidden break' or 'gap deletion' phenomenon is common in protostomes and is thought to be convergently evolved in some of non-metazoan eukaryotes and vertebrates[191,192]. The NMR and rodents of the genus *Ctenomys* (or tuco-tuco) are the only vertebrates found to possess this hidden break[193]. Alignment with the mouse 28S rRNA sequence identified a 263-nt fragment excised from the NMR 28S rRNA divergence region 6 (D6), which contained a 118-nt unique insertion that was non-homologous to other known sequences and was nearly 300 bp upstream of the conserved proteosome hidden break site[71,192]. It was proposed that an AU-rich (and thus less stable) region in 28S rRNAs could induce the cleavage, but no such region was found near or within the breakage site of the NMR 28S rRNA[71,192,194]. The excised fragment is flanked by two 5-nt direct repeats (5'-CGGAC-3'), suggesting that the insert may originate from a transposable element[71]. However, experiments showed that *in vitro* transcribed NMR 28S rRNA could not be processed by a self-cleaving ribozyme encoded by the D6 region as reported previously in the R2 transposon system[71,195]. Further investigations are needed to understand the mechanisms for the NMR 28S rRNA cleavage.

It was postulated that the 28S rRNA cleavage and the resulting structural alteration might change the folding or dynamics of the large ribosomal subunit, thus affecting the fidelity of protein synthesis in the NMR, which may contribute to less protein misfolding or aggregation and reduced proteotoxic stress[71]. It was shown that NMR fibroblasts had higher protein translational fidelity than mouse cells, and particularly at 32°C, NMR cells displayed 10-fold lower amino acid misincorporation frequency; no significant differences were seen between the translation rates of NMR and mouse cells[71]. Remarkably, the tuco-tuco also showed a high fidelity of protein synthesis, although the maximum lifespan was not established for this species[196]. In addition, a strong correlation between the frequency of mistranslating the first and second codon positions and the maximum lifespan was reported in 16 rodent species (including the NMR), suggesting that the translational fidelity could be a determining factor in the evolution of longevity[196]. Structural studies such as cryo-EM of NMR ribosomes may also shed light on the ribosomal organisation and mechanisms by which this unique 28S rRNA cleavage may lead to improved fidelity of protein synthesis.

3.3. Establishing an *Xbp1* splicing assay in the NMR-KF1 cell line

We first determined the appropriate doses of TU or TG that would cause mild-to-moderate levels of ER stress but not result in massive cell death in NMR-KF1 cells. Results from an ATP-based luminescent assay showed that over 90% of the cells remained viable after 6-hr treatment with < 5 μg/mL TU or 4-hr treatments with < 300 nM TG (**Figure 3.3**) and therefore could be analysed within these dose ranges.

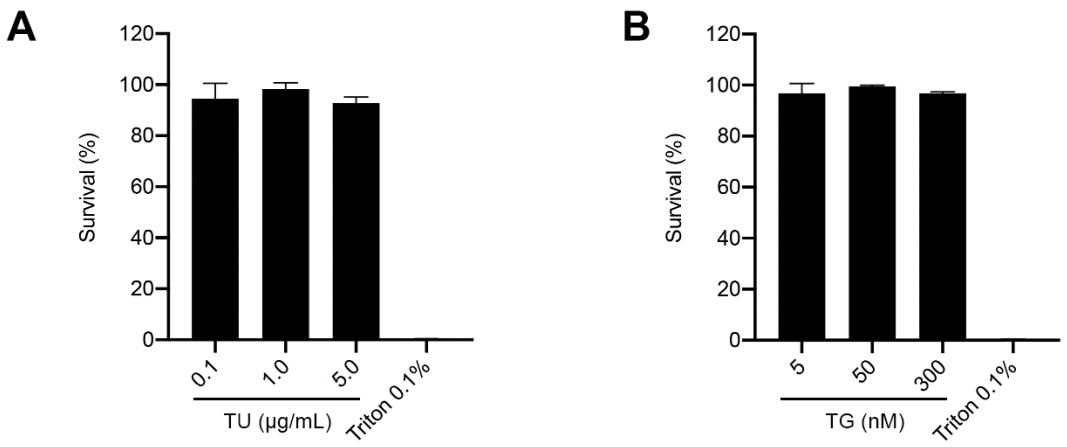

Figure 3. 3. Viability of NMR-KF1 cells after exposure to 4-hr TU (A) or 6-hr TG (B). Percentage of viable cells was measured by the CellTiter-Glo luminescent assay and compared to the untreated controls. 0.1% Triton was used as a positive control. Results were presented as mean ± S.D. of the percentage survival (%) of treated cells compared with untreated controls (n=3).

Primers used to amplify the NMR *Xbp1* transcripts were originally designed based on the NCBI sequence KM_486796.1. The annotation was updated several times within the past four years but did not affect the primer regions. The melting temperatures of the forward primer (5'-gaaccaggaattaaggatgcg-3') and the reverse primer (5'-atccatggggagatgttctg-3') were 55.5°C and 54.2°C respectively, as calculated by the nearest neighbour method[197]. Gradient PCR reactions were performed at various annealing temperatures between 50°C to 60°C, and the optimal annealing temperature was determined to be 55°C with the minimal presence of non-specific bands on a 6% TBE gel.

RT-PCR reactions were performed using the optimised conditions. Products of the *Xbp1* splicing (*Xbp1u* ~171bp, *Xbp1s* ~145bp) were observed on the 6% TBE gel, suggesting the activation of the IRE1-XBP1 pathway in NMR-KF1 cells after exposure to TU or TG. A concentration dependent titration of TU and TG established that the *Xbp1* splicing was induced in NMR-KF1 cells at 1 µg/mL TU (6 hr) (n=3; *p=0.0257) and 5 nM TG (4 hr) (n=3; **p=0.0022) (**Figure 3.4**). The *Xbp1s*-to-*Xbp1u* ratio increased when higher doses of TU or TG were applied to the NMR-KF1 cells.

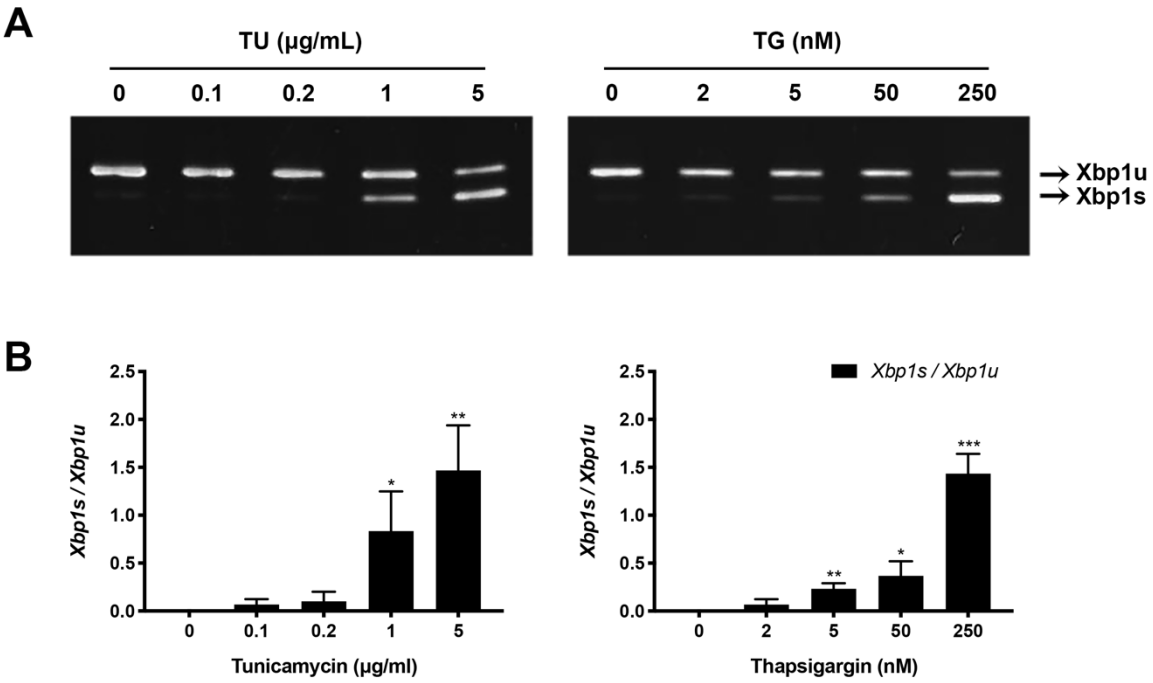

Figure 3. 4. *Xbp1* splicing in the NMR-KF1 cell line upon exposure to TU or TG. (**A**) Representative images of the RT-PCR products of *Xbp1s* and *Xbp1u* on 6% TBE gels. The graphs in (**B**) show the mean ± S.D. of *Xbp1s*-to-*Xbp1u* ratios in response to TU (left) and TG (right). Results were tested for statistical significance in reference to the untreated controls by unpaired t-tests (n=3, *p<0.05, **p<0.01, ***p<0.001).

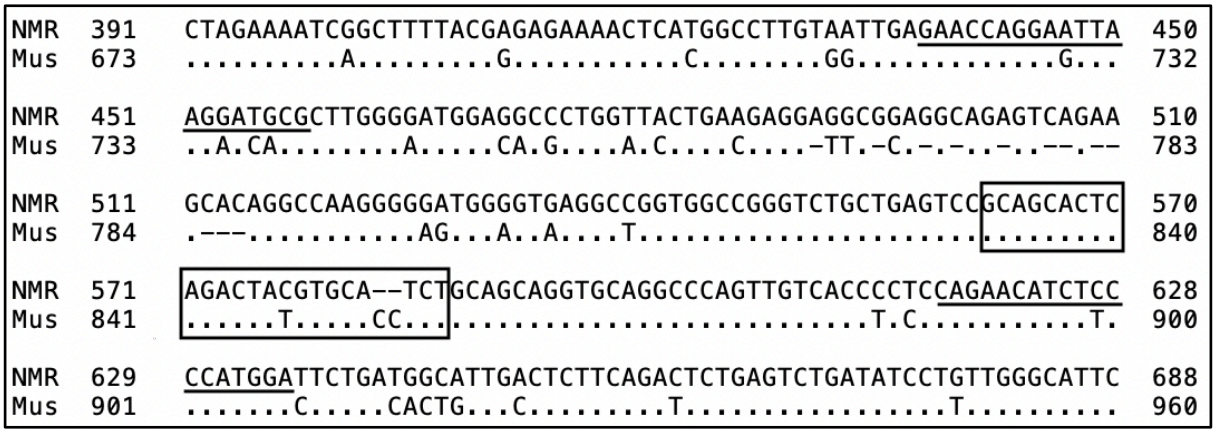

Figure 3. 5. Sequence alignment of the NMR and mouse *Xbp1u* transcripts. NMR and mouse *Xbp1u* transcripts were aligned using BLAST and shown in pairs with dots for identities. NMR *Xbp1* primers (underlined) were designed to flank the putative intron (boxed) within the NMR *Xbp1u* transcript.

A pairwise alignment of the initial NCBI reference of the NMR *Xbp1u* (KM_486796.1) with the mouse *Xbp1u* (NCBI: NM_013842.3) using BLAST suggested a putative 26-nucleotide intron to be excised from the NMR *Xbp1u*[198]. This 26-bp intron is highly conserved with only one nucleotide difference between the NMR and mouse transcripts. The resulting NMR XBP1s protein consists of 383 amino acid and shares over 81% identity with the mouse XBP1s protein (NCBI: NP_001258659.1). The presence of an N-terminal bZIP DNA-binding domain was confirmed by InterPro analysis of the NMR XBP1s, suggesting its role as a transcription factor regulating downstream UPR targets was also conserved[199]. However, the latest NCBI entry (NCBI: XM_013071981.2) has revealed a different annotation of the NMR *Xbp1u*, with two nucleotides ('cc') missing from the 26-nt intron (**Figure 3.5**), thus shifting the open reading frame of the NMR *Xbp1u* and altering the C-terminal XBP1u sequence which plays a critical role in regulating the XBP1u turnover and the efficiency of *Xbp1* splicing[93,200]. In addition, XBP1u is thought to be a negative feedback regulator of XBP1s to prevent prolonged activation of the UPR during recovery of ER stress[94]. In this study, expression of XBP1s target genes including those involved in ERAD were further analysed in NMR-KF1 cells to examine the net effect of *Xbp1* splicing. Sequence and structural analyses are outside the scope of this study but can be conducted in order to fully understand the sophisticated interplay between XBP1u and XBP1s in NMR-KF1 cells during ER stress.

3.4. Developing reliable qPCR assays for the NMR UPR markers

3.4.1. Primer design and validation of qPCR efficiency

All NMR primers were either taken from literature or self-designed using Primer-BLAST[75,160,162]. The primers were designed to have similar melting temperatures (T_m) (optimal T_m at 60°C, maximal T_m difference between forward and reverse primers of 2°C), balanced GC contents of 40-60%, and minimised self-complementary and hairpin structures. The primers targeted all relevant isoforms or splice variants of the gene of interest according to the latest NCBI annotation, and the size of PCR products were within 70-200 nucleotides. When the exon/intron structure of a gene was available, one of the primers was designed to span an exon/exon junction to be better guided to mRNA. Based on the requirements stated above, Primer-BLAST generated a list of primer pairs from which the most specific pair (i.e., the one that produced the least number of nonspecific PCR products) was selected. The important parameters of primers (Tm, GC% and structure) were also verified by OligoCalc[201]. The efficiency of all qPCR assays was confirmed to be 90-110% with R^2 values greater than 99%, which met the requirements needed to apply the ddCt method[159] (**Table 2.1**).

3.4.2. Selection of appropriate UPR reference genes by geNORM

Normalisation with proper reference genes is a critical step in obtaining accurate qPCR results where at least two reference genes are recommended[163,190]. In this study, we used the geNORM algorithm, one of the most commonly used methods, to select the appropriate reference gene pair in NMR-KF1 cells that showed the most stable expression under TU and TG-treated conditions[158,163]. We first selected six housekeeping genes that had been used as reference genes in previous NMR studies (*Gapdh, Hprt1, ACTB, B2m*) or in other mammalian systems for decades (*Rpl13a, 18r RNA*)[34,75,162,163]. *18s rRNA* was first eliminated because the corresponding C_q values (the threshold cycle at which fluorescence from amplification exceeds the background fluorescence in a qPCR reaction) were too low (<10 cycles, suggesting a very high expression level of *18r RNA*) and out of the reliable C_q range, whereas other genes showed valid C_q values of 20-30 cycles when cDNA was analysed at an ideal input (5 ng)[202]. *ACTB* (actin beta) was also excluded as double peaks were observed during the melting curve analysis using the published primer pair[34] suggesting the formation of by-products. This was confirmed

on the 2% agarose gel, which showed two clear DNA bands, one corresponding to the targeted *ACTB* product at 178bp and the other of an unknown product at ~50bp (**Figure 3.6**).

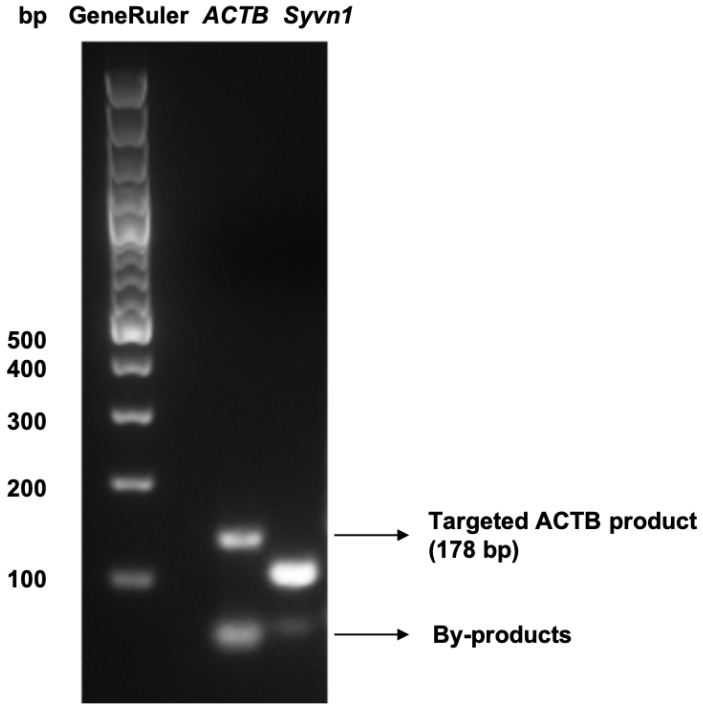

Figure 3. 6. qPCR products analysis on a 2% agarose gel. *ACTB* primers used in an earlier study produced two qPCR products suggesting the formation of by-products (either dimers or non-specific amplification products), while the specific *Syvn1* primers designed in house resulted in the formation of one distinct band corresponding to the correct product (at 114bp).

Stability of expression levels of the remaining four housekeeping genes (*B2m, Gapdh, Hprt1 and Rpl13a*) were ranked based on the average expression stability value (M) calculated using the geNORM algorithm in which a lower M value suggests a more stable mRNA expression level throughout all conditions tested (**Table 3.1**)[163]. The best reference gene pair was selected after stepwise exclusion of the gene which had the highest M value (or the least stable expression level), and the average M value of the remaining reference genes kept decreasing after each round of exclusion (**Figure 3.7 A**). In the NMR-KF1 cell line, the best reference gene pairs were *Hprt1/Rpl13a* under TU-treated conditions and *B2m*/*Gapdh* under TG-treated conditions. Both pairs showed a mean coefficient of variance (CV) < 25% and a mean M value < 0.5, which was required for good reference genes in homogenous samples including cell lines[163]. We calculated the pairwise variation ($V_{n/n+1}$) (**Figure 3.7 B**) and showed that the $V_{2/3}$

values in both TU- and TG-treated conditions were below the cut-off value of 0.15, indicating that two reference genes were sufficient for the data normalisation in this study[163].

Table 3. 1. Evaluation of reference genes in the NMR-KF1 cells in response to TU or TG.

Tunicamycin (TU)				Thapsigargin (TG)			
Genes	M	Mean CV (%)	Mean M	Genes	M	Mean CV (%)	Mean M
Rpl13a	0.198	13.5%	0.222	*Gapdh*	0.115	11.4%	0.123
Hprt1	0.245			*B2m*	0.131		
B2m	0.267	Excluded in the 2nd round		*Rpl13a*	0.141	Excluded in the 2nd round	
Gapdh	0.810	Excluded in the 1st round		*Hprt1*	0.188	Excluded in the 1st round	

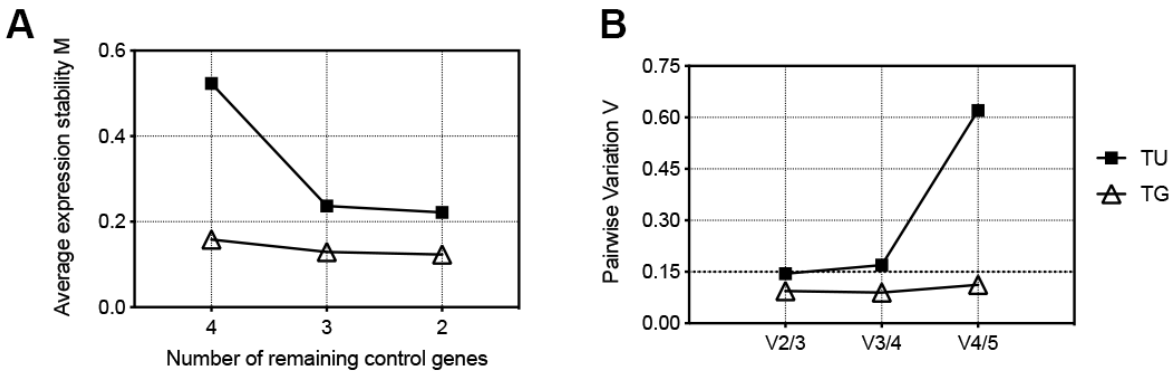

Figure 3. 7. Average stability (M) and pairwise variation (V) of reference genes in the NMR-KF1 cells. (A) Average expression stability (M) of remaining control genes during stepwise exclusion of the least stable control gene. **(B)** Determination of the optimal number of control gene for normalisation by pairwise variation ($V_{n/n+1}$, n represents the number of genes used for normalisation) analysis in the NMR-KF1 cells.

3.4.3. qPCR results of UPR markers in the NMR-KF1 cells

We determined select UPR markers by qPCR assays after the qPCR efficiency was validated and the proper reference genes were selected. Results revealed that induction of *Hspa5* and *Ddit3* transcripts were observed when cells were exposed to 1 μg/mL TU (6 hr) or 50 nM TG (4 hr) (**Figure 3.8**). Induction of *Syvn1* was only observed at 5 μg/mL TU (6 hr) or 250 nM TG

(4 hr), and the level of induction was lower than that of *Hspa5* or *Ddit3*, likely because of a time-dependent transition in the mammalian UPR where an ATF6-regulated transcriptional programme including the *Hspa5* and *Ddit3* induction was followed by an XBP1s-regulated programme including the *Syvn1* induction[92]. The expression of all three UPR markers were elevated with increasing doses of the drugs, similar to the pattern of *Xbp1* splicing, suggesting the dose-dependent UPR activation in the NMR-KF1 cells.

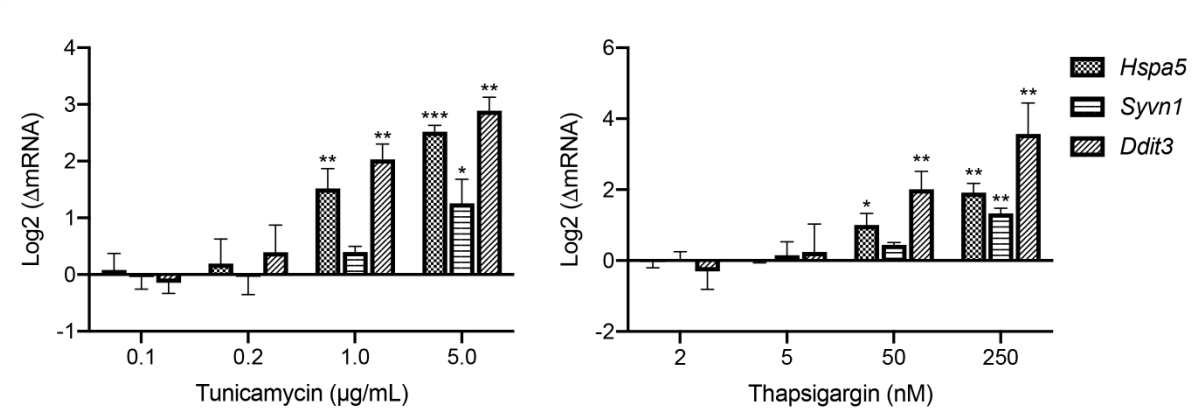

Figure 3. 8. Induction of UPR markers in NMR-KF1 cells in response to TU or TG treatments measured by RT-qPCR assays. Data were normalised to the mRNA levels of reference genes and presented as mean ± S.D. of log-transformed mRNA fold change compared with the basal-level expression in untreated controls. Results (i.e., dCq values) were tested for statistical significance in reference to the untreated controls by unpaired t-tests (n=3, *p<0.05, **p<0.01, ***p<0.001, ****p<0.0001).

3.5. Conclusions

This chapter establishes the first set of analytical tools to monitor the transcriptional outputs of UPR activation in the NMR, including the *Xbp1* splicing assay and RT-qPCR assays. These assays have been validated in an immortalised NMR kidney fibroblast line and are able to generate highly sensitive and reliable results. This robust toolkit has laid a solid foundation for this study and is further expanded to investigate transcriptional changes in genes of interest within NMR cells that are treated with UPR inducers (in Chapter 4), autophagy inducers (in Chapter 5) and disease-related species including Aβ and α-synuclein (in Chapter 6).

4. Comparing transcriptional changes in the UPR of NMR and mouse fibroblasts in response to pharmacologically induced ER stress

*Data from this chapter are published in "Du, Z., Chakrabarti, S., Kulaberoglu, Y., Smith, E. S. J., Dobson, C. M., Itzhaki, L. S., & Kumita, J. R. Probing the unfolded protein response in long-lived naked mole-rats. Biochemical and biophysical research communications **529**, 1151-1157 (2020)".*

4.1. Selection of suitable reference genes for RT-qPCR assays for NMR and mouse primary kidney fibroblasts

Using the *Xbp1* splicing and RT-qPCR assays established in Chapter 3, we compared the outputs of the UPR activation in NMR primary kidney fibroblasts with those in mouse primary kidney fibroblasts (C57BL/6J) when both species were exposed to TU or TG. Appropriate reference genes for RT-qPCR assays under TU or TG-treated conditions were selected by geNORM and should have a mean CV (%) value of < 50% and a mean M value of < 1 in heterogenous samples including primary cells[158] (Table 4.1).

Table 4. 1. Reference genes selected by geNORM in NMR and mouse primary kidney fibroblasts in response to TU or TG.

	Tunicamycin (TU)				Thapsigargin (TG)			
Species	Genes	M	Mean CV	Mean M	Genes	M	Mean CV	Mean M
NMR	*Gapdh*	0.157	19.7%	0.178	*Gapdh*	0.233	31.9%	0.268
	Rpl13a	0.198			*Rpl13a*	0.302		
Mouse C57BL/6J	*Hprt1*	0.155	29.6%	0.161	*Rpl13a*	0.295	37.8	0.305
	Rpl13a	0.167			*Gapdh*	0.315		

4.2. A higher threshold of UPR activation in NMR kidney fibroblasts in response to mild ER stress

We first evaluated IRE1 activation in the NMR and mouse primary kidney fibroblasts by probing the levels of *Xbp1* splicing and regulated IRE1-dependent decay (RIDD). In mammalian cells, activated IRE1 may degrade ER-localised mRNAs and select microRNAs via RIDD during ER stress in an XBP1-independent manner[96–98].

When cells were treated with low doses of TU for 6 hr or TG for 4 hr, *Xbp1* splicing was readily measurable in the mouse primary kidney fibroblasts at 0.2 μg/mL TU (n=5; **p=0.0022) and 5 nM TG (n=5; ****p<0.0001) when compared with untreated controls (**Figure 4.1 A, B**). In the NMR primary kidney fibroblasts, no significant levels of *Xbp1* splicing were detected when compared with untreated controls until 1 μg/mL TU (n=5; *p=0.0240) or 50 nM TG (n=5; **p=0.0034) was applied (**Figure 4.1 A, B**). No basal-level *Xbp1* splicing was present in either species, suggesting these cells were healthy and not pre-stressed before TU or TG treatments. At all TU or TG concentrations, the *Xbp1s*-to-*Xbp1u* ratios were considerably lower in the NMR primary kidney fibroblasts.

We also examined IRE1-mediated RIDD in the NMR and mouse primary kidney fibroblasts, which degraded select UPR genes and could be monitored by qPCR as well. We chose to probe the levels of *Bloc1s1*, which was the only RIDD target consistently identified in all published microarray data[203]. Results showed that the degradation of *Bloc1s1* mRNA was observed in the mouse primary kidney fibroblasts at 0.2 μg/mL TU (6 hr) and 5 nM TG (4 hr) (**Figure 4.1 C**). Levels of NMR *Bloc1s1* transcripts, however, did not change after the NMR fibroblasts were treated with TU (6 hr) or TG (4 hr) at any dose tested in this study, even when over half of the *Xbp1u* substrate had been spliced at > 1 μg/mL TU or 250 nM TG (**Figure 4.1 C**).

Combined results from *Xbp1* splicing and *Bloc1s1* degradation indicate that the NMR primary kidney fibroblasts showed a lower level of IRE1 activation, suggesting a lower level of ER stress than the mouse homologues when both species were exposed to the same concentration of TU or TG.

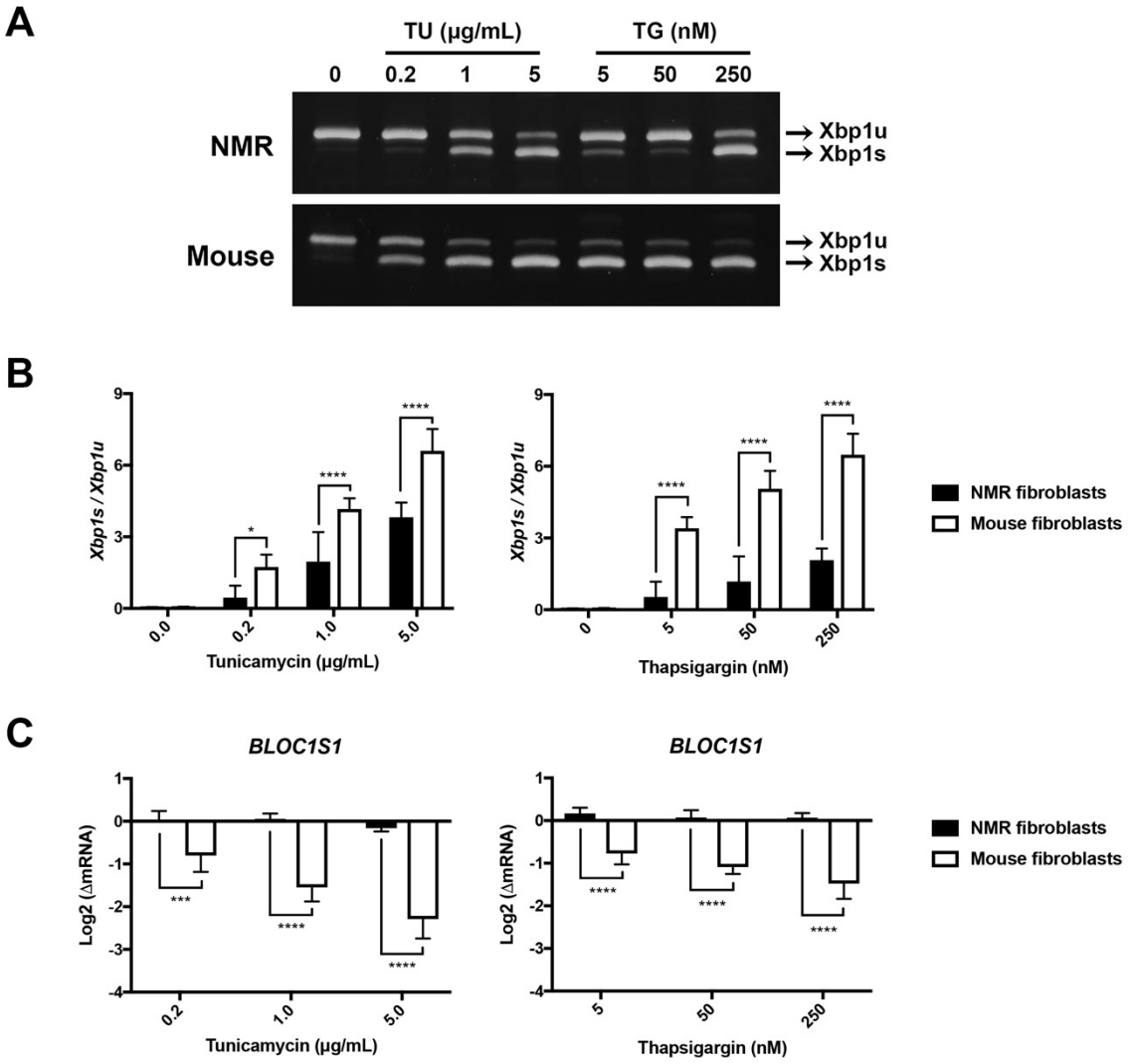

Figure 4. 1. ***Xbp1*** **splicing and RIDD degradation in the NMR and mouse primary kidney fibroblasts in response to TU (6 hr) and TG (4 hr). (A)** Representative images of the RT-PCR products of *Xbp1s* and *Xbp1u* on 6% TBE gels. The graphs in **(B)** show the mean ± S.D. of *Xbp1s*-to-*Xbp1u* ratios in the NMR and mouse fibroblasts as a response to increasing concentrations of TU (B, left) or TG (B, right). n=5 pairs; *p<0.05; ****p<0.0001; two-way ANOVA tests, Sidak's multiple comparisons tests. **(C)** *Bloc1s1* degradation measured by RT-qPCR. Results were normalised to the mRNA levels of reference genes and were presented as mean ± S.D. of log-transformed mRNA fold change compared with the basal-level expression in untreated controls. n=5 pairs; *p<0.05, ***p<0.001, ****p<0.0001; two-way ANOVA tests, Sidak's multiple comparisons tests.

We next examined the activation of the ATF6 and PERK pathways in the NMR and mouse primary kidney fibroblasts by probing levels of target genes. *Pdia4* encodes ERP72, a member of the protein disulphide isomerase family, which is upregulated by ATF6 under TU and TG-treated conditions[204,205]. *Hspa5* and *Pdia4* expression were markedly induced in the mouse primary kidney fibroblasts by approximately a four-fold increase of *Hspa5* and a two-fold increase of *Pdia4* compared with untreated controls even when the lowest doses of TU (0.2 μg/mL for 6 hr) or TG (5 nM for 4 hr) were applied (**Figure 4.2 A, B**). Induction of *Hspa5* and *Pdia4* was not significant in the NMR primary kidney fibroblasts compared with untreated controls until 1 μg/mL TU (6 hr) or 250 nM TG (4 hr) were added (**Figure 4.2 A, B**). The induction of *Ddit3* in the mouse fibroblasts was seven-fold or seventeen-fold when the cells were treated with 0.2 μg/mL TU (6 hr) or with 5 nM TG (4 hr), respectively (**Figure 4.2 C**). In the NMR primary kidney fibroblasts, a mild level of *Ddit3* induction was first observed at 1 μg/mL TU (6 hr) or 50 nM TG (4 hr) but not at 0.2 μg/mL TU (n=5; ns, p=0.0564) or 5 nM TG (n=5; ns, p=0.2387) when compared with untreated controls (**Figure 4.2 C**).

These results collectively indicate that the NMR kidney fibroblasts appear to have a higher threshold for UPR activation. Changes in the UPR markers of all three branches suggest slower progression of ER stress in the NMR kidney fibroblasts compared with the mouse fibroblasts when both species were treated with relatively low doses of TU and TG. Ca^{2+} imaging assays confirmed that TG increased cytosolic Ca^{2+} concentrations similarly within the NMR and mouse primary kidney fibroblasts at each given dose, suggesting that the attenuated ER stress response in the NMR primary kidney fibroblasts was unlikely due to differences in drug uptake between the species (**Figure 4.3**). Growth curve analyses also determined that the NMR kidney fibroblasts had a mean ± S.D. doubling time of 28.1 ± 1.9 hr, similar to the doubling time of the mouse kidney fibroblasts (27.8 ± 1.1 hr). Interestingly, although a higher dose of TU and TG was required to induce *Ddit3* expression in the NMR primary kidney fibroblasts, levels of *Ddit3* upregulation within the two species did not seem to differ significantly after exposure to higher doses of drugs including 1 μg/mL TU for 6 hr (n=5 pairs; p=0.1073) or 50 nM TG for 4 hr (n=5 pairs; p=0.3430) (**Figure 4.2 C**). This prompted us to further trace the development of ER stress and examine the effects of severe ER stress in the NMR and mouse primary kidney fibroblasts.

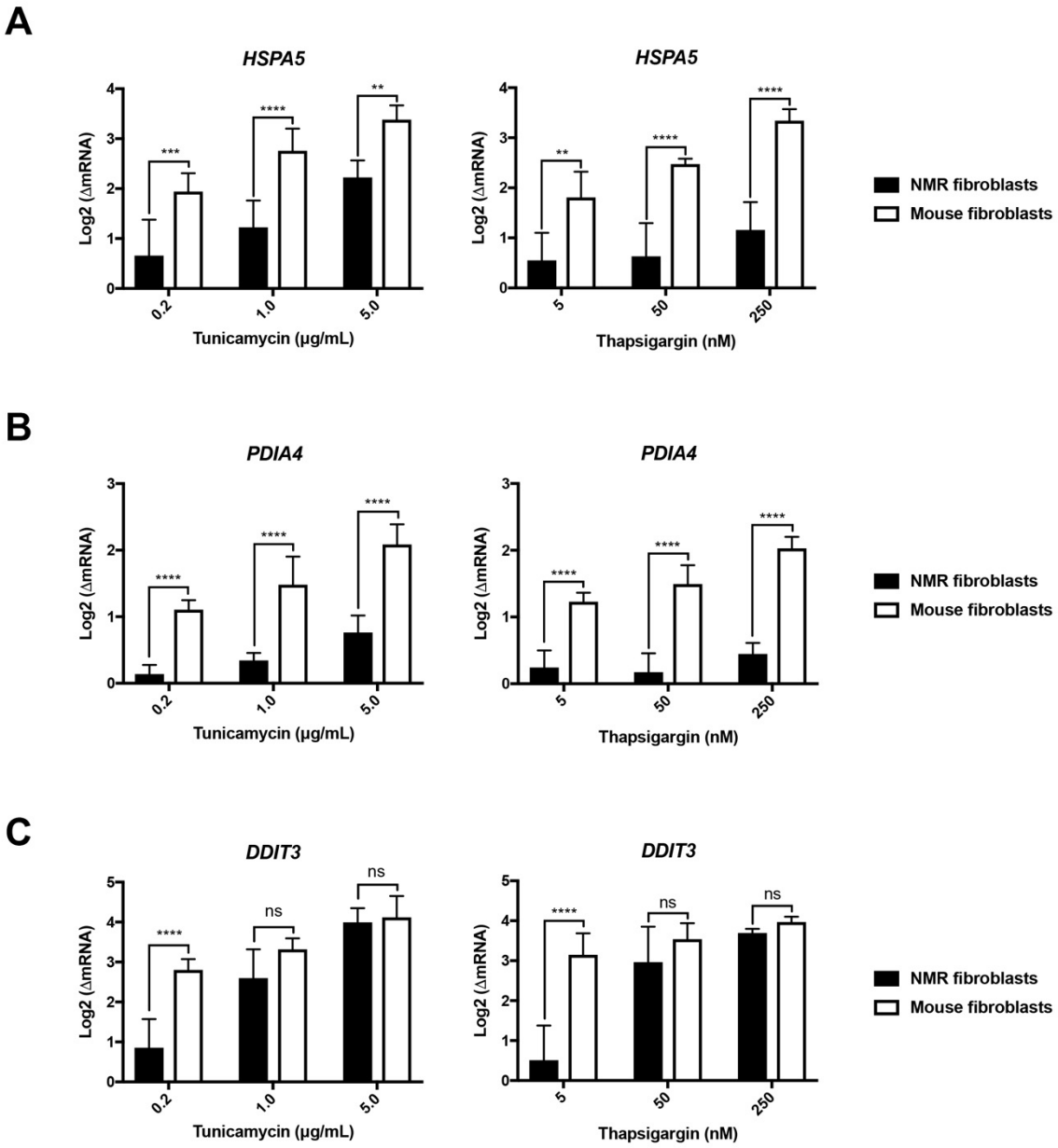

Figure 4. 2. Induction of BiP/*Hspa5* (A), PDIA4/*Pdia4* (B) and CHOP/*Ddit3* (C) in the NMR and mouse primary kidney fibroblasts in response to TU (6 hr) and TG (4 hr). Data were normalised to the mRNA levels of reference genes. Results were presented as mean ± S.D. of log-transformed mRNA fold change compared with the basal-level expression in untreated cells. n=5 pairs; ns, $p>0.5$, **$p<0.01$, ***$p<0.001$, ****$p<0.0001$; two-way ANOVA tests, Sidak's multiple comparisons tests.

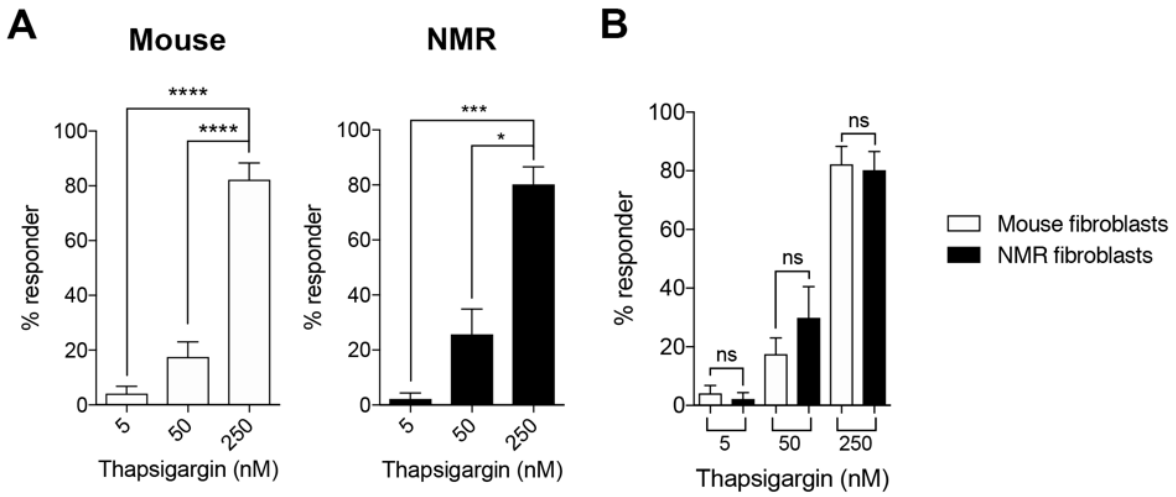

Figure 4. 3. The efficacy of TG on the NMR and mouse primary kidney fibroblasts was measured by Ca^{2+} imaging. Data were obtained from 5 mice and 5 NMRs, and >350 cells were imaged in each condition. TG increased [Ca^{2+}] in mouse and NMR primary kidney fibroblasts in a similar dose-dependent manner (**A**, n=5; *p<0.05, ***p<0.001; paired t-tests)**.** Similar proportions of mouse and NMR primary kidney fibroblasts responded to TG at all doses (**B**, n=5 pairs; ns, p>0.5; two-way ANOVA tests; Sidak's multiple comparisons tests). Ionomycin was used as a positive control for data normalisation. These data were collected and analysed by Dr. Sampurna Chakrabarti.

4.3. A similar level of UPR activation in NMR and mouse primary kidney fibroblasts under TG-induced severe ER stress

We treated the NMR and mouse kidney fibroblasts with a higher dose of TG (500 nM) for longer times to induce severe ER stress and inspected changes in the UPR markers at different time points. We first evaluated changes for select UPR markers including *Bloc1s1*, *Hspa5* and *Ddit3*. Reduction of *Bloc1s1* was observed in the NMR primary kidney fibroblasts after a 12-hr treatment with 500 nM TG (n=5; **p=0.0038). This reduction continued and reached a constant level (i.e., a three-fold decrease) that was comparable to the level of *Bloc1s1* degradation in the mouse primary kidney fibroblasts after both were subjected to a 24-hr treatment with 500 nM TG (**Figure 4.4 A**). Induction of *Hspa5* was significantly higher in the mouse primary kidney fibroblasts after 6-hr and 12-hr treatments with 500 nM TG compared to the NMR fibroblasts (n=5 pairs; ****p<0.001), but such differences diminished after 24-hr

treatment (n=5 pairs; p=0.0560) (**Figure 4.4 A**). Induction of *Ddit3* seemed to reach a plateau in both species after a 6-hr treatment with 500 nM TG, and no further upregulation was observed after a 12-hr treatment with 500 nM TG (**Figure 4.4 A**). These findings imply that despite having a lower level of UPR activation under conditions representing rather mild-level ER stress, the NMR kidney fibroblasts show no differences on the transcriptional UPR outputs to the mouse kidney fibroblasts when harsher TG-treated conditions were introduced, suggesting similar levels of ER stress in both species under severe-stress induction.

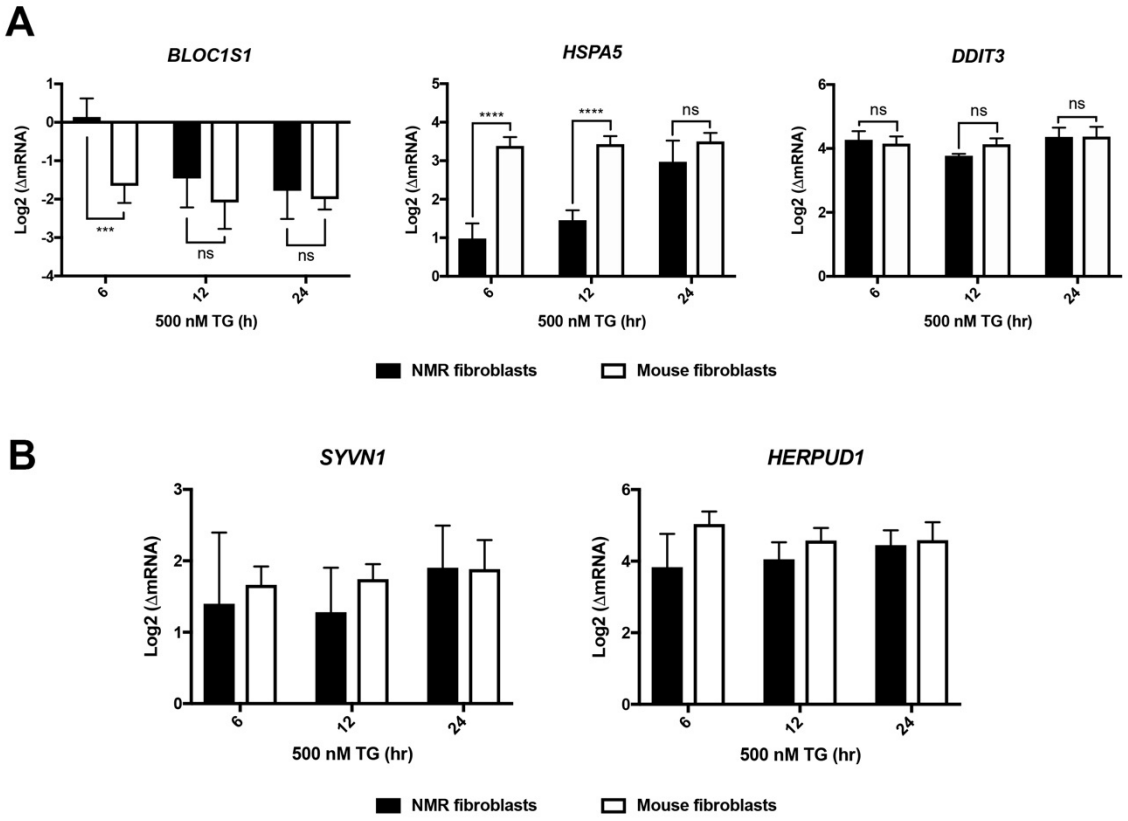

Figure 4. 4. Changes of the UPR and ERAD markers in response to long-term treatment with 500 nM TG in the NMR and mouse primary kidney fibroblasts. Levels of *Bloc1s1, Hspa5* and *Ddit3* **(A)** and *Syvn1* and *Herpud1* **(B)** were measured by RT-qPCR assays. All results were normalised to the mRNA levels of reference genes and were presented as mean ± S.D. of log-transformed mRNA fold change compared with the basal-level expression in untreated cells. n=5 pairs; ns, p>0.5, **p<0.01, ***p<0.001, ****p<0.0001; two-way ANOVA tests, Sidak's multiple comparisons tests.

In addition, we examined the effects of high-dose TG on ERAD using two markers *Syvn1* and *Herpud1*. *Herpud1* is also amongst the most highly inducible genes by the UPR during ER stress, and it encodes HERP, an ER-localised protein which interacts with HRD1 and other ERAD components and shows cytoprotective functions, though its role remains to be fully understood[206–210]. The *Herpud1* promoter contains a C/EBP-ATF composite site, an ERSE and an ERSE-II (ATTGG-N-CCACG) and therefore is believed to be regulated by all three UPR branches [206,211,212]. Induction of *Syvn1*and *Herpud1* was observed in the NMR and mouse kidney fibroblasts after a 6-hr treatment with 500 nM TG, although the induction of *Syvn1* in the NMR fibroblasts was not statistically significant compared with untreated controls due to large variance among animals (n=5; ns, p=0.0864) (**Figure 4.4 B**). Induction of *Herpud1* was more dramatic, as indicated by a ten-fold increase from the basal-level expression in both species after a 6-hr treatment with 500 nM TG (**Figure 4.4 B**). The NMR and mouse fibroblasts showed similar levels of *Syvn1*and *Herpud1* upregulation after exposure to 500 nM TG for 24 hr, suggesting that severe ER stress and the resulting UPR activation did not result in differences of ERAD induction between the NMR and mouse kidney fibroblasts.

4.4. Similar resistance of NMR and mouse kidney fibroblasts to ER stress

Salmon and colleagues previously reported unexpected sensitivity of NMR skin fibroblasts to TU and TG compared to mouse skin fibroblasts, but no molecular details were investigated[76]. Therefore, to determine whether NMR kidney fibroblasts demonstrate similar sensitivity to TU and TG and to further understand the transcriptional outputs of the UPR, we measured the cell viability of the NMR kidney fibroblasts after overnight exposure to TU and TG at different concentrations and compared the results with their mouse counterparts. Both NMR and mouse primary kidney fibroblasts showed 10% cell death when treated with >1 μg/mL TU and 20-30% cell death when treated with >50 nM TG (**Figure 4.5 A**) in comparison to vehicle controls. No differences were observed in the percentage survival between the two species, suggesting that the NMR and mouse kidney fibroblasts had similar levels of resistance to TU (up to 10 μg/mL) and TG (up to 500 nM) at any given dose tested in this study (**Figure 4.5 A**). We verified the viability results by measuring cellular caspase 3/7 activities, an indicator of levels of apoptosis in the cell population. The results show that apoptosis was observed at >10 μg/mL TU and >50 nM TG after overnight exposure in the NMR kidney fibroblasts, which ensured that our data

reflected a true percentage survival or death of the NMR fibroblasts and thereby their resistance to TU and TG (**Figure 4.5 B**).

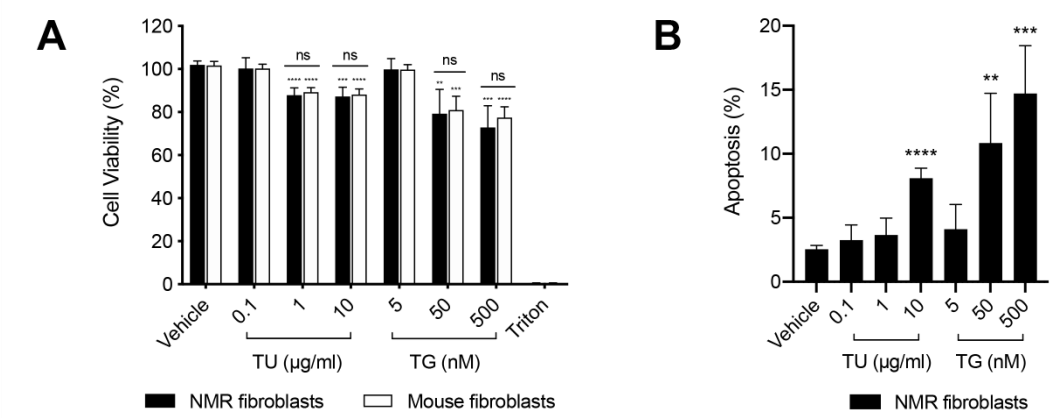

Figure 4. 5. (A) Percentage of the viable NMR and mouse primary kidney fibroblasts after exposure to TU or TG. Results were presented as mean ± S.D. of the percentage survival (%) of treated samples compared with vehicle-treated controls (n=5; $^{**}p<0.01$, $^{***}p<0.001$, $^{****}p<0.0001$; unpaired t-tests). No significant difference was observed in the NMR and mouse primary kidney fibroblasts under these conditions (n=5 pairs; ns, p>0.5; two-way ANOVA tests; Sidak's multiple comparisons tests). **(B)** Percentage of apoptotic NMR fibroblasts in response to TU and TG at various doses. Results were presented as mean ± S.D. of the percentage apoptosis (%) of treated samples compared with staurosporine-treated positive controls (n=5; $^{**}p<0.01$, $^{***}p<0.001$, $^{****}p<0.0001$; unpaired t-tests).

4.5. Discussion

In this chapter, we used the established methods to compare the NMR and mouse UPR under pharmacologically induced ER stress. We first determined the appropriate reference genes for qPCR analysis in NMR and mouse kidney fibroblasts under TU and TG-treated conditions. We noticed that selection of reference genes was not consistent across the immortalised NMR-KF1 line (**Table 3.1**), primary NMR fibroblasts and primary mouse fibroblasts. We concluded that such differences were due to variances in animal species, experimental conditions including types of drugs and given doses, and heterogeneity of samples. Using the same geNORM algorithm, Schuhmacher and co-workers examined twelve housekeeping genes in the NMR nervous system and identified that the best reference gene pair was *ACTB*/*EIF4A2*[213].

In this study, we tested four widely used housekeeping genes and found that expression of these genes was more stable in the primary kidney fibroblasts than in the nervous system, as indicated by mean CV and M values, strongly suggesting that the choice of reference genes was also dependent on tissue type and should be assessed stringently on a case-by-case basis.

We identified that under low-dose TU or TG-induced ER stress, NMR kidney fibroblasts had a higher threshold of UPR activation. *Xbp1s* splicing was consistently maintained at low levels in the NMR fibroblasts, a similar phenotype that had been reported in a long-lived *daf*-2(-) mutant strain of *C. elegans* with reduced insulin/insulin-like growth factor 1 signalling (IIS)[214]. This mutant also showed strong resistance to ER stress, which was attributed to the induction of a set of genes involved in ER proteostasis modulated by an interaction between XBP1 and DAF-16, a major target of IIS[214]. A broader analysis of the transcriptional profile can therefore be conducted to investigate the relationship between the ISS and UPR in the NMR. Skin fibroblasts from the snell dwarf mouse also showed diminishing *Xbp1* splicing but surprising sensitivity to TG-induced ER stress because of heightened pro-apoptotic signalling including CHOP[215], which was not observed in our NMR kidney fibroblasts. Lower induction of ER chaperones and PDI in NMR fibroblasts suggest less compensation for the protein-folding capacity, as NMR fibroblasts may have higher basal levels of these chaperones. Several comparative studies have shown that the NMR and other longer-lived animals possess higher constitutive levels of heat shock proteins and chaperones which enhance protein folding and refolding under both basal and stressed conditions[72,74,216]. To fully understand this, studies at the protein-level would be required; however, NMR-specific antibodies are not widely available.

Under high-dose TG-induced ER stress, we found that NMR and mouse kidney fibroblasts demonstrate similar levels of UPR activation and resistance to a broad dose range of TU and TG. These conflicting results when compared with the previous study of NMR skin fibroblasts might result from differences in the experimental settings where we minimised the introduction of additional stresses by keeping the NMR cells in a 32 °C hypoxic environment of 3% O_2 (instead of 37°C with 20% O_2), which has been shown to enable their optimum growth, and by eliminating the serum-starvation step prior to TU or TG treatment suggested by Salmon and co-workers[76]. Discrepancies between the two studies may also simply reflect differences between cells derived from different organs. Further studies can be performed to investigate

tissue/organ-specific or cell-type-specific UPR in the NMR, for example, the UPR in pancreatic β cells that are constantly challenged by ER stress.

4.6. Conclusions

This chapter constitutes the first investigation of the UPR in the NMR at the transcript level. The assays established in the NMR fibroblasts have been validated and show insights into the differences between the UPR mechanisms in NMR and mouse kidney fibroblasts. The attenuated development of ER stress in the NMR fibroblasts suggests that NMR fibroblasts are able to withstand pharmacologically induced *in vitro* ER stress and may largely increase the chances of survival under these conditions. Fully understanding the complex roles of the UPR and its interplay with other proteotoxic stress responses is daunting, particularly in emerging species where molecular tools and knowledge are limited. Our assays, however, can be easily modified to explore expression of a wide range of genes involved in cellular and molecular mechanisms under different scenarios in the NMR. With discoveries of drugs that modulate individual UPR branches, more studies can be conducted to elucidate the mechanisms behind each UPR arm and their contributions to the stress resistance of the NMR, thereby promoting a better understanding of the relationship between proteostasis and ageing.

5. Probing autophagy in NMR fibroblasts

5.1. Introduction

In this chapter, we develop methods to probe the autophagy pathway in the NMR, including a LC3B-II turnover assay and RT-qPCR analysis. The LC3B-II turnover assay was established following the Guidelines for the Use and Interpretation of Assays for Monitoring Autophagy (3rd edition)[217]. RT-qPCR assays were built upon the methodology described in Chapter 3. Combining these tools, we examined the effects of two FDA-approved compounds, rapamycin (RA) and chloroquine (CQ), on the NMR cells, and highlighted the differences among the NMR skin fibroblasts (NMR-SK cell line[36]), kidney fibroblasts (NMR-KF2 cell line[36]) and mouse NIH3T3 embryonic fibroblasts at the transcriptional and posttranslational levels in response to these drug treatments.

5.1.1. LC3-II turnover

The hallmark of autophagy is the formation of the autophagosome, and central to this process is the ATG8 lipid conjugation system which was first identified in yeast[218] (**Figure 5.1**). In mammals, two subfamilies of ATG8 orthologues have been identified based on their sequence homology, including LC3 (MAP1LC3A, B, B2 and C isoforms) and GABARAP (GABARAP, GABARAPL1 and GABARAPL2 isoforms), which have shown different tissue distributions and post-translational modifications[219–221]. Both the LC3 and GABARAP subfamilies are found to be localised to autophagosome membranes and possess a ubiquitin-like core and two additional, characteristic N-terminal α-helices, which vary substantially among different mammalian ATG8 orthologues and have been shown to mediate membrane tethering and fusion required for autophagosome biogenesis[136,141,222–224]. Previous studies have suggested that these two subfamilies play crucial but distinct roles in autophagosome biogenesis (including phagophore formation, elongation and closure) and fusion with the lysosome, but the precise function of each isoform remains to be defined[225–227]. In this study, we probe the autophagic activity in the NMR using the most extensively studied isoform LC3B, which is known to decorate autophagosomes and recruit specific autophagy receptors such as p62[228].

Mammalian LC3 is initially synthesised as proLC3. The C-terminus of this precursor protein is rapidly processed by the cysteine protease ATG4B, which is the functionally dominant ATG4 isoform in mammalian autophagy and has broad specificity for LC3 paralogues, to expose a glycine residue and produce the primed LC3 known as LC3-I[136,137]. Upon activation of autophagy, the carboxyl base of the glycine in LC3-I is covalently conjugated to phospholipids such as phosphatidylethanolamine (PE) on the autophagosome membrane via an amine bond through sequential ubiquitination-like reactions mediated by ATG7 (E1-like activating enzyme), ATG3 (E2-like conjugation enzyme) and ATG12-ATG5·ATG16L1 complex (E3-like ligase) to produce the PE-conjugated LC3-II[136,138–142]. During autophagosome maturation, the LC3-II on the outer autophagosome membrane can be removed by ATG4B-mediated deconjugation for recycling[229], while the LC3-II on the inner membrane remains associated with the completed autophagosome and will be degraded in the acidic autolysosome after the autophagosome-lysosome fusion.

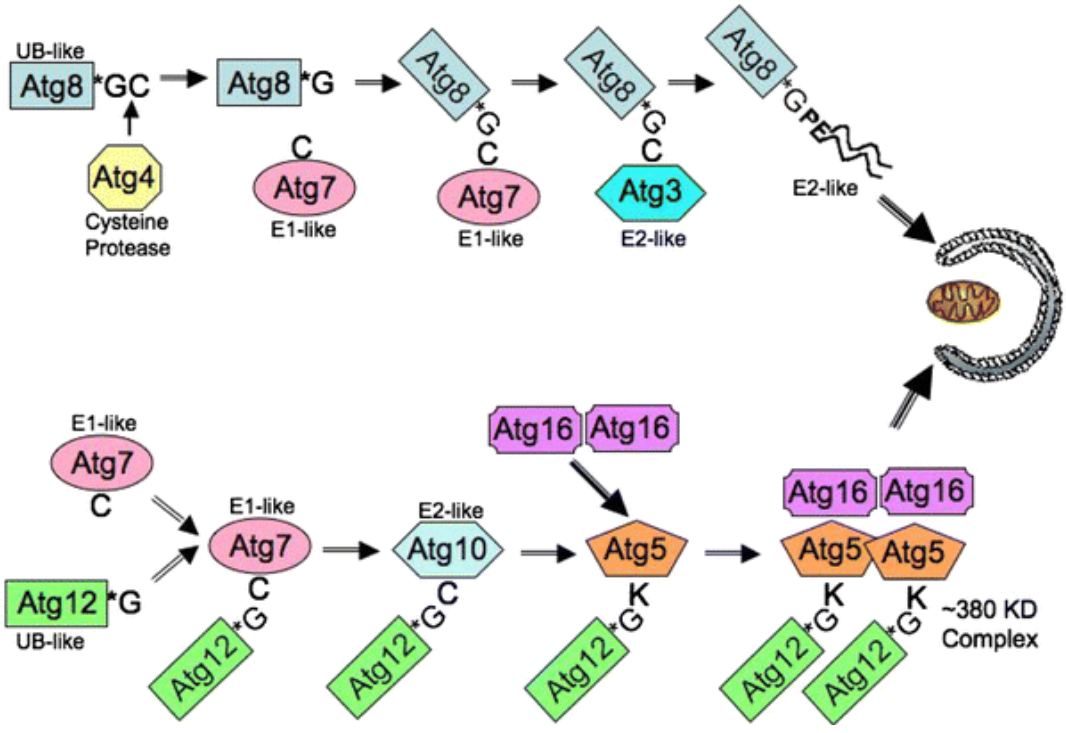

Figure 5. 1. ATG8 (LC3) conversion is the hallmark of autophagosome formation. This process is mediated by two ubiquitination-like reactions carried out by a number of ATG proteins. Figure reprinted from the reference with permission[230].

LC3-II has been the most widely exploited protein marker in the detection of autophagy so far. Autophagic activity is often inferred on the basis of LC3-II turnover, reflected by the difference in the amount of LC3-II normalised to a loading control (housekeeping protein) in the presence and absence of lysosomal degradation, which can be monitored by western blotting[217,231]. Increased levels of LC3-II in the presence of lysosome degradation are indicative of an active autophagic flux (to the stage of autophagosome reaching the lysosome). Lysosomal degradation can be inhibited through the use of chloroquine (CQ) (**Figure 5.2**), bafilomycin A_1, and protease inhibitor cocktails including pepstatinA, E-64d and leupeptin[217]. CQ is an FDA-approved drug that has been shown to impair the fusion of autophagosomes with lysosomes and raise or neutralise lysosomal pH, but discrepancies in the literature suggest that the precise mechanisms of how CQ blocks autophagy remains to be determined[232,233]. This rule also applies when assessing whether a particular treatment alters autophagy flux, where the levels of LC3-II obtained with the treatment plus a lysosomal inhibitor must be compared to those obtained with the treatment alone as well as the inhibitor alone. For example, autophagy inducers, such as rapamycin (RA) and starvation, should result in an additive effect on LC3-II levels, thereby suggesting an enhanced autophagic flux[217]. RA is an FDA-approved macrolide compound and an inhibitor of mTOR (**Figure 5.2**), which suppresses autophagy through modulation of ATG13, ULK1 and ULK2 and prevention of the nuclear transport of TFEB[129,234,235]. Upon entering cells, RA forms a gain-of-function complex with the 12-kDa FK506-binding protein (FKBP12) (**Figure 5.3**), which interacts with the FKBP12-rapamycin binding domain (FRB) of the mTORC1, thus inhibiting mTORC1 function and inducing autophagy[236].

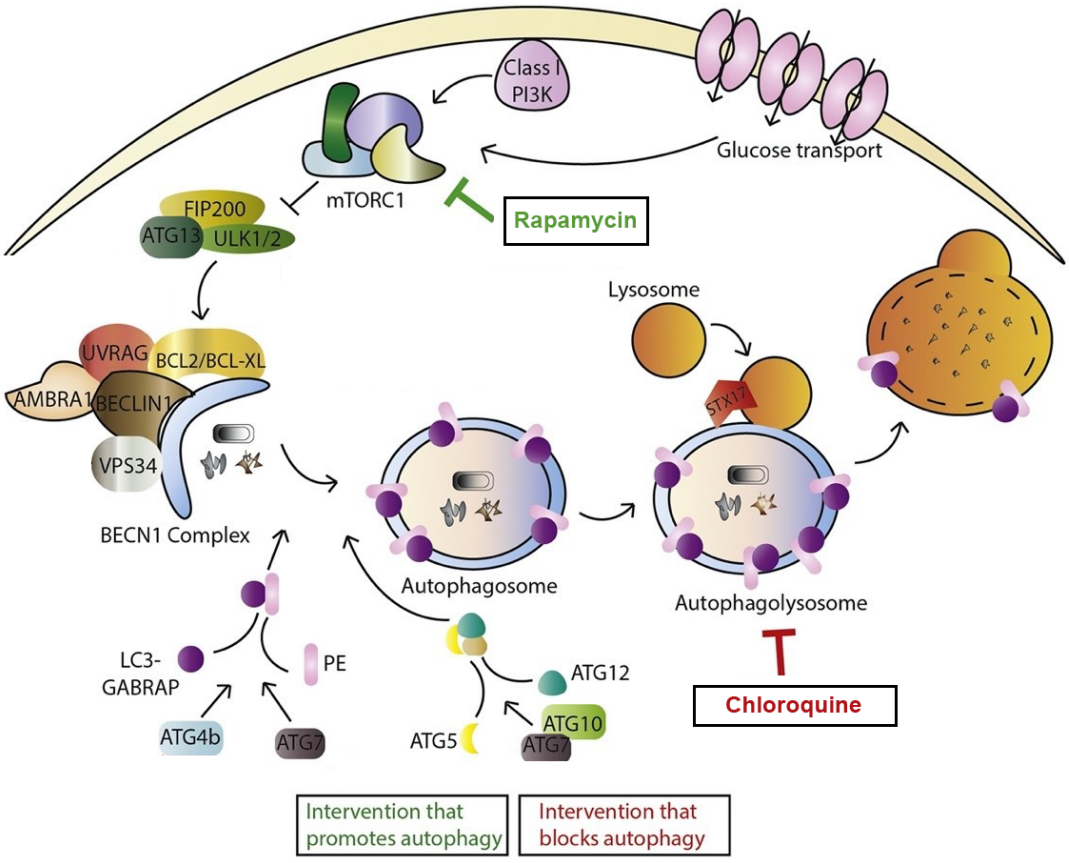

Figure 5. 2. Interventions that target autophagy. Rapamycin (RA) inhibits the activity of mTOR1 complex (which prevents autophagy under normal conditions through binding to ULK1/2 complex) and thus is a potent autophagy inducer. Conversely, chloroquine (CQ) is an autophagy inhibitor which can inhibit lysosomal degradation and/or autophagosome-lysosome fusion, although the mechanisms remain to be defined. Figure modified from the reference[237].

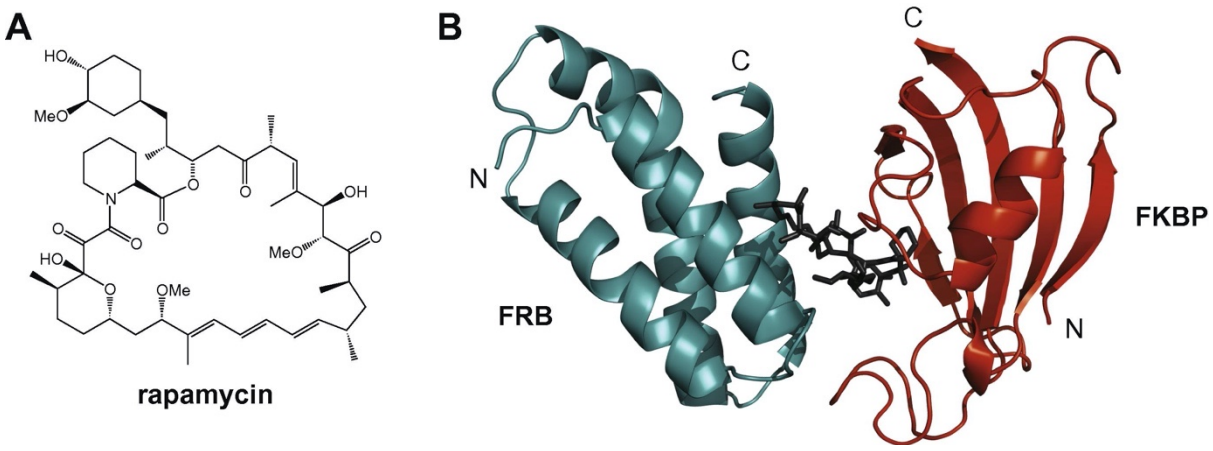

Figure 5. 3. Structure and actions of rapamycin. In a cell, rapamycin **(A)** first binds to FKBP12 and the FKBP12–rapamycin complex binds to the FRB (FKBP and rapamycin binding) domain of mTOR, rendering mTORC1 enzymatically inactive **(B)**. Figures reprinted from the references with permission[238].

5.1.2. Transcriptional regulation of autophagy

The early years of autophagy research focused on the cytosolic processes including dynamic membrane rearrangements and post-translational modifications of ATG proteins, neglecting a potential nuclear regulation, although induction of *Atg8* by nitrogen starvation was observed in yeast back in 1999[239]. In the past decade, over 20 transcription factors have been shown to be associated with autophagy, including TFEB and ZKSCAN3, the FOXO family, p53, E2F1 and NF-κB, the PPARα-FXR-CREB axis, C/EBPβ, GATA1, and Jun[240] (**Figure 5.4**).

TFEB is a member of the microphthalmia-TFE (MiT) subfamily of basic helix-loop-helix-leucine zipper (bHLH-Zip) transcription factors that regulates a multitude of autophagy and lysosomal genes[241–243]. TEFB binds to the coordinated lysosomal expression and regulation (CLEAR) element, a 10-base E-box-like palindromic motif (GTCACGTGAC) present in the promoters of target genes, and enhances the expression of a wide range of genes important for autophagy initiation (*Becn1*, *Wipi1, Atg9b*, *Nrbf2*), autophagosome formation (*Gabarap*, *Map1lc3b*, *Atg5*), substrate capture (*Sqstm1*), autophagosome trafficking and fusion with lysosomes (*Uvrag*, *Vps11*, *Vps18*), and lysosomal biogenesis (*Lamp1*, *Clcn7*, *Ctsf*, *Ctsb*)[243,244]. The subcellular localisation and activity of TFEB are tightly controlled by phosphorylation of

conserved serine residues, including mTOR1-mediated phosphorylation of Ser122 and Ser211, ERK2 (extracellular signal-regulated kinase)-mediated phosphorylation of Ser142, and mTOR-independent phosphorylation of Ser138 and Ser134[234,242,245,246]. Under nutrient-repleted conditions, phosphorylated TFEB is kept inactive in the cytosol, whereas conditions including starvation, oxidative stress and lysosomal disorder cause dephosphorylation of TFEB, leading to its rapid translocation to the nucleus to induce the expression of target genes[234,242,243]. Nutrient depletion also induces the release of lysosomal Ca^{2+} through mucolipin 1 (MCOLN1), which activates the phosphatase calcineurin, leading to TFEB activation and autophagy induction[247]. In addition, many factors that regulate TFEB activity are, in turn, transcriptionally regulated by TFEB, and TFEB activation also promotes its own transcription[248]. Regulation of autophagy by TFEB-mediated transcriptional activity also plays an important role in various pathological conditions. For example, TFEB overexpression alleviates toxicity of α-synuclein and protects dopaminergic neurons in a rat model of Parkinson's disease[152]. The zinc-finger protein with KRAB and SCAN domain 3 (ZKSCAN3) is a master transcriptional counterpart of TFEB, which represses the transcription of a number of autophagy-related genes including *ULK1* and *Map1lc3b*[249].

The FOXO family of transcription factors (FOXOs), particularly FOXO3 and FOXO1, was one of the first transcriptional regulators to be associated with autophagy, similar to TFEB, which is also regulated by phosphorylation and translocated to the nucleus to induce the expression of a number of target genes (*Atg4*, *Atg12*, *Becn1*, *Bnip3*, *Map1lc3b*, *Ulk1*/2, *Vps34*)[250–252]. The most extensively characterised tumour suppressor, p53, regulates autophagy depending on its cellular localisation. Nuclear p53 promotes autophagy by inducing the expression of the autophagy modulators DRAM (damaged-regulated autophagy modulator) and Sestrin and by directly binding to autophagy genes (*Atg4*, Atg7, *Atg10*, *Ulk1/2*, *Lkb1*)[253–255]. In contrast, cytoplasmic p53 acts as an autophagy repressor with a yet elusive mechanism; downregulation of *Map1lc3b* at a posttranscriptional level may be partly responsible[256,257]. The phosphorylated version of the N-terminally truncated p63 isoform (p-ΔNp63α), a member of the p53 tumour suppressor family, induces autophagy via binding to the promoters of target genes (*Ulk1*, *Atg5*, *Atg7*) as well as miRNA modulation[258]. One of the partners of p53 in life-or-death decisions made by the cells, E2F1 (E2F transcription factor 1), induces autophagy by upregulating genes such as *Map1lc3b*, *Ulk1*, *Atg5* and *Dram1*[259]. E2F1 also induces *Bnip3*, a hypoxia-induced death factor which activates autophagy by disrupting the inhibitory binding of B-cell lymphoma 2 (BCL-2) to Beclin 1, while NF-kB (nuclear factor kappa-light-chain-

enhancer of activated B cells) transactivates *Bnip3* under basal nonapoptotic conditions[260,261]. NF-κB has also been shown to induce autophagy genes including *Becn1* and *Sqstm1*[262,263]. The PPARα (peroxisome proliferator-activated receptor-α)-FXR (farnesoid X receptor)-CREB (cAMP response element-binding protein) axis regulates hepatic autophagy during feeding and fasting cycles. During nutrient-deprived fasting, CREB and its coactivator CRTC2 activate transcription of autophagy genes including *Atg7*, *Ulk1* and *Tfeb*, while bile-acid-activated FXR disrupts the CREB-CRT2 complex by interacting with CREB and forming a repressive transcriptional complex which inhibits autophagy genes during feeding[264]. PPARα is also activated by feeding and competes with FXR for the same DNA-binding sites (DR1 elements) in the promoters of autophagy genes, thus inducing activation of these genes[265]. CCAAT/enhancer binding protein beta (C/EBPβ) is a transcription factor that activates several *Atg* genes including *Map1lc3a*, *Map1lc3b* and *Gabarapl1* in response to the circadian cycle in the liver[266]. In addition, the master regulator of haematopoiesis GATA-binding factor 1 (GATA1) activates transcription of *Map1lc3b* and its homologous, which has been suggested to rely on transcriptional induction of *Foxo3* by GATA-1[267]. The c-Jun NH2-terminal kinase (JNK) pathway, which can be activated by various cellular stresses, mediates transcriptional induction of *Becn1* and *Map1lc3b* in autophagy-dependent cell death in vascular smooth muscle cells isolated from atherosclerotic plaques and ceramide-treated cancer cells[268–270].

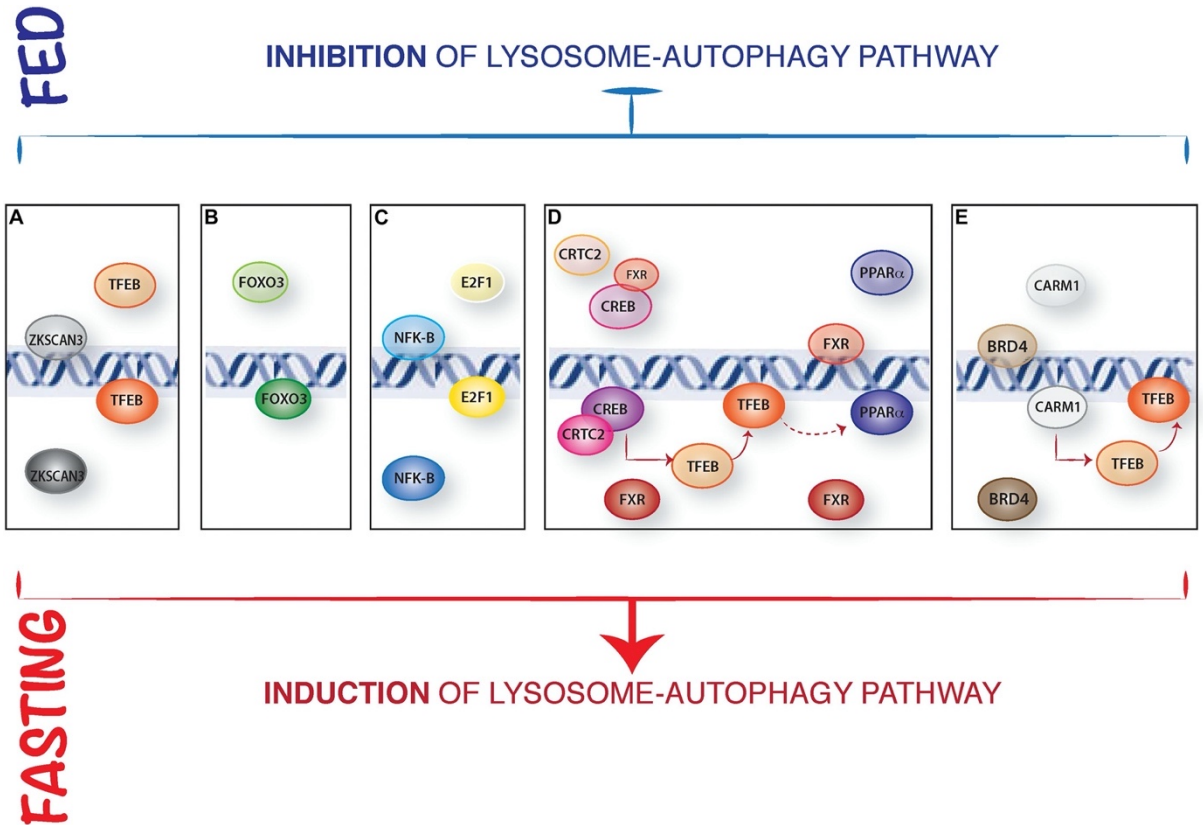

Figure 5. 4. Representative mechanisms of transcriptional regulation of autophagy. A few transcription factors have been recently identified that control autophagy under nutrient-abundant (light coloured) and -depleted (dark coloured) conditions through nuclear binding to DNA, including TFEB and its counterpart ZKSCAN3 **(A)**, the FOXO family such as FOXO3 **(B)**, the E2F1/NF-kB axis **(C)**, CREB-FXR and PPARα-FXR Circuits **(D)**, and epigenetic regulation of autophagy **(E)**. Figure reprinted from the reference with permission[271].

An increasing number of transcription factors involved in all steps of the process have been linked to the transcriptional regulation of autophagy. Changes in autophagy protein levels, although generally considered better to follow with regards to the initiation and completion of autophagy, sometimes are not sufficient evidence of autophagy induction and hence must be accompanied by additional assays such as RT-qPCR to monitor changes at the mRNA level of *Atg* genes and/or autophagy regulators[217]. Development of these assays may be particularly useful in emerging model systems, such as the NMR, where commercial antibodies are limited.

5.2. LC3B proteins in the NMR

Based on the latest NCBI annotation, seven ATG8 orthologous have been identified in the NMR, including three LC3 members (LC3Av1 [XP_004867972.1], LC3Av2 [XP_012922183.1] and LC3B [XP_004842818.1]) and four GABARAP members (GABARAP [XP_004857437.1], GABARAPL1v1 [XP_021114839.1], GABARAPL1v2 [XP_004845947.1] and GABARAPL2 [XP_004842886.2]). In this study, we chose to use the best-characterised autophagic marker, LC3B, to monitor the autophagic activity in the NMR. Alignment of the NMR proLC3B protein with the human (NP_073729.1) and mouse proLC3B (NP_080436.1) shows the sequences are highly conserved among the three species, particularly at the N-terminus (**Figure 5.5**). Assuming that the mechanisms of LC3 processing and conjugation to PE are also conserved in the NMR, we have identified the Gly120 to be exposed for lipidation after cleavage by ATG4B and, therefore, we have obtained the sequences of LC3B-I and LC3B-II in the NMR. The NMR LC3B-I and LC3B-II proteins essentially differ from the human and mouse orthologues by one and three amino acids, respectively, suggesting that the functions mediated by their structures should also be preserved (**Figure 5.6**).

```
Mus                 MPSEKTFKQRRSFEQRVEDVRLIREQHPTKIPVIIERYKGEKQLPVLDKTKFLVPDHVNM
Homo                MPSEKTFKQRRTFEQRVEDVRLIREQHPTKIPVIIERYKGEKQLPVLDKTKFLVPDHVNM
Heterocephalus      MPSEKTFKQRRTFEQRVEDVRLIREQHPTKIPVIIERYKGEKQLPVLDKTKFLVPDHVNM
                    ***********:**************************************************

Mus                 SELIKIIRRRLQLNANQAFFLLVNGHSMVSVSTPISEVYESERDEDGFLYMVYASQETFG
Homo                SELIKIIRRRLQLNANQAFFLLVNGHSMVSVSTPISEVYESEKDEDGFLYMVYASQETFG
Heterocephalus      SELIKIIRRRLQLNANQAFFLLVNGHSMVSVSTPISEVYESEKDGDGFLYMVYASQETFG
                    ****************************************.* ***************

Mus                 TAMAV--
Homo                MKLSV--
Heterocephalus      RGLSVCD
                      ::*
```

Figure 5. 5. Sequence alignment of the NMR proLC3B protein (bottom) with the human (middle) and mouse proLC3B (top) proteins. The analysis was performed using the MUSCLE software[272].

```
>XP_004842818.1 NMR proLC3B
MPSEKTFKQRRTFEQRVEDVRLIREQHPTKIPVIIERYKGEKQLPVLDKTKFLVPDHVNMSELIKIIRRR
LQLNANQAFFLLVNGHSMVSVSTPISEVYESEKDGDGFLYMVYASQETFGRGLSVCD (soluble)
127 amino acids

> NMR LC3B-I
MPSEKTFKQRRTFEQRVEDVRLIREQHPTKIPVIIERYKGEKQLPVLDKTKFLVPDHVNMSELIKIIRRR
LQLNANQAFFLLVNGHSMVSVSTPISEVYESEKDGDGFLYMVYASQETFG (soluble)
120 amino acids


> NMR LC3B-II
MPSEKTFKQRRTFEQRVEDVRLIREQHPTKIPVIIERYKGEKQLPVLDKTKFLVPDHVNMSELIKIIRRR
LQLNANQAFFLLVNGHSMVSVSTPISEVYESEKDGDGFLYMVYASQETFG-PE (membrane-associated)
120 amino acids + phosphatidylethanolamine(PE)
```

Figure 5. 6. Sequences of the NMR proLC3B, LC3B-I and LC3B-II proteins.

5.3. Induction of autophagy by rapamycin in the NMR skin fibroblasts at both posttranslational and transcriptional levels

We first monitored the levels of LC3B proteins in an NMR skin fibroblast cell line (NMR-SF) using the anti-LC3B antibody (#2775, Cell Signalling Technology) produced by immunising animals with a synthetic peptide corresponding to the N-terminal human LC3B, that should be able to target and detect NMR LC3B proteins based on sequence homology. The LC3B-II, despite being larger in mass, migrates faster on gels than the LC3B-I protein as a consequence of increased hydrophobicity[217] (**Figure 5.7 A**). The two proteins could be well separated from each other on 15% homemade SDS-PAGE gels for quantification but not on 12% Bolt or 4-12% gradient NuPAGE precast gels.

The NMR skin fibroblasts treated for 24-hr with 100 μM CQ demonstrated a four-fold increase in the normalised LC3B-II level (to GAPDH) compared to the DMSO-treated control, reflecting the accumulation of basal-level autophagosome formation as well as the induction of autophagy by the long-term CQ treatment through mTOR inhibition, similar to what was reported by Zhao *et al* (**Figure 5.7 A Lane 1&3, B, C**)[273]. When the NMR-SF cells were treated with 100 nM RA alone for 24 hr, the normalised LC3B-II protein level showed a nearly two-fold increase compared to that of the DMSO-treated control (**Figure 5.7 A Lane 1&2, B, C**). When the cells were treated with 100 nM RA and 100 μM CQ (abbreviated as RCQ hereafter) for 24 hr, the LC3B-II protein level also showed a nearly two-fold increase compared to that of the CQ-treated control (**Figure 5.7 A Lane 3&4, B, C**). These findings suggested that RA

increased the formation of LC3B-II and is an inducer of autophagosome synthesis in the NMR-SF. No differences were observed in the cells treated with medium and with the 0.05% DMSO control.

LC3B can also undergo substantial transcriptional regulation[274]. We applied an RT-qPCR assay to measure the changes of LC3B/*Map1lc3b* mRNA levels to discriminate between changes that were strictly reflected in altered amounts of protein versus those that were due to changes in transcription. The qPCR assay was established following the methods described in Chapter 3. The NMR *Map1lc3b* primers were validated to have a 106.4% reaction efficiency (**Table 2.2**), and *Gapdh* and *B2m* were selected as the reference genes based on lower M values under RA, CQ and RCQ-treated conditions (**Table 5.1**). Results revealed a slight transcriptional induction of *Map1lc3b* mRNA when the NMR-SF cells were treated with RA or with RCQ for 24 hr, suggesting that the increased LC3B-II amounts observed in the western blot were a result of both the upregulation of *Map1lc3b* at the transcriptional level and the increased LC3B lipidation *per se* (**Figure 5.7 D, left**). No changes of *Map1lc3b* mRNA levels were found in the NMR-SF cells treated with CQ alone (**Figure 5.7 D, left**). These results suggested that RA induced autophagy of the NMR-SF at both transcriptional and posttranslational levels.

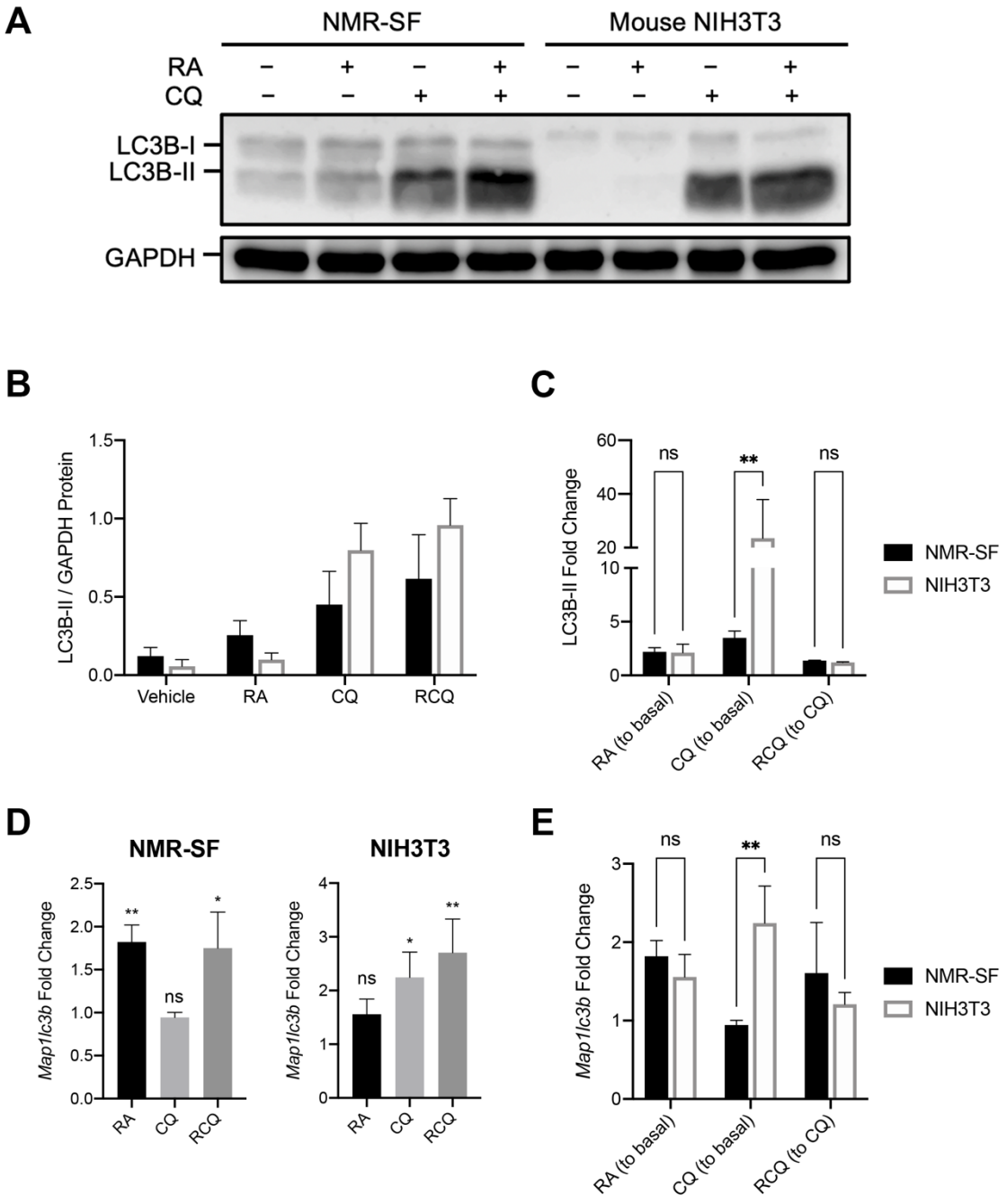

Figure 5. 7. Probing the autophagy in the NMR skin fibroblast cell line (NMR-SF) and the mouse NIH3T3 cells (3T3). Cells were treated with or without 100 nM RA for 24 hr in the presence or absence of 100 μM CQ. Total protein (20 μg) collected per sample was separated by SDS-PAGE, and the amounts of LC3B-II were determined by immunoblotting. Representative western blots are shown in **(A)**. The graph in **(B)** shows the mean ± S.D. of LC3B-II protein levels normalised to the levels of the loading control (GAPDH) in the NMR-SF and 3T3 as a response to the treatments (n=3). **(C)** The fold change of LC3B-II protein

levels in RA-treated cells was compared to the LC3B-II levels in the vehicle (DMSO)-treated controls, while the fold change of LC3B-II protein levels in the RCQ-treated samples was compared to the LC3B-II levels in the CQ-treated controls. (D) Changes of *Map1lc3b* mRNA levels in the NMR-SF and 3T3 cells were determined by RT-qPCR. Results were normalised to the mRNA levels of reference genes and were presented as mean ± S.D. of mRNA fold change compared with the basal-level expression in negative controls. Results were tested for statistical significance in reference to the vehicle-treated controls by unpaired t-tests (n=3; ns, p>0.5, *p<0.05, **p<0.01; unpaired t-test). Interspecies comparison of mRNA fold changes of *Map1lc3b* in response to RA, CQ and RCQ (compared to the CQ-treated controls) treatments was conducted using two-way ANOVA tests, Sidak's multiple comparisons tests as shown in (E) (n=3 pairs; ns, p>0.5, **p<0.01).

Table 5. 1. Selection of reference genes in the NMR-SF, NMR-KF2 and mouse NIH3T3 for RT-qPCR analysis of autophagy markers.

NMR skin fibroblast (NMR-SF)				NMR kidney fibroblast (NMR-KF2)				Mouse NIH3T3 fibroblast			
Genes	M	Mean CV	Mean M	Genes	M	Mean CV	Mean M	Genes	M	Mean CV	Mean M
Gapdh	0.099	22.2%	0.131	*Gapdh*	0.209	22.4%	0.216	*Hprt1*	0.262	24.1%	0.296
B2m	0.110			*Rpl13a*	0.223			*Rpl13a*	0.330		
Hprt1	0.180	Excluded in the 2nd round		*B2m*	0.245	Excluded in the 2nd round		*Gapdh*	0.428	Excluded in the 2nd round	
Rpl13a	0.407	Excluded in the 1st round		*Hprt1*	0.528	Excluded in the 1st round		*B2m*	0.679	Excluded in the 1st round	

5.4. Comparable levels of autophagic flux but different transcriptional regulation in the NMR skin fibroblasts and mouse NIH3T3 embryonic fibroblasts in response to RA and CQ treatment

Using the established methods above, we compared the changes of autophagic flux and levels of *Map1lc3b* in the NMR-SF cell line to those in the mouse NIH3T3 embryonic fibroblast cell line (abbreviated as 3T3 hereafter) in response to RA and CQ.

Western blotting results showed that in the absence of RA and CQ, a higher level of LC3B-II was observed in the NMR-SF cells than in the 3T3 cells, suggesting the presence of more autophagosomes in the NMR-SF cells (**Figure 5.7 A Lane 1&5, C**). When CQ was added, the LC3B-II protein level in the 3T3 cells increased significantly to the amount that was equivalent to (or even higher than, although not statistically significant) the LC3B-II protein level in the NMR-SF cells (**Figure 5.7 A Lane 3&8, B**). The much more robust increase of the LC3B-II protein level in the 3T3 cells than that in the NMR-SF cells might be a result of (1) a higher level of induction of *Map1lc3b* in the 3T3 cells, (2) a higher basal level of autophagic flux in the 3T3 cells, and/or (3) differences of other regulatory mechanisms, such as TFEB-mediated induction of autophagy, between the two cell lines in response to CQ.

RT-qPCR determined a two-fold increase of *Map1lc3b* induced by CQ in the 3T3 cells when normalised to *Hprt1* and *Rpl13a* (**Table 5.1, Figure 5.7 D, right**), which contributed to the increased total level of LC3B-II protein in the 3T3 cells (**Figure 5.7 C, E**), whereas in the NMR-SF cells, no induction of *Map1lc3b* was observed (**Figure 5.7 D, left**).

The effects of RA were similar on the levels of LC3-II and *Map1lc3b* upregulation in the NMR-SF and 3T3 cells either in the absence or presence of CQ (**Figure 5.7 A, C, E**). To further explore the effects of RA and CQ on the transcriptional regulation of the NMR and mouse cells, we expanded our RT-qPCR analysis and examined changes of more autophagy markers under RA or CQ-treated conditions.

5.5. Different transcriptional regulation by RA and CQ in the NMR skin fibroblasts, the NMR kidney fibroblasts and the mouse NIH3T3 fibroblasts

We selected five more proteins (in addition to LC3B) that are involved in several steps of autophagy and have been reported to be regulated at the transcriptional level (Table 5.3). ATG5 contains a ubiquitin fold that is an essential component of the ATG12-ATG5·ATG16L1 complex, which mediates LC3-PE conjugation in phagophore expansion and autophagosome formation. Beclin 1 encoded by *Becn1* is a yeast VPS30/ATG6 orthologue which forms the PIK3C3 complex for autophagy activation. P62 is encoded by *Sqstm1* and is a mammalian autophagy receptor which recognises and links ubiquitinated proteins to LC3 via a LIR (LC3-interacting region) motif. TFEB is a master transcription factor that regulates autophagy and lysosomal biogenesis. LAMP1 (lysosomal-associated membrane protein 1) resides primarily across lysosomal membranes and is routinely used as a marker for lysosomes.

Table 2. 4. A panel of autophagy proteins selected for the analysis of the transcriptional regulation by RA and CQ[240].

Gene	Role in autophagy	Transcription factor linked to autophagy
Atg5	Autophagosome formation	DDIT3, CREB, E2F1, FOXO1, ΔNp63α, FXR, GATA-1
Becn1	Autophagy initiation	Jun, FOXO1, FOXO3A, NF-κB, PPARα, TFEB, XBP1, ΔNp63α, FXR, STAT-1
Map1lc3b	Autophagosome formation	ATF4, C/EBPβ, Jun, CREB, E2F1, FOXO1, FOXO3A, GATA-1, MITF and TFE3, PPARα, SREBP-2, TFEB, FOXK1, FXR, ZKSCAN3
Sqstm1	Autophagy receptor/substrate	C/EBPβ, KLF4, MITF and TFE3, NF-κB, TFEB, β-catenin and/or TCF
Tfeb	Transcription factor	TFEB, CREB, FXR
Lamp1	Lysosomal formation	TFEB

Following the methodology established in Chapter 3, we self-designed all primers for these selected autophagy-related genes, validated qPCR efficiency to be between 90 and 110% (**Table 2.2**), and determined the appropriate reference genes using the geNORM algorithm under RA and CQ-treated conditions for the three cell lines (**Table 5.1**).

We first determined changes of expression of these autophagy-related genes in the NMR-SF cell lines under RA and CQ-treatment conditions. Our qPCR results showed that 24-hr treatment with 100 nM RA increased transcript levels of all these markers, suggesting that RA induced autophagy by modulating several steps of the process (**Figure 5.8**). In contrast, 24-hr treatment with 100 μM CQ significantly downregulated expression of *Tfeb* in the NMR-SF but did not affect other markers, except a mild level of *Atg5* induction (**Figure 5.8**).

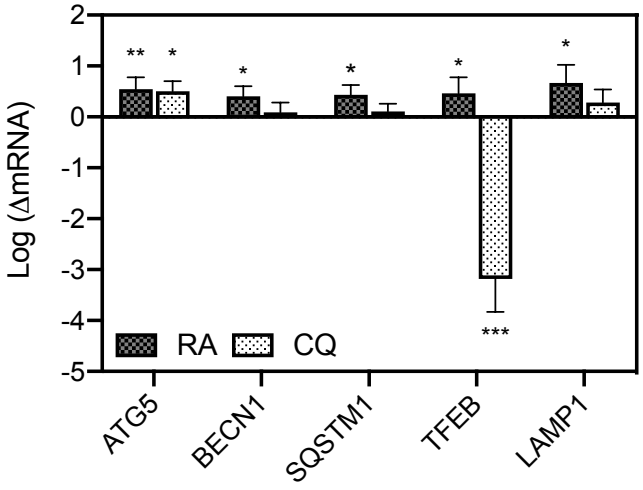

Figure 5. 8. Changes of autophagy-related mRNA levels in response to the treatment of 100 nM RA or 100 μM CQ were measured by RT-qPCR in the NMR-SF cells. Results were normalised to the mRNA levels of reference genes and presented as mean ± S.D. of log-transformed mRNA fold change compared with the basal-level expression in untreated cells. Results (i.e., dCq values) were tested for statistical significance in reference to the untreated controls by unpaired t-tests (n=3, *p<0.05, **p<0.01, ***p<0.001, ****p<0.0001).

The NMR-KF2 cells showed a similar induction pattern of the autophagy genes when treated with RA, except for lower induction of *Atg5*, suggesting that effects of RA on the NMR fibroblasts derived from different tissues seemed to be largely the same (**Figure 5.9 A**). When the NMR-KF2 cells were treated for 24-hr with 100 μM CQ, *Tfeb* expression was again found to be downregulated but to a much lower extent compared to the level of reduction observed in the NMR-SF cells (**Figure 5.9 B**). Levels of other autophagy markers did not appear to change at the transcriptional level when the NMR-KF2 were treated with CQ, similar to the trend seen in the NMR-SF (**Figure 5.9 B**).

We also determined levels of these autophagy markers in the mouse NIH3T3 cells. Results showed a notably higher level of *Sqstm1* induction in the 3T3 compared to the NMR-SF and NMR-KF2 cells but slight reduction of *Becn1* under RA-treated conditions, while no significant differences were identified in other autophagy markers among the three cell lines (**Figure 5.9 A**). Similar to what was observed in the NMR-SF and NMR-KF2 cell lines, the 24-hr CQ treatment also repressed *Tfeb* expression in the 3T3 cells, suggesting that the effect of CQ on the *Tfeb* transcript was likely to be universal and not species-specific (**Figure 5.9 B**). The level of *Tfeb* downregulation in the 3T3 cells was comparable to that in the NMR-KF2 cells and was much lower than that in the NMR-SF cells (**Figure 5.9 B**). In addition, the 24-hr CQ treatment induced *Map1lc3b* expression in the 3T3 cells but not in the NMR-SF and NMR-KF2 cells, which contributed to the increased LC3B-II protein level in the 3T3 cells, as shown in the previous section (**Figure 5.9 B**).

We further explored whether different profiles of gene expression would impact sensitivity of three cell lines to RA and CQ. Results showed that RA did not affect cell viabilty in the three cell lines (**Figure 5.9 C**). The 24-hr treatment with CQ, however, led to 20% cell death in the NMR-KF2 cells and 3T3 cells, and less than half of the NMR-SF cells survived. The higher sensitivity of the NMR-SF cells to CQ correlated with a higher level of *Tfeb* downregulation observed in the NMR-SF cells compared with the NMR-KF2 and 3T3 cells, suggesting the potential role of *Tfeb* in promoting cell survival under CQ-treated conditions (**Figure 5.9 C**).

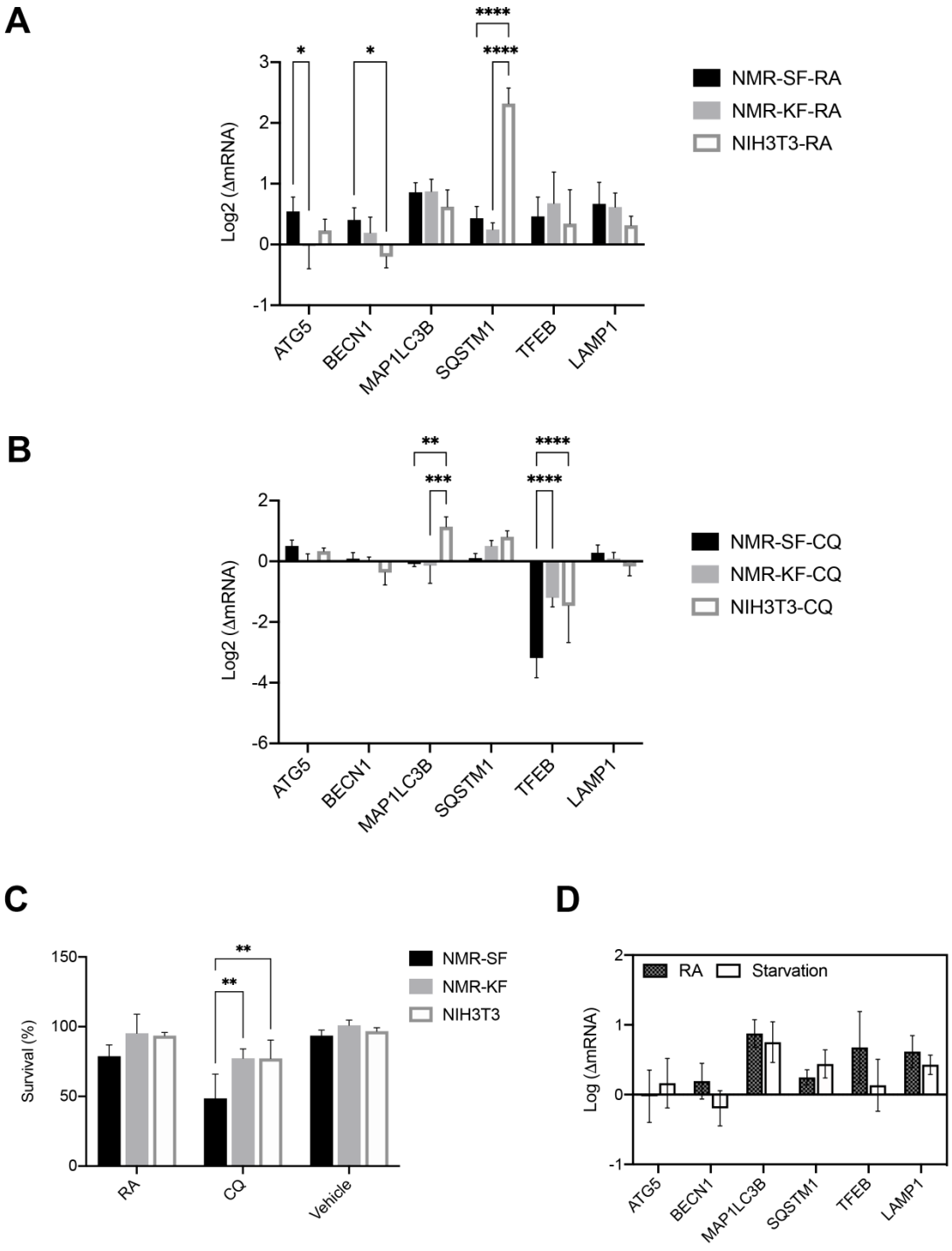

Figure 5. 9. Probing the effects of autophagy modulators on the NMR-SF, NMR-KF2 and mouse NIH3T3 cell lines. (A) Changes of autophagy-related mRNA levels in response to 100 nM RA were measured by RT-qPCR in the three cell lines. Results were normalised to the mRNA levels of reference genes and presented as mean ± S.D. of log-transformed mRNA fold change compared with the basal-level expression in controls. n=3 pairs; *p<0.05, ****p<0.0001; two-way ANOVA tests, Sidak's multiple comparisons tests. **(B)** Changes of

autophagy-related mRNA levels in response to 100 μM CQ were measured by RT-qPCR in the three cell lines. Results were normalised to the mRNA levels of reference genes and presented as mean ± S.D. of log-transformed mRNA fold change compared with the basal-level expression in controls. n=3 pairs; **p<0.01, ***p<0.001, ****p<0.0001; two-way ANOVA tests, Sidak's multiple comparisons tests. **(C)** Percentage of the viable cells after each treatment was measured by the CellTiter-Glo assay. Results were presented as mean ± S.D. of the percentage survival of treated samples compared with controls. n=3 pairs; **p<0.001; two-way ANOVA tests, Sidak's multiple comparisons tests. **(D)** Autophagy markers were evaluated at the transcriptional level in response to 100 nM RA or starvation (HBSS) in the NMR-KF2 cells. Results were normalised to the mRNA levels of reference genes and presented as mean ± S.D. of log-transformed mRNA fold change compared with the basal-level expression in untreated controls. n=3 pairs; ns, p>0.5; two-way ANOVA tests, Sidak's multiple comparisons tests.

Using the same methodology, we also determined the effects of starvation, the most extensively studied condition that induces autophagy, on the panel of selected autophagy markers in the NMR. By culturing the NMR-KF2 cells in HBSS, all autophagy genes showed similar levels of transcriptional modulation as those found in RA-treated conditions, including the induction of *Map1lc3b*, *Sqstm1* and *Lamp1* (**Figure 5.9 D**).

5.6. Discussion and future work

In this chapter, we developed tools to investigate the transcriptional and posttranslational modulation of autophagy in the NMR, including the LC3B-II turnover assay and RT-qPCR assays. Using these assays, we first confirmed the role of RA as a potent inducer of autophagy in the NMR fibroblasts. Previously Zhao and colleagues showed an increased level of LC3-II proteins in the NMR hepatic cells treated with RA compared to the negative controls, but they did not assess the LC3-II protein levels in the presence of any autophagy inhibitors, and no transcriptional changes of *Map1lc3b* were probed[75]. Here we reported a more comprehensive analysis which proved that RA modulated LC3B/*Map1lc3b* at both transcriptional and posttranslational levels to induce autophagy in the NMR-SF. However, our protocol of the LC3B-II turnover assay could be improved, as the LC3B-II band on the PVDF membrane was

smearing which resulted in the large variance between replicates, and ideally, the LC3B-I and LC3B-II proteins should provide two distinct bands for accurate quantification.

Previously Zhao *et al.* reported higher levels of endogenous LC3B-II protiens without the presence of any autophagy inhibitors in the tissue lysates from multiple organs in one-day-old NMRs compared to those in one-day-old C57BL/6 mice, and they reached a conclusion that NMRs displayed higher basal levels of autophagy[75]. This interpretation could be problematic, as the higher LC3B-II levels might represent the accumulation of non-degraded cargos resulting from the inhibition of autophagosome-lysosome fusion and/or lower levels or rates of lysosomal degradation in NMRs, suggesting a reduced basal level of autophagosome turnover and/or the inefficient turnover to keep pace with increased autophagosome formation in the NMRs instead of higher basal levels of autophagosome formation *per se*. Pride *et al*. showed a higher ratio of (macro)atuophagy to chaperone-mediated auotphagy (CMA) in the NMR skin fibroblasts compared to that of the mouse counterparts, but the percentage of total proteolysis by (macro)autophagy in the NMR cells did not seem to differ from that in the mouse[74]. In addition, Beclin 1, which is an essential component in the PIK3C3 interactome that signals the onset of autophagy and another widely used marker for autophagy induction, has been found to be expressed at lower levels in the various tissues of young and adult NMRs compared to the mouse counterparts, suggesting that the Beclin-1-dependent pathways of autophagy induction in the NMR might be less active than those in the mouse[75].

Our results suggested that the mouse 3T3 cells seemed to have a more robust machinery of autophagosome synthesis than the NMR-SF cells, which was partly attributed to the induction of *Map1lc3b* under CQ-induced stress. However, some modifications will need to be made to the current protocol in order to properly determine the levels of the basal autophagic flux in the 3T3 and NMR-SF cells. An appropriate concentration of CQ should first be established by dose- and time-dependent curves at which the autophagic flux is inhibited completely without cell death. Then, a series of measurements of the LC3B-II protein levels can be conducted by immunoblotting as described in this study at every 60 min post-inhibition using the established CQ concentration. Other inhibitors of autophagosome-lysosome fusion or lysosomal degradation such as bafilomycin A_1 and protease inhibitor cocktails can also be employed to validate the results obtained under the CQ-treated conditions. In addition, primary cells or tissues should be used for direct comparisons between species (i.e., NMR versus other short-lived species) to explore the potential relationship between enhanced autophagy and longevity.

We also found that compared to the NMR-KF2 and mouse 3T3 cells, the NMR-SF cells were more sensitive to CQ-induced lysosomal stress, which might be associated with the significant suppression of TFEB, a master transcription factor of the autophagy-lysosomal pathway. Previous studies showed that CQ-induced apoptosis in the NMR skin fibroblasts, as suggested by the increased ratio of BAX/BCL-2 ratio, was linked to the inhibition of the pro-survival PI3K/Akt signalling pathway[273]. Here, we reported, from the transcriptional point of view, that levels of downregulation of *Tfeb* seemed to be associated with the CQ-dependent cell death. *Map1lc3b* and *Sqstm1* were among the most significantly upregulated genes affected by TFEB overexpression as they carry at least one TFEB binding site in their promoters[242]. Under lysosomal stress, more severe *Tfeb* downregulation in the NMR-SF cells might result in the production of fewer TFEB proteins, leading to lower levels of *Map1lc3b* induction than that in the 3T3 cells. TFEB-regulated *Sqstm1* was also slightly more upregulated in the 3T3 and NMR-KF2 cells compared to the NMR-SF cells, although not statistically significant. Similar to our results, it has also been reported that expression of TFEB target genes including *Map1lc3b* and *Sqstm1* were upregulated in hepatocytes from control mice after treatment with CQ, but the upregulation was hampered in hepatocytes from *Tfeb* knockout mice[275]. Since a wide range of genes involved in autophagy and lysosomal function have been shown to be regulated by TFEB, it is likely that *Tfeb* downregulation could impair the induction of autophagy, thereby leading to cell death under lysosomal stress. In HeLa cells, CQ-induced nuclear translocation was also accompanied by a decrease in the overall levels of TFEB after 15-hr exposure as shown in a western blot assay[276]. As TFEB activity is primarily regulated by its phosphorylation state and subcellular localisation, it is important to examine the direct impact of *Tfeb* downregulation on its nuclear translocation in the NMR, which can be monitored by immunofluorescence. The NMR TFEB protein (XP_004846657.1) is predicted to contain 463 amino acids and shares 88% identity with the human TFEB (NP_001258873.1; 476 amino acids), with all critical serine residues (Ser122, 134, 138, 142 and 211) conserved in the sequence. A TFEB nuclear assay using a cell line stably transfected with a TFEB-GFP probe can be used instead when the expression level of endogenous TFEB is too low to be detected (as suggested by high Cq values in qPCR assays) by antibodies. mTOR activity may also be monitored since CQ-induced TFEB translocation is mediated by mTORC1 inhibition as shown in other mammalian systems. TFEB overexpression, which is believed to improve overall autophagy and lysosomal function and promote cellular clearance, has been applied as a therapeutic strategy in several age-associated disease models including lysosomal storage disorders and neurodegenerative disease[277].

Investigation of TFEB activity in the long-lived NMR will provide insights into the regulation of autophagy and offer new tools to promote cellular clearance in heath and disease.

Finally, we provide some preliminary results of the transcriptional modulation in NMR kidney fibroblasts under starvation. Although both RA and starvation can activate autophagy through mTOR inhibition, starvation but not RA induces TFEB nuclear translocation, probably because RA is a partial inhibitor of mTOR and some mTOR substrates could still be efficiently phosphorylated[278]. It was also reported that RA and amino acid starvation had opposite effects on the expression of genes involved in the synthesis, transport and use of amino acids[279]. In addition, a couple of studies showed a higher level of autophagy in the NMR than that in the mouse under serum-starved conditions based on a higher LC3-I-to-LC3-II ratio, suggesting a superior mechanism in the NMR to ensure protein quality may be associated with longevity[14,74]. However, it has been shown that the comparison of the LC3-II amount among samples is more accurate than the LC3-I-to-LC3-II ratio as the LC3B-II has higher sensitivity than LC3B-I in immunoblotting, particularly when probed by antibodies generated against the N-terminal peptide of LC3[217,280]. It has also been recently reported that GABARAP subfamily, instead of LC3 members, is a primary driver of starvation-induced autophagy, which may be a better readout of the level of autophagy under starvation[227]. Thus, more autophagy markers can be investigated to better characterise the transcriptional and posttranslational modulations of autophagy induced by starvation in the NMR and establish the role of autophagy in long-lived species versus that in short-lived counterparts.

6. Investigating the effects of disease-relevant amyloid-β and α-synuclein oligomers on the UPR and autophagy in the NMR

6.1. Introduction

The involvement of UPR and autophagy has been implicated in neurodegenerative diseases, but their exact roles remain to be defined. NMRs have higher levels of soluble amyloid-β (Aβ), but do not display any amyloid plaques, which is a hallmark of Alzheimer's disease[78,79], in their brains. Therefore, it has been hypothesised that the long-lived NMRs must possess certain mechanisms that protect them from developing age-associated neurodegenerative diseases. In this Chapter, we set out to investigate the effects of Aβ and α-synuclein oligomers, which are believed to be the major pathogenic species in Alzheimer's disease (AD) and Parkinson's disease (PD), respectively, on the UPR and autophagy pathways of the NMR as a simplified disease model. For this, we used a cell culture system wherein NMR and mouse cells were exposed to exogeneous Aβ and α-synuclein oligomers prepared by established protocols with proven neurotoxicity[153,154]. Using the quantitative methods established in the previous chapters, we determined changes in expression of sentinel UPR and autophagy-related genes in NMR kidney fibroblasts, mouse NIH3T3 fibroblasts and primary cultures of sensory neurons following the exposure to different exogeneous protein species. In particular, we identified different transcriptional changes of the UPR markers in fibroblasts and sensory neurons in response to the same level of exogeneous Aβ oligomers, which were associated with distinct patterns of membrane binding and cellular uptake of these oligomers. In addition, by comparing acute and chronic responses of the UPR and autophagy in NMR kidney fibroblasts, we correlated increased toxicity of α-synuclein oligomers with the levels of transcriptional suppression of XBP1 and ATF6 signalling as well as autophagy-related proteins, thus providing insights into the pathogenic effects of α-synuclein oligomers and evidence of molecular targets for therapeutic intervention.

6.1.1. Stable $A\beta_{1-42}$ oligomers

While extracellular amyloid deposits or structurally equivalent intracellular inclusions are the hallmarks of neurodegenerative disorders, it is widely accepted that soluble, diffusible protein

oligomers, which are populated during the process of amyloid formation or released by mature fibrils, are the most pathogenic species linked to synaptic loss and the level of dementia[48–53]. Extensive investigations have been conducted to characterise disease-relevant oligomers such as Aβ and α-synuclein. However, the transient nature of oligomeric intermediates results in the extremely low abundance of these species during aggregation. The conformational heterogeneity of any given oligomeric population and the different polymorphs obtained from multiple parallel pathways further complicate the process of determining their structural and biological properties associated with pathogenicity.

A variety of oligomers have been isolated and characterised for the widely studied Aβ peptides, and preparation of stable Aβ oligomers have provided a useful tool to elucidate the role of these soluble species in AD. In this study, we use an established low-salt, low-temperature protocol to generate small, stable $A\beta_{1-42}$ oligomers *in vitro* that are often referred to as amyloid-derived diffusible ligands (ADDLs)[153,281,282]. Chemically synthesised $A\beta_{1-42}$ peptides are pre-treated with TFA/HFIP to remove pre-aggregated materials. Oligomers are formed by resuspending these monomerised peptides in DMSO and incubating overnight at 4 °C in the low-salt phosphate buffer. Antibodies raised against ADDLs can detect elevated levels of soluble oligomers in the AD brain, suggesting that ADDLs provide an appropriate model system resembling naturally occurred species[283,284]. These oligomers range in size from trimers to higher order oligomers up to 24-mers and are neurotoxic at nanomolar concentrations[153,285]. Atomic force microscopy analysis has shown that they are spherical, up to 5 nm in height, and can be further categorised into two subgroups, ranging from 1.5-2.5 nm and 3-4 nm in height[281,285]. Circular dichroism spectroscopy measurements have also revealed that $A\beta_{1-42}$ oligomers prepared using this method display a considerably lower β-sheet content than $A\beta_{1-42}$ fibrils, indicative of a less ordered molecular arrangement in the former[282].

6.1.2. Kinetically trapped α-synuclein oligomers

A variety of oligomeric species have also been described for α-synuclein. Of particular interest are the results of single molecule fluorescence resonance energy transfer (smFRET) studies in which two distinct types of oligomers, denoted type A and type B, have been identified[286]. The initially formed and readily degradable type A α-synuclein oligomers are converted to compact and highly structured type B oligomers through a remarkably slow process during the fibril formation[286]. These latter oligomers also induce a substantially higher level of ROS production

in neuronal cells as compared with their precursor oligomers, monomeric and fibrillar α-synuclein, thus suggesting that they are more damaging to cells[154,286]. Different approaches have been applied to produce kinetically trapped α-synuclein oligomers for detailed biophysical characterisation, including lyophilisation or the use of stabilising agents such as small molecules[154,287]. FRET efficiencies and cellular toxicities of oligomers prepared by lyophilisation are almost identical to those of the type B oligomers and thus have been named type B*[154,288]. In contrast, oligomers prepared by the addition of epigallocatechin gallate (EGCG) do not affect membrane integrity of neurons and have been named type A* for their structural and biological similarity to the benign type A oligomers[287,288].

In this study, we follow an established, lyophilisation-based approach to prepare the type B* oligomers, although the exact mechanisms by which lyophilisation induces oligomer formation is unclear[154]. Purified α-synuclein protein is lyophilised, resuspended and incubated at high concentrations, followed by removal of monomeric and fibrillar species by ultracentrifugation. The resulting oligomers are fairly homogenous, highly stable and resistant to dissociation[154,289]. Purified type B* oligomers demonstrate spherical morphologies, with heights ranging between 3-16 nm, and consist of two major subpopulations (10S and 15S) that have been identified by analytical ultracentrifugation and cryo-EM[154]. The 15S oligomers containing 19-39 monomers with an average mass of 420 kDa exhibit higher levels of antiparallel β-sheet contents (~40%) and surface hydrophobicity, suggesting a strong correlation between the size of the oligomers and both the β-sheet content and the degree of exposed hydrophobicity[154]. These kinetically trapped species have been used to understand how oligomers induce toxicity through membrane permeabilisation. Solid-state nuclear magnetic resonance spectroscopy has revealed that, although both type A* and type B* oligomers interact with membranes that mimicking the composition of synaptic vesicles, only type B* oligomers have been found to readily permeabilise lipid membranes. This is facilitated by the presence of helical structure in the N-terminus which acts as the membrane anchor and a rudimentary β-sheet core structure that can insert into the membrane to disrupt its integrity[288].

6.2. Effects of Aβ1-42 oligomers on the UPR

The involvement of ER stress has been increasingly implicated in Aβ-mediated neurotoxicity. In particular, *in vitro* studies have shown that extracellularly applied $A\beta_{1\text{-}42}$ oligomers can

trigger ER stress in neuronal systems, as indicated by ER Ca^{2+} depletion[290], increased *Xbp1* mRNA splicing[117,291] and elevated expression of XBP1, BiP and CHOP proteins[292,293], although detailed mechanisms by which oligomers induce UPR activation remains unclear. Since the NMR exhibits high levels of soluble Aβ levels but does not develop signs of neurodegeneration[78], it is of great interest to investigate whether UPR signalling in the long-lived NMR may display unique properties which protect the animal from Aβ toxicity in comparison with short-lived mice. One of the earlier studies has reported that $Aβ_{1-42}$ peptides can be internalised by cultured human skin fibroblasts via endocytosis and accumulated as higher-molecular-weight aggregates intracellularly[294], indicating that fibroblasts may be a suitable system for investigations when the neuronal materials are scarce. Therefore, we started by investigating the activation of UPR in response to $Aβ_{1-42}$ oligomers in NMR kidney fibroblasts and mouse NIH3T3 fibroblasts and later examined these responses in mouse sensory neurons.

6.2.1. Lack of activation of UPR in NMR kidney fibroblasts and mouse NIH3T3 fibroblasts in response to $Aβ_{1-42}$ oligomers

It was reported that $Aβ_{1-42}$ oligomers induced *Xbp1* splicing in the rat pheochromocytoma PC12 and human neuroblastoma SH-SY5Y cells[117,291]. The *Xbp1* splicing was observed in PC12 cells treated with $Aβ_{1-42}$ oligomers for 6 hr, starting from 0.5 μM $Aβ_{1-42}$ with the maximal levels of *Xbp1s* and total *Xbp1* transcripts found following the treatment with 2 μM $Aβ_{1-42}$[117]. Increasing the concentration of $Aβ_{1-42}$ oligomers to 4 μM not only reduced levels of *Xbp1s* and total *Xbp1* but also comprised cell viability[117].

To establish whether exogenous $Aβ_{1-42}$ oligomers could induce *Xbp1* splicing, an indicator of UPR activation, in the NMR, we treated the NMR kidney fibroblast cell line (NMR-KF2) using $Aβ_{1-42}$ oligomers and probed levels of *Xbp1* transcripts using the assay established in Chapter 3. We initially tried to build a dose-dependent curve of *Xbp1* splicing following an 8-hr short-term treatment of oligomers but failed to detect any increase in the levels of *Xbp1s* as reported in the PC12 and SH-SY5Y5 cells (**Figure 6.1**)[117,291]. We then extended the time of exposure to $Aβ_{1-42}$ oligomers to 24 hr, but still no *Xbp1* splicing was observed, suggesting that the IRE1-XBP1 branch was not activated in response to these $Aβ_{1-42}$ treatments. Similarly, we treated

mouse NIH3T3 fibroblasts with $A\beta_{1-42}$ oligomers under the same conditions but did not find any *Xbp1* splicing or changes of *Xbp1s* levels (**Figure 6.1**).

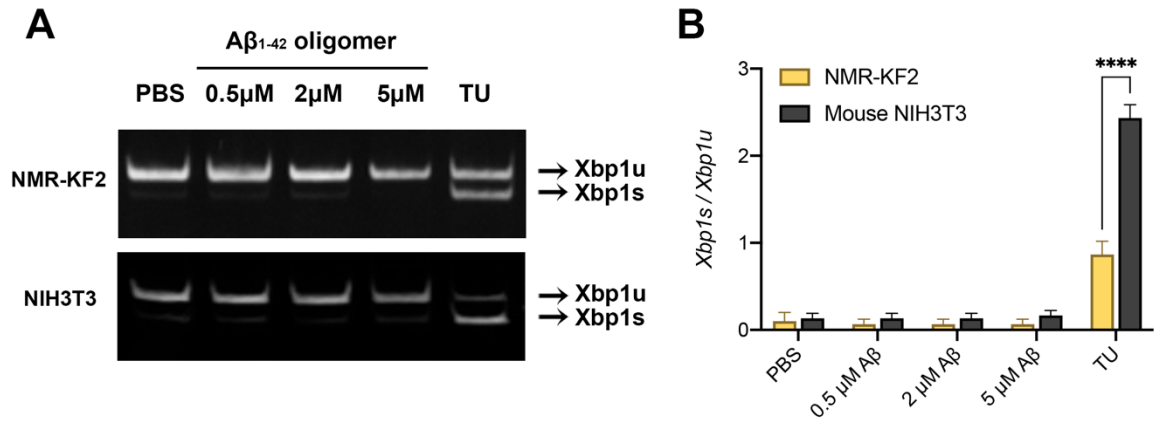

Figure 6. 1. *Xbp1* splicing in the NMR-KF2 and mouse NIH3T3 fibroblasts upon the exposure to $A\beta_{1-42}$ oligomers. PBS (negative control) and tunicamycin (TU) (positive control) were used as controls. **(A)** Representative images of the RT-PCR products of *Xbp1s* and *Xbp1u* on 6% TBE gels in the NMR-KF2 (top) and 3T3 cells (bottom). The graphs in **(B)** show the mean ± S.D. of *Xbp1s*-to-*Xbp1u* ratios in response to $A\beta_{1-42}$ and controls in the NMR-KF2 (yellow) and 3T3 (grey). n=3 pairs; ****p<0.0001; unpaired t-tests.

We also monitored changes in expression of the UPR sentinel genes using RT-qPCR assays, including *Atf4* (encoding ATF4, a transcription factor in the PERK pathway), *Ddit3* (encoding CHOP, the major pro-apoptotic UPR protein) and *Hspa5* (encoding BiP, a master chaperone in the ER), in the NMR-KF2 treated with 2 μM $A\beta_{1-42}$ oligomers for 8 and 24 hr. None of these conditions induced significant changes of *Atf4*, *Ddit3* and *Hspa5* expression in the NMR-KF2 (**Figure 6.2**). Similar UPR outputs were observed in the mouse 3T3 fibroblasts under the same conditions (**Figure 6.2**). Taken together, these results from *Xbp1s* splicing and RT-qPCR assays suggested that $A\beta_{1-42}$ oligomers did not induce UPR activation in the NMR-KF2 and mouse 3T3 embryonic fibroblasts.

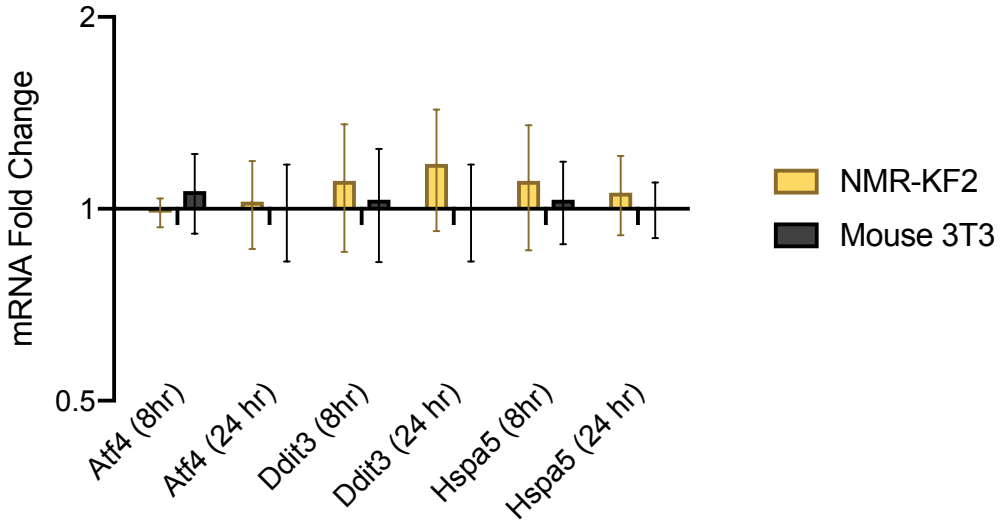

Figure 6. 2. Changes in expression of UPR markers in NMR-KF2 and mouse 3T3 cells in response to Aβ$_{1-42}$ oligomers. The NMR-KF2 (yellow) and mouse 3T3 fibroblasts (grey) were treated with 2 μM Aβ$_{1-42}$ oligomers for 8 hr and 24 hr. Expression of *Atf4, Ddit3* and *Hspa5* was measured by RT-qPCR. Results were normalised to the mRNA levels of reference genes and were presented on a log scale as mean ± S.D. of mRNA fold change relative to the basal-level expression in the PBS-treated controls (n=3); unpaired t-tests.

6.2.2. Lack of activation of UPR in NMR kidney fibroblasts and mouse NIH3T3 fibroblasts in response to Aβ$_{1-42}$ monomers and fibrils

Some studies have reported UPR activation in cells treated with Aβ$_{1-42}$ monomers and fibrils, although this is still controversial[295–297]. Therefore, we also examined expression of these UPR markers in response to Aβ$_{1-42}$ peptide and fibrils that were prepared using established protocols (Hook SH, PhD thesis). Before the treatment, we characterised different assemblies of Aβ$_{1-42}$ prepared in this study by transmission electron microscopy (TEM) (**Figure 6.3**). The preparation of Aβ$_{1-42}$ oligomer or ADDLs resulted in small aggregates that were spherical (<15 nm) or rod-shaped (20-100 nm) with different sizes. These rod-shaped aggregates resembled protofibril oligomers[281], albeit, the majority of the sample appeared to be the small ADDL-like aggregates. In contrast, the Aβ$_{1-42}$ fibrillar sample showed a more elongated and ribbon-like morphology, and a mature fibril could span over 2 μm in length. These size and morphological distributions were comparable to those reported earlier using the same preparation method (Hook SH, PhD thesis) and were similar to those prepared by Casas-Tinto *et al.* that induced

Xbp1 splicing[117]. Surface hydrophobicity of $A\beta_{1-42}$ species was also probed by the use of 1-anilinonaphthalene 8-sulfonate (ANS), a dye whose fluorescence emission increases upon interacting with exposed hydrophobic regions in native or partially unfolded proteins[298]. Compared to monomers, $A\beta_{1-42}$ oligomers displayed a remarkable increase in the ANS fluorescence intensity, indicating an increased level of exposed hydrophobic patches, which have been linked to increased toxicity (**Figure 6.4**)[299]. The fibrillar sample contained a small population of prefibrillar structures, as observed under TEM, alongside the highly ordered fibrils, thus corresponding to the middle-level ANS fluorescence between $A\beta_{1-42}$ monomers and oligomers. Some fluorescence signal was observed in the monomer sample indicating that hydrophobic surfaces were present, either in the monomeric protein or due to the presence of some pre-existing oligomers.

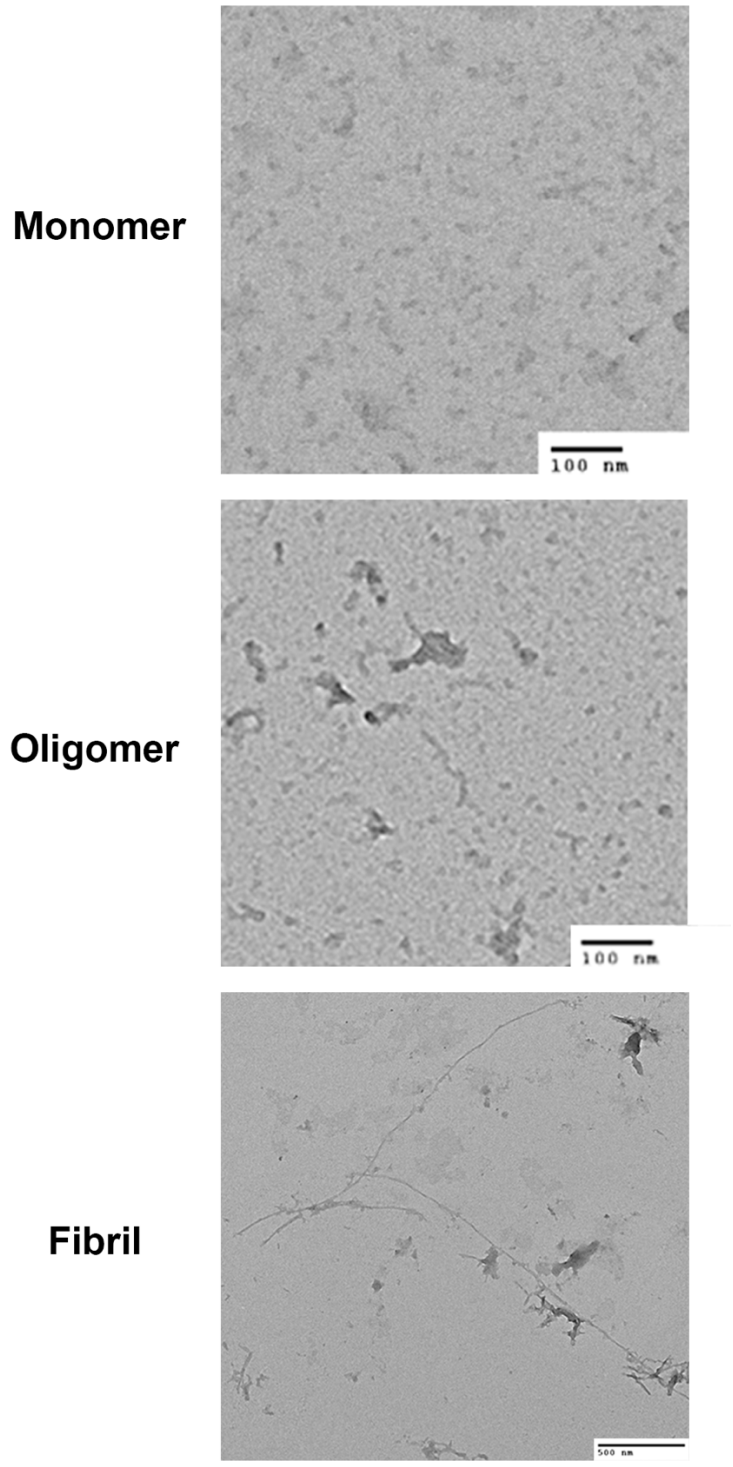

Figure 6. 3. Representative TEM images of Aβ$_{1-42}$ monomers, oligomers and fibrils. Oligomers and fibrils prepared in this study showed distinct size and morphological distributions. Scale bar = 100 nm in monomers and oligomers; scale bar = 500 nm in fibrils.

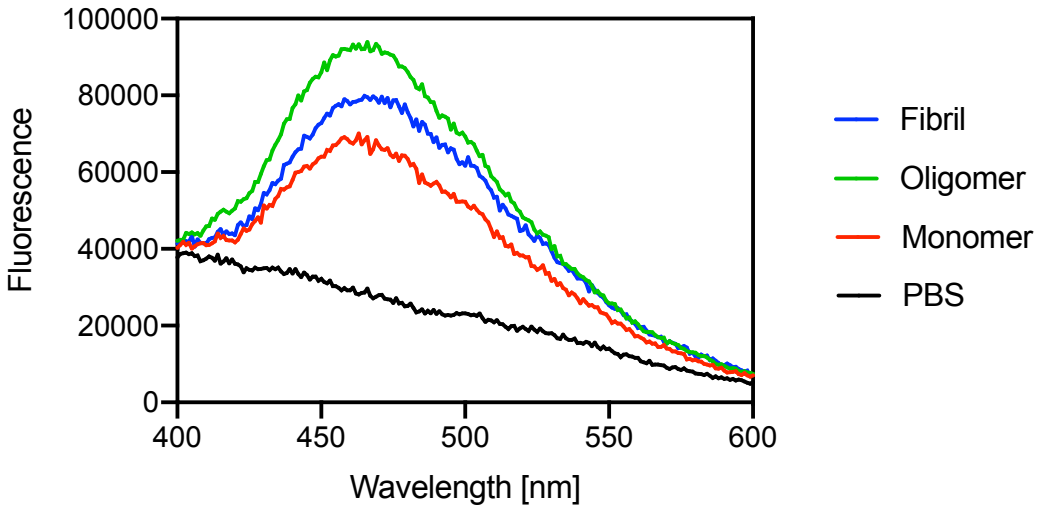

Figure 6. 4. Representative ANS fluorescence spectra upon binding $A\beta_{1-42}$ monomers (red), oligomers (green) and fibrils (blue). PBS buffer (black) was used as a control. (n=3)

In both NMR-KF2 and 3T3 fibroblasts which had shown UPR activation under TU-treated conditions (**Figure 6.1 B**), neither *Xbp1* splicing nor changes in expression of the selected UPR markers were observed under monomer- or fibril-treated conditions (**Figure 6.5**), suggesting that $A\beta_{1-42}$, regardless of size, structure and type of assemblies, seemed not to induce ER stress in the NMR-KF2 and mouse 3T3 fibroblasts following the 24-hr treatment. However, data from more biological replicates can be collected as the changes of these UPR markers in response to $A\beta_{1-42}$ might be too minute to be observed from the three replicates, and more conditions such as extended time of exposure and increased $A\beta_{1-42}$ concentrations may also be tested.

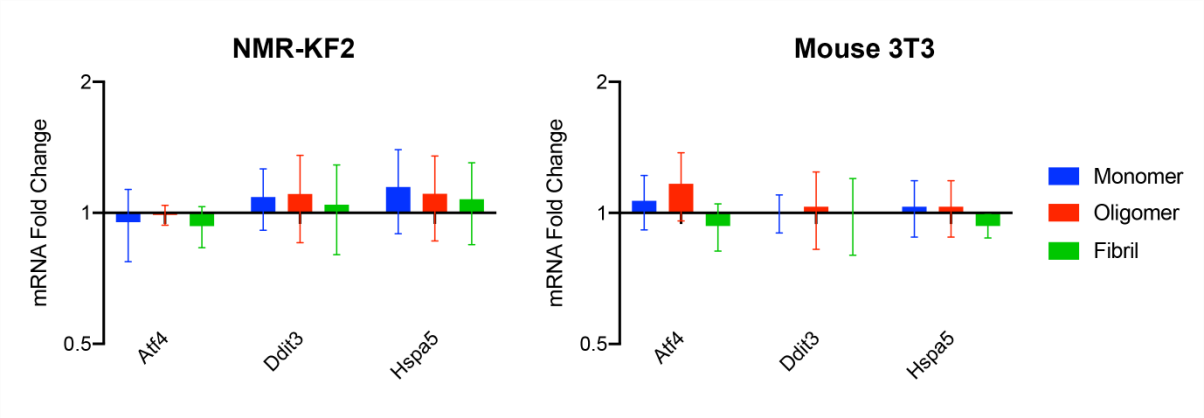

Figure 6. 5. Changes in expression of UPR markers in the NMR-KF2 and mouse 3T3 cells treated with different Aβ$_{1-42}$ species. The NMR-KF2 and mouse 3T3 fibroblasts were treated with 2 μM Aβ$_{1-42}$ monomers, oligomers and fibrils for 24 hr. Expression of *Atf4, Ddit3* and *Hspa5* was measured by RT-qPCR. Results were normalised to the mRNA levels of reference genes and were presented on a log scale as mean ± S.D. of mRNA fold change relative to the basal-level expression in the PBS-treated controls (n=3); unpaired t-tests.

6.2.3. Downregulation of UPR markers in mouse sensory neurons in response to Aβ$_{1-42}$ oligomers

Since most previous studies of Aβ$_{1-42}$-mediated ER stress were performed in neuronal systems, we next investigated the effects of Aβ$_{1-42}$ oligomers on the UPR of sensory neurons, starting by optimising the protocol in mouse before sacrificing NMRs. Sensory neurons were pooled from mouse dorsal root ganglia (DRG) and trigeminal ganglia and were probed for changes in expression of the UPR markers in response to the 24-hr treatment with 2 μM Aβ$_{1-42}$ oligomers. Due to the small amounts of sensory neurons collected per animal (5000 cells per treatment), carrier RNA (supplied in the Qiagen RNeasy Kit) was used to improve the RNA yield to ~50 ng per sample and ensure the quality for downstream RT-qPCR application. The carrier RNA is a poly-A RNA that prevents the small amount of target RNA in the sample from being irretrievably bound and does not interfere with subsequent RT-qPCR according to the manufacturer (Qiagen).

No *Xbp1* splicing was observed in the sensory neurons treated with Aβ$_{1-42}$ oligomers (**Figure 6.6 A**), but the levels of *Ddit3* and *Hspa5* were reduced compared to the PBS-treated controls

(**Figure 6.6 B**). Expression of *Hspa5* was reduced to half of the basal expression in the PBS-treated sample. The amount of *Atf4* transcripts diminished slightly but this was not statistically significant. Whereas the UPR in 3T3 fibroblasts was not affected by treatment with $A\beta_{1-42}$ oligomers, the sensory neurons displayed an overall suppression of the UPR when the same amounts of $A\beta_{1-42}$ oligomers were applied.

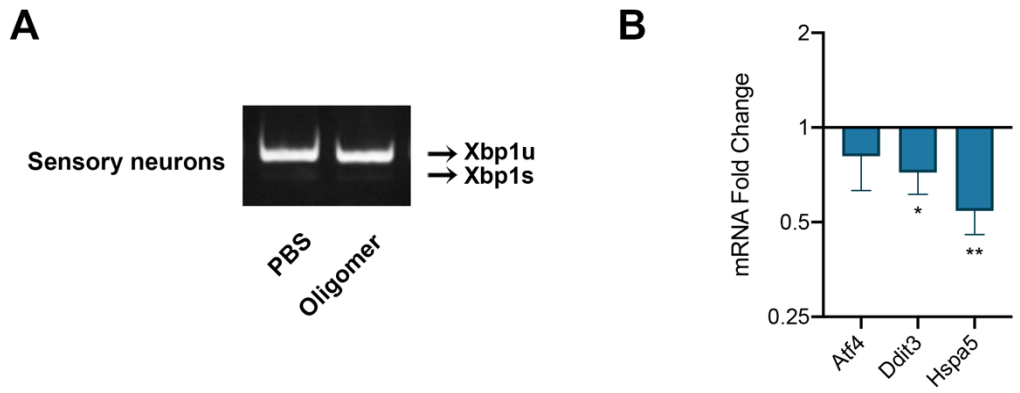

Figure 6. 6. Changes in the expression of UPR markers in primary cultures of mouse sensory neurons. Sensory neurons were isolated from mouse dorsal root ganglia (DRG) and trigeminal ganglia and treated with 2 μM $A\beta_{1-42}$ oligomers for 24 hr. **(A)** Representative images of the RT-PCR products of *Xbp1s* and *Xbp1u* in sensory neurons treated with and PBS for 24 hr. **(B)** Expression of *Atf4, Ddit3* and *Hspa5* was measured by RT-qPCR. Results were normalised to the mRNA levels of reference genes and were presented on a log scale as mean ± S.D. of mRNA fold change relative to the basal-level expression in the PBS-treated controls. n=3 animals; *p<0.05, **p<0.01; unpaired t-tests.

6.2.4. Distinct patterns of membrane binding and cellular uptake of $A\beta_{1-42}$ oligomers by sensory neurons and fibroblasts

In our experimental setup, cells were treated with exogenous $A\beta_{1-42}$ oligomers that had no direct access to the ER. Thus, the ability of the oligomers to enter the cell or interact with cellular membrane and/or surface receptors was the main determinant of UPR modulation. Therefore, we sought to investigate interactions between $A\beta_{1-42}$ oligomers and fibroblasts/sensory neurons by confocal microscopy. Fluorescent $A\beta_{1-42}$ oligomers were

prepared from HiLyte Fluor 488-labelled $A\beta_{1-42}$ peptide and applied to the cells for 5 hr. These fluorescent $A\beta_{1-42}$ oligomers have been characterised to display similar morphological and size distributions when compared to unlabelled $A\beta_{1-42}$ oligomers, thus suggesting that the addition of the dye did not perturb the system to any significant degree (Hook SH, PhD thesis). We observed distinct patterns of membrane binding and internalisation of $A\beta_{1-42}$ oligomers in the different cell types after the 5-hr treatment. In NMR-KF2 and 3T3 fibroblasts, $A\beta_{1-42}$ oligomers were found to bind to only a couple of cells within the population. The majority of fibroblasts did not interact with $A\beta_{1-42}$ oligomers (**Figure 6.7**), and extremely few intracellular puncta of oligomers were observed (< 5 cells out of the entire sample slide) (**Figure 6.8**). In contrast, $A\beta_{1-42}$ oligomers co-localised well with the cell membrane of over half of the population of mouse DRG neurons. Fluorescent puncta were also found intracellularly in approximately 30% of the DRG neurons, suggesting the internalisation of these oligomers, which was validated by Z-stack analysis (**Figure 6.9**).

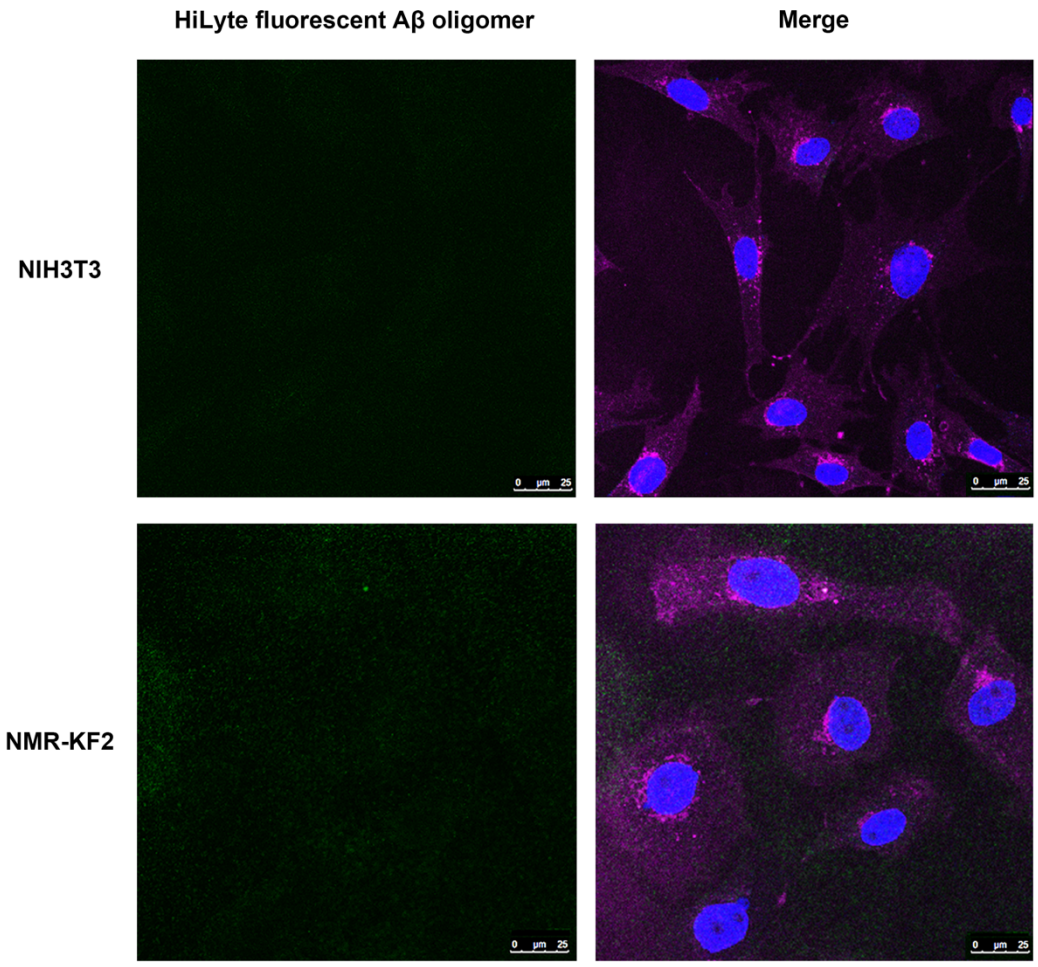

Figure 6. 7. The majority of mouse NIH3T3 fibroblasts and NMR-KF2 cells did not interact with $A\beta_{1-42}$ oligomers after the 5-hr treatment. Blue: DAPI for nucleus, purple: Alexa Fluor 647-labelled wheat germ agglutinin (WGA), green: oligomers prepared from HiLyte Fluor 488-labelled $A\beta_{1-42}$ peptides. Scale bar = 25 μm.

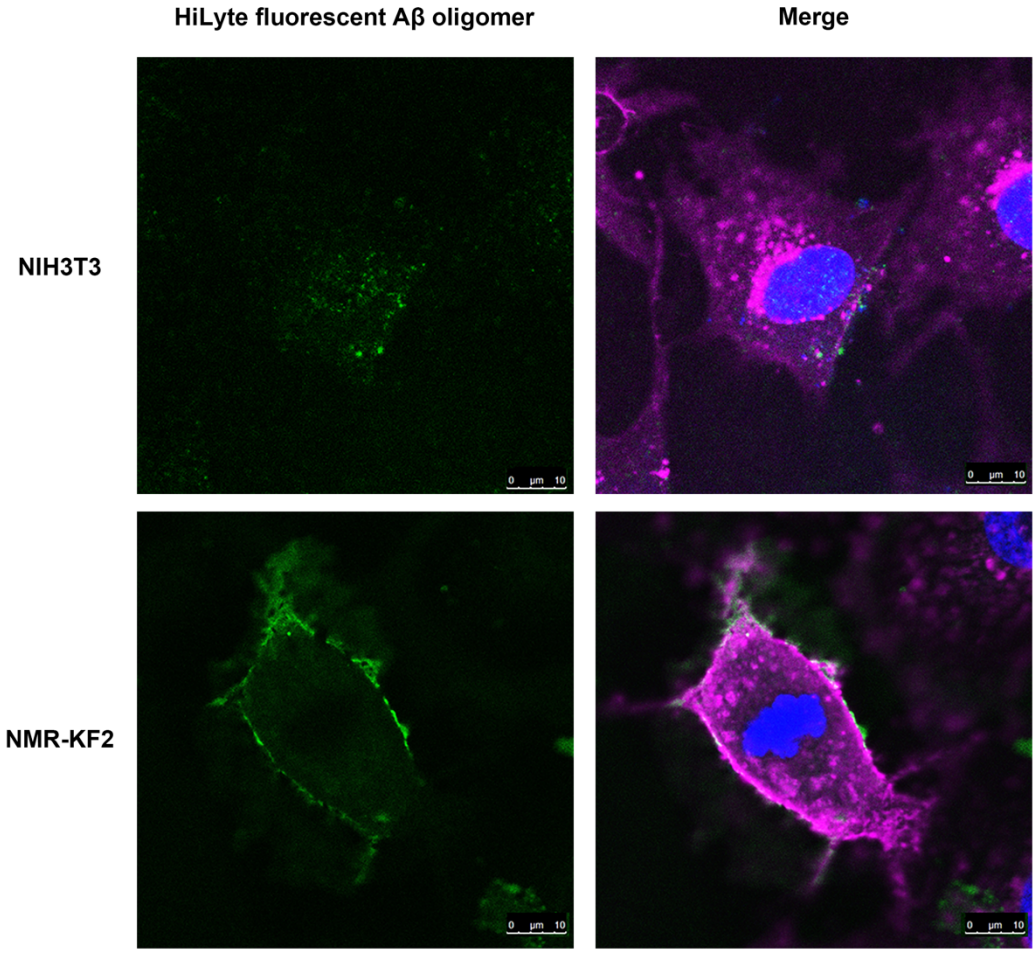

Figure 6. 8. Representative confocal images of the interaction of $A\beta_{1-42}$ oligomers with mouse NIH3T3 fibroblasts and NMR-KF2 cells after the 5-hr treatment. Blue: DAPI for nucleus, purple: Alexa Fluor 647-labelled wheat germ agglutinin (WGA), green: oligomers prepared from HiLyte Fluor 488-labelled $A\beta_{1-42}$ peptides. Scale bar = 10 µm.

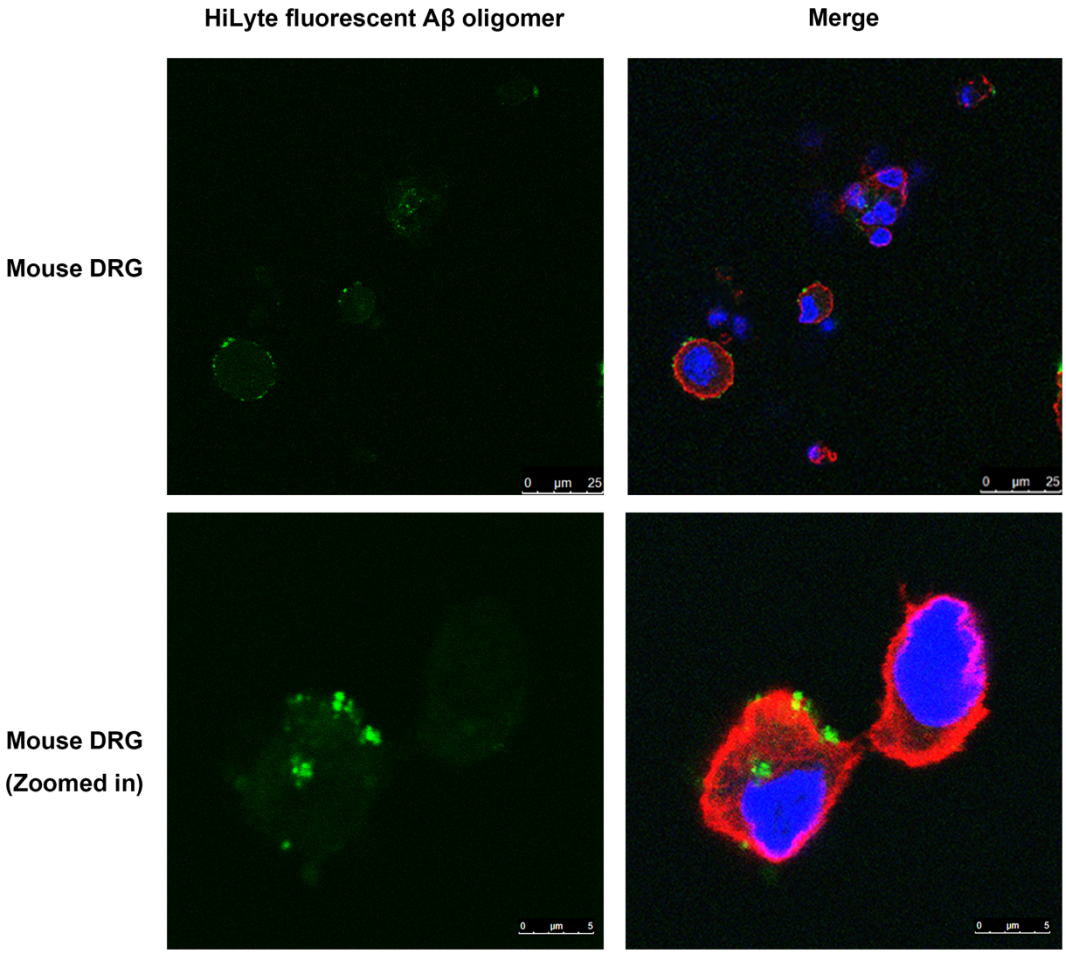

Figure 6. 9. Representative confocal images of the interaction of $A\beta_{1-42}$ oligomers with mouse DRGs after the 5-hr treatment. Oligomers were associated with the membrane of most neurons, and a small portion of cells internalised $A\beta_{1-42}$ oligomers. Blue: DAPI for nucleus, red: tubulin, green: oligomers prepared from HiLyte Fluor 488-labelled $A\beta_{1-42}$ peptide. Z-stack analysis was performed to confirm the internalisation of oligomers into the cells. Scale bar = 25 µm (top); scale bar = 5 µm (bottom).

6.2.5. Discussion

Taken together, these results suggest that the lack of activation of the UPR in the NMR-KF2 and 3T3 fibroblasts was probably due to a lack of interaction between exogenous $A\beta_{1-42}$ oligomers and the cell membrane. In contrast, the highly efficient binding of $A\beta_{1-42}$ oligomers to the cell membrane of sensory neurons may mediate oligomer internalisation and/or activate specific membrane receptors that are constitutively expressed on the neuronal cells to initiate signalling cascades leading to ER stress and other neurotoxic effects. For example, $A\beta_{1-42}$ oligomers has been shown to activate the *N*-methyl-D-aspartate receptor (NMDAR), a glutamate receptor and ion channel protein found in nerve cells, through the interaction with the GluN2B subunit and to trigger ER stress, thus leading to apoptosis[293]. Oligomeric $A\beta_{1-42}$ has also been demonstrated to activate phospholipase C and disrupt ER Ca^{2+} homeostasis through channels associated with ryanodine receptors, which display different isoform distribution and expression levels in brain and other tissues[290]. In addition, the increased susceptibility of neurons to $A\beta_{1-42}$ oligomers has been linked to higher contents of lipid rafts enriched in ganglioside GM1 and cholesterol where soluble ADDLs accumulate[300,301]. This was supported by the fact that oligomers from salmon calcitonin, another neurotoxic amyloid protein, increased intracellular Ca^{2+} levels and induced apoptosis in mouse mature hippocampal neurons, but not in NIH3T3 fibroblasts which had significantly lower contents of lipid rafts[300]. Interestingly, a recent study has reported that NMR brain lipids have higher cholesterol and lower sphingomyelin levels compared to mouse brain lipids, resulting in a higher degree of phase separation and sensitivity to $A\beta_{1-42}$-induced damage, further suggesting that the NMR may have evolved neuroprotective mechanisms that are not based on mechanical resistance to support a healthy brain within an Aβ-rich environment[302].

We showed an overall suppression of the UPR in mouse sensory neurons following the 24-hr treatment of $A\beta_{1-42}$ oligomer, which is different from the findings of previous studies where potent UPR activation was observed. Decreased expression in almost all UPR genes analysed in this study may be a result of pronounced apoptosis induced by $A\beta_{1-42}$ oligomers, which can be determined by assessment of cell viability based on microscopy or flow cytometry given the limited number of neurons. Previously reported *Xbp1* splicing and elevated BiP expression within hours of treatment with $A\beta_{1-42}$ oligomers in neuronal cultures suggested that UPR might have been activated as an early, acute response before detrimental effects were

observed[117,291,292]. Therefore, time-dependent responses should be monitored to trace the progress and shift of UPR signalling and to help elucidate the role played by UPR in the course of exposure to exogenous $A\beta_{1-42}$ oligomers. Moreover, although our current approach provides a powerful tool to measure an average level of mRNA expression, it may miss the changes in a subset of the cells as they are diluted out. In fact, it was reported that $A\beta_{1-42}$ oligomers induced only mild ER stress that could hardly be detected in a pool of cells[303]. Given the heterogeneity of membrane binding and cellular uptake of $A\beta_{1-42}$ oligomers that we observed, single-cell RT-qPCR may provide a better means of determining gene expression in individual cells with and without the $A\beta_{1-42}$ binding/uptake and reveal more insights.

6.3. Effects of α-synuclein oligomers on UPR and autophagy in the NMR

It has long been thought that α-synuclein exerts its toxic effects intracellularly. This concept was challenged when α-synuclein, in particular pathogenic oligomeric species, was detected in the plasma and cerebrospinal fluid from PD patients[304]. Furthermore, it has been shown that neuronal cells overexpressing α-synuclein can produce oligomeric species that are secreted by exocytosis or in exosomes and can be taken up by neighbouring cells to induce significant toxicity, providing strong evidence for prion-like cell-to-cell propagation of α-synuclein[305–307]. Extracellular α-synuclein oligomers can be taken up by cells via several different mechanisms, including endocytosis[308] and permeabilisation of lipid membranes by direct penetration[288] or the formation of pore-like ion channels[309,310]. Using a similar approach described in the previous section, we examined the effects of exogenously applied stable α-synuclein oligomers on the UPR and autophagy in the NMR.

6.3.1. Reduced *Xbp1* splicing following the chronic treatment of α-synuclein oligomers

Primary kidney fibroblasts were isolated from NMRs, followed by treatment of exogenous α-synuclein oligomers for 8 hr. We titrated with 0.1, 0.5 and 1 μM α-synuclein oligomers, doses that have been used in various cell models for α-synuclein transfer, but we did not observe any *Xbp1* splicing in the NMR fibroblasts as reported previously in the SH-SY5Y cells[291]. We then extended our treatments to 24 hr and 6 days. For 6-day treatments, we replenished the oligomers with the same concentration every 48 hr, as they have been shown to be stable only

up to 48 hr. No *Xbp1s* splicing was found in the cells treated for 24 hr. However, levels of *Xbp1* splicing, indicated by both the *Xbp1s*-to-*Xbp1u* ratios and normalised *Xbp1s* amounts relative to the basal-level expression in controls, decreased significantly in the NMR fibroblasts that had been treated with α-synuclein oligomers for 6 days (**Figure 6.10**). The chronic treatment of α-synuclein oligomers reduced the normalised *Xbp1s* amount by half and the *Xbp1s*-to-*Xbp1u* ratio by two thirds, suggesting suppression of IRE-1XBP1 signalling in the NMR fibroblasts. Total levels of *Xbp1* transcripts including *Xbp1s* and *Xbp1u* did not change compared to the PBS-treated controls.

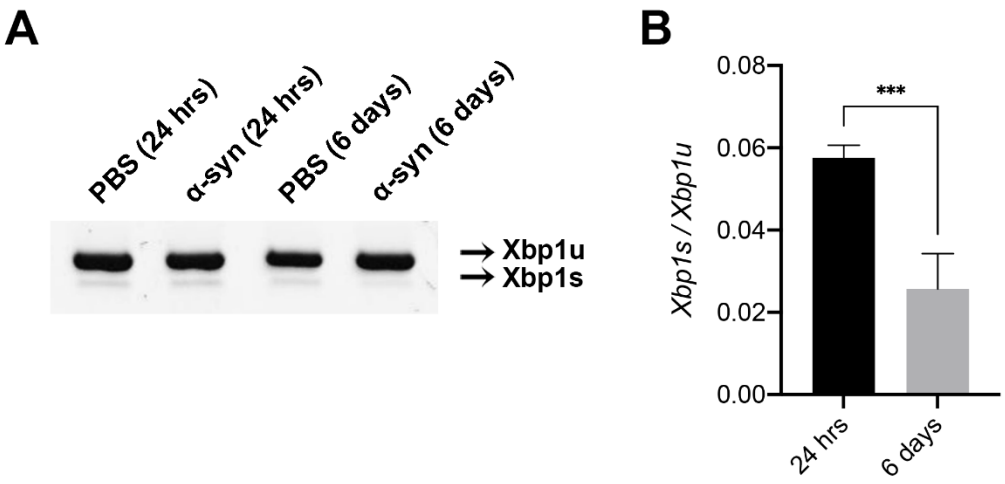

Figure 6. 10. *Xbp1* splicing in NMR primary kidney fibroblasts after the treatment of 0.5 μM α-synuclein oligomers for 24 hr and 6 days. For 6-day treatments, α-synuclein oligomers were replaced every 48 hr. **(A)** Representative images of the RT-PCR products of *Xbp1s* and *Xbp1u* on 6% TBE gels. The graph in **(B)** shows the mean ± S.D. of *Xbp1s*-to-*Xbp1u* ratios. n=4 animals; ***p<0.001, unpaired t-tests.

6.3.2. Suppression of ER chaperones in NMR kidney fibroblasts following the chronic treatment of α-synuclein oligomers

Using RT-qPCR, we also probed UPR genes in the NMR kidney fibroblasts that were treated with α-synuclein oligomers for 24 hr and 6 days. The level of *Bloc1s1* mRNA, which is a proximate reporter of XBP1-independent RIDD mediated by IRE1, did not change following the 6-day α-synuclein oligomer treatment (**Figure 6.11**). The expression of *Atf4* and pro-

apoptotic *Ddit3* also showed no changes under treated conditions compared to that in the PBS-treated controls (**Figure 6.11**), suggesting that PERK-mediated signalling was not induced in response to α-synuclein oligomers. Levels of *Hspa5*/BiP*,* however, showed slight decreases after the 24-hr treatment, and continued to diminish, remaining suppressed remarkably after the 6-day treatment with α-synuclein oligomers (**Figure 6.11**). We also surveyed other major ER-resident chaperones including GRP94 (encoded by *Hsp90b1*) and PDIA4 (encoded by *Pdia4*), as well as a BiP cofactor DNAJB11 (encoded by *Dnajb11*), all of which are transcriptionally regulated by ATF6 signalling. Primers for probing genes encoding NMR ER chaperones and cofactors were designed and validated for qPCR efficiency as described in Chapter 3 (**Table 2.1**). We found that this subset of UPR genes displayed similar downregulation to *Hspa5* (**Figure 6.11**). We also assessed the expression of ER chaperones by immunoblotting using an antibody that targets specifically the KDEL ER-retention motif on the ER chaperones. The results showed that BiP, GRP94 and PDIA3 expression were suppressed following 6-day treatments with α-synuclein oligomers, in good agreement with the RT-qPCR results (**Figure 6.12**). These results indicated that the chronic treatment of α-synuclein oligomers suppressed ATF6-mediated induction of ER chaperones and cofactors below the basal-level expression, which may result in the impairment of the protein quality-control machinery in the NMR fibroblasts. The E3 ubiquitin ligase HRD1 (encoded by *Syvn1*) involved in the ERAD pathway, which is mainly regulated by XBP1s and co-regulated by ATF6, was also downregulated. The expression of *Herpud1*, which encodes HERP involved in ERAD and is regulated by all of the UPR branches, showed no change in response to the 6-day treatment with α-synuclein oligomers.

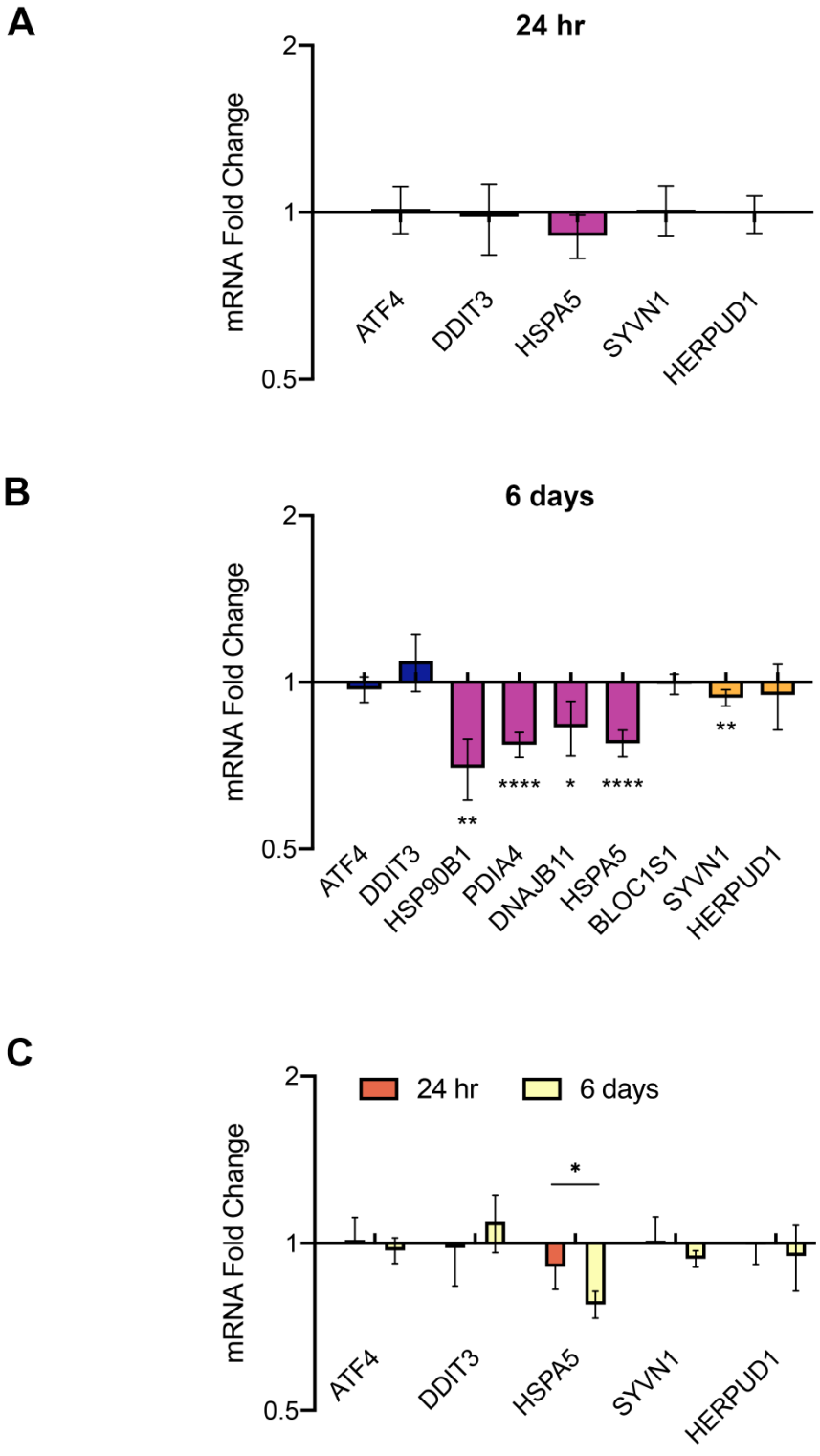

Figure 6. 11. NMR primary kidney fibroblasts were treated with 0.5 µM α-synuclein oligomers for 24 hr (A) and 6 days (B). For 6-day treatments, α-synuclein species were replaced every 48 hr. Expression of UPR markers was measured by RT-qPCR. Results were

normalised to the mRNA levels of reference genes and were presented on a log scale as mean ± S.D. of mRNA fold change relative to the basal-level expression in the PBS-treated controls. Genes were categorised into four groups: 1) *Atf4* and *Ddit3* regulated by PERK-eIF2α pathway (blue), 2) *Hsp90b1, Pdia4, Dnajb11* and *Hspa5* encoding ER chaperones and cofactors (purple), 3) *Bloc1s1* targeted by RIDD (red), and 4) *Syvn1* and *Herpud1* encoding ERAD proteins (orange). (C) Changes of UPR markers after the 24-hr treatment were compared with those after the 6-day treatment. n=4 animals; ns, p>0.05, *p<0.05, **p<0.01, ***p<0.001, ****p<0.0001; unpaired t-tests.

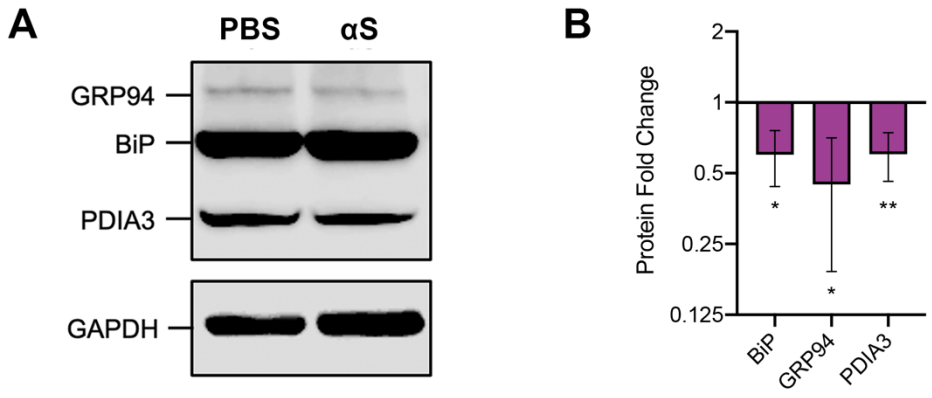

Figure 6. 12. NMR primary kidney fibroblasts were treated with 0.5 µM α-synuclein oligomers for 6 days. Expression of ER chaperones (GRP94/*Hsp90b1*, BiP/*Hspa5* and PDIA3/*Pdia3*) in cell lysates was measured by immunoblotting. A representative western-blot image is shown in **(A)** on which the ER chaperones were probed using an anti-KDEL antibody. The intensity of protein bands on the blots was determined by Image J. Results were presented in **(B)** as the mean ± S.D. of protein fold change in α-synuclein-treated NMR fibroblasts relative to the basal-level protein expression in fibroblasts treated with PBS (controls). n=3 animals, *p<0.05, **p<0.01; unpaired t-tests.

6.3.3. Induction followed by suppression of autophagy genes following the chronic treatment of α-synuclein oligomers

We further examined the expression of selected autophagy markers in NMR kidney fibroblasts. We observed the induction of *Tfeb*, which encodes a master transcription factor of autophagy and lysosomal functions, after the 24-hr treatment of 0.5 μM α-synuclein oligomers (**Figure 6.13**). Genes that are regulated by TFEB in several steps of the autophagy-lysosomal pathway were also upregulated, including *Atg5* and *Maplc3b*, that encode critical autophagy components ATG5 and LC3B in the elongation of phagophore and autophagosome formation, and *Lamp1* which encodes the lysosomal membrane protein, suggesting the improved overall autophagy after the 24-hr exposure to 0.5 μM α-synuclein oligomers (**Figure 6.13**).

We also investigated the effects of chronic treatment of α-synuclein oligomers on the autophagy in NMR kidney fibroblasts by qPCR and observed significant changes in the expression of autophagy-related genes following the 6-day treatment compared to those after the 24-hr treatment. The levels of *Tfeb*, *Sqstm1* and *Lamp1* mRNAs, which were found to be induced previously in response to the 24-hr treatment, as well as *Becn1* (encoding Beclin1), were downregulated below the basal-level expression. The suppression of these key autophagy genes suggested a decreased level of autophagy, including reduced autophagy initiation (Beclin1), cargo/substrate recruitment (p62) and lysosomal membrane biogenesis (LAMP1) in the NMR kidney fibroblasts. Intriguingly, we observed a two-fold increase in the expression of *Map1lc3b*, which was further upregulated as compared to the 24-hr treatment, despite the downregulation of the master transcription factor TFEB, and was the only autophagy gene that remained induced in acute and chronic conditions (**Figure 6.13**). These results indicated that acute and chronic treatments of α-synuclein oligomers seemed to lead to distinct transcriptional profiles of autophagy in the NMR kidney fibroblasts. Protein-level assays including the LC3B analysis are required to confirm whether these transcriptional changes correlate well with the autophagosome turnover at the protein level.

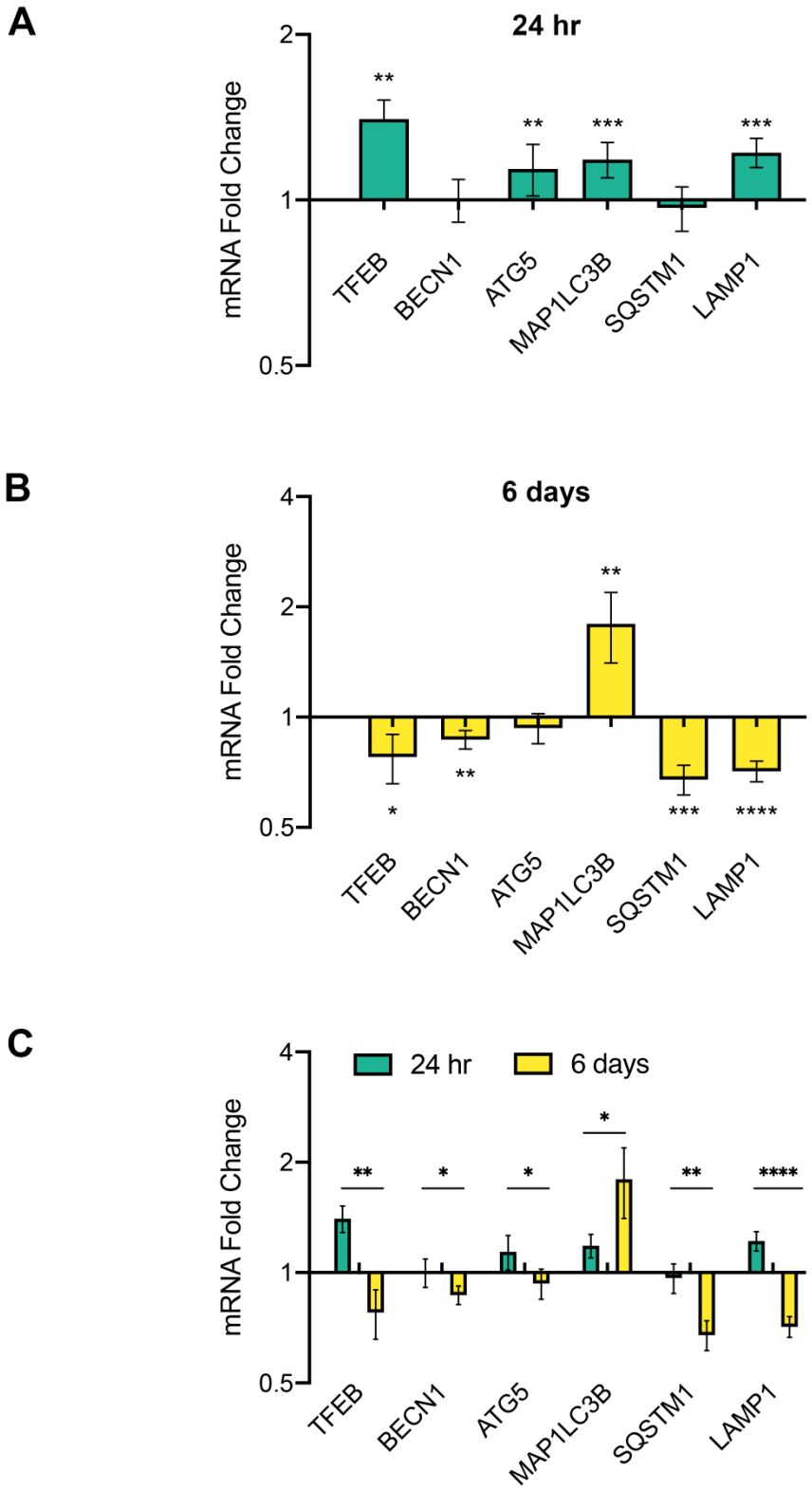

Figure 6. 13. NMR primary kidney fibroblasts were treated with 0.5 µM α-synuclein oligomers for 24 hr (A) and 6 days (B). For 6-day treatments, α-synuclein species were replaced every 48 hr. Expression of selected autophagy-related markers was measured by RT-

qPCR. Results were normalised to the mRNA levels of reference genes and were presented on a log scale as mean ± S.D. of mRNA fold change relative to the basal expression in the PBS-treated controls. **(C)** Changes of autophagy-related genes after the 24-hr α-synuclein treatment were compared with those after the 6-day treatment. n=4 animals; ns, $p>0.05$, *$p<0.05$, **$p<0.01$, ***$p<0.001$, ****$p<0.0001$; unpaired t-tests.

6.3.4. Toxicity induced by chronic but not acute treatments of α-synuclein oligomers

We next investigated the toxicity of α-synuclein oligomers on NMR kidney fibroblasts. Cells were treated with 0.5 μM α-synuclein oligomers for 24 hr, and the cell viability was measured using the CellTiter-Glo luminescent assay. The NMR kidney fibroblasts showed no sign of cell death and maintained an average post-treatment cell viability of 102.7% (S.D. = 5.7%), indicating their resistance to αS oligomers (**Figure 6.14**). The percentage of viable populations in the human neuroblastoma SH-SY5Y cells, which served as a positive control, reduced to 83.8% (S.D. = 8.4%) and was in good agreement with previous studies[311], suggesting the significantly higher toxicity of α-synuclein oligomers to the SH-SY5Y cells than to the NMR fibroblasts (**Figure 6.14**). However, when the NMR fibroblasts were exposed to α-synuclein oligomers for 6 days, the cell viability decreased significantly to 80.7% (S.D. = 4.6%), indicating the chronic toxic effects exerted by α-synuclein oligomers (**Figure 6.14**). All of the results were normalised to the viability data obtained from PBS-treated controls (2.5% v/v), which showed no differences in the resulting cell viability when compared to the untreated controls.

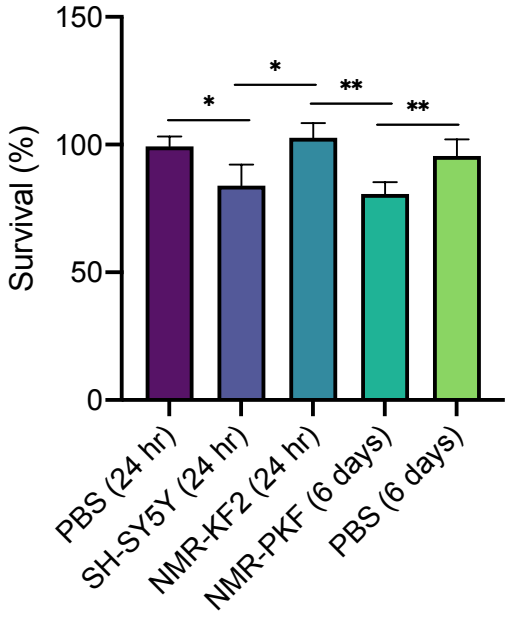

Figure 6. 14. The human neuroblastoma SH-SY5Y and NMR kidney fibroblasts were treated with 0.5 μM α-synuclein oligomers for 24 hr or 6 days. Percentage of viable cells after the treatment was measured by CellTiter-Glo assay. Results were presented as mean ± S.D. of the percentage survival (%) of treated samples in comparison to the PBS-treated controls. NMR-PKF = NMR primary kidney fibroblasts. n=3; *p<0.05, **p<0.01; unpaired t-tests.

6.3.5. Different transcriptional profiles induced by chronic treatments of α-synuclein monomers, oligomers and fibrils

We also examined the effects of different conformers of α-synuclein on the UPR and autophagy in NMR primary kidney fibroblasts. Fibrils were prepared from wild-type α-synuclein using the established protocol (CK Xu, PhD thesis). We applied 0.5 μM monomers and fibrils to the NMR primary kidney fibroblasts and measured the expression of those UPR and autophagy genes using *Xbp1* splicing assay and RT-qPCR.

In all of the four NMRs examined, α-synuclein oligomers and fibrils induced opposite effects on *Xbp1s* splicing. While the normalised *Xbp1s* levels and *Xbp1s*-to-*Xbp1u* ratios in oligomer-treated fibroblasts were reduced compared to the basal expression of *Xbp1s* in the PBS-treated controls, the fibroblasts treated with fibrils showed increased levels of *Xbp1s* mRNA (**Figure**

6.15). The normalised amounts of *Xbp1s* in fibril-treated NMR fibroblasts were slightly elevated compared to the controls and were twice as high as that in oligomer-treated cells, suggesting mild activation of IRE1-XBP1 signalling by α-synuclein fibrils. No change in *Xbp1s* splicing was observed in monomer-treated fibroblasts. Levels of total *Xbp1* transcripts were not altered under any of these conditions (**Figure 6.15**).

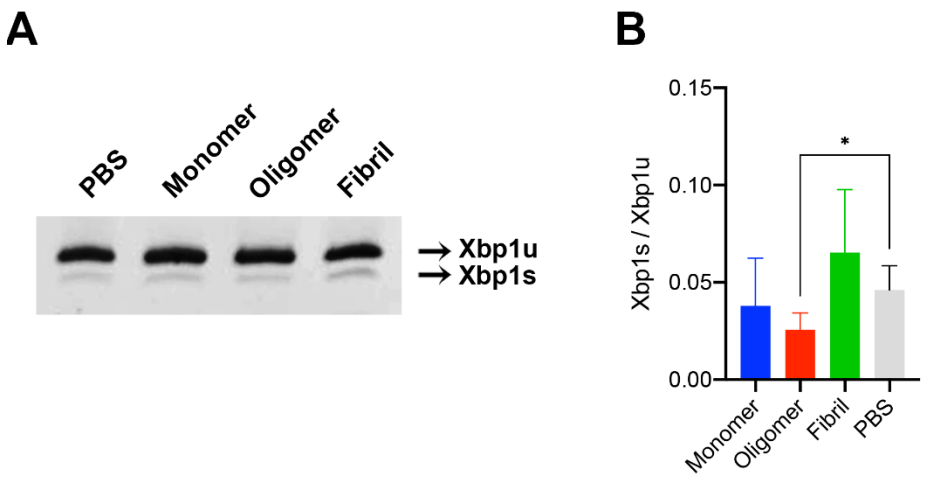

Figure 6. 15. *Xbp1* splicing in NMR primary kidney fibroblasts after the treatment of 0.5 μM α-synuclein monomers, oligomers and fibrils for 6 days. **(A)** Representative images of the RT-PCR products of *Xbp1s* and *Xbp1u* on 6% TBE gels. The graph in **(B)** shows the mean ± S.D. of *Xbp1s*-to-*Xbp1u* ratios. n=4 animals; *p<0.05, **p<0.01, ***p<0.001, unpaired t-tests.

RT-qPCR results showed that neither α-synuclein monomers nor fibrils induced any *Bloc1s1* degradation (**Figure 6.16**). No significant changes were observed in the expression of *Atf4* and *Ddit3* mRNAs in the NMR fibroblasts treated with monomers and fibrils compared to the basal expression in the PBS-treated controls (**Figure 6.16**). These data indicate that both RIDD and PERK pathways in the UPR remained inactive in response to α-synuclein monomers and fibrils, similar to the results collected under oligomer-treated conditions.

However, significant differences were found in the expression of selected genes encoding ER chaperones and autophagy proteins among the samples treated with monomers, oligomers and fibrils. While expression of the ER chaperones and cofactors examined in the fibroblasts treated

with α-synuclein oligomers, including *Hsp90b1, Hspa5, Pdia3* and *Dnajb11*, were found to be highly suppressed following the chronic treatment, levels of these transcripts were not altered when the NMR kidney fibroblasts were treated with α-synuclein monomers and fibrils, with the only exception of *Hsp90b1* downregulation found in monomer-treated samples. Reduction in gene expression of the three ER chaperones, *Hsp90b1*, *Pdia4* and *Hspa5,* were more significant in oligomer-treated NMR fibroblasts compared to monomer- and fibril-treated samples. Levels of *Dnajb11* downregulation were not statistically significant among different conditions due to the large variation among biological replicates.

With regards to autophagy, NMR kidney fibroblasts treated with α-synuclein monomers and fibrils displayed no significant changes at the transcriptional level compared to the PBS-treated controls. Levels of *Map1lc3b* were much more heightened in the oligomer-treated fibroblasts compared to monomer- and fibril-treated samples, whereas expression of *Sqstm1* and *Lamp1* was more suppressed under oligomer-treated conditions in comparison to monomer- and fibril-treated conditions (**Figure 6.16**). No differences were observed in expression of *Tfeb*, *Becn1* and *Atg5* among samples treated with different forms of α-synuclein.

Cell viability results showed that only oligomers exhibited significant toxicity following the 6-day treatment at 0.5 μM (**Figure 6.17**). α-synuclein monomers seemed slightly toxic to the NMR fibroblasts, reducing the percentage of survival to 85.9% (S.D. =7.6%), though not statistically significant compared to the PBS-treated controls. Fibrils were benign to these NMR fibroblasts and did not affect the cell viability after the treatment with an average viability of 104.2 % (S.D. =2.7%).

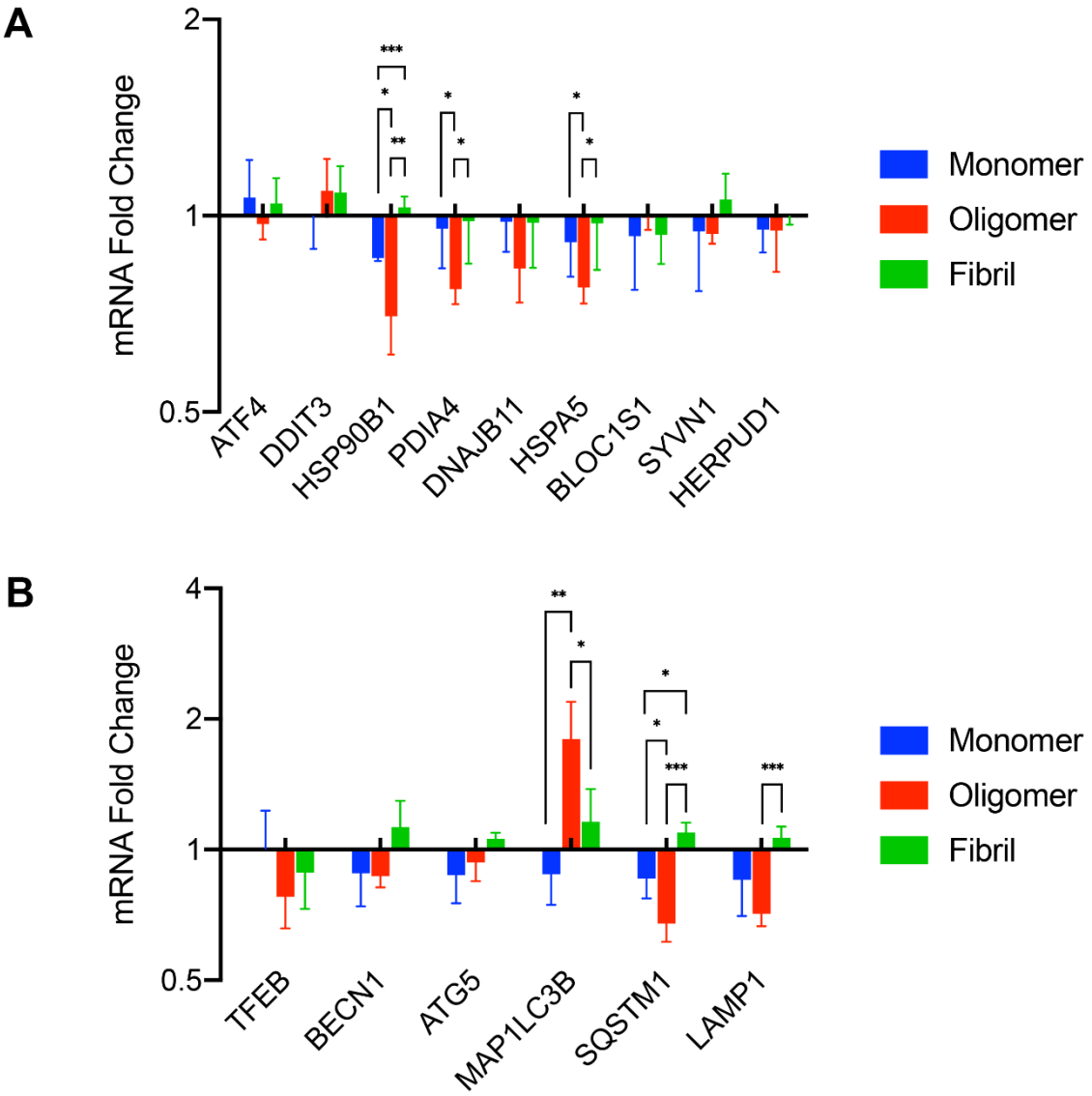

Figure 6. 16. NMR primary kidney fibroblasts were treated with 0.5 µM α-synuclein monomers, oligomers and fibrils for 6 days. Expression of UPR and autophagy markers was determined by RT-qPCR and was given in **(A)** and **(B)**, respectively. Results were normalised to the mRNA levels of reference genes and were presented on a log scale as mean ± S.D. of mRNA fold change relative to the basal-level expression in the PBS-treated controls. n=4 animals; *p<0.05, **p<0.01, ***p<0.001, ****p<0.0001; unpaired t-tests.

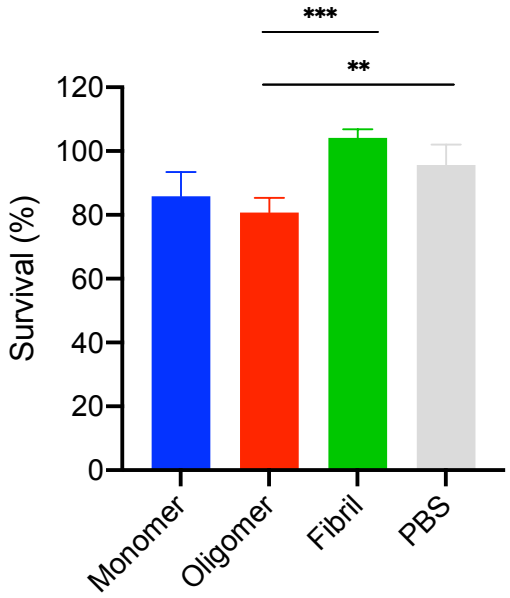

Figure 6. 17. Percentage of the viable NMR primary kidney fibroblasts after the 6-day treatment of 0.5 µM α-synuclein monomers, oligomers and fibrils. Cell viability was measured by CellTiter-Glo assay. Results were shown as mean ± S.D. of the percentage survival (%) of treated samples relative to the PBS-treated controls, n=4 animals; **p<0.01, ***p<0.001; unpaired t-tests.

6.3.6. Discussion

Taken together, these results indicate a strong correlation between the toxicity of α-synuclein oligomers and the level of suppression of pro-survival XBP1 and ATF6 pathways in the UPR signalling. The increased toxicity of oligomers might also be associated with their incremental local concentration accumulated on the cell membrane, as a result of the regular replacement of oligomers. Many studies have suggested a neuroprotective role played by XBP1s and ATF6 signalling in PD which can serve as potential therapeutic targets. For instance, local injections of adenoviruses or adeno-associated viruses expressing XBP1s into the substantia nigra pars compacta (SNc) of adult mice enhances survival of dopaminergic neurons (DNs) against 6-hydroxydopamine (6-OHDA) and 1-methyl-4-phenyl-1,2,3,6-tetrahydropyridine (MPTP)-induced neurotoxicity[312,313]. ATF6 also prevents degeneration of DNs in the MPTP-induced PD model through induction of chaperones and ERAD and has been shown to protect cells

from chronic ER stress[122,314]. Overexpression of BiP reduces apoptosis and promotes the survival of DNs in a rat PD model with elevated levels of human α-synuclein in the SNc[315]. Disruption of XBP1 and ATF6 signalling would result in a decay of the UPR transcriptional programmes, including genes encoding ER chaperones and ERAD components which may be particularly important in protecting cells from chronic ER stress, exacerbating the cytotoxic consequences of α-synuclein oligomers. A previous study showed that chronic ER stress in the mouse liver induced by repeated injections of a low dose of tunicamycin suppressed *Hspa5* and *Hsp90b1* mRNAs, which was due to the silencing of ATF6 pathway and enhancement of RIDD[316]. In this study, we did not observe signs of increased RIDD, as indicated by unaltered *Bloc1s1* levels, suggesting that the suppression of ER chaperones was mainly attributed to decreased activity of ATF6 and possibly XBP1s. It was shown that α-synuclein inhibited ATF6 activity directly through physical interactions and indirectly through the disruption of COPII ER-Golgi transport, a pathway necessary for the processing and activation of ATF6, thus leading to the downregulation of ERAD, although levels of BiP expression were paradoxically upregulated[317]. Detailed mechanisms by which these oligomers modulate XBP1 and ATF6 activity need to be established in the future. Interestingly, previously reported increased expression of PERK downstream targets including ATF4 and CHOP in PD tissue and models was not observed in our study, suggesting that α-synuclein-oligomer-mediated toxicity in the NMR fibroblasts was independent of the pro-apoptotic PERK-ATF4-CHOP activation.

The toxicity of α-synuclein oligomers also appeared to be associated with the level of autophagy in the NMR fibroblasts. Our results suggest a model in which autophagy is initially induced upon the uptake of α-synuclein oligomers to enhance their clearance; subsequently, this autophagic machinery is chronically suppressed by the increasing amounts of oligomers accumulated in the cell, leading to the impairment of autophagy which may contribute to the cell death. These results obtained from the transcriptional level, however, need to be validated by the standard means of assaying autophagy such as the LC3-II analysis to test whether autophagic flux is truly compromised by the α-synuclein challenge. A recent study of α-synuclein transmission showed that the accumulation of deficient lysosomes was induced by internalised α-synuclein oligomers in recipient neuronal cells, linking autophagic dysfunction to α-synucleinopathies[318]. In pathological conditions, decreased α-synuclein clearance due to autophagy impairment may also induce exosomal secretion of α-synuclein amounts and mediate cell-to-cell propagation of the toxic protein[237].

In addition, we demonstrated that the effects of exogenous α-synuclein species depended on their aggregation states. Only oligomeric species showed potent toxicity following the 6-day treatment in the NMR fibroblasts. The transcriptional signature in oligomer-treated fibroblasts was distinctive from those in monomeric and fibrillar α-synuclein-treated fibroblasts, further suggesting that the modulation of UPR and autophagy played a critical role in determining the ability of cells to tolerate stress induced by different α-synuclein species.

6.4. Conclusions and future work

This chapter constitutes the first investigation of the relationship between UPR/autophagy and pathogenesis linked to Aβ/α-synuclein oligomers using NMR cells. We find that membrane binding and cellular uptake of exogenous Aβ oligomers plays an important role in modulating intracellular UPR signalling. Inefficient binding of Aβ oligomers to the membrane of NMR and mouse fibroblasts leads to a silent UPR response, whereas pronounced Aβ binding and internalisation by mouse sensory neurons seem to induce cell death. Further optimisation of current experimental systems is required to determine the effects of Aβ oligomers on the UPR in the NMR under appropriate conditions. We also demonstrate that exogenous α-synuclein oligomers induce transcriptional modulation of the UPR and autophagy in the NMR kidney fibroblasts. Chronic toxicity of exogenously applied α-synuclein oligomers is associated with the transcriptional suppression of the pro-survival UPR mechanisms, including IRE1-XBP1 and ATF6 branches, and the autophagy-lysosomal pathway. This transcriptional signature is induced only by oligomeric α-synuclein but not by monomeric and fibrillar species, suggesting a unique mechanism by which α-synuclein oligomers exert detrimental effects during cell-to-cell propagation. In light of our preliminary findings of the effects of chronic exposure of NMR fibroblasts to α-synuclein oligomers, future experiments to investigate the effects of these types of exposures on mouse homologues will help to confirm whether the impairment of autophagy observed here is unique to the NMR. In these future experiments, it would be ideal to use neuronal cells from both animals, given our findings that fibroblasts cells are less amenable to binding and cellular uptake of Aβ oligomers. It would also be useful to examine the interactions of the α-synuclein oligomers with the cells using confocal microscopy in combination with the comparison of UPR and autophagy responses.

7. Development of a specific NMR anti-LC3B probe using a CTPR scaffold

7.1. Introduction

Probing the molecular details of emerging animal models, such as the NMR, can be challenging due to the lack of available molecular tools, including antibodies that are routinely used for protein-level analysis. In this chapter, we develop a probe for the detection of the NMR LC3B protein by grafting a LC3-interacting-region (LIR) onto a consensus-designed tetratricopeptide repeat protein (CTPR) scaffold as a proof-of-concept study. We characterise the key features of this probe and prove its binding to the target LC3B protein, thus demonstrating the ability to rationally design CTPR-based probes as a useful alternative to commercial antibodies, which can be further optimised and expanded for wider applications.

7.1.1. Repeat proteins and CTPR scaffolds

Repeat proteins are widely distributed across nature and are involved in a myriad of cellular processes. The high frequency of these non-globular tandem-repeat arrays is likely the result of DNA replication slippage and recombination events[319]. Repeat proteins are arranged in tandem arrays of small basic motifs of 20-40 amino acids that stack in a linear fashion, creating elongated and superhelical architectures[320]. Unlike globular proteins that are stabilised by sequence-distant contacts; repeat proteins have simple topologies comprised exclusively of interactions between residues within a repeat or between adjacent repeats and can fold in a cooperative manner[155,320]. The repeat protein family can be categorised based on their secondary structure content, and tetratricopeptide repeats (TPRs) are one of the most common forms of α-helical repeat proteins. The TPR consists of a 34-residue motif that adopts an antiparallel helix-turn-helix arrangement[321,322], with between 2 to 20 repeats arranged in tandem linked by a short loop usually four residues in length[323]. The first crystal structure of a TPR motif (**Figure 7.1**), the three-TPR domain of protein phosphatase 5, revealed that the repeats are packed together in a parallel array to produce a right-handed superhelical structure with a continuous helical groove, which is commonly the site for recognition of target proteins[324]. TPRs have been found in over 300 proteins and generally function as scaffolds in

mediating protein-protein interactions and the assembly of multiprotein complexes[325]. TPR-containing proteins include Hsp70-Hsp90 organising protein (HOP) (**Figure 7.1**), three essential subunits of the anaphase promoting complex/cyclosome (APC/C) (Cdc16, Cdc23 and Cdc27)[322], the NADPH oxidase subunit p67[phox][326] and many others[324].

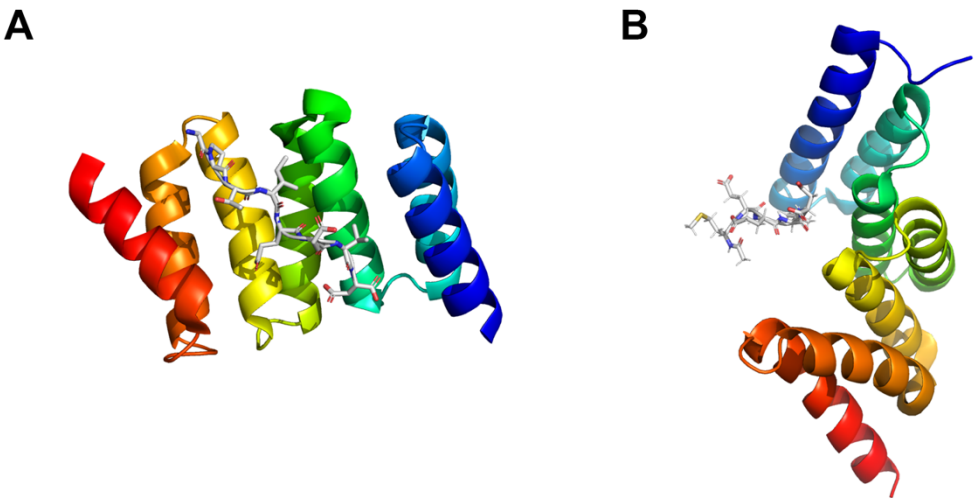

Figure 7. 1. TPR domains in HOP (PDB: 1elw) and protein phosphatase 5 (PDB: 2bug). **(A)** Crystal structure of the TPR1 domain of HOP in complex with an HSC70 derived peptide (GPTIEEVD)[326]. **(B)** Solution structure of the TPR domain of protein phosphatase 5 in complex with an Hsp90-derived peptide (MEEVD)[327]. Peptides are displayed as ball-and-stick structures. Figures were prepared using PYMOL.

By applying the concept of consensus design[328], - i.e. engineering a protein to have the most common residue at each position determined by multiple sequence alignments - many groups have designed artificial proteins that have greatly enhanced stabilities in comparison to their natural counterparts[320]. The first consensus TPR (CTPR) constructs were made by the Regan group[325]. The consensus sequence consists of the residues with the highest global propensity from sequence alignment at each position of the TPR motif, with a replacement of cysteine by alanine (C10A) to prevent disulphide bond formation and the additional incorporation of an N-capping, helix-stabilising sequence (Gly-Asn-Ser) and a 'solvating helix'[325]. Two mutations (D18Q and E19K) were introduced later to increase the stability of individual repeat units through the promotion of charge-charge interactions[329,330]. Chemical and thermal denaturation studies have shown that CTPRs are highly stable[325,330], and the stabilising interactions are

predominantly due to the large hydrophobic residues that force the α-helices apart into the characteristic elongated structure[320].

The exceptionally high thermostability, simple topology and modular nature make CTPR scaffolds extremely amenable for rational engineering to introduce novel functionalities. TPR proteins can utilise varied modes of bindings to their partners, ranging from short linear peptide motifs to large globular protein domains[323]. The most common interaction involves the concave groove formed by two to three TPR repeats binding to a short negative charged peptide of around five amino acids, first identified in the C-terminal domain of Hsp90 bound to HOP[323,331]. Exploiting this binding mode, Cortajarena *et al.* created a functional TPR-based module interacting with the C-terminus of Hsp90 with improved specificity and affinity by grafting the residues from the natural TPR domains in HOP onto the α-helices of the concave face of a three-repeat CTPR (CTPR3)[332]. Rational design and library screening approaches were subsequently used to optimise these TPR-based modules with potential applications in protein-based detection and inhibition of cellular protein-protein interactions, although the affinities were fairly weak (low- to mid-micromolar), presumably due to the small area of the interfaces involved[333,334]. Our group has recently shown that CTPRs can tolerate extensions of an inter-repeat loop up to 25 residues, which does not disrupt the overall protein structure and allows binding sequences for target proteins to be constrained in bioactive conformations[155]. Taking advantage of this malleability, we have developed a new approach for engineering high-affinity binding properties into CTPR proteins by grafting functional peptides into the loop between adjacent repeats[335]. We used a short peptide derived from the nuclear factor erythroid-2-related factor (Nrf2) and created artificial CTPR proteins that bound the Kelch-like ECH-associated protein 1 (Keap1) with nanomolar affinities, and this engineered protein could be expressed in *E. coli* with extremely high yields (1-2 mg from 90 mL of culture) and showed high thermostability (>65°C)[335]. Using this 'cut-and-paste' grafting strategy, here we explore the application of rationally engineered CTPR proteins for detecting target proteins in the NMR as potential antibody replacement. As a proof of concept, we choose to develop a probe that targets specifically the NMR LC3B protein, which is a standard marker for assaying autophagy, by grafting a known LC3-interacting region (LIR) onto a CTPR4 scaffold. Additionally, although here we use the LC3B protein, which has very similar sequence between NMR and human, so the human antibody could be used as a positive control and be directly compared to our designed probe, this approach could be used in future to designed NMR probes where the 'antigen' epitope is too different from those in other organisms for those antibodies to be used.

7.1.2. LC3-interacting region (LIR) in LC3B-binding proteins

ATG8/LC3/GABARAP proteins are conjugated to autophagosomes and interact with two broad classes of partners: autophagy receptors and adaptors. The interaction depends on a LC3-interacting region (LIR) comprising of 15 to 20 amino acids, which binds to the LIR docking site (LDS) of ATG8 proteins[144]. Autophagy receptors bind directly to lipidated ATG8 anchored on the inner autophagosomal membrane and mediate the docking of autophagosome to cargo (**Figure 7.2**), for example, organelles, intracellular pathogens, protein aggregates and ribosomes, which can be specifically targeted by autophagy receptors for subsequent sequestration and delivery for degradation[144,336]. Another class of proteins, autophagy adaptors - interact with lipidated ATG8 proteins via LIR on the convex autophagosome membrane and can regulate autophagosome formation, transport, crosstalk with the endocytic network and autophagosome formation but are themselves not degraded by autophagy[337]. The LIR motif was originally mapped to a 22-residue sequence in an intrinsically disordered region of p62, the first identified mammalian autophagy receptor (**Figure 7.2**), which contained an evolutionarily conserved motif[228]. Structural data on LC3-p62 and ATG8-ATG19 (in yeast) identified a four-amino-acid motif, W-X_1-X_2-L (X represents any amino acid) in p62 and ATG19 where the side chains of tryptophan (W) and leucine (L) interact with two different hydrophobic pockets (HP1 and HP2) in the core ubiquitin-like (Ubl) domain of LC3B/ATG8[338,339]. Mutation analyses and binding assays, together with a compilation of structural information of verified LIR-ATG8 (LC3 and GABARAP) complexes, revealed the canonical LIR motif that consists of Θ-X_1-X_2-Γ motif, where Θ represents an aromatic residue (W/F/Y) and Γ an aliphatic residue (L/V/I)[336] (**Figure 7.3**). Most LIR motifs have W or F at the Θ position, and the Y732W mutation in the NBR1 LIR can significantly enhance binding affinity by a 7.5-fold increase[340]. The X_1 and X_2 positions are often populated by acidic or hydrophobic residues, with the X_2 being the most promiscuous, sometimes harbouring basic residues[144]. The core motif is flanked by N- and C-terminal sequences that often contain acidic residues and contribute to binding affinity and specificity[144]. It has been shown that the N-terminal acid residues engage in electrostatic interactions with basic residues in the LDS of LC3/GABARAP proteins[341,342], while the C-terminal extended LIRs in autophagy adaptors such as ALFY (autophagy-linked FYVE protein) and FYCO1 (FYVE and coiled-coil domain containing 1) confer specificity and stabilise the LIR-LDS interaction[145,343–345].

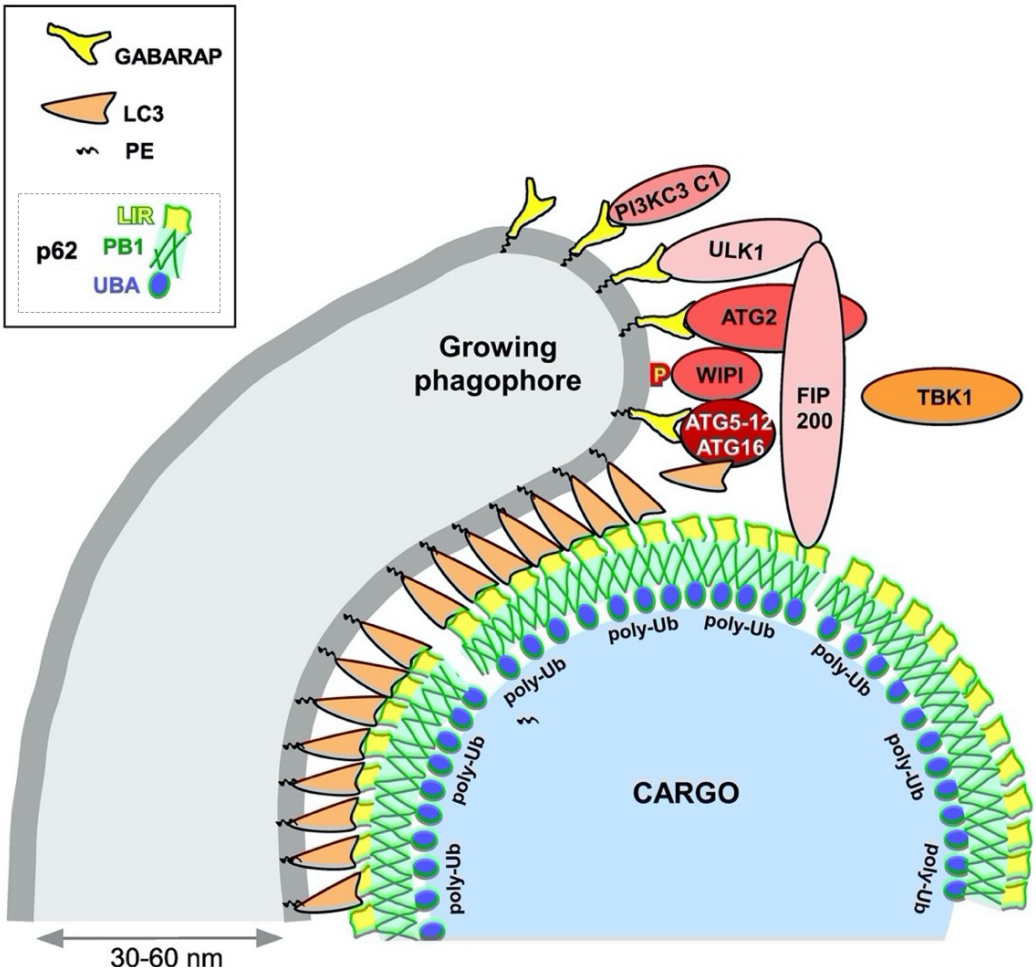

Figure 7. 2. Model of phagophore expansion along a p62-coated ubiquitinated cargo. At the rim of the phagophore, lipidated GABARAP proteins act as scaffolds for the assembly of core autophagy components including ULK complex[346], PI3KC3 Complex 1[347] and ATG5-ATG12-ATG16[348] via LIR motifs. The major components of p62 include an N-terminal PB1 domain, a LIR motif and a C-terminal ubiquitin binding UBA domain[144]. The phagophore-to-cargo docking is mediated by oligomerisation of p62 via its PB1 domain[349], enabling multiple interactions between the LIR motif and lipidated LC3B. This strong binding outcompetes other interactions of p62 with core autophagy proteins such as FIP200, thus preventing the degradation of these core autophagy proteins by autophagy[350]. Figure modified from the reference with permission[144].

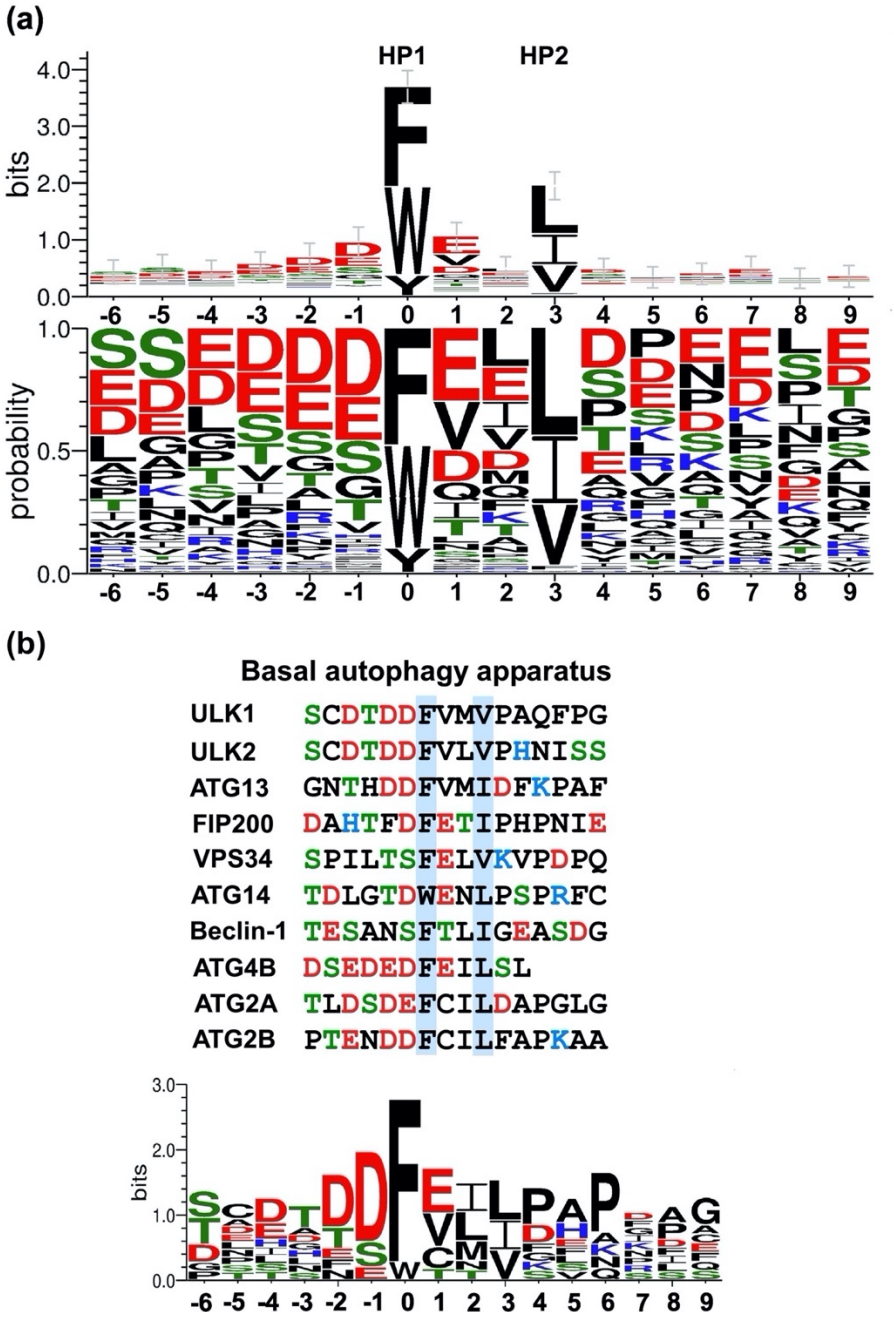

Figure 7. 3. LIR sequences. (a) Sequence logos based on 100 LIR motifs, with 48 LIRs with F, 42 with W and 10 with Y in position X0 shown as information content in bits (upper panel) and residue probabilities (lower panel). **(b)** LIRs in the core autophagy components. Figure reprinted from the reference with permission[144].

To date, over 40 LIR-containing proteins have been identified as interacting with ATG8 family proteins[344]. In this study, a 17-amino-acid LIR peptide derived from FUN14 domain containing 1 (FUNDC1)[351], which is an essential mitochondrial outer-membrane protein acting as a

specific receptor for hypoxia-induced mitophagy in mammalian cells[352], was chosen for grafting into a CTPR4 scaffold. The peptide sequence corresponds to the residues 10-26 of human FUNDC1 and contains a canonical LIR motif (Y18-E19-V20-L21)[351]. The sequence located immediately to the N-terminus of the LIR motif (S13-D14-D15-D16-S17) includes acidic residues (D) engaging in electrostatic interactions and serine (S) that can be phosphorylated[351]. Under normal conditions, S13 and Y18 are phosphorylated by CSNK2/CK2 kinase and SRC kinase, respectively, which inhibits the interaction of FUNDC1 and LC3, whereas hypoxia induces dephosphorylation of FUNDC1 enhances its binding to LC3-II and subsequently activates mitophagy[352,353]. The solution structure of the LC3B-FUNDC1-LIR peptide complex revealed a nonconventional binding conformation in which V20 was also inserted into the HP1 of LC3B, together with the highly conserved Y18 and L21 residues[351] (**Figure 7.4**). This FUNDC1-LIR peptide thereby adopts a loop conformation when binding LC3B and abolishes an intermolecular β-sheet that is seen in other LC3-LIR complexes such as LC3B-p62[339,351]. Isothermal titration calorimetry (ITC) showed that the dissociation constant (K_D) for the interaction of this FUNDC1-LIR peptide with LC3B was 0.40 μM[351], which is stronger than most of the LIR peptides derived from other binding partners of LC3B. FYCO1, an autophagy adaptor protein which mediates microtubule plus end-directed autophagosome transport[354], demonstrates a superior binding affinity (0.19 μM) because of a unique LIR conformation upon binding which comprises a β-strand flanked by a C-terminal α-helix and negatively charged residues at the N-terminus[344]. However, in our first design attempts, we reasoned that these secondary structure elements and associated binding functionality in FYCO1 might not be preserved after grafting directly into the inter-repeat loop of our CTPR scaffold, resulting in sub-optimal interactions with the LC3B protein. In addition, Rogov and colleagues have determined that, out of the 30 LIRs investigated, only FUNDC1-LIR shows a preferential interaction with LC3B over LC3C and GABARAP proteins[337]. In summary, the FUNDC1-LIR peptide was selected as an appropriate candidate for grafting because of its reasonably high affinity, its relatively short sequence which adopts a loop-like structure that should be amenable to grafting into the CTPR loop, and its selectivity towards LC3B over other LC3/GABARAP paralogues. As a starting point, we used the human FUNDC1-LIR because it has been well characterised, and it differs from the predicted NMR FUNDC1-LIR sequence (NCBI: XP_004871590.1) by only one amino acid at residue 10 (**Figure 7.5**). The D-to-E substitution would not be expected to have a large impact on the structure or binding affinity as both residues are negatively charged. The sequence homology between the NMR and human LC3B is 97% with all critical amino acids forming the HP1

(Asp19, Ile23, Lys51, and Leu53) and HP2 (Phe52, Val54, Leu63, Ile66 and Ile67) are conserved[351] (**Figure 5.6**), making the human FUNDC1-LIR and NMR LC3B an ideal pairing to investigate.

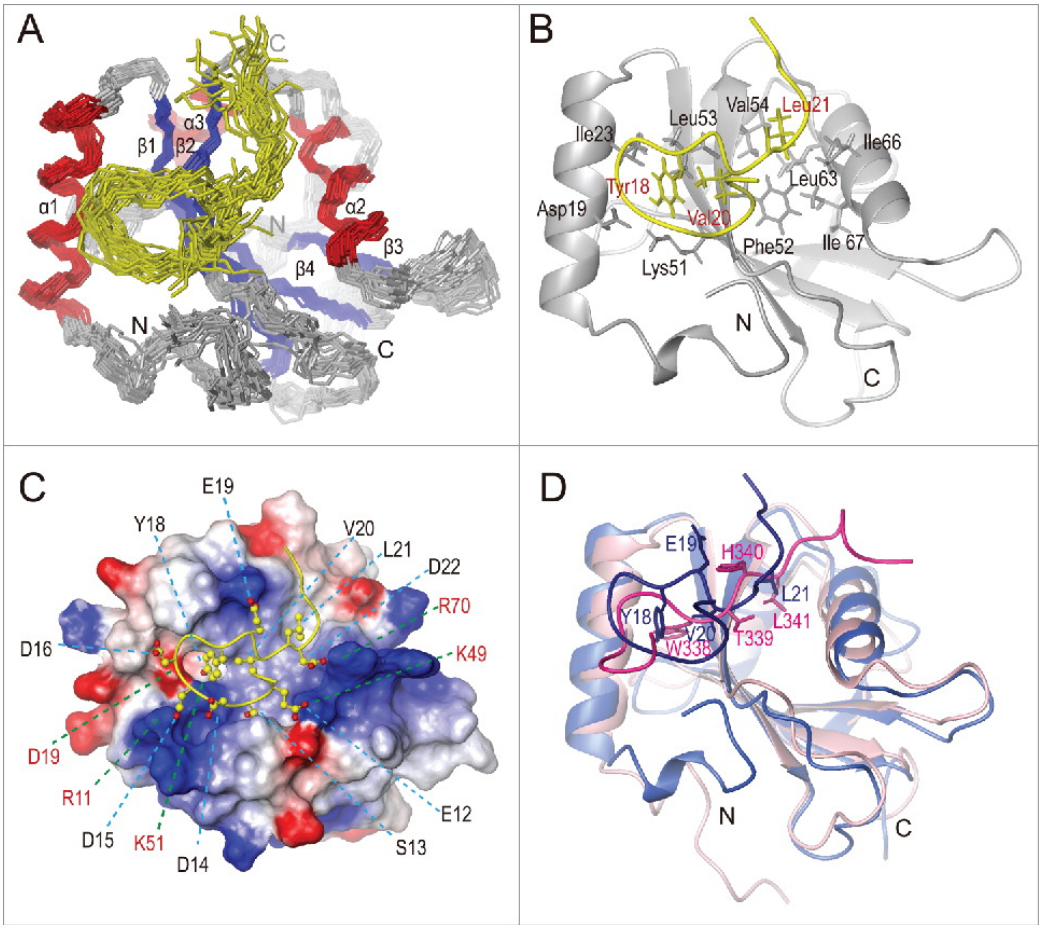

Figure 7. 4. Solution structure of LC3 in complex with a synthetic FUNDC1 peptide containing the LIR resolved by nuclear magnetic resonance spectroscopy. (A) Superimposition of the backbones of the ensemble of 20 structures of the LC3-FUNDC1 complex. Red: α helices, blue: β sheets, yellow: LIR-containing peptide. **(B)** Ribbon representation of the LC3-FUNDC1 mean structure. Grey: LC3, yellow: LIR-containing peptide. Side chains of LC3 residues that form the HP1 and HP2 are labelled in black, and the three critical residues inserted into the HP1 are labelled in red. **(C)** Electrostatic potential surface of LC3. Blue: positively charged residues, red: negatively charged residues, grey: neutral residues. **(D)** Superimposed ribbon structures of the LC3-FUNDC1 peptide (blue) and LC3-p62 peptide (pink) complexes. The LIR residues in both complexes are labelled. Figure reprinted with permission[351].

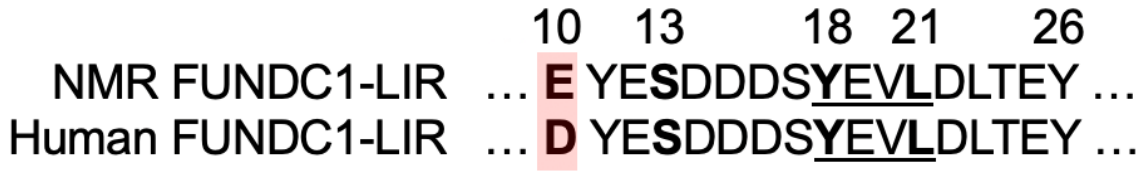

Figure 7. 5. Sequence alignment of human and NMR FUNDC1-LIR peptides. Key amino acid residues are in bold. There is only one amino acid difference (E to D, highlighted in red) between the two peptides. The core LIR domain (residues 18-21, underlined, is identical in the two peptides. Ser13, which plays a critical role in modulating phosphorylation and binding of FUNDC1 to LC3, is also conserved.

7.2. Design of the CTPR4-LIR probe

We chose the CTPR sequence used by Grove *et al.* due to its high stability and solubility[329,335]. The inter-repeat loop of the CTPR scaffold comprises four amino acids (DPNN). Using the similar design described in our previous study, the FUNDC1-LIR peptide sequence was inserted into the loop of CTPR4 and flanked by a DPNN sequence on both sides so as to preserve the chemical environment of the residues adjacent to the loop[335]. An N-terminal 6*His tag was incorporated into the protein construct to allow a one-step purification by affinity chromatography, along with a thrombin cleavage site for the His tag removal. Additionally, a HiBiT tag, with a proceeding GS linker (EFSGGGGS), was used as a luminescent reporter[355]. The small size (11 amino acids) of HiBiT means that it can be fused to the C-terminus of the CTPR4-LIR probe without disrupting the overall protein structure. Due to its exceptionally high affinity (K_D = 700 pM) to LgBiT, the HiBiT-tagged probe can produce a potent luminescent signal after a short period of incubation with LgBiT, which is significantly more sensitive than fluorophore-based techniques such as GFP[355]. The design and predicted structure of the CTPR4-LIR probe is shown in **Figure 7.6**. A randomly scrambled FUNDC1-LIR sequence was also designed and grafted onto the CTPR4 scaffold as a negative control (CTPR4-RS), that should not bind to LC3B.

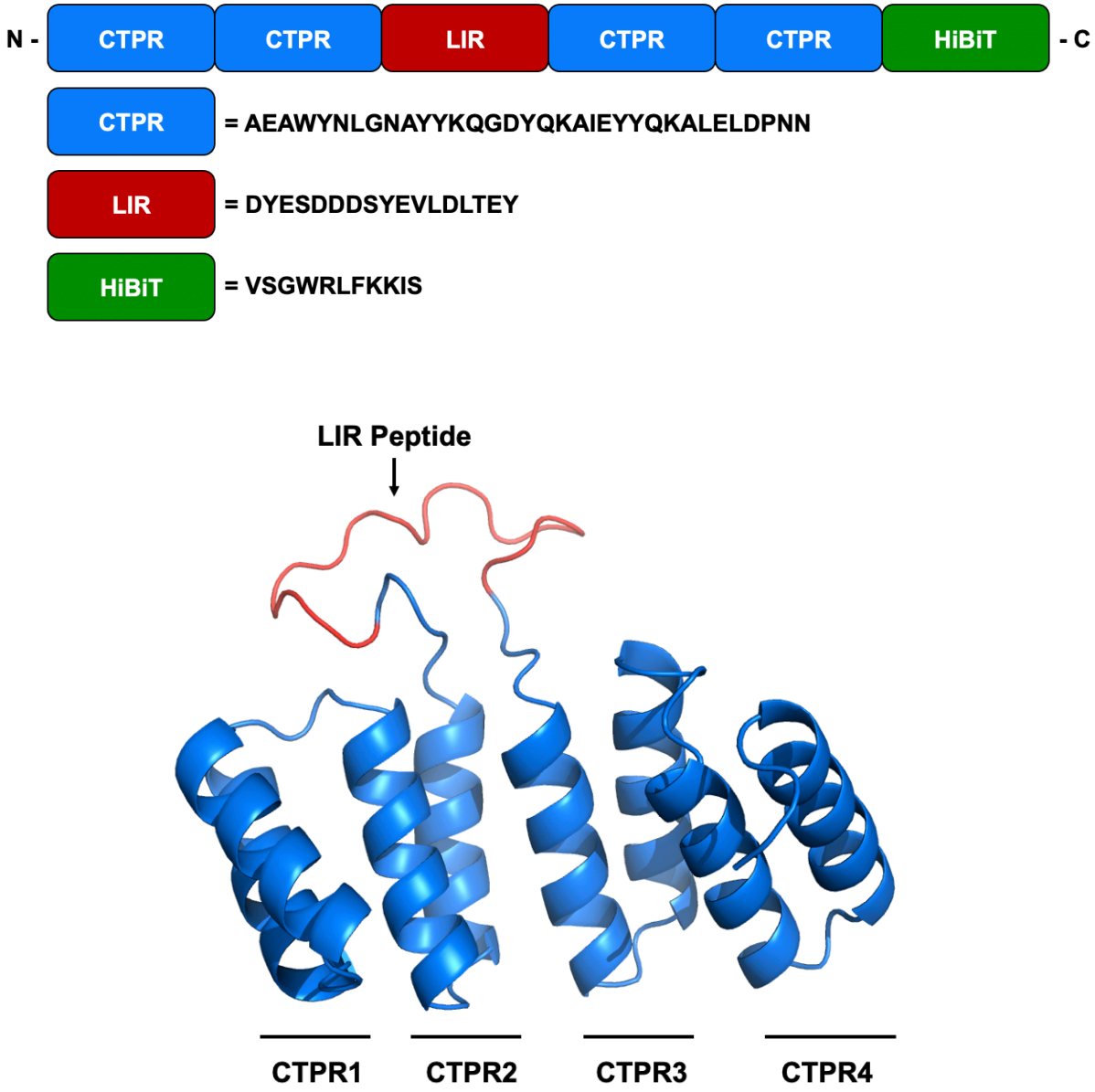

Figure 7. 6. Design (top) and structure (bottom) of the CTPR4-LIR probe targeting the NMR LC3B protein. The structure of the designed probe without the HiBiT tag was predicted using SWISS-MODEL[356] on the basis of the crystal structure of CTPR reported by the Regan Group (PDB: 2fo7)[357] and was made using PYMOL.

7.3. Protein expression and purification

The complete list of protein constructs made in this study is summarised in **Table 7.1**. All CTPR4-LIR constructs were expressed extremely well in *E. coli* C41 (DE3) cells (~10 mg per

100 mL of culture). SDS-PAGE showed that the 5-mL HisTrap column was overloaded with the CTPR4-LIR proteins, which were collected in the flow through and wash fractions in addition to the elution fractions (**Figure 7.7**). A similar yield was achieved for the CTPR4-RS protein expression. Overnight incubation at 4°C with higher amounts of thrombin was sufficient to cleave ~50% of the CTPR4-LIR or CTPR4-RS constructs.

The recombinant NMR LC3B protein was also well expressed (~5 mg per 100 mL of *E. coli* culture) and was purified using the same approach. 1 mM DTT was added in the elution buffer during the purification to prevent cystine oxidation, but we still obtained dimers during the SDS-PAGE analysis which were quite resistant to the addition of β-mercaptoethanol in the loading buffer, combined heating. When fresh DTT was added to the sample in combination with extended heating, the dimers disappeared (**Figure 7.8**). 1 mM DTT or TCEP was added to the buffers in subsequent downstream analysis.

All purified protein samples were analysed by mass spectroscopy and were confirmed to have the expected molecular weights as predicted by Expasy[358] with high purity (**Table 7.1, Figure 7.7, 7.8**).

Table 7. 1. Protein constructs made in this study.

Construct	Tag	Sequence	Molecular Weight (Da)	pI	Experiments
CTPR4-LIR	None	GSAEAWYNLGNAYYKQGDYQKAIEYYQKALELDPNN AEAWYNLGNAYYKQGDYQKAIEYYQKALELDPNNDYESDDDSYEVLDLTEYDPNN AEAWYNLGNAYYKQGDYQKAIEYYQKALELDPNN AEAWYNLGNAYYKQGDYQKAIEYYQKALELDPNN	18765.1	4.11	ITC, CD
6His-CTPR4-LIR	6*His	MRGSHHHHHHGLVPRGSAEAWYNLGNAYYKQGDYQKAIEYYQKALELDPNN AEAWYNLGNAYYKQGDYQKAIEYYQKALELDPNNDYESDDDSYEVLDLTEYDPNN AEAWYNLGNAYYKQGDYQKAIEYYQKALELDPNN AEAWYNLGNAYYKQGDYQKAIEYYQKALELDPNN	20542.1	4.61	Pull-down, CD
CTPR4-LIR-HibiT	HiBiT	GSAEAWYNLGNAYYKQGDYQKAIEYYQKALELDPNN AEAWYNLGNAYYKQGDYQKAIEYYQKALELDPNNDYESDDDSYEVLDLTEYDPNN AEAWYNLGNAYYKQGDYQKAIEYYQKALELDPNN AEAWYNLGNAYYKQGDYQKAIEYYQKALELDPNNEFSGGGGSVSGWRLFKKIS	20746.3	4.27	Dot blot, ITC
6His-CTPR4-RS	6*His	MRGSHHHHHHGLVPRGSAEAWYNLGNAYYKQGDYQKAIEYYQKALELDPNN AEAWYNLGNAYYKQGDYQKAIEYYQKALELDPNNDVEYEYTYDSSDELDLDDPNN AEAWYNLGNAYYKQGDYQKAIEYYQKALELDPNN AEAWYNLGNAYYKQGDYQKAIEYYQKALELDPNN	20542.1	4.61	Pull-down
CTPR4- RS-HibiT	HiBiT	GSAEAWYNLGNAYYKQGDYQKAIEYYQKALELDPNN AEAWYNLGNAYYKQGDYQKAIEYYQKALELDPNNDVEYEYTYDSSDELDLDDPNN AEAWYNLGNAYYKQGDYQKAIEYYQKALELDPNN AEAWYNLGNAYYKQGDYQKAIEYYQKALELDPNNEFSGGGGSVSGWRLFKKIS	20746.3	4.27	Dot blot, ITC
NMR LC3B	None	GSMPSEKTFKQRRTFEQRVEDVRLIREQHPTKIPVIIERYKGEKQLPVLDKTKFLVPDH VNMSELIKIIRRRLQLNANQAFFLLVNGHSMVSVSTPISEVYESEKDGDGFLYMVYASQETFGRGLSVCD	14932.2	8.75	All

Molecular weight and pI were determined by Expasy[358]. The FUNDC1-LIR and scrambled motifs are highlighted in yellow and grey, respectively. CD = circular dichroism, ITC = isothermal titration calorimetry.

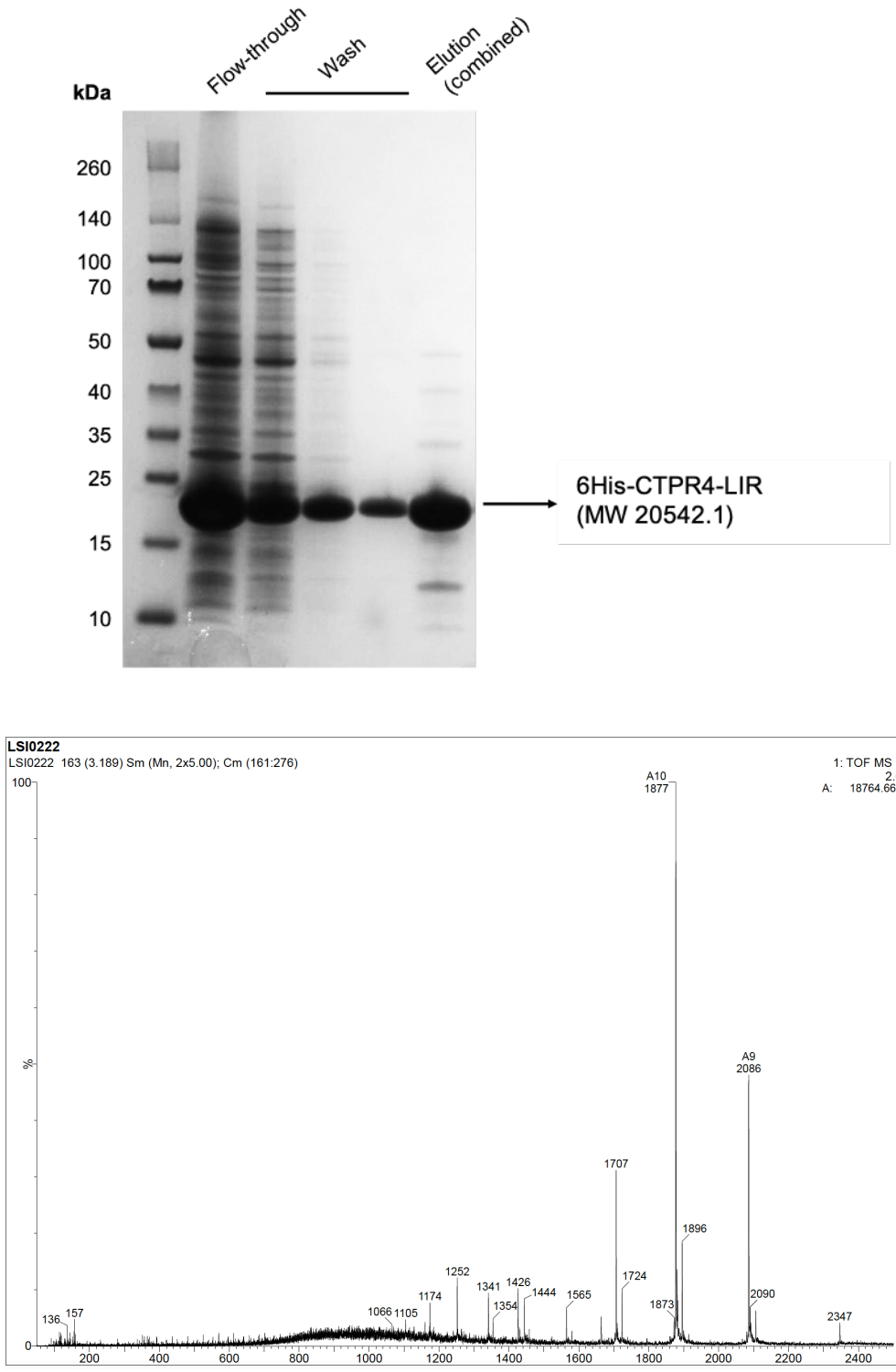

Figure 7. 7. Purification of CTPR4-LIR. (Top) a representative image of SDS-PAGE analysis of fractions collected during the CTPR4-LIR purification. MW = protein molecular weight predicted by Expasy[358]. **(Bottom)** a representative mass spectrum of the purified CTPR4-LIR after thrombin cleavage. The MW determined by mass spectroscopy is in agreement with the predicted MW (18765.1 Da).

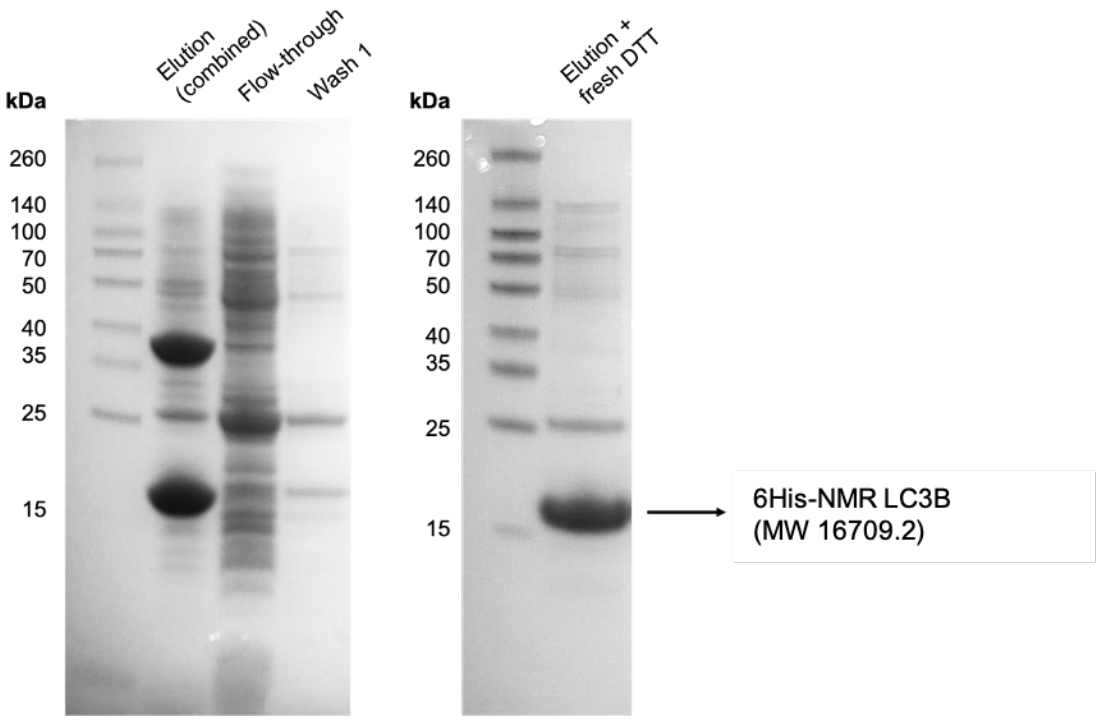

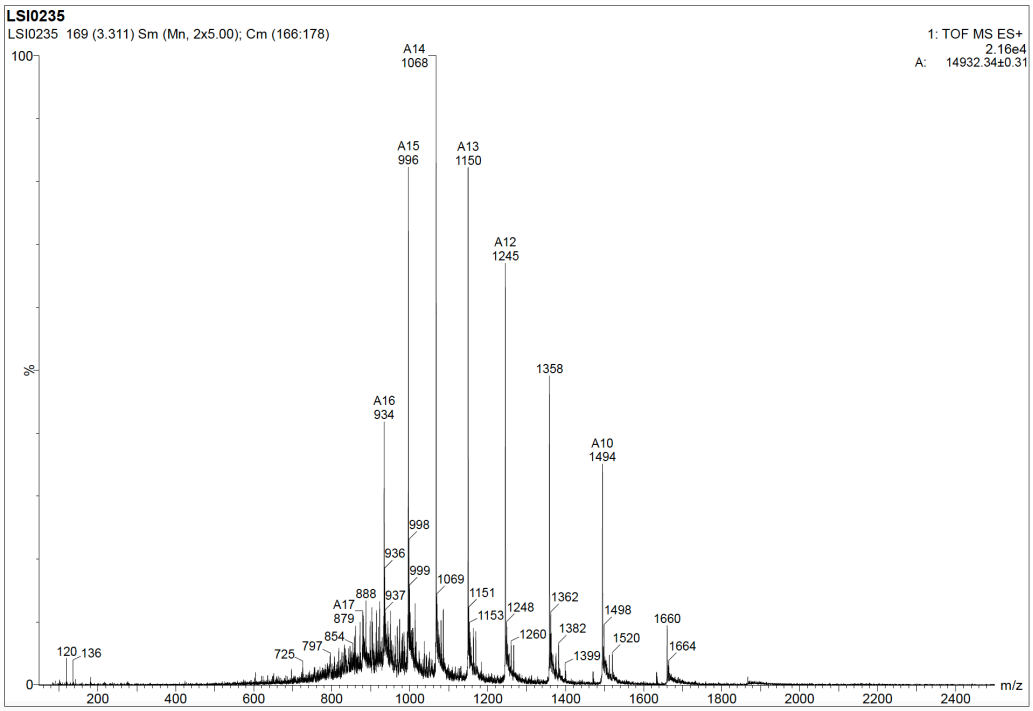

Figure 7. 8. Purification of NMR LC3B. (Top) representative images of SDS-PAGE analysis of fractions collected during the NMR LC3B purification. MW = protein molecular weight predicted by Expasy[358]. **(Bottom)** a representative mass spectrum of the purified NMR LC3B after thrombin cleavage. The MW determined by mass spectroscopy is in agreement with the predicted MW (14932.2 Da).

7.4. Biophysical characterisation of the CTPR4-LIR probe

Circular dichroism (CD) spectroscopy is defined as the unequal absorption of left-handed and right-handed circularly polarised light and is an excellent tool for determining the secondary structure elements within proteins, such as α-helix, β-sheet and random coils, that have characteristic CD spectra[359]. Proteins having high α-helical content typically display double negative peaks at 222 nm and 208 nm and a positive band at 193 nm[360]. Far-UV CD spectra revealed that the CTPR4-LIR probe contained a high degree of α-helicity and remained properly folded without significant changes in secondary structure even when the temperature was increased to 95°C, indicating its remarkable thermostability (**Figure 7.9**). In contrast, CD spectra of the His-tagged CTPR4-LIR showed attenuated signals at 80°C and 95°C, suggesting that the attachment of an N-terminal 6*His tag compromised thermostability of the CTPR4-LIR protein. The thermostability of CTPR4-LIR constructs is much higher than that of the multi-domain immunoglobulin G (IgG), which displays two unfolding transitions wherein the more heat-sensitive Fab fragment denatures at ~61°C and the Fc fragment at ~71°C[361].

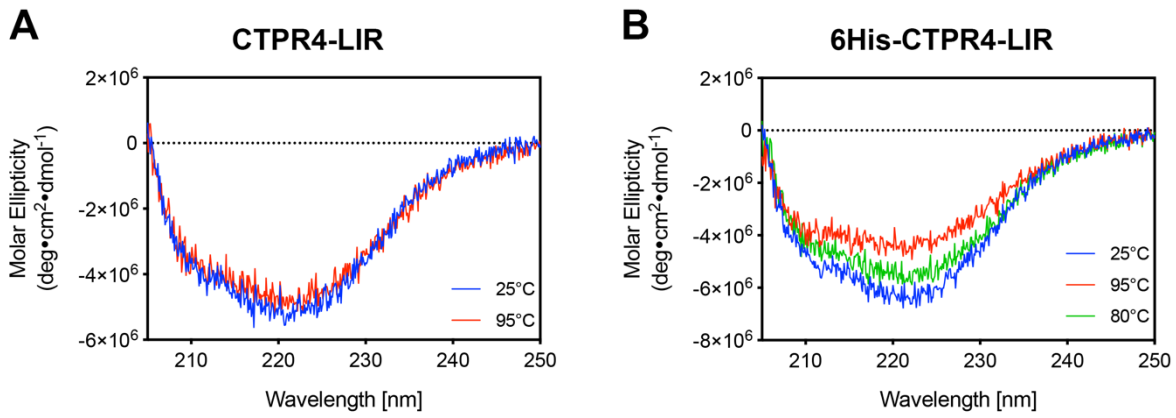

Figure 7. 9. Far-UV CD spectra (205 nm to 250 nm) of the CTPR4-LIR protein (20 µM). (A) and his-tagged CTPR-LIR protein (20 µM) **(B)** in a 50 mM sodium phosphate buffer, pH 6.8. The data were shown for different temperature values, 25°C (blue), 80°C (green, only for his-tagged CTPR4-LIR), and 95°C (red) and representative of three independent experiments.

Next, we analysed the chemical denaturation of CTPR4-LIR using an established assay that monitors changes in the intrinsic fluorescence of tryptophan residues within the CTPR4-LIR

as it unfolds with increasing concentrations of guanidinium chloride (GdmHCl)[166] (**Figure 7.10**). The denaturation curve was then fitted to a two-state model to determine $D_{50\%}$ (the concentration of GdmHCl at which 50% of the proteins are unfolded), *m*-value (the dependence of the free energy of unfolding on concentration of denaturant), and ΔG_{D-N}^{H2O} (the free energy of unfolding in water)[166,362]. The *m*-value is a measure of the change in solvent-accessible surface area (ΔSASA) upon unfolding and is therefore an indicator of the folding/unfolding cooperativity of the protein [362,363]. Larger proteins and more cooperatively folded proteins (i.e. proteins that unfold in a two-state manner without population of any partly folded states) have larger ΔSASA and thus higher *m*-values[363]. The results for CTPR4-LIR are shown in **Table 7.2** and compared to the previous data obtained from the CTPR4 scaffold[166].

Table 7. 2. Thermodynamic parameters of CTPR4-LIR compared to CTPR4. Data is an average of three experiments.

Protein	$D_{50\%}$ (M)	*m*-value (kcal mol^{-1} M^{-1})	ΔG_{D-N}^{H2O} (kcal mol^{-1})
CTPR4-LIR	3.81 ± 0.02	2.86 ± 0.18	-10.9 ± 0.7
CTPR4[166]	4.81 ± 0.01	4.0 ± 0.3	-19.2 ± 0.9

The $D_{50\%}$ and *m*-value obtained for CTPR4-LIR were lower than those of the parent CPTR4 scaffold[166], indicating that the insertion of 17-residue LIR peptide lowers the overall stability and folding cooperativity of the CTPR4 array, consistent with the findings from our previous study of CTPR proteins with various loop insertions[166]. When compared to IgG which showed a $D_{50\%}$ value between 2-3 M[364], the CTPR4-LIR displayed a higher $D_{50\%}$ close to 4 M, suggesting that the CTPR4-LIR maintains a higher stability than antibodies.

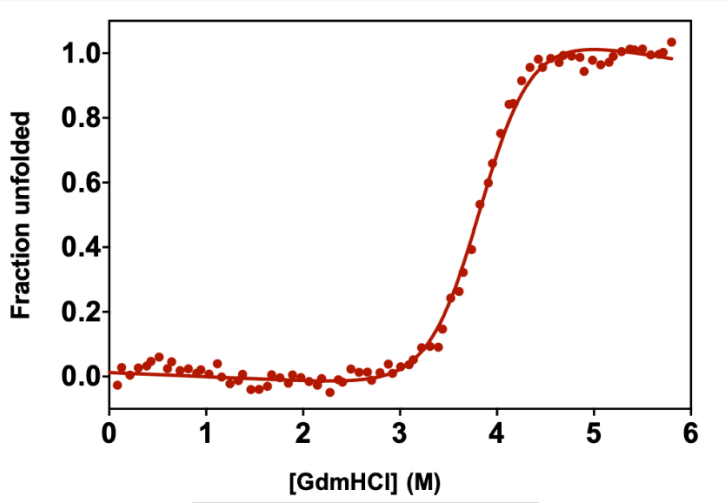

Figure 7. 10. A representative chemical denaturation profile of CTPR4-LIR. The denaturation curve was fitted to a two-state model. Measurements were performed at 25°C in 50 mM sodium phosphate buffer, pH 6.8, 150 mM NaCl from three independent experiments.

7.5. Binding of CTPR4-LIR to LC3B

Dot blot assays were performed to test whether the CTPR4-LIR-HiBiT probe could recognise and quantify LC3B. We successfully observed the luminescent signals indicating the binding of CTPR4-LIR to the recombinant NMR LC3B, and by establishing a titration curve with the amount of LC3B varying from 5 to 0.01 µg, we determined that the CTPR4-LIR probe had a detection limit of 0.1 µg LC3B (**Figure 7.11**). The commercial anti-LC3B antibody (34 ng/mL), which we had used to probe the LC3B turnover in the NMR cells (described in Chapter 5), was able to detect the NMR LC3B with a limit of 0.025 µg, approximately four times more sensitive than the CTPR4-LIR probe (25 µg/mL). The K_D values of good commercial antibodies are in the nanomolar range, whereas the K_D for the binding of FUNDC1-LIR to the human LC3B is 0.4 µM[351]. The anti-HRP secondary antibody further amplified the signals of the primary antibody, whereas CTPR4-LIR relied solely on the HiBiT reporter per probe. It was therefore not surprising that our designed CTPR4-LIR-HiBiT probe was not as sensitive as the commercial antibody, but its detection limit can be improved by increasing the concentration during incubation and further optimisation of the probe design. No signal was observed using the CTPR4-RS control (**Figure 7.11**).

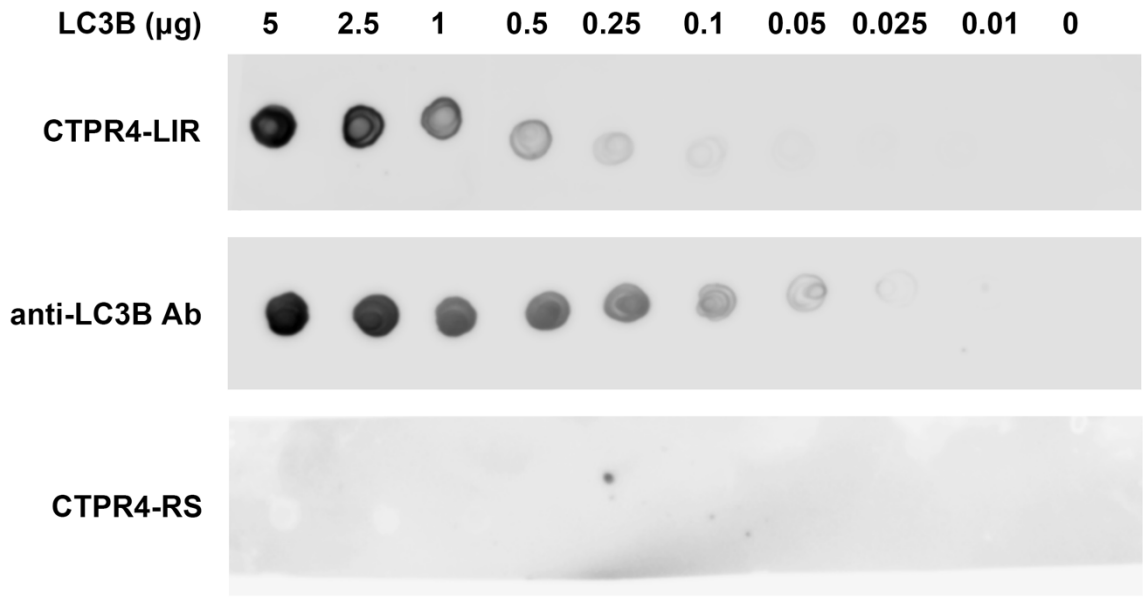

Figure 7. 11. Dot blot analysis using CTPR4-LIR-HiBiT (top) to probe the recombinant NMR LC3B protein in comparison with the commercial anti-LC3B antibody (middle) and CTPR4-RS-HiBiT control (bottom).

ITC is an analytical tool to measure the heat discharged or absorbed during a bimolecular reaction and was used to determine the K_D of CTPR4-LIR to NMR LC3B. We used a similar experimental setting that was reported previously, where the CTPR4-LIR (ligand) was injected to LC3B in the main cell at 25°C in the same buffer system[351]. However, we failed to observe any heat change during the reaction because of massive protein precipitation in the main cell once the CTPR4-LIR was injected. We modified conditions by adjusting the temperature (4°C, 10°C and 20°C), stirring speed (305 and 498 rpm), molar ratios of CTPR4-LIR-to-LC3B, as well as addition of detergents (0.05% Triton), but none of these improved the outcome. We then altered the setting by placing the CTPR4-LIR in the main cell, to which the LC3B protein was injected. Less precipitation was observed, as indicated by smaller pellets after the reaction, and a sigmoidal curve of heat change was observed, indicating an exothermic reaction, that is similar to previous studies (**Figure 7.12**). When the LC3B protein was injected to the CTPR4-RS control, no heat change was observed, suggesting no binding between the two biomolecules. When fitting the data using a one-site binding model, however, we found that the N value, which indicates the number of sites of binding and was expected to be close to 1, was abnormal, presumably due to the protein precipitation, and it remained an issue when a number of other conditions were tried. We also performed control experiments by injecting buffer to CTPR4-

LIR or LC3B and vice versa but did not observe any precipitation, thus suggesting that the precipitation occurred only when the two proteins were mixed, although the mechanism by which the proteins precipitate was unclear. Therefore, although we could observe binding using ITC, it was not an ideal approach to measure the affinity of CTPR4-LIR for NMR LC3B. In future, alternative techniques such as surface plasmon resonance could be used in order to determine accurately the K_D value of the CPTR4-LIR probe.

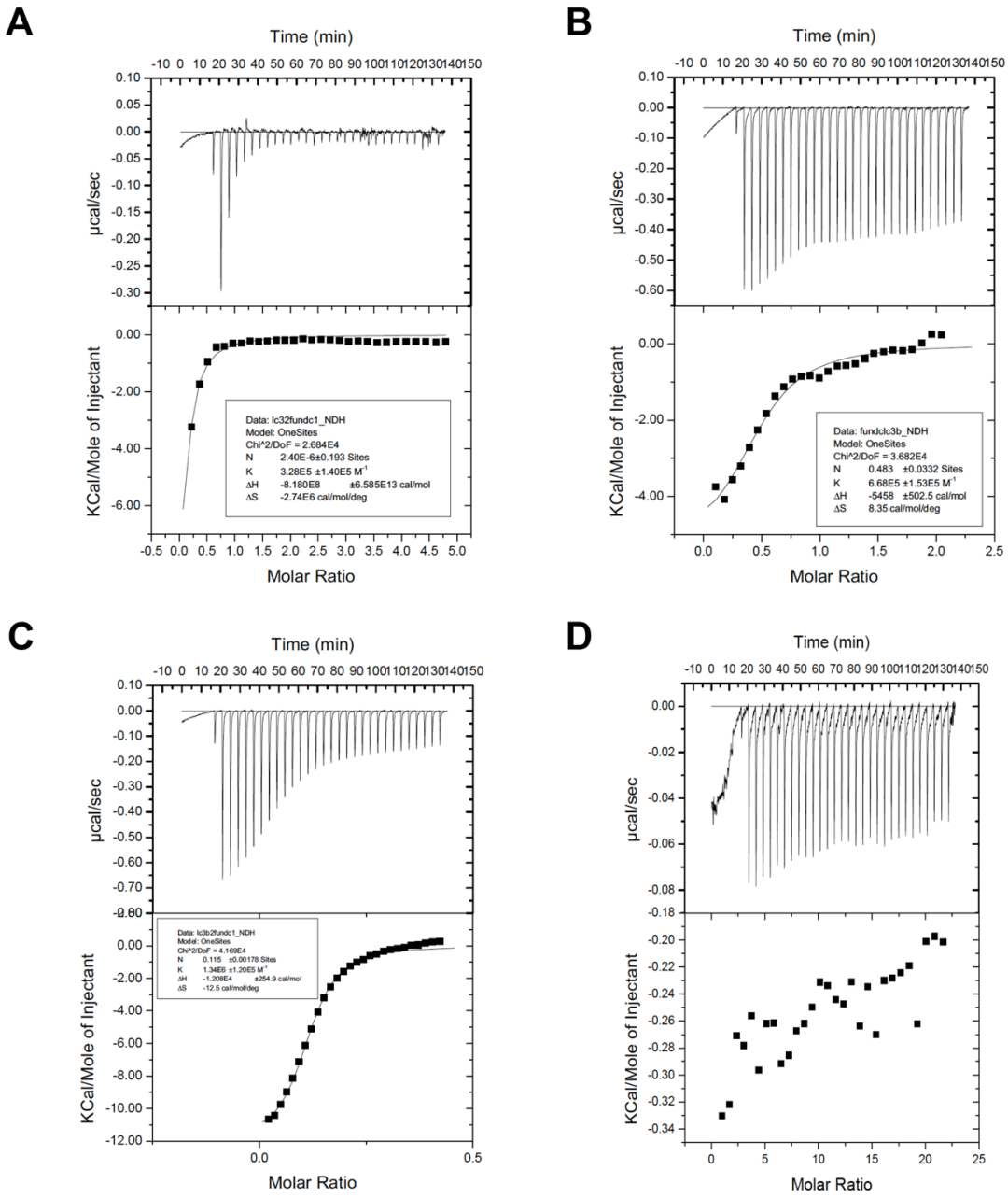

Figure 7. 12. Representative ITC measurements of the binding of the CTPR4-LIR probe and the NMR LC3B protein. Experiments were performed at 25°C, 305 rpm. A wide range

of CTPR4-LIR-to-LC3B molar ratios were tested, including 12 μM CTPR4-LIR, 256 uM LC3B (1:21) (A), 12 μM CTPR4-LIR, 120 μM LC3B (1:10) (B) and 60 μM CTPR4-LIR, 119 μM LC3B (1:2) (C) but all resulted in aberrant N values with slight protein precipitation. (D) LC3B (100 μM) was also titrated into the CTPR-RS negative control (10 μM). No heat change or binding was observed. All samples were dialysed overnight at 4°C or 3 hr at room temperature against the ITC buffer made up of 25 mM sodium phosphate buffer, 100 mM NaCl, 1 mM TCEP at pH 7.0.

We next performed a pull-down assay to determine whether the CTPR4-LIR probe could bind endogenous LC3B from NMR fibroblast lysates. CTPR4-LIR was able to pull down the LC3B-I, which was the predominant LC3B form under normal conditions and matched with the size of purified LC3B (**Figure 7.13**). No binding was observed for the CTPR4-RS, further indicating that the interaction of CTPR4-LIR with NMR LC3B was due to the grafted LIR motif and not non-specific binding. The selectivity of the CTPR4-LIR probe for LC3B over other LC3/GABARAP proteins can be also determined using anti-LC3/GABARAP antibodies.

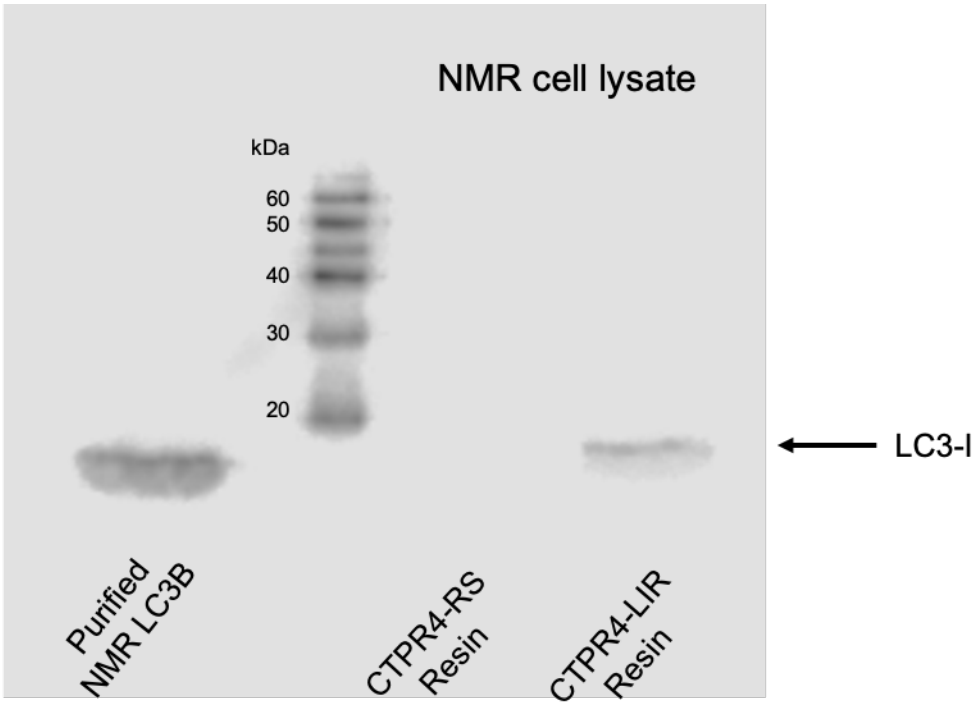

Figure 7.13. The pull-down assay using immobilised His-tagged CTPR4-LIR and CTPR4-RS and lysates of NMR skin fibroblasts as the source of LC3B. Western blot was performed using an anti-LC3B antibody. Purified NMR LC3B was loaded as a control. Experiments performed by Dr. Janet Kumita.

7.6. Discussion and future work

This chapter presents a new approach to design and create a detection probe specific for the endogenous NMR LC3B based on CTPR protein scaffolds and LIR motifs.

Compared to those expensive and relatively unstable commercial antibodies, the CTPR4-LIR probe displayed a more robust stability towards both thermal and chemical denaturation and can be expressed in *E. coli* and purified via a single-step affinity chromatography with remarkably high yields and purity. Our data suggested that the CTPR4-LIR probe was able to bind the NMR LC3B protein with a micromolar affinity, although the precise K_D value needs to be further determined using alternative tools such as SPR. The incorporation of HiBiT tag streamlined the detection process with no need of secondary antibody and prolonged incubation time.

This CTPR4-LIR probe can be used in a range of applications such as western blot and ELISA, and further optimisation of the probe can be made to enhance its binding affinity and selectivity. For example, mutation analysis can be performed to test if altering specific residues in the core LIR motif and adjacent N/C-terminal sequences will improve binding affinity to LC3B. Ser8 in the FUNDC1-LIR peptide is one of the few residues that does not closely interacting with LC3B. An S8E mutation may give rise to a new interaction between the polar amino group of the Gln26 of LC3B[351]. In addition, changing the composition of the linker sequence flanking either side of the binding peptide, which enables the peptide to maximally adopt its bioactive conformation, may also increase binding affinity[335]. Traditional fluorophore-based detection systems can also be introduced, such as maleimide coupling of a fluorophore to an engineered cysteine residue on a CTPR repeat, to create a novel CTPR4-LIR probe that is compatible with cell assays including flow cytometry and confocal microscopy.

Li *et al*. recently discovered the structural basis for a potent GABARAP binder derived from ANK3/Ankyrin G in the axons of neurons and rendered the ANK3-LIR peptide (E1991R) into a selective inhibitor, preferentially targeting GABARAP with a nanomolar affinity (K_D = 6.9 nM) but not LC3s in cells[365]. The exceptionally tight interaction was mediated by an extended amphipathic C-terminal helix in addition to the core LIR domain presented in the ANK3-LIR peptide and its mutational variants[365], a mechanism described earlier in the FYCO1-LIR

peptide which had a shorter C-helix and thus a much weaker affinity[345]. Although thus far we have applied the loop grafting strategy which is appropriate for short linear binding motifs, helix grafting could be explored whereby the GABARAP-targeting peptide containing the ANK3-LIR motif and a C-terminal helix could be grafted onto the N/C-terminus of the CTPR scaffold to create a potentially high-affinity probe as an alternative to anti-GABARAP antibodies.

It has been shown that yeast ATG19 harbours multiple LIR-like ATG8 binding sites at its C-terminus, while mammalian p62 oligomerises via an N-terminal PB1 domain to facilitate the multivalent LIR-ATG8/LC3 interactions[349,366,367]. CTPR provides an excellent platform to exploit multivalency, for instance, by grafting an LIR motif onto multiple inter-repeat loops, which may result in higher avidity and stronger interaction with ATG8 proteins in the cell. This may be particularly useful when developing a CTPR-based therapeutic molecule which recruits specific substrates such as disease-relevant aggregates to autophagosome thus inducing autophagic degradation. The Itzhaki lab has recently used a designed multi-valent CTPR protein to inhibit the cancer-associated tankyrase proteins[368].

In summary, this proof-of-concept study has validated the loop-grafting approach and rationale using CTPR scaffolds to generate detection probes targeting specific proteins, which is particularly useful for the studies in emerging animal models like the NMR where molecular tools are scarce and/or when the protein sequence homology between species is too low to be detected by commercial antibodies. The moderate affinity to target proteins via LIR motifs and the malleability of CTPR also suggest potential applications of these constructs as therapeutic molecules to drive the recruitment and degradation of specific cargo via autophagy within the cell, which can be further explored in different disease-relevant contexts.

8. Final discussion and future studies

The NMR is the longest-living rodent which shows negligible senescence over the majority of its lifespan and displays no signs of neurodegeneration. Increasing evidence has suggested that proteostatic mechanisms may contribute to the NMR's exceptional longevity and resistance to neurodegenerative disorders. However, current understanding of the proteostasis network in the NMR is heavily based on protein-level and/or cell-viability analyses. The publication of an NMR genome assembly[23] ignited analyses using genomic and transcriptomic approaches, but later scrutiny and re-analyses suggested that some of the identified traits might be resulted from incorrect annotation and did not overlap when different bioinformatics tools were applied[27]. In this study, we aimed to develop tools for studying protein homeostasis within NMRs and to use these methods to establish a relationship between proteostatic mechanisms including the UPR and autophagy with age-associated diseases from a molecular perspective.

Several key conclusions can be drawn from this study:

First of all, we have established a set of rigorous mRNA-based assays to monitor changes of key proteins involved in the UPR and autophagy in NMR cells. The RT-(q)PCR protocol was developed strictly following the MIQE guidelines and was optimised to successfully probe the changes of UPR and autophagy markers in NMR fibroblasts when exposed to different stress inducers. This methodology is probably the most reliable approach to monitor gene expression within MNRs given the poor quality of genome annotation and is more sensitive than the semi-quantitative immunoblotting analysis which has been widely used in the previous studies. In addition, this protocol can be easily modified to suit investigations into other cellular pathways and/or samples of different types.

Using the established methodology, we have observed a higher threshold of the UPR activation in the NMR kidney fibroblasts when compared to the mouse kidney fibroblasts under the treatment of mild-dose ER stress inducers. Our study constitutes the first investigation of the UPR in NMRs which is predominantly regulated at the transcript level. The higher threshold of the UPR activation in the NMR kidney fibroblasts was supported by the significantly lower induction of the UPR markers in all of the three branches, thus indicating a much lower level of ER stress induced in the NMR fibroblasts than that in the mouse fibroblasts under low-dose

TU or TG-treated ER stress. The lower induction of ER chaperones and PDIs found in the NMR fibroblasts was surprising but could suggest less compensation for the protein-folding capacity, as NMRs might possess higher constitutive levels of heat shock proteins and chaperones[72,74,216]. Since the NMR has a more stable proteome, it is also reasonable to postulate that its ER chaperones may be more resilient to oxidative stress and can maintain potent activities under stressed conditions[16]. A closer examination of structural and kinetic properties of ER chaperones in the NMR may help address these questions. The similar phenotype of low-level *Xbp1* splicing during TU or TG treatments was previously seen in a long-lived, IIS-impaired *daf*-2(-) mutant strain of *C. elegans* which also displayed resistance to ER stressors, possibly due to the induction of a new set of genes involved in longevity and ER proteostasis regulated by an interplay between the UPR and insulin/insulin-like signalling (IIS)[214]. A broader transcriptional profile can be studied using our established assays to investigate the relationship between the ISS and UPR in the NMR and how this may contribute to longevity. Another follow-up experiment that may be worth conducting is to treat these cells continuously with low-dose ER stressors for a longer period of time, which better mimics the chronic stress usually present in the context of diseases, and subsequently probe the UPR activation together with the cell viability to see (1) whether the milder level of UPR activation is sustained in the NMR cells, and (2) how this phenotype will contribute to the long-term cell survival or death in a more physiologically relevant setting. And if these NMR fibroblasts could indeed better tolerate chronic ER stress despite the lower induction of pro-survival UPR mechanisms, what might lead to their adaption to the chronic stress? The underlying mechanisms will need to be further determined. Although RT-qPCR is a powerful tool to study the UPR, posttranslational modification such as IRE1 and PERK phosphorylation still requires traditional immunoblotting analysis, which could be used, with a careful choice of suitable antibodies, together with the RT-qPCR assays to provide a more comprehensive picture of the UPR within NMRs.

We also found that the downregulation of Tfeb seemed to be universal among NMR and mouse fibroblasts when treated with chloroquine (CQ), a potent autophagy inhibitor and an anti-tumour drug. Interestingly, NMR skin fibroblasts were particularly sensitive to CQ, suggesting that the level of Tfeb repression correlated with the resistance/sensitivity to the drug. The vast majority of autophagy research mainly studied posttranslational modifications of ATG proteins until transcriptional factors were discovered and shown to play an important role in regulating autophagy-lysosomal pathways in the last decade. Current knowledge of autophagy in NMRs is also very limited based almost solely on protein-level analysis. Here we present the first

study which shows clues of the transcriptional regulation of autophagy in NMRs under stressed conditions. Although TFEB is believed to be primarily regulated by phosphorylation, which facilitates its translocation to the nucleus and subsequent activation of autophagy and lysosomal genes, transcriptional regulation of *Tfeb* may also play a role when treated with CQ, although the mechanisms by which CQ modulates *Tfeb* expression remains unknown. A closer examination of TFEB localisation within the NMR and mouse fibroblasts will allow us to determine how the altered total expression of *Tfeb* would affect relative amounts of nuclear versus cytosolic TFEB, together with the analysis of a broader range of TFEB-regulated genes and the LC3B-II turnover assay, thus establishing the relationship between the level of *Tfeb* downregulation with (1) the level of autophagic flux, (2) the transcriptional changes of TFEB target genes, and (3) sensitivity to CQ-induced lysosomal stress. In addition, fibroblasts originated from NMR skin and kidney have shown different gene expression profiles and sensitivity to CQ-induced lysosomal stress, suggesting that the effects of CQ may also be tissue-specific, which can be explored in the future as well.

We have also investigated how NMRs respond to the misfolded protein species that are known to accumulate and cause toxicity in neurodegenerative disorders. The initial study was designed to compare the effects of protein species on NMR and mouse fibroblasts, but we failed to observe any signs of UPR activation, which might be resulted from the lack of bindings of $A\beta_{1-42}$ oligomers to the fibroblast cell membrane. Instead, sensory neurons (and other neuronal cells) seemed to be a better system which could interact with and even internalise $A\beta_{1-42}$ oligomers, although experimental conditions needed to be optimised in order to probe UPR and autophagy responses before cell death. Nevertheless, *we observed that exogenously added α-synuclein oligomers could modulate transcriptional changes of the UPR and autophagy pathways and thus lead to toxic effects following an extended treatment, including decreased expression of Xbp1s, genes encoding ER chaperones and co-factors regulated by ATF6, and autophagy-related genes involved in multiple steps of the pathway.* These results suggest that α-synuclein oligomers could induce a collapse of ER-folding machinery and a decrease of autophagy clearance in the NMR kidney fibroblasts, which are only observed following long-term treatments but not acute treatments. A previous study showed that α-synuclein inhibited ATF6 activity in a cellular PD model in SH-SY5Y neuronal cells through physical interactions and the disruption of COPII ER-Golgi transport, which might ultimately disrupt signal integration among the UPR branches through reduced cooperation between ATF6 and XBP1[317]. The exact mechanisms by which α-synuclein oligomers suppress the expression of UPR and autophagy

genes in the NMR cells need to be further determined. The comparison of NMR fibroblasts with mouse cells in the context of α-synuclein treatment has not been accomplished due to the disruption caused by COVID-19 but can be continued in the future using the same approach to determine (1) whether mouse fibroblasts show different levels of sensitivity to α-synuclein, and (2) differences in the UPR and autophagy after the treatment of α-synuclein oligomers. Furthermore, fluorescent microscopy can be applied to examine the intracellular and intercellular trafficking routes of α-synuclein oligomers to (1) identify the subcellular compartments (such as lysosomes or ER) and binding partners of α-synuclein (such as ATF6) that may be affected by the cellular uptake and accumulation of α-synuclein oligomers, and (2) determine whether such trafficking is different in the NMR versus mouse cells. When samples are available, we will ideally carry out these experiments in neuronal cultures which better resemble the actual disease context. In addition, since the α-synuclein is produced intracellularly, it is worth establishing a genetically modified NMR cell line which overexpresses α-synuclein to see whether NMR cells may counteract cellular stress and toxicity induced by α-synuclein in a different way than mouse and human counterparts.

Finally, we developed and characterised a consensus-designed tetratricopeptide repeat protein (CTPR)-based probe that showed remarkable stability and moderate binding affinity specifically towards the NMR LC3B protein. Although it was not possible to determine the binding affinity using a classic ITC experiment, alternative methods such as surface plasmon resonance and ELISA may be used. A western blot assay can be performed using NMR lysates to confirm the applicability of our CTPR4-LIR probe as a detection tool in immunoblotting. Based on our current results, the binding affinity is within the micromolar range but ideally needed to be further improved in order to be comparable to commercial antibodies. Several approaches have been proposed to optimise the binding affinity of our probe to the NMR LC3B protein, including point mutation of specific residues and the incorporation of linkers to achieve better peptide display. With the success of developing such a CTPR4-LIR probe for the NMR LC3B, we can try to design other UPR probes that will target proteins which show relatively low sequence homology with mouse or human orthologues, and more importantly, explore the potential application of designed CTPR constructs to target specific proteins such as disease-related aggregation-prone α-synuclein for autophagy-mediated degradation.

In summary, using these newly established methods, we have been able to identify some unique features of the proteostasis network in the NMR that are different from the short-lived mouse,

particularly stress-response pathways including the UPR and autophagy under proteotoxic conditions. Further studies can be carried out based on our findings and using our established molecular tools to understand how these features may contribute to the NMR's exceptional longevity and resistance to age-associated neurodegeneration, and these results can be applied towards therapeutic developments to combat neurodegenerative diseases

References

1. Buffenstein, R. The Naked Mole Rat--A New Record for the Oldest Living Rodent. *Sci. Aging Knowl. Environ.* **21**, pe7 (2002).
2. Hill, W. C. O., Porter, A., Bloom, R. T., Seago, J. & Southwick, M. D. Field and laboratory studies on the naked mole rat, Heterocephalus glaber. *Proc. Zool. Soc. London.* **28**, 455-514 (1957).
3. Edrey, Y. H., Hanes, M., Pinto, M., Mele, J. & Buffenstein, R. Successful Aging and Sustained Good Health in the Naked Mole Rat: A Long-Lived Mammalian Model for Biogerontology and Biomedical Research. *ILAR J.* **52**, 41–53 (2011).
4. Buffenstein, R. Negligible senescence in the longest living rodent, the naked mole-rat: Insights from a successfully aging species. *J. Comp. Physiol. B, Biochem. Syst. Environ. Physiol.* **178**, 439–445 (2008).
5. López-Otín, C., Blasco, M. A., Partridge, L., Serrano, M. & Kroemer, G. The hallmarks of aging. *Cell* **153**, 1194-1217 (2013).
6. Jarvis, J. U. Eusociality in a mammal : cooperative breeding in naked mole-rat colonies. *Science* **212**, 571–573 (1981).
7. Buffenstein, R. *et al.* Probing pedomorphy and prolonged lifespan in naked mole-rats and dwarf mice. *Physiology* **35**, 96-111 (2020).
8. Brett, R.A., The ecology of naked mole-rat colonies: burrowing, food, and limiting factors. In: *The Biology of The Naked Mole-rat*. Princeton (NJ): Princeton University Press. pp 137-184 (1991).
9. Buffenstein, R., Woodley, R., Thomadakis, C., Daly, T. J. & Gray, D. A. Cold-induced changes in thyroid function in a poikilothermic mammal, the naked mole-rat. *Am. J. Physiol. Regul. Integr. Comp. Physiol.* **280**, R149-55 (2001).
10. Ilacqua, A. N., Kirby, A. M. & Pamenter, M. E. Behavioural responses of naked mole rats to acute hypoxia and anoxia. *Biol. Lett.* **13**, 20170545 (2017).
11. Edrey, Y. H., Park, T. J., Kang, H., Biney, A. & Buffenstein, R. Endocrine function and neurobiology of the longest-living rodent, the naked mole-rat. *Exp. Gerontol.* **46**, 116–123 (2011).
12. Harman, D. Aging: a theory based on free radical and radiation chemistry. *J. Gerontol.* **11**, 298-300 (1956).
13. Labinskyy, N. *et al.* Comparison of endothelial function, O_2-. and H_2O_2 production,

and vascular oxidative stress resistance between the longest-living rodent, the naked mole rat, and mice. *Am. J. Physiol. - Hear. Circ. Physiol.* **291**, H2698-H2704 (2006).

14. A. Rodriguez, K. *et al.* Walking the oxidative stress tightrope: a perspective from the naked mole-rat, the longest-living rodent. *Curr. Pharm. Des.* **17**, 2290-2307 (2011).
15. Andziak, B. & Buffenstein, R. Disparate patterns of age-related changes in lipid peroxidation in long-lived naked mole-rats and shorter-lived mice. *Aging Cell* **5**, 525-532 (2006).
16. Perez, V. I. *et al.* Protein stability and resistance to oxidative stress are determinants of longevity in the longest-living rodent, the naked mole-rat. *Proc. Natl. Acad. Sci.* **106**, 3059–3064 (2009).
17. Edrey, Y. H. *et al.* Oxidative damage and amyloid-β metabolism in brain regions of the longest-lived rodents. *J. Neurosci. Res.* **92**, 195-205 (2014).
18. Andziak, B. *et al.* High oxidative damage levels in the longest-living rodent, the naked mole-rat. *Aging Cell* **5**, 463–471 (2006).
19. Munro, D., Baldy, C., Pamenter, M. E. & Treberg, J. R. The exceptional longevity of the naked mole-rat may be explained by mitochondrial antioxidant defenses. *Aging Cell* **18**, e12916 (2019).
20. Lewis, K. N. *et al.* Regulation of Nrf2 signaling and longevity in naturally long-lived rodents. *Proc. Natl. Acad. Sci.* **112**, 3722-3727 (2015).
21. Heinze, I. *et al.* Species comparison of liver proteomes reveals links to naked mole-rat longevity and human aging. *BMC Biol.* **16**, 1-18 (2018)
22. Shay, J. W. Role of telomeres and telomerase in aging and cancer. *Cancer Discovery* **6**, 584-593 (2016).
23. Kim, E. B. *et al.* Genome sequencing reveals insights into physiology and longevity of the naked mole rat. *Nature* **479**, 223–227 (2011).
24. Morgan, C. C. *et al.* Molecular adaptation of telomere associated genes in mammals. *BMC Evol. Biol.* **13**, 1-13 (2013).
25. Macrae, S. L. *et al.* Comparative analysis of genome maintenance genes in naked mole rat, mouse, and human. *Aging Cell* **14**, 288-291 (2015).
26. Evfratov, S. A. *et al.* Structural features of the telomerase RNA gene in the naked mole rat Heterocephalus glaber. *Acta Naturae* **6**, 21 (2014).
27. Lewis, K. N. *et al.* Unraveling the message: insights into comparative genomics of the naked mole-rat. *Mammalian Genome* **27**, 259-278 (2016).
28. Seluanov, A. *et al.* Telomerase activity coevolves with body mass not lifespan. *Aging*

Cell **6**, 45–52 (2007).

29. Gomes, N. M. V. *et al.* Comparative biology of mammalian telomeres: Hypotheses on ancestral states and the roles of telomeres in longevity determination. *Aging Cell* **10**, 761-768 (2011).
30. Shekhidem, H. A. *et al.* Telomeres and longevity: A cause or an effect? *Int. J. Mol. Sci.* **20**, 3233 (2019).
31. Liang, S., Mele, J., Wu, Y., Buffenstein, R. & Hornsby, P. J. Resistance to experimental tumorigenesis in cells of a long-lived mammal, the naked mole-rat (Heterocephalus glaber). *Aging Cell* **9**, 626–635 (2010).
32. Seluanov, A. *et al.* Hypersensitivity to contact inhibition provides a clue to cancer resistance of naked mole-rat. *Proc. Natl. Acad. Sci.* **106**, 19352–19357 (2009).
33. Tian, X. *et al. INK4* locus of the tumor-resistant rodent, the naked mole rat, expresses a functional p15/p16 hybrid isoform. *Proc. Natl. Acad. Sci.* **112**, 1053–1058 (2015).
34. Miyawaki, S. *et al.* Tumour resistance in induced pluripotent stem cells derived from naked mole-rats. *Nat. Commun.* **7**, 11471 (2016).
35. Tian, X. *et al.* High-molecular-mass hyaluronan mediates the cancer resistance of the naked mole rat. *Nature* **499**, 346–349 (2013).
36. Hadi, F. *et al.* Transformation of naked mole-rat cells. *Nature* **583**, E1-E7 (2020).
37. Hilton, H. G. *et al.* Single-cell transcriptomics of the naked molerat reveals unexpected features of mammalian immunity. *PLoS Biol.* **17**, e3000528 (2019).
38. Treaster, S. B. *et al.* Superior proteome stability in the longest lived animal. *Age* **36**, 1009-1017 (2014).
39. Strecker, V. *et al.* Aging of different avian cultured cells: Lack of ROS-induced damage and quality control mechanisms. *Mech. Ageing Dev.* **131**, 48-59 (2010).
40. Dobson, C. M. Protein folding and misfolding. *Nature* **426**, 884-890 (2003).
41. Hipp, M. S., Kasturi, P. & Hartl, F. U. The proteostasis network and its decline in ageing. *Nat. Rev. Mol. Cell Biol.* **20**, 421-435 (2019).
42. Hartl, F. U. & Hayer-Hartl, M. Protein folding. Molecular chaperones in the cytosol: From nascent chain to folded protein. *Science* **295**, 1852-1858 (2002).
43. Mardones, P., Martínez, G. & Hetz, C. Control of systemic proteostasis by the nervous system. *Trends Cell Biol.* **25**, 1-10 (2015).
44. Labbadia, J. & Morimoto, R. I. The biology of proteostasis in aging and disease. *Annual Review of Biochemistry* **84**, 435-464 (2015).
45. Taylor, R. C. & Dillin, A. Aging as an event of proteostasis collapse. *Cold Spring*

Harb. Perspect. Biol. **3**, a004440 (2011).

46. Rubinsztein, D. C., Mariño, G. & Kroemer, G. Autophagy and aging. *Cell* **146**, 682-695 (2011).
47. Chiti, F. & Dobson, C. M. Protein misfolding, amyloid formation, and human disease: A summary of progress over the last decade. *Annu. Rev. Biochem.* **86**, 27-68 (2017).
48. Billings, L. M., Oddo, S., Green, K. N., McGaugh, J. L. & LaFerla, F. M. Intraneuronal Aβ causes the onset of early Alzheimer's disease-related cognitive deficits in transgenic mice. *Neuron* **45**, 675-688 (2005).
49. Bucciantini, M. *et al.* Inherent toxicity of aggregates implies a common mechanism for protein misfolding diseases. *Nature* **416**, 507-511 (2002).
50. Cleary, J. P. *et al.* Natural oligomers of the amyloid-β protein specifically disrupt cognitive function. *Nat. Neurosci.* **8**, 79-84 (2005).
51. Koffie, R. M. *et al.* Oligomeric amyloid β associates with postsynaptic densities and correlates with excitatory synapse loss near senile plaques. *Proc. Natl. Acad. Sci. U. S. A.* **106**, 4012-4017 (2009).
52. Lesné, S. *et al.* A specific amyloid-β protein assembly in the brain impairs memory. *Nature* **440**, 352-357 (2006).
53. Winner, B. *et al.* In vivo demonstration that α-synuclein oligomers are toxic. *Proc. Natl. Acad. Sci. U. S. A.* **108**, 4194-4199 (2011).
54. Fargnoli, J., Kunisada, T., Fornace, A. J., Schneider, E. L. & Holbrook, N. J. Decreased expression of heat shock protein 70 mRNA and protein after heat treatment in cells of aged rats. *Proc. Natl. Acad. Sci. U. S. A.* **87**, 846-850 (1990).
55. Heydari, A. R., Wu, B., Takahashi, R., Strong, R. & Richardson, A. Expression of heat shock protein 70 is altered by age and diet at the level of transcription. *Mol. Cell. Biol.* **13**, 2909-2918 (1993).
56. Hall, D. M. *et al.* Aging reduces adaptive capacity and stress protein expression in the liver after heat stress. *J. Appl. Physiol.* **89**, 749-759 (2000).
57. Hussain, S. G. & Ramaiah, K. V. A. Reduced eIF2α phosphorylation and increased proapoptotic proteins in aging. *Biochem. Biophys. Res. Commun.* **355**, 365-370 (2007).
58. Ferber, M., Pack, A. I., Zhu, Y., Naidoo, N. & Master, M. Aging impairs the unfolded protein response to sleep deprivation and leads to proapoptotic signaling. *J. Neurosci.* **28**, 6539-6548 (2008).
59. Nuss, J. E., Choksi, K. B., DeFord, J. H. & Papaconstantinou, J. Decreased enzyme activities of chaperones PDI and BiP in aged mouse livers. *Biochem. Biophys. Res.*

Commun. **365**, 355-361 (2008).

60. Keller, J. N., Huang, F. F. & Markesbery, W. R. Decreased levels of proteasome activity and proteasome expression in aging spinal cord. *Neuroscience* **98**, 149-156 (2000).
61. Ferrington, D. A., Husom, A. D. & Thompson, L. V. Altered proteasome structure, function, and oxidation in aged muscle. *FASEB J.* **19**, 1-24 (2005).
62. Cuervo, A. M. *et al.* Autophagy and aging: the importance of maintaining 'clean' cells. *Autophagy* **1**, 131-140 (2005).
63. Taylor, R. C. & Dillin, A. XBP-1 is a cell-nonautonomous regulator of stress resistance and longevity. *Cell* **153**, 1435-47 (2013).
64. Ben-Zvi, A., Miller, E. A. & Morimoto, R. I. Collapse of proteostasis represents an early molecular event in Caenorhabditis elegans aging. *Proc. Natl. Acad. Sci. U. S. A.* **106**, 14914–9 (2009).
65. Auluck, P. K., Chan, H. Y. E., Trojanowski, J. Q., Lee, V. M. Y. & Bonini, N. M. Chaperone suppression of alpha-synuclein toxicity in a Drosophila model for Parkinson's disease. *Science* **295**, 865–868 (2002).
66. Hoshino, T. *et al.* Suppression of Alzheimer's disease-related phenotypes by expression of heat shock protein 70 in mice. *J. Neurosci.* **31**, 5225–5234 (2011).
67. Sekiya, M. *et al.* EDEM function in ERAD protects against chronic ER proteinopathy and age-related physiological decline in Drosophila. *Dev. Cell* **41**, 652-664 (2017).
68. Spencer, B. *et al.* Beclin 1 gene transfer activates autophagy and ameliorates the neurodegenerative pathology in α-synuclein models of Parkinson's and Lewy body diseases. *J. Neurosci.* **29**, 13578-13588 (2009).
69. Hu, Z. Y., Chen, B., Zhang, J. P. & Ma, Y. Y. Up-regulation of autophagy-related gene 5 (ATG5) protects dopaminergic neurons in a zebrafish model of Parkinson's disease. *J. Biol. Chem.* **292**, 18062-18074 (2017).
70. De Waal, E. M. *et al.* Elevated protein carbonylation and oxidative stress do not affect protein structure and function in the long-living naked-mole rat: A proteomic approach. *Biochem. Biophys. Res. Commun.* **434**, 815-819 (2013)
71. Azpurua, J. *et al.* Naked mole-rat has increased translational fidelity compared with the mouse, as well as a unique 28S ribosomal RNA cleavage. *Proc. Natl. Acad. Sci.* **110**, 17350–17355 (2013).
72. Rodriguez, K. A. *et al.* Determinants of rodent longevity in the chaperone-protein degradation network. *Cell Stress Chaperones* **21**, 453-466 (2016).

73. Rodriguez, K. A. *et al.* A cytosolic protein factor from the naked mole-rat activates proteasomes of other species and protects these from inhibition. *Biochim. Biophys. Acta - Mol. Basis Dis.* **1842**, 2060–2072 (2014).
74. Pride, H. *et al.* Long-lived species have improved proteostasis compared to phylogenetically-related shorter-lived species. *Biochem. Biophys. Res. Commun.* **457**, 669-675 (2015).
75. Zhao, S. *et al.* High autophagy in the naked mole rat may play a significant role in maintaining good health. *Cell. Physiol. Biochem.* **33**, 321–332 (2014).
76. Salmon, A. B., Sadighi Akha, A. A., Buffenstein, R. & Miller, R. A. Fibroblasts from naked mole-rats are resistant to multiple forms of cell injury, but sensitive to peroxide, ultraviolet light, and endoplasmic reticulum stress. *J. Gerontol. A. Biol. Sci. Med. Sci.* **63**, 232–41 (2008).
77. Buffenstein, R. The Naked Mole-Rat: A New Long-Living Model for Human Aging Research. *Journals Gerontol. Ser. A Biol. Sci. Med. Sci.* **60**, 1369–1377 (2005).
78. Edrey, Y. H. *et al.* Amyloid beta and the longest-lived rodent: The naked mole-rat as a model for natural protection from alzheimer's disease. *Neurobiol. Aging* **34**, 2352–2360 (2013).
79. Orr, M. E., Garbarino, V. R., Salinas, A. & Buffenstein, R. Sustained high levels of neuroprotective, high molecular weight, phosphorylated tau in the longest-lived rodent. *Neurobiol. Aging* **36**, 1496–1504 (2015).
80. Triplett, J. C. *et al.* Age-related changes in the proteostasis network in the brain of the naked mole-rat: Implications promoting healthy longevity. *Biochim. Biophys. Acta - Mol. Basis Dis.* **1852**, 2213–2224 (2015).
81. Sunchu, B. *et al.* Aggresome-Like Formation Promotes Resistance to Proteotoxicity in Cells from Long-Lived Species. *J. Gerontol. A. Biol. Sci. Med. Sci.* (2020). doi:10.1093/gerona/glaa069
82. Ron, D. & Walter, P. Signal integration in the endoplasmic reticulum unfolded protein response. *Nat. Rev. Mol. Cell Biol.* **8**, 519–529 (2007).
83. Tsai, B., Ye, Y. & Rapoport, T. A. Retro-translocation of proteins from the endoplasmic reticulum into the cytosol. *Nat. Rev. Mol. Cell Biol.* **3**, 246-255 (2002).
84. Ogata, M. *et al.* Autophagy is activated for cell survival after endoplasmic reticulum stress. *Mol. Cell. Biol.* **26**, 9220-9231 (2006).
85. Lee, K. P. K. *et al.* Structure of the Dual Enzyme Ire1 Reveals the Basis for Catalysis and Regulation in Nonconventional RNA Splicing. *Cell* **132**, 89–100 (2008).

86. Korennykh, A. V. *et al.* The unfolded protein response signals through high-order assembly of Ire1. *Nature* **457**, 687–693 (2009).
87. Ali, M. M. U. *et al.* Structure of the Ire1 autophosphorylation complex and implications for the unfolded protein response. *EMBO J.* **30**, 894–905 (2011).
88. Calfon, M. *et al.* IRE1 couples endoplasmic reticulum load to secretory capacity by processing the XBP-1 mRNA. *Nature* **415**, 92–96 (2002).
89. Jurkin, J. *et al.* The mammalian tRNA ligase complex mediates splicing of XBP1 mRNA and controls antibody secretion in plasma cells. *EMBO J.* **33**, 2922-2936 (2014).
90. Lu, Y., Liang, F. X. & Wang, X. A synthetic biology approach identifies the mammalian UPR RNA Ligase RtcB. *Mol. Cell* **22**, 2922-2936 (2014).
91. Lee, A.-H., Iwakoshi, N. N. & Glimcher, L. H. XBP-1 regulates a subset of endoplasmic reticulum resident chaperone genes in the unfolded protein response. *Mol. Cell. Biol.* **23**, 7448-7459 (2003).
92. Yoshida, H. *et al.* A time-dependent phase shift in the mammalian unfolded protein response. *Dev. Cell* **4**, 265–271 (2003).
93. Yanagitani, K., Kimata, Y., Kadokura, H. & Kohno, K. Translational pausing ensures membrane targeting and cytoplasmic splicing of XBP1u mRNA. *Science* **331**, 586-589 (2011).
94. Yoshida, H., Oku, M., Suzuki, M. & Mori, K. pXBP1(U) encoded in XBP1 pre-mRNA negatively regulates unfolded protein response activator pXBP1(S) in mammalian ER stress response. *J. Cell Biol.* **172**, 565-575 (2006).
95. Hetz, C., Zhang, K. & Kaufman, R. J. Mechanisms, regulation and functions of the unfolded protein response. *Nat. Rev. Mol. Cell Biol.* **21**, 421-438 (2020).
96. Han, D. *et al.* IRE1α Kinase Activation Modes Control Alternate Endoribonuclease Outputs to Determine Divergent Cell Fates. *Cell* **138**, 562–575 (2009).
97. Hollien, J. *et al.* Regulated Ire1-dependent decay of messenger RNAs in mammalian cells. *J. Cell Biol.* **186**, 323-331 (2009).
98. Upton, J.-P. *et al.* IRE1 Cleaves select microRNAs during ER stress to derepress translation of proapoptotic caspase-2. *Science* **338**, 818–822 (2012).
99. Yoneda, T. *et al.* Activation of caspase-12, an endoplastic reticulum (ER) resident caspase, through tumor necrosis factor receptor-associated factor 2-dependent mechanism in response to the ER Stress. *J. Biol. Chem.* **276**, 13935-13940 (2001).

100. Urano, F. *et al.* Coupling of stress in the ER to activation of JNK protein kinases by transmembrane protein kinase IRE1. *Science* **287**, 664-666 (2000).
101. Yoshida, H. *et al.* ATF6 Activated by proteolysis binds in the presence of NF-Y (CBF) directly to the cis-acting element responsible for the mammalian unfolded protein response. *Mol. Cell. Biol.* **20**, 6755-6767 (2000).
102. Yamamoto, K. *et al.* Transcriptional induction of mammalian ER quality control proteins is mediated by single or combined action of ATF6α and XBP1. *Dev. Cell* **13**, 365–376 (2007).
103. Lu, P. D., Harding, H. P. & Ron, D. Translation reinitiation at alternative open reading frames regulates gene expression in an integrated stress response. *J. Cell Biol.* **167**, 27–33 (2004).
104. B'Chir, W. *et al.* The eIF2α/ATF4 pathway is essential for stress-induced autophagy gene expression. *Nucleic Acids Res.* **41**, 7683–7699 (2013).
105. Marciniak, S. J. *et al.* CHOP induces death by promoting protein synthesis and oxidation in the stressed endoplasmic reticulum. *Genes Dev.* **18**, 3066–3077 (2004).
106. Novoa, I., Zeng, H., Harding, H. P. & Ron, D. Feedback inhibition of the unfolded protein response by GADD34-mediated dephosphorylation of eIF2α. *J. Cell Biol.* **153**, 1011-1022 (2001).
107. Li, Y., Guo, Y., Tang, J., Jiang, J. & Chen, Z. New insights into the roles of CHOP-induced apoptosis in ER stress. *Acta Biochim. Biophys. Sin.* **8**, 860 (2014).
108. Fawcett, T. W., Martindale, J. L., Guyton, K. Z., Hai, T. & Holbrook, N. J. Complexes containing activating transcription factor (ATF)/cAMP-responsive-element-binding protein (CREB) interact with the CCAAT/enhancer-binding protein (C/EBP)-ATF composite site to regulate Gadd153 expression during the stress response. *Biochem. J.* **339**, 135-141 (1999).
109. Harding, H. P. *et al.* Regulated translation initiation controls stress-induced gene expression in mammalian cells. *Mol. Cell* **6**, 1099–1108 (2000).
110. Lu, M. *et al.* Opposing unfolded-protein-response signals converge on death receptor 5 to control apoptosis. *Science* **345**, 98–101 (2014).
111. Novoa, I. *et al.* Stress-induced gene expression requires programmed recovery from translational repression. *EMBO J.* **22**, 1180-1187 (2003).
112. Han, J. *et al.* ER-stress-induced transcriptional regulation increases protein synthesis leading to cell death. *Nat. Cell Biol.* **15**, 481–490 (2013).
113. Hoozemans, J. J. M. *et al.* The unfolded protein response is activated in pretangle

neurons in alzheimer's disease hippocampus. *Am. J. Pathol.* **174**, 1241–1251 (2009).

114. Hoozemans, J. J. M. *et al.* The unfolded protein response is activated in Alzheimer's disease. *Acta Neuropathol.* **110**, 165-172 (2005).
115. Hoozemans, J. J. M. *et al.* Activation of the unfolded protein response in Parkinson's disease. *Biochem. Biophys. Res. Commun.* **354**, 707–711 (2007).
116. Chung, C. Y. *et al.* Identification and rescue of α-synuclein toxicity in Parkinson patient-derived neurons. *Science* **342**, 983-987 (2013).
117. Casas-Tinto, S. *et al.* The ER stress factor XBP1s prevents amyloid-β neurotoxicity. *Hum. Mol. Genet.* **20**, 2144–2160 (2011).
118. Marcora, M. S., Belfiori-Carrasco, L. F., Bocai, N. I., Morelli, L. & Castaño, E. M. Amyloid-β42 clearance and neuroprotection mediated by X-box binding protein 1 signaling decline with aging in the Drosophila brain. *Neurobiol. Aging* **60**, 57–70 (2017).
119. Duran-Aniotz, C. *et al.* IRE1 signaling exacerbates Alzheimer's disease pathogenesis. *Acta Neuropathol.* **134**, 489-506 (2017).
120. Baleriola, J. *et al.* Axonally synthesized ATF4 transmits a neurodegenerative signal across brain regions. *Cell* **158**, 1159-1172 (2014).
121. Silva, R. M. *et al.* CHOP/GADD153 is a mediator of apoptotic death in substantia nigra dopamine neurons in an in vivo neurotoxin model of parkinsonism. *J. Neurochem.* **95**, 974-986 (2005).
122. Egawa, N. *et al.* The endoplasmic reticulum stress sensor, ATF6α, protects against neurotoxin-induced dopaminergic neuronal death. *J. Biol. Chem.* **286**, 7947-7957 (2011).
123. Hashida, K. *et al.* ATF6alpha promotes astroglial activation and neuronal survival in a chronic mouse model of Parkinson's disease. *PLoS One* **7**, e47950 (2012).
124. Hetz, C. & Saxena, S. ER stress and the unfolded protein response in neurodegeneration. *Nat. Rev. Neurol.* **13**, 477 (2017).
125. Deter, R. L. & De Duve, C. Influence of glucagon, an inducer of cellular autophagy, on some physical properties of rat liver lysosomes. *J. Cell Biol.* **33,** 437-449 (1967).
126. Dikic, I. & Elazar, Z. Mechanism and medical implications of mammalian autophagy. *Nat. Rev. Mol. Cell Biol.***19**, 349-364 (2018).
127. Glick, D., Barth, S. & Macleod, K. F. Autophagy : cellular and molecular mechanisms. *J. Pathol.* **221**, 3–12 (2010).
128. Saxton, R. A. & Sabatini, D. M. mTOR signaling in growth, metabolism, and disease.

Cell **168**, 960-976 (2017).

129. Jung, C. H. *et al.* ULK-Atg13-FIP200 complexes mediate mTOR signaling to the autophagy machinery. *Mol. Biol. Cell* **20**, 1992-2003 (2009).
130. Ganley, I. G. *et al.* ULK1·ATG13·FIP200 complex mediates mTOR signaling and is essential for autophagy. *J. Biol. Chem.* **284**, 12297-12305 (2009).
131. Russell, R. C. *et al.* ULK1 induces autophagy by phosphorylating Beclin-1 and activating VPS34 lipid kinase. *Nat. Cell Biol.* **15**, 741–750 (2013).
132. Volinia, S. *et al.* A human phosphatidylinolsitol 3-kinase complex related to the yeast Vps34p-Vps15p protein sorting system. *EMBO J.* **14**, 3339-3348 (1995).
133. Axe, E. L. *et al.* Autophagosome formation from membrane compartments enriched in phosphatidylinositol 3-phosphate and dynamically connected to the endoplasmic reticulum. *J. Cell Biol.* **182**, 685-701 (2008).
134. Hamasaki, M. *et al.* Autophagosomes form at ER-mitochondria contact sites. *Nature* **495**, 389-393 (2013).
135. Nascimbeni, A. C. *et al.* ER –plasma membrane contact sites contribute to autophagosome biogenesis by regulation of local PI 3P synthesis. *EMBO J.* **36**, 2018-2033 (2017).
136. Kabeya, Y. *et al.* LC3, a mammalian homologue of yeast Apg8p, is localized in autophagosome membranes after processing. *EMBO J.* **19**, 5720-5728 (2000).
137. Hemelaar, J., Lelyveld, V. S., Kessler, B. M. & Ploegh, H. L. A single protease, Apg4B, is specific for the autophagy-related ubiquitin-like proteins GATE-16, MAP1-LC3, GABARAP, and Apg8L. *J. Biol. Chem.* **278**, 51841-51850 (2003).
138. Mizushima, N., Sugita, H., Yoshimori, T. & Ohsumi, Y. A new protein conjugation system in human: The counterpart of the yeast Apg12p conjugation system essential for autophagy. *J. Biol. Chem.* **273**, 33889-33892 (1998).
139. Mizushima, N. *et al.* Dissection of autophagosome formation using Apg5-deficient mouse embryonic stem cells. *J. Cell Biol.* **152**, 657-668 (2001).
140. Tanida, I., Tanida-Miyake, E., Ueno, T. & Kominami, E. The human homolog of Saccharomyces cerevisiae Apg7p is a protein-activating enzyme for multiple substrates including human Apg12p, GATE-16, GABARAP, and MAP-LC3. *J. Biol. Chem.* **276**, 1701-1706 (2001).
141. Tanida, I., Tanida-Miyake, E., Komatsu, M., Ueno, T. & Kominami, E. Human Apg3p/Aut1p homologue is an authentic E2 enzyme for multiple substrates, GATE-16, GABARAP, and MAP-LC3, and facilitates the conjugation of hApg12p to

hApg5p. *J. Biol. Chem.* **277**, 13739-13744 (2002).

142. Mizushima, N. *et al.* Mouse Apg16L, a novel WD-repeat protein, targets to the autophagic isolation membrane with the Apg12-Apg5 conjugate. *J. Cell Sci.* **116**, 1679-1688 (2003).
143. Dooley, H. C. *et al.* WIPI2 Links LC3 Conjugation with PI3P, Autophagosome Formation, and Pathogen Clearance by Recruiting Atg12-5-16L1. *Mol. Cell* **55**, 238-252 (2014).
144. Johansen, T. & Lamark, T. Selective Autophagy: ATG8 Family Proteins, LIR Motifs and Cargo Receptors. *J. Mol. Biol.* **432**, 80-103 (2020).
145. Olsvik, H. L. *et al.* FYCO1 contains a C-terminally extended, LC3A/B-preferring LC3-interacting region (LIR) motif required for efficient maturation of autophagosomes during basal autophagy. *J. Biol. Chem.* **290**, 29361-29374 (2015).
146. Itakura, E., Kishi-Itakura, C. & Mizushima, N. The hairpin-type tail-anchored SNARE syntaxin 17 targets to autophagosomes for fusion with endosomes/lysosomes. *Cell* **151**, 1256-1269 (2012).
147. Jiang, P. *et al.* The HOPS complex mediates autophagosome-lysosome fusion through interaction with syntaxin 17. *Mol. Biol. Cell* **25**, 1327-1337 (2014).
148. Diao, J. *et al.* ATG14 promotes membrane tethering and fusion of autophagosomes to endolysosomes. *Nature* (2015). doi:10.1038/nature14147
149. Diao, J. *et al.* ATG14 promotes membrane tethering and fusion of autophagosomes to endolysosomes. *Nature* **520**, 563-566 (2015).
150. Chang, D. *et al.* A meta-analysis of genome-wide association studies identifies 17 new Parkinson's disease risk loci. *Nat. Genet.* **49**, 1511 (2017).
151. Zhu, J. H., Guo, F., Shelburne, J., Watkins, S. & Chu, C. T. Localization of Phosphorylated ERK/MAP Kinases to Mitochondria and Autophagosomes in Lewy Body Diseases. *Brain Pathol.* **13**, 473-481 (2003).
152. Decressac, M. *et al.* TFEB-mediated autophagy rescues midbrain dopamine neurons from α-synuclein toxicity. *Proc. Natl. Acad. Sci. U. S. A.* **110**, E1817-1826 (2013).
153. Lambert, M. P. *et al.* Diffusible, nonfibrillar ligands derived from Aβ1-42 are potent central nervous system neurotoxins. *Proc. Natl. Acad. Sci. U. S. A.* **95**, 6448-6453 (1998).
154. Chen, S. W. *et al.* Structural characterization of toxic oligomers that are kinetically trapped during α-synuclein fibril formation. *Proc. Natl. Acad. Sci. U. S. A.* **112**, E1994-2003 (2015).

155. Perez-Riba, A., Lowe, A. R., Main, E. R. G. & Itzhaki, L. S. Context-dependent energetics of loop extensions in a family of tandem-repeat proteins. *Biophys. J.* **114**, 2552-2562 (2018).
156. Omerbašić, D. *et al.* Hypofunctional TrkA accounts for the absence of pain sensitization in the African naked mole-rat. *Cell Rep.* **17**, 748-758 (2016).
157. Chakrabarti, S. *et al.* Acute inflammation sensitizes knee-innervating sensory neurons and decreases mouse digging behavior in a TRPV1-dependent manner. *Neuropharmacology* **143**, 49-62 (2018).
158. Hellemans, J., Mortier, G., De Paepe, A., Speleman, F. & Vandesompele, J. qBase relative quantification framework and software for management and automated analysis of real-time quantitative PCR data. *Genome Biol.* **8**, R19 (2007).
159. Schmittgen, T. D. & Livak, K. J. Analyzing real-time PCR data by the comparative CT method. *Nat. Protoc.* **3**, 1101–1108 (2008).
160. Ye, J. *et al.* Primer-BLAST: a tool to design target-specific primers for polymerase chain reaction. *BMC Bioinformatics* **13**, 1-11 (2012).
161. Pruitt, K. D., Tatusova, T., Klimke, W. & Maglott, D. R. NCBI reference sequences: Current status, policy and new initiatives. *Nucleic Acids Res.* **37**, D32-36 (2009).
162. Smith, E. S. J. *et al.* The molecular basis of acid insensitivity in the African naked mole-rat. *Science* **334**, 1557–1560 (2011).
163. Vandesompele, J. *et al.* Accurate normalization of real-time quantitative RT-PCR data by geometric averaging of multiple internal control genes. *Genome Biol.* **3**, 1-12 (2002).
164. Iwakoshi, N. N. *et al.* Plasma cell differentiation and the unfolded protein response intersect at the transcription factor XBP-1. *Nat. Immunol.* **4**, 321–329 (2003).
165. Schneider, C. A., Rasband, W. S. & Eliceiri, K. W. NIH Image to ImageJ: 25 years of image analysis. *Nat. Methods* **9**, 671–675 (2012).
166. Perez-Riba, A. & Itzhaki, L. S. A method for rapid high-throughput biophysical analysis of proteins. *Sci. Rep.* **7**, 1-6 (2017).
167. Cooper, A. Thermodynamics of protein folding and stability. In: *Protein: a comprehensive treatise*, Vol. 2. Stamford (CN): JAI Press, pp 217– 270 (1999).
168. Fersht, A. *Structure and Mechanism in Protein Science: A Guide to Enzyme Catalysis and Protein Folding*. New York: W.H. Freeman (1999).
169. Brandts, J., Brown, R., O'Brien, R. & Peters, W. ITC-derived binding constants: using microgram quantities of protein. In: *Label-Free Biosensors: Techniques and*

Applications. Cambridge, UK: Cambridge University Press (2007).

170. Oslowski, C. M. & Urano, F. Measuring ER stress and the UPR using mammalian tissue culture system. *Methods Enzymol.* **490**, 71-92 (2011).
171. Takatsuki, A., Arima, K. & Tamura, G. Tunicamycin, a new antibiotic. I. Isolation and characterization of tunicamycin. *J. Antibiot.* **24**, 215-223 (1971).
172. Tkacz, J. S. & Lampen, J. O. Tunicamycin inhibition of polyisoprenyl N-acetylglucosaminyl pyrophosphate formation in calf-liver microsomes. *Biochem. Biophys. Res. Commun.* **65**, 248-257 (1975).
173. Thastrup, O., Cullen, P. J., Drobak, B. K., Hanley, M. R. & Dawson, A. P. Thapsigargin, a tumor promoter, discharges intracellular Ca^{2+} stores by specific inhibition of the endoplasmic reticulum Ca^{2+}-ATPase. *Proc. Natl. Acad. Sci. U. S. A.* **87**, 2466-2470 (1990).
174. Lytton, J., Westlin, M. & Hanley, M. R. Thapsigargin inhibits the sarcoplasmic or endoplasmic reticulum Ca-ATPase family of calcium pumps. *J. Biol. Chem.* **266**, 17067-17071 (1991).
175. Conn, P. M. Methods in enzymology. In: *The unfolded protein response and cellular stress, Part C. Preface.* London, UK: Academic Press (2011).
176. Wu, J. *et al.* Tunicamycin specifically aggravates ER stress and overcomes chemoresistance in multidrug-resistant gastric cancer cells by inhibiting N-glycosylation. *J. Exp. Clin. Cancer Res.* **37**, 1-12 (2018).
177. Lindner, P., Christensen, S. B., Nissen, P., Møller, J. V. & Engedal, N. Cell death induced by the ER stressor thapsigargin involves death receptor 5, a non-autophagic function of MAP1LC3B, and distinct contributions from unfolded protein response components. *Cell Commun. Signal.* **18**, 1-23 (2020).
178. Liou, H. C. *et al.* A new member of the leucine zipper class of proteins that binds to the HLA DRα promoter. *Science* **247**, 1581-1584 (1990).
179. Yoshida, H., Matsui, T., Yamamoto, A., Okada, T. & Mori, K. XBP1 mRNA is induced by ATF6 and spliced by IRE1 in response to ER stress to produce a highly active transcription factor. *Cell* **107**, 881–891 (2001).
180. Shamu, C. E. & Walter, P. Oligomerization and phosphorylation of the Ire1p kinase during intracellular signaling from the endoplasmic reticulum to the nucleus. *EMBO J.* **15**, 3028-3039 (1996).
181. Cox, J. S. & Walter, P. A novel mechanism for regulating activity of a transcription factor that controls the unfolded protein response. *Cell* **87**, 391–404 (1996).

182. Travers, K. J. *et al.* Functional and genomic analyses reveal an essential coordination between the unfolded protein response and ER-associated degradation. *Cell* **101**, 249-258 (2000).
183. Zhang, K. *et al.* The unfolded protein response transducer IRE1α prevents ER stress-induced hepatic steatosis. *EMBO J.* **30**, 1357-1375 (2011).
184. Acosta-Alvear, D. *et al.* XBP1 controls diverse cell type-and condition-specific transcriptional regulatory networks. *Mol. Cell* **27**, 53-66 (2007).
185. Kaneko, M., Ishiguro, M., Niinuma, Y., Uesugi, M. & Nomura, Y. Human HRD1 protects against ER stress-induced apoptosis through ER-associated degradation. *FEBS Lett.* **532**, 147–152 (2002).
186. Yamamoto, K. *et al.* Human HRD1 promoter carries a functional unfolded protein response element to which XBP1 but not ATF6 directly binds. *J. Biochem.* **144**, 477-486 (2008).
187. Yoshida, H., Haze, K., Yanagi, H., Yura, T. & Mori, K. Identification of the cis-acting endoplasmic reticulum stress response element responsible for transcriptional induction of mammalian glucose-regulated proteins: involvement of basic leucine zipper transcription factors. *J. Biol. Chem.* **273**, 33741–33749 (1998).
188. Yoshida, H. *et al.* Endoplasmic reticulum stress-induced formation of transcription factor complex ERSF including NF-Y (CBF) and activating transcription factors 6α and 6β that activates the mammalian unfolded protein response. *Mol. Cell. Biol.* **21**, 1239-1248 (2001).
189. Ma, Y., Brewer, J. W., Alan Diehl, J. & Hendershot, L. M. Two distinct stress signaling pathways converge upon the CHOP promoter during the mammalian unfolded protein response. *J. Mol. Biol.* **18**, 1351-1365 (2002).
190. Bustin, S. a. *et al.* The MIQE guidelines:Minimum Information for publication of quantitative real-time PCR experiments. *Clin. Chem.* **55**, 611–622 (2009).
191. Ishikawa, H. Evolution of ribosomal RNA. *Comp. Biochem. Physiol. B* **58**, 1-7 (1977).
192. Natsidis, P., Schiffer, P. H., Salvador-Martínez, I. & Telford, M. J. Computational discovery of hidden breaks in 28S ribosomal RNAs across eukaryotes and consequences for RNA Integrity Numbers. *Sci. Rep.* **9**, 1-10 (2019).
193. Melen, G. J., Pesce, C. G., Rossi, M. S. & Kornblihtt, A. R. Novel processing in a mammalian nuclear 28S pre-rRNA: Tissue-specific elimination of an 'intron' bearing a hidden break site. *EMBO J.* **18**, 3107-3118 (1999).
194. Fujiwara, H. & Ishikawa, H. Molecular mechanism of introduction of the hidden break

into the 28S rRNA of insects: Implication based on structural studies. *Nucleic Acids Res.* **14**, 6393-6401 (1986).

195. Eickbush, D. G. & Eickbush, T. H. R2 Retrotransposons Encode a Self-Cleaving Ribozyme for Processing from an rRNA Cotranscript. *Mol. Cell. Biol.* **30**, 3142-3150 (2010).
196. Ke, Z. *et al.* Translation fidelity coevolves with longevity. *Aging Cell* **16**, 988-993 (2017).
197. Sugimoto, N., Nakano, S. I., Yoneyama, M. & Honda, K. I. Improved thermodynamic parameters and helix initiation factor to predict stability of DNA duplexes. *Nucleic Acids Res.* **24**, 4501-4505 (1996).
198. Zhang, Z., Schwartz, S., Wagner, L. & Miller, W. A greedy algorithm for aligning DNA sequences. *J. Comput. Biol.* **7**, 203-214 (2000).
199. Hunter, S. *et al.* InterPro: The integrative protein signature database. *Nucleic Acids Res.* **37**, D211-215 (2009).
200. Tirosh, B., Iwakoshi, N. N., Glimcher, L. H. & Ploegh, H. L. Rapid turnover of unspliced Xbp-1 as a factor that modulates the unfolded protein response. *J. Biol. Chem.* **281**, 5852-5860 (2006).
201. Kibbe, W. A. OligoCalc: An online oligonucleotide properties calculator. *Nucleic Acids Res.* **35**, W43-46 (2007).
202. Nolan, T., Hands, R. E. & Bustin, S. A. Quantification of mRNA using real-time RT-PCR. *Nat. Protoc.* **1**, 1559-1582 (2006).
203. Bright, M. D., Itzhak, D. N., Wardell, C. P., Morgan, G. J. & Davies, F. E. Cleavage of BLOC1S1 mRNA by IRE1 is sequence specific, temporally separate from XBP1 splicing, and dispensable for cell viability under acute endoplasmic reticulum stress. *Mol. Cell. Biol.* **35**, 2186-2202 (2015).
204. Arai, M. *et al.* Transformation-associated gene regulation by ATF6α during hepatocarcinogenesis. *FEBS Lett.* **580**, 184-190 (2006).
205. Wang, S. *et al.* ATF6 safeguards organelle homeostasis and cellular aging in human mesenchymal stem cells. *Cell Discov.* **4**, 1-19 (2018).
206. Kokame, K., Agarwal, K. L., Kato, H. & Miyata, T. Herp, a new ubiquitin-like membrane protein induced by endoplasmic reticulum stress. *J. Biol. Chem.* **275**, 32846–32853 (2000).
207. Hori, O. *et al.* Role of Herp in the endoplasmic reticulum stress response. *Genes to Cells* **9**, 457–469 (2004).

208. Chan, S. L. *et al.* Herp stabilizes neuronal Ca2+ homeostasis and mitochondrial function during endoplasmic reticulum stress. *J. Biol. Chem.* **279**, 28733–28743 (2004).

209. Schulze, A. *et al.* The ubiquitin-domain protein HERP forms a complex with components of the endoplasmic reticulum associated degradation pathway. *J. Mol. Biol.* **354**, 1021–1027 (2005).

210. Okuda-Shimizu, Y. & Hendershot, L. M. Characterization of an ERAD pathway for nonglycosylated BiP substrates, which require Herp. *Mol. Cell* **28**, 544-554 (2007).

211. Ma, Y. & Hendershot, L. M. Herp Is Dually Regulated by Both the Endoplasmic Reticulum Stress-specific Branch of the Unfolded Protein Response and A Branch That Is Shared with Other Cellular Stress Pathways. *J. Biol. Chem.* **279**, 13792–13799 (2004).

212. Yamamoto, K., Yoshida, H., Kokame, K., Kaufman, R. J. & Mori, K. Differential contributions of ATF6 and XBP1 to the activation of endoplasmic reticulum stress-responsive cis-acting elements ERSE, UPRE and ERSE-II. *J. Biochem.* **136**, 343–350 (2004).

213. Schuhmacher, L.-N. & Smith, E. S. J. Expression of acid-sensing ion channels and selection of reference genes in mouse and naked mole rat. *Mol. Brain* **9**, 97 (2016).

214. Henis-Korenblit, S. *et al.* Insulin/IGF-1 signaling mutants reprogram ER stress response regulators to promote longevity. *Proc. Natl. Acad. Sci. U. S. A.* **107**, 9730-9735 (2010).

215. Sadighi Akha, A. A. *et al.* Heightened induction of proapoptotic signals in response to endoplasmic reticulum stress in primary fibroblasts from a mouse model of longevity. *J. Biol. Chem.* **286**, 30344–30351 (2011).

216. Salway, K. D., Gallagher, E. J., Page, M. M. & Stuart, J. A. Higher levels of heat shock proteins in longer-lived mammals and birds. *Mech. Ageing Dev.* **132**, 287-297 (2011).

217. Klionsky, D. J. *et al.* Guidelines for the use and interpretation of assays for monitoring autophagy (3rd edition). *Autophagy* **12**, 1-222 (2016).

218. Ichimura, Y. *et al.* A ubiquitin-like system mediates protein lipidation. *Nature* **408**, 488-492 (2000).

219. He, H. *et al.* Post-translational modifications of three members of the human MAP1LC3 family and detection of a novel type of modification for MAP1LC3B. *J. Biol. Chem.* **278**, 29278-29287 (2003).

220. Bai, H., Inoue, J., Kawano, T. & Inazawa, J. A transcriptional variant of the LC3A gene is involved in autophagy and frequently inactivated in human cancers. *Oncogene* **31**, 4397-4408 (2012).
221. Koukourakis, M. I. *et al.* Autophagosome proteins LC3A, LC3B and LC3C have distinct subcellular distribution kinetics and expression in cancer cell lines. *PLoS One* **10**, e0137675 (2015).
222. Coyle, J. E., Qamar, S., Rajashankar, K. R. & Nikolov, D. B. Structure of GABARAP in two conformations: Implications for GABAA receptor localization and tubulin binding. *Neuron* **33**, 63-74 (2002).
223. Sugawara, K. *et al.* Crystallization and preliminary X-ray analysis of LC3-I. *Acta Crystallogr. - Sect. D Biol. Crystallogr.* **59**, 1464-1465 (2003)
224. Weidberg, H. *et al.* LC3 and GATE-16 N termini mediate membrane fusion processes required for autophagosome biogenesis. *Dev. Cell* **20**, 444-454 (2011).
225. Sou, Y. S. *et al.* The Atg8 conjugation system is indispensable for proper development of autophagic isolation membranes in mice. *Mol. Biol. Cell* **19**, 4762-4775 (2008).
226. Weidberg, H. *et al.* LC3 and GATE-16/GABARAP subfamilies are both essential yet act differently in autophagosome biogenesis. *EMBO J.* **29**, 1792-1802 (2010).
227. Nguyen, T. N. *et al.* Atg8 family LC3/GAB ARAP proteins are crucial for autophagosome-lysosome fusion but not autophagosome formation during PINK1/Parkin mitophagy and starvation. *J. Cell Biol.* **215**, 857-874 (2016).
228. Pankiv, S. *et al.* p62/SQSTM1 binds directly to Atg8/LC3 to facilitate degradation of ubiquitinated protein aggregates by autophagy*[S]. *J. Biol. Chem.* **282**, 24131-24145 (2007).
229. Tanida, I. *et al.* HsAtg4B/HsApg4B/autophagin-1 cleaves the carboxyl termini of three human Atg8 homologues and delipidates microtubule-associated protein light chain 3- and GABAA receptor-associated protein-phospholipid conjugates. *J. Biol. Chem.* **279**, 36268-36276 (2004).
230. Gottlieb, R. A., Finley, K. D. & Mentzer, R. M. Cardioprotection requires taking out the trash. *Basic Res. Cardiol.* **104**, 169-180 (2009).
231. Tanida, I., Minematsu-Ikeguchi, N., Ueno, T. & Kominami, E. Lysosomal turnover, but not a cellular level, of endogenous LC3 is a marker for autophagy. *Autophagy* **1**, 84-91 (2005).
232. Mauthe, M. *et al.* Chloroquine inhibits autophagic flux by decreasing autophagosome-lysosome fusion. *Autophagy* **14**, 1435-1455 (2018).

233. Seglen, P. O., Grinde, B. & Solheim, A. E. Inhibition of the lysosomal pathway of protein degradation in isolated rat hepatocytes by ammonia, Methylamine, Chloroquine and Leupeptin. *Eur. J. Biochem.* **95**, 215-225 (1979).
234. Martina, J. A., Chen, Y., Gucek, M. & Puertollano, R. MTORC1 functions as a transcriptional regulator of autophagy by preventing nuclear transport of TFEB. *Autophagy* **8**, 903-914 (2012).
235. Nazio, F. *et al.* MTOR inhibits autophagy by controlling ULK1 ubiquitylation, self-association and function through AMBRA1 and TRAF6. *Nat. Cell Biol.* **15**, 406-416 (2013).
236. Laplante, M. & Sabatini, D. M. mTOR signaling at a glance. *J. Cell Sci.* **122**, 3589-3594 (2009).
237. Arotcarena, M.-L., Teil, M. & Dehay, B. Autophagy in synucleinopathy: the overwhelmed and defective machinery. *Cells* **8**, 565 (2019).
238. Putyrski, M. & Schultz, C. Protein translocation as a tool: The current rapamycin story. *FEBS Letters* **586**, 2097-2105 (2012).
239. Kirisako, T. *et al.* Formation process of autophagosome is traced with Apg8/Aut7p in yeast. *J. Cell Biol.* **147**, 435-446 (1999).
240. Füllgrabe, J., Ghislat, G., Cho, D.-H. & Rubinsztein, D. C. Transcriptional regulation of mammalian autophagy at a glance. *J. Cell Sci.* **129**, 3059–3066 (2016).
241. Hemesath, T. J. *et al.* microphthalmia, A critical factor in melanocyte development, defines a discrete transcription factor family. *Genes Dev.* **8**, 2770-2780 (1994).
242. Settembre, C. *et al.* TFEB Links Autophagy to Lysosomal Biogenesis. *Science* **332**, 1429–1433 (2011).
243. Sardiello, M. *et al.* A gene network regulating lysosomal biogenesis and function. *Science* **325**, 473-477 (2009).
244. Palmieri, M. *et al.* Characterization of the CLEAR network reveals an integrated control of cellular clearance pathways. *Hum. Mol. Genet.* **20**, 3852-3866 (2011).
245. Vega-Rubin-de-Celis, S., Peña-Llopis, S., Konda, M. & Brugarolas, J. Multistep regulation of TFEB by MTORC1. *Autophagy* **13**, 464-472 (2017).
246. Napolitano, G. *et al.* mTOR-dependent phosphorylation controls TFEB nuclear export. *Nat. Commun.* **9**, 1-10 (2018).
247. Medina, D. L. *et al.* Lysosomal calcium signalling regulates autophagy through calcineurin and TFEB. *Nat. Cell Biol.* **17**, 288-299 (2015).
248. Settembre, C. *et al.* TFEB controls cellular lipid metabolism through a starvation-

induced autoregulatory loop. *Nat. Cell Biol.* **15**, 647-658 (2013).

249. Chauhan, S. *et al.* ZKSCAN3 is a master transcriptional repressor of autophagy. *Mol. Cell* **50**, 16-28 (2013).
250. Zhao, J. *et al.* FoxO3 coordinately activates protein degradation by the autophagic/lysosomal and proteasomal pathways in atrophying muscle cells. *Cell Metab.* **6**, 472–483 (2007).
251. Mammucari, C. *et al.* FoxO3 controls autophagy in skeletal muscle in vivo. *Cell Metab.* **6**, 458-471 (2007).
252. Sanchez, A. M. J. *et al.* AMPK promotes skeletal muscle autophagy through activation of forkhead FoxO3a and interaction with Ulk1. *J. Cell Biochem.* **113**, 695-710 (2012).
253. Crighton, D. *et al.* DRAM, a p53-induced modulator of autophagy, is critical for apoptosis. *Cell* **126**, 121-134 (2006).
254. Budanov, A. V. & Karin, M. p53 Target genes sestrin1 and sestrin2 connect genotoxic stress and mTOR signaling. *Cell* **134**, 451-460 (2008).
255. Kenzelmann Broz, D. *et al.* Global genomic profiling reveals an extensive p53-regulated autophagy program contributing to key p53 responses. *Genes Dev.* **27**, 1016-1031 (2013).
256. Tasdemir, E. *et al.* Regulation of autophagy by cytoplasmic p53. *Nat. Cell Biol.* **10**, 676-687 (2008).
257. Scherz-Shouval, R. *et al.* p53-dependent regulation of autophagy protein LC3 supports cancer cell survival under prolonged starvation. *Proc. Natl. Acad. Sci. U. S. A.* **107**, 18511-18516 (2010).
258. Huang, Y., Guerrero-Preston, R. & Ratovitski, E. A. Phospho-ΔNp63α-dependent regulation of autophagic signaling through transcription and micro-RNA modulation. *Cell Cycle* **11**, 1247-1259 (2012).
259. Polager, S., Ofir, M. & Ginsberg, D. E2F1 regulates autophagy and the transcription of autophagy genes. *Oncogene* **27**, 4860-4864 (2008).
260. Tracy, K. *et al.* BNIP3 Is an RB/E2F Target Gene Required for Hypoxia-Induced Autophagy. *Mol. Cell. Biol.* **27**, 6229-6242 (2007).
261. Shaw, J. *et al.* Antagonism of E2F-1 regulated Bnip3 transcription by NF-κB is essential for basal cell survival. *Proc. Natl. Acad. Sci. U. S. A.* **105**, 20734-20739 (2008).
262. Copetti, T., Bertoli, C., Dalla, E., Demarchi, F. & Schneider, C. p65/RelA modulates BECN1 transcription and autophagy. *Mol. Cell. Biol.* **29**, 2594-2608 (2009).

263. Ling, J. *et al.* KrasG12D-induced IKK2/β/NF-κB activation by IL-1α and p62 feedforward loops is required for development of pancreatic ductal adenocarcinoma. *Cancer Cell* **21**, 105-120 (2012).
264. Seok, S. *et al.* Transcriptional regulation of autophagy by an FXR-CREB axis. *Nature* **516**, 108-111 (2014).
265. Lee, J. M. *et al.* Nutrient-sensing nuclear receptors coordinate autophagy. *Nature* **516**, 112-115 (2014).
266. Ma, D., Panda, S. & Lin, J. D. Temporal orchestration of circadian autophagy rhythm by C/EBPβ. *EMBO J.* **30**, 4642-4651 (2011).
267. Kang, Y.-A. *et al.* Autophagy driven by a master regulator of hematopoiesis. *Mol. Cell. Biol.* **32**, 226-239 (2012).
268. Jia, G., Cheng, G., Gangahar, D. M. & Agrawal, D. K. Insulin-like growth factor-1 and TNF-α regulate autophagy through c-jun N-terminal kinase and Akt pathways in human atherosclerotic vascular smooth cells. *Immunol. Cell Biol.* **84**, 448-454 (2006).
269. Li, D. D. *et al.* The pivotal role of c-Jun NH2-terminal kinase-mediated Beclin 1 expression during anticancer agents-induced autophagy in cancer cells. *Oncogene* **28**, 886-898 (2009).
270. Sun, T. *et al.* C-Jun NH2-terminal kinase activation is essential for up-regulation of LC3 during ceramide-induced autophagy in human nasopharyngeal carcinoma cells. *J. Transl. Med.* **9**, 1-10 (2011).
271. Di Malta, C., Cinque, L. & Settembre, C. Transcriptional regulation of autophagy: Mechanisms and diseases. *Frontiers in Cell and Developmental Biology* **7**, 114 (2019).
272. Edgar, R. C. MUSCLE: Multiple sequence alignment with high accuracy and high throughput. *Nucleic Acids Res.* **32**, 1792-1797 (2004).
273. Zhao, S. *et al.* H_2O_2 treatment or serum deprivation induces autophagy and apoptosis in naked mole-rat skin fibroblasts by inhibiting the PI3K/Akt signaling pathway. *Oncotarget* **7**, 84839 (2016).
274. Engedal, N. *et al.* Modulation of intracellular calcium homeostasis blocks autophagosome formation. *Autophagy* **9**, 1475-1490 (2013).
275. Settembre, C. *et al.* A lysosome-to-nucleus signalling mechanism senses and regulates the lysosome via mTOR and TFEB. *EMBO J.* **31**, 1095-1108 (2012).
276. Roczniak-Ferguson, A. *et al.* The transcription factor TFEB links mTORC1 signaling to transcriptional control of lysosome homeostasis. *Sci. Signal.* **5**, ra42-ra42 (2012).
277. Napolitano, G. & Ballabio, A. TFEB at a glance. *J. Cell Sci.* **129**, 2475-2481 (2016).

278. Thoreen, C. C. *et al.* An ATP-competitive mammalian target of rapamycin inhibitor reveals rapamycin-resistant functions of mTORC1. *J. Biol. Chem.* **284**, 8023-8032 (2009).
279. Peng, T., Golub, T. R. & Sabatini, D. M. The immunosuppressant rapamycin mimics a starvation-like signal distinct from amino acid and glucose deprivation. *Mol. Cell. Biol.* **22**, 5575-5584 (2002).
280. Mizushima, N. & Yoshimori, T. How to interpret LC3 immunoblotting. *Autophagy* **3**, 542-545 (2007).
281. A Ahmed, M. *et al.* Structural conversion of neurotoxic amyloid-β 1–42 oligomers to fibrils. *Nat. Struct. Mol. Biol.* **17**, 561 (2010).
282. Aran Terol, P., Kumita, J. R., Hook, S. C., Dobson, C. M. & Esbjörner, E. K. Solvent exposure of Tyr10 as a probe of structural differences between monomeric and aggregated forms of the amyloid-β peptide. *Biochem. Biophys. Res. Commun.* **468**, 696-701 (2015).
283. Gong, Y. *et al.* Alzheimer's disease-affected brain: Presence of oligomeric Aβ ligands (ADDLs) suggests a molecular basis for reversible memory loss. *Proc. Natl. Acad. Sci. U. S. A.* **100**, 10417-10422 (2003).
284. Lambert, M. P. *et al.* Vaccination with soluble Aβ oligomers generates toxicity-neutralizing antibodies. *J. Neurochem.* **79**, 595-605 (2001).
285. Chromy, B. A. *et al.* Self-assembly of Aβ1-42 into globular neurotoxins. *Biochemistry* **42**, 12749-12760 (2003).
286. Cremades, N. *et al.* Direct observation of the interconversion of normal and toxic forms of α-synuclein. *Cell* **149**, 1048-1059 (2012).
287. Ehrnhoefer, D. E. *et al.* EGCG redirects amyloidogenic polypeptides into unstructured, off-pathway oligomers. *Nat. Struct. Mol. Biol.* **15**, 558 (2008).
288. Fusco, G. *et al.* Structural basis of membrane disruption and cellular toxicity by a-synuclein oligomers. *Science* **358**, 1440-1443 (2017).
289. Paslawski, W. *et al.* High stability and cooperative unfolding of α-Synuclein Oligomers. *Biochemistry* **53**, 6252-6263 (2014).
290. Resende, R., Ferreiro, E., Pereira, C. & Resende de Oliveira, C. Neurotoxic effect of oligomeric and fibrillar species of amyloid-beta peptide 1-42: involvement of endoplasmic reticulum calcium release in oligomer-induced cell death. *Neuroscience* **155**, 725-737 (2008).
291. Castillo-Carranza, D. L. *et al.* Differential activation of the ER stress factor XBP1 by

oligomeric assemblies. *Neurochem. Res.* **37**, 1707–1717 (2012).

292. Resende, R., Ferreiro, E., Pereira, C. & Oliveira, C. R. ER stress is involved in Aβ-induced GSK-3β activation and tau phosphorylation. *J. Neurosci. Res.* **86**, 2091-2099 (2008).
293. Costa, R. O. *et al.* Endoplasmic reticulum stress occurs downstream of GluN2B subunit of N-methyl-d-aspartate receptor in mature hippocampal cultures treated with amyloid-β oligomers. *Aging Cell* **11**, 823-833 (2012).
294. Knauer, M. F., Soreghan, B., Burdick, D., Kosmoski, J. & Glabe, C. G. Intracellular accumulation and resistance to degradation of the Alzheimer amyloid A4/β protein. *Proc. Natl. Acad. Sci. U. S. A.* **89**, 7437-7441 (1992).
295. Yu, M. S. *et al.* Beta-amyloid peptides induces neuronal apoptosis via a mechanism independent of unfolded protein responses. *Apoptosis* **11**, 687-700 (2006).
296. Costa, R. O., Ferreiro, E., Cardoso, S. M., Oliveira, C. R. & Pereira, C. M. F. ER stress-mediated apoptotic pathway induced by aβ peptide requires the presence of functional mitochondria. *J. Alzheimer's Dis.* **20**, 625-636 (2010).
297. Lee, D. Y. *et al.* Activation of PERK signaling attenuates Aβ-mediated ER stress. *PLoS One* **5**, e10489 (2010).
298. Hawe, A., Sutter, M. & Jiskoot, W. Extrinsic fluorescent dyes as tools for protein characterization. *Pharm. Res.* **25**, 1487-1499 (2008).
299. Bolognesi, B. *et al.* ANS binding reveals common features of cytotoxic amyloid species. *ACS Chem. Biol.* **5**, 735-740 (2010).
300. Malchiodi-Albedi, F. *et al.* Lipid raft disruption protects mature neurons against amyloid oligomer toxicity. *Biochim. Biophys. Acta - Mol. Basis Dis.* **1802**, 406-415 (2010).
301. Williamson, R., Usardi, A., Hanger, D. P. & Anderton, B. H. Membrane-bound β-amyloid oligomers are recruited into lipid rafts by a fyn-dependent mechanism. *FASEB J.* **22**, 1552-1559 (2008).
302. Frankel, D. *et al.* Cholesterol-rich naked mole-rat brain lipid membranes are susceptible to amyloid beta-induced damage in vitro. *Aging (Albany. NY).* **12**, 22266 (2020).
303. Chafekar, S. M., Hoozemans, J. J. M., Zwart, R., Baas, F. & Scheper, W. Aβ1-42 induces mild endoplasmic reticulum stress in an aggregation state-dependent manner. *Antioxid. Redox Signal.* **9**, 2245-2254 (2007).
304. El-Agnaf, O. M. A. *et al.* Detection of oligomeric forms of α-synuclein protein in

human plasma as a potential biomarker for Parkinson's disease. *FASEB J.* **20**, 419-425 (2006).

305. Danzer, K. M. *et al.* Heat-shock protein 70 modulates toxic extracellular α-synuclein oligomers and rescues trans-synaptic toxicity. *FASEB J.* **25**, 326-336 (2011).
306. Danzer, K. M. *et al.* Exosomal cell-to-cell transmission of alpha synuclein oligomers. *Mol. Neurodegener.* **7**, 1-18 (2012).
307. Kim, C. *et al.* Neuron-released oligomeric α-synuclein is an endogenous agonist of TLR2 for paracrine activation of microglia. *Nat. Commun.* **4**, 1-12 (2013).
308. Lee, H. J. *et al.* Assembly-dependent endocytosis and clearance of extracellular α-synuclein. *Int. J. Biochem. Cell Biol.* **40**, 1835-1849 (2008).
309. Lashuel, H. A., Hartley, D., Petre, B. M., Walz, T. & Lansbury, P. T. Amyloid pores from pathogenic mutations. *Nature* **418**, 291 (2002).
310. Quist, A. *et al.* Amyloid ion channels: A common structural link for protein-misfolding disease. *Proc. Natl. Acad. Sci. U. S. A.* **102**, 10427-10432 (2005).
311. Perni, M. *et al.* A natural product inhibits the initiation of α-synuclein aggregation & suppresses its toxicity. *Proc. Natl. Acad. Sci. U. S. A.* **114**, E1009-E1017 (2017).
312. Valdés, P. *et al.* Control of dopaminergic neuron survival by the unfolded protein response transcription factor XBP1. *Proc. Natl. Acad. Sci. U. S. A.* **111**, 6804-6809 (2014).
313. Sado, M. *et al.* Protective effect against Parkinson's disease-related insults through the activation of XBP1. *Brain Res.* **1257**, 16-24 (2009).
314. Wu, J. *et al.* ATF6α optimizes long-term endoplasmic reticulum function to protect cells from chronic stress. *Dev. Cell* **13**, 351-364 (2007).
315. Gorbatyuk, M. S. *et al.* Glucose Regulated Protein 78 Diminishes α-Synuclein Neurotoxicity in a Rat Model of Parkinson Disease. *Mol. Ther.* **20**, 1327–1337 (2012).
316. Gomez, J. A. & Rutkowski, D. T. Experimental reconstitution of chronic ER stress in the liver reveals feedback suppression of BiP mRNA expression. *Elife* **5**, e20390 (2016).
317. Credle, J. J. *et al.* α-Synuclein-mediated inhibition of ATF6 processing into COPII vesicles disrupts UPR signaling in Parkinson's disease. *Neurobiol. Dis.* **76**, 112-125 (2015).
318. Hoffmann, A. C. *et al.* Extracellular aggregated alpha synuclein primarily triggers lysosomal dysfunction in neural cells prevented by trehalose. *Sci. Rep.* **9**, 1-18 (2019).
319. Kajava, A. V. Review: Proteins with repeated sequence - Structural prediction and

modeling. *Journal of Structural Biology* **134**, 132-144 (2001).

320. Itzhaki, L. S. & Lowe, A. R. From artificial antibodies to nanosprings: the biophysical properties of repeat proteins. *Advances in Experimental Medicine and Biology* **747**, 153–166 (2012).
321. Hirano, T., Kinoshita, N., Morikawa, K. & Yanagida, M. Snap helix with knob and hole: Essential repeats in S. pombe nuclear protein nuc2+. *Cell* **60**, 319-328 (1990).
322. Sikorski, R. S., Boguski, M. S., Goebl, M. & Hieter, P. A repeating amino acid motif in CDC23 defines a family of proteins and a new relationship among genes required for mitosis and RNA synthesis. *Cell* **60**, 307-317 (1990).
323. Perez-Riba, A. & Itzhaki, L. S. The tetratricopeptide-repeat motif is a versatile platform that enables diverse modes of molecular recognition. *Current Opinion in Structural Biology* **54**, 43-49 (2019).
324. Das, A. K., Cohen, P. T. W. & Barford, D. The structure of the tetratricopeptide repeats of protein phosphatase 5: Implications for TPR-mediated protein-protein interactions. *EMBO J.* **17**, 1192-1199 (1998).
325. Main, E. R. G., Xiong, Y., Cocco, M. J., D'Andrea, L. & Regan, L. Design of stable α-helical arrays from an idealized TPR motif. *Structure* **11**, 497-508 (2003).
326. Lapouge, K. *et al.* Structure of the TPR domain of p67(phox) in complex with Rac·GTP. *Mol. Cell* **6**, 899-907 (2000).
327. Cliff, M. J., Harris, R., Barford, D., Ladbury, J. E. & Williams, M. A. Conformational diversity in the TPR domain-mediated interaction of protein phosphatase 5 with Hsp90. *Structure* **14**, 415-426 (2006).
328. Desjarlais, J. R. & Berg, J. M. Use of a zinc-finger consensus sequence framework and specificity rules to design specific DNA binding proteins. *Proc. Natl. Acad. Sci. U. S. A.* **90**, 2256-2260 (1993).
329. Grove, T. Z., Osuji, C. O., Forster, J. D., Dufresne, E. R. & Regan, L. Stimuli-responsive smart gels realized via modular protein design. *J. Am. Chem. Soc.* **132**, 14024-14026 (2010).
330. Cortajarena, A. L., Mochrie, S. G. J. & Regan, L. Modulating repeat protein stability: The effect of individual helix stability on the collective behavior of the ensemble. *Protein Sci.* **20**, 1042-1047 (2011).
331. Scheufler, C. *et al.* Structure of TPR domain-peptide complexes: Critical elements in the assembly of the Hsp70-Hsp90 multichaperone machine. *Cell* **101**, 199-210 (2000).
332. Cortajarena, A. L., Yi, F. & Regan, L. Designed TPR modules as novel anticancer

agents. *ACS Chem. Biol.* **3**, 161-166 (2008).

333. Jackrel, M. E., Valverde, R. & Regan, L. Redesign of a protein-peptide interaction; Characterization and applications. *Protein Sci.* **18**, 762-774 (2009).
334. Cortajarena, A. L., Liu, T. Y., Hochstrasser, M. & Regan, L. Designed proteins to modulate cellular networks. *ACS Chem. Biol.* **5**, 545-552 (2010).
335. Madden, S. K., Perez-Riba, A. & Itzhaki, L. S. Exploring new strategies for grafting binding peptides onto protein loops using a consensus-designed tetratricopeptide repeat scaffold. *Protein Sci.* **28**, 738-745 (2019).
336. Birgisdottir, Å. B., Lamark, T. & Johansen, T. The LIR motif - crucial for selective autophagy. *J. Cell Sci.* **126**, 3237-3247 (2013).
337. Rogov, V. V *et al.* Structural and functional analysis of the GABARAP interaction motif (GIM). *EMBO Rep.* **18**, 1382-1396 (2017).
338. Ichimura, Y. *et al.* Structural basis for sorting mechanism of p62 in selective autophagy. *J. Biol. Chem.* **283**, 22847-22957 (2008).
339. Noda, N. N. *et al.* Structural basis of target recognition by Atg8/LC3 during selective autophagy. *Genes to Cells* **13**, 1211-1218 (2008).
340. Rozenknop, A. *et al.* Characterization of the interaction of GABARAPL-1 with the LIR motif of NBR1. *J. Mol. Biol.* **410**, 477-487 (2011).
341. Shvets, E., Fass, E., Scherz-Shouval, R. & Elazar, Z. The N-terminus and Phe52 residue of LC3 recruit p62/SQSTM1 into autophagosomes. *J. Cell Sci.* **121**, 2685-2695 (2008).
342. Shvets, E., Abada, A., Weidberg, H. & Elazar, Z. Dissecting the involvement of LC3B and GATE-16 in p62 recruitment into autophagosomes. *Autophagy* **7**, 683-688 (2011).
343. Ichimura, Y. *et al.* Structural determinants in GABARAP required for the selective binding and recruitment of ALFY to LC3B-positive structures. *EMBO Rep.* **15**, 557-565 (2014).
344. Cheng, X. *et al.* Structural basis of FYCO1 and MAP1LC3A interaction reveals a novel binding mode for Atg8-family proteins. *Autophagy* **12**, 1330-1339 (2016).
345. Sakurai, S., Tomita, T., Shimizu, T. & Ohto, U. The crystal structure of mouse LC3B in complex with the FYCO1 LIR reveals the importance of the flanking region of the LIR motif. *Acta Crystallogr. Sect. Struct. Biol. Commun.* **73**, 130-137 (2017).
346. Alemu, E. A. *et al.* ATG8 family proteins act as scaffolds for assembly of the ULK complex: Sequence requirements for LC3-interacting region (LIR) motifs. *J. Biol. Chem.* **287**, 39275-39290 (2012).

347. Birgisdottir, Å. B. *et al.* Members of the autophagy class III phosphatidylinositol 3-kinase complex I interact with GABARAP and GABARAPL1 via LIR motifs. *Autophagy* **15**, 1333-1355 (2019).
348. Kaufmann, A., Beier, V., Franquelim, H. G. & Wollert, T. Molecular mechanism of autophagic membrane-scaffold assembly and disassembly. *Cell* **156**, 469-481 (2014).
349. Wurzer, B. *et al.* Oligomerization of p62 allows for selection of ubiquitinated cargo and isolation membrane during selective autophagy. *Elife* **4**, e09841 (2015).
350. Turco, E. *et al.* FIP200 claw domain binding to p62 promotes autophagosome formation at ubiquitin condensates. *Mol. Cell* **74**, 330-346 (2019).
351. Kuang, Y. *et al.* Structural basis for the phosphorylation of FUNDC1 LIR as a molecular switch of mitophagy. *Autophagy* **12**, 2363-2373 (2016).
352. Liu, L. *et al.* Mitochondrial outer-membrane protein FUNDC1 mediates hypoxia-induced mitophagy in mammalian cells. *Nat. Cell Biol.* **14**, 177-185 (2012).
353. Chen, G. *et al.* A regulatory signaling loop comprising the PGAM5 phosphatase and CK2 controls receptor-mediated mitophagy. *Mol. Cell* **54**, 362-377 (2014).
354. Pankiv, S. *et al.* FYCO1 is a Rab7 effector that binds to LC3 and PI3P to mediate microtubule plus end - Directed vesicle transport. *J. Cell Biol.* **188**, 253-269 (2010).
355. Schwinn, M. K. *et al.* CRISPR-mediated tagging of endogenous proteins with a luminescent peptide. *ACS Chem. Biol.* **13**, 467-474 (2018).
356. Waterhouse, A. *et al.* SWISS-MODEL: Homology modelling of protein structures and complexes. *Nucleic Acids Res.* **46**, W296-W303 (2018).
357. Kajander, T., Cortajarena, A. L., Mochrie, S. & Regan, L. Structure and stability of designed TPR protein superhelices: Unusual crystal packing and implications for natural TPR proteins. *Acta Crystallogr. Sect. D Biol. Crystallogr.* **63**, 800-811 (2007).
358. Gasteiger, E. *et al.* ExPASy: The proteomics server for in-depth protein knowledge and analysis. *Nucleic Acids Res.* **31**, 3784-3788 (2003).
359. Greenfield, N. J. Using circular dichroism spectra to estimate protein secondary structure. *Nat. Protoc.* **1**, 2876 (2007).
360. Holzwarth, G. & Doty, P. The ultraviolet circular dichroism of polypeptides. *J. Am. Chem. Soc.* **87**, 218-228 (1965).
361. Vermeer, A. W. P. & Norde, W. The thermal stability of immunoglobulin: Unfolding and aggregation of a multi-domain protein. *Biophys. J.* **78**, 394-404 (2000).
362. Batey, S., Randles, L. G., Steward, A. & Clarke, J. Cooperative folding in a multi-domain protein. *J. Mol. Biol.* **349**, 1045-1059 (2005).

363. Myers, J. K., Nick Pace, C. & Martin Scholtz, J. Denaturant m values and heat capacity changes: Relation to changes in accessible surface areas of protein unfolding. *Protein Sci.* **4**, 2138-2148 (1995).
364. Sedlák, E., Schaefer, J. V., Marek, J., Gimeson, P. & Plückthun, A. Advanced analyses of kinetic stabilities of iggs modified by mutations and glycosylation. *Protein Sci.* **24**, 1100-1113 (2015).
365. Li, J. *et al.* Potent and specific Atg8-targeting autophagy inhibitory peptides from giant ankyrins. *Nat. Chem. Biol.* **14**, 778-787 (2018).
366. Sawa-Makarska, J. *et al.* Cargo binding to Atg19 unmasks additional Atg8 binding sites to mediate membrane-cargo apposition during selective autophagy. *Nat. Cell Biol.* **15**, 425-433 (2014).
367. Abert, C., Kontaxis, G. & Martens, S. Accessory interaction motifs in the Atg19 cargo receptor enable strong binding to the clustered ubiquitin-related Atg8 protein. *J. Biol. Chem.* **291**, 18799-18808 (2016).
368. Diamante, A. *et al.* Engineering mono- and multi-valent inhibitors on a modular scaffold. *Chem. Sci.* **12**, 880-895 (2021).